Mitteilungen aus dem Institut für Mechanik

Sandra Ilic

Application of the multiscale FEM to the modeling of composite materials

Heft Nr. 147

RUHR-UNIVERSITÄT BOCHUM

RUHR-UNIVERSITÄT BOCHUM
Institut für Mechanik

Sandra Ilic

Application of the multiscale FEM to the modeling of composite materials

Mitteilungen aus dem Institut für Mechanik Nr. 147

Herausgeber:

Institut für Mechanik
— Schriftenreihe —
Ruhr-Universität Bochum
D-44780 Bochum

ISBN 3-935892-25-4

Printed in Germany

To my mother

Abstract

This thesis deals in particular with the concept and application of the multiscale finite element method, resulting from a combination of the homogenization theory and the theory of the finite elements. The method is used to simulate the behavior of a macroscopic body with material properties defined by the geometry and structure of a representative volume element and is suitable for cases where the ratio of the characteristic lengths of the scales tends to zero. Accordingly, the terminology "macro" relates to the problem of the real body simulation and "micro" to the problem considering the representative volume element. The property making this method attractive, is that it can be applied to nonlinear composite materials and finite deformations without greater difficulties. The work examines materials with periodic and random microstructure, explaining three examples in detail: the calculation of the effective material parameters of microporous media, the studying of deformations caused by solution-precipitation creep and the simulation of the behavior of cancellous bone under ultrasonic excitation.

Zusammenfassung

Diese Arbeit behandelt insbesondere das Konzept und die Anwendung der Multiskalen Finite Elemente Methode, welche eine Verbindung der Homogenisierungsmethode und der Theorie der Finiten Elemente darstellt. Diese Methode wird benutzt, um das Verhalten eines makroskopischen Körpers zu simulieren. Dessen Materialeigenschaften werden durch Geometrie und Struktur eines repräsentativen Volumenelementes bestimmt. Die Methode ist für die Fälle geeignet, in welchen das Verhältnis der charakteristischen Längen der Skalen gegen Null geht. Daher bezieht sich der Ausdruck "makro" auf das Problem der Simulation des wirklichen Körpers und "mikro" auf das Problem, welches das repräsentative Volumenelement betrifft. Die Vorteile dieser Methode liegen in der effizienten Anwendung für nichtlineare Verbundmaterialien und finite Verformungen. Diese Arbeit behandelt Materialien mit periodischer bzw. zufälliger Mikrostruktur. Hierbei werden drei Beispiele ausführlich erklärt: die Berechnung der effektiven Materialparameter für mikroporöse Medien, die Analyse der Verformungen, die durch Lösungs-Fällungs-Kriechen verursacht werden, sowie die Simulation des Verhaltens einer schwammartigen Knochenstruktur unter dem Einfluss von Ultraschallwellen.

Vorwort

Die vorliegende Arbeit entstand während meiner Tätigkeit als wissenschaftliche Mitarbeiterin am Institut für Mechanik im Rahmen des Sonderforschungsbereiches 526 "Rheology of the Earth - from the upper crust to the subduction zone." Die Arbeit wurde von der Fakultät für Bau- und Umweltingenieurwissenschaften als Dissertation angenommen.

Den herzlichen Dank möchte ich zuerst meinem Doktorvater, Herrn Professor K. Hackl, aussprechen. Unsere gemeinsame Arbeit wurde durch zahlreiche Diskussionen geprägt, in denen ich neben dem aktuellen Thema immer eine feine Andeutung über die Erweiterung der Arbeit erhalten habe. Gerade diese unauffällige Art, eine Herausforderung zu stellen, habe ich sehr geschätzt und sie war mir die größte Anregung für die weitere Forschungsarbeit.

Mein besonderer Dank geht auch an Professor Emeritus G. Schmid, dessen Vielfältigkeit und Weltoffenheit alle Studenten des Kurses "Computational Engineering" erfahren haben. Ich danke auch seinem Nachfolger, Herrn Professor R. Höffer, für das wissenschaftliche Interesse an meiner Arbeit und Herrn Professor O.T. Bruhns für die Übernahme des Koreferats.

Weiterhin möchte ich sehr gerne meine Kollegen U. Hoppe, G. Kotucha, B. Thorsten, R. Heinen, D. Kochmann, H. Schütte und M.K. Abbasi erwähnen. Den Tagungen und Vorlesungen, den Vorträgen und Klausuren haben sie oft einen ganz anderen, entspannenden und lustigen Ton gegeben.

Mein ausdrücklicher Dank gilt auch meinem Freund Jan Klinge, der mir die nötige Geduld, Verständnis und Unterstützung entgegengebracht hat. Seine von meinen oft unterschiedlichen Ansichten und Interessen waren mir eine zusätzliche Bereicherung, ein notwendiger Ausgleich für die Themen und Aufgaben, die Arbeit und Forschung mit sich gebracht haben.

Bochum, im August 2008 Sandra Ilic

Mündliche Prüfung: 18.02.2008

1. Gutachter: Prof. D. rer. nat. K. Hackl
2. Gutachter: Prof. Prof. Dr.-Ing. O.T. Bruhns

Contents

1 Introduction

In contrast to linear composite materials, which have already been well explored using many different modeling methods, the modeling of nonlinear composite materials is a relatively new subject. Analytical approaches to such materials are based on determining the bounds of the effective material parameters using the energy functional of a comparison material, consisting of linear homogeneous material in the simpler cases, and linear composite in more precise models. However, both of these approximations yield solutions which are too complicated and only suitable for materials with a simple microstructure, so that numerical methods often have to be used as a necessary alternative.

This thesis will mainly look at the concept and application of the multiscale finite element method, which is used to simulate the behavior of a macroscopic body with material properties defined by the geometry and structure of a representative volume element. The method is suitable for cases in which the ratio of the characteristic lengths of the scales tends to zero, with the advantage that it can be used for nonlinear materials and finite deformations without greater difficulties. The multiscale method and the alternative solutions are presented in the thesis as follows.

- After a brief overview, the second chapter formulates the problem for different types of composite materials with a detailed description of the most important solution procedures. All of the methods discussed here are based on the assumption of small deformations.

- The concept of the multiscale homogenization method is presented in the third chapter. A summary of the basic quantities characteristic for the theory of finite deformations is followed by a definition of the macroquantities dependent on the microquantities acting on the boundary of the representative volume element using the concept of the volume average. Finally, an explanation for the transformation of Hill's macrohomogeneity condition and the derivation of the boundary conditions for the representative volume element is provided.

- The fourth chapter considers a combination of the homogenization method and FEM. It compares the singlescale and the multiscale formulation pointing out the differences in the interest of a clear presentation. This is illustrated choosing two types of potential energy: the standard type dependent only on deformation, and the mixed type dependent on deformation, pressure and effective volume change.

- The simulation of a microporous material is presented as a first example of applying multiscale FEM. To this end, a representative volume element of square shape containing an elliptical pore is chosen; the random structure is simulated by assuming that the orientation of the pores is different at each point of the macrostructure. The matrix material is described by a mixed form of the energy potential and free energy corresponding to the Neo-Hook material. The idea of the simulation is to follow the change in effective material parameters with growing pore size.

- The sixth chapter looks at modeling solution-precipitation creep, which is a deformation process based on the diffusion of the material particles within intercrystalline space. Although very slow, this process can cause large deformation over an extended time period. Together with the preliminary results obtained from the Taylor particle model, an explanation is provided for the simulation of polycrystals based on FEM application, estimating the effective material parameters with multiscale FEM.

- The last example models the representative volume element of cancellous bone. These investigations are motivated by the observation that during the process of osteoporosis the bone structure and its strength may change significantly. As the representative volume element of this material contains a liquid phase, a dynamic investigation of the sample and a problem formulation in the complex domain will be consid-

ered.

- The thesis closes with a brief discussion of the results and conclusions.

The previous overview indicates that together with a presentation of the concept and the results of one particular method the objective of this thesis is to provide information about the alternative procedures. The intention is also to illustrate the importance of modeling composite materials. To this end, elucidating examples typical for different research fields are elaborated.

2 Modeling of composite materials

Composite materials consist of material phases whose type, disposition and kind of bonding can differ greatly. Even a small change in the type or concentration of constituent materials can yield a significant improvement in overall properties, thus making this sort of materials especially attractive for investigation.

The first results in this field were obtained by Voigt [87] and Reuss [77] who proposed different expressions for calculating the effective elasticity tensor of linear composites. These solutions are often used even today, although introducing the idea of bounds, Hill [40] showed that these are just limiting cases of possible effective elasticity tensors. Furthermore, Hashin and Shtrikman [36]-[38] developed a procedure providing more precise solutions. Their method is based on transforming the energy functional of the original material for which the energy functional of a homogeneous comparison material is used. Together with better results, this formulation provides a simpler calculation procedure than the standard variational approach. Other significant work looking at the behavior of linear composite materials has been contributed by Hill [41, 42], Budianski [15], Kröner [54], Beran [9], Mori-Tanaka [68], Willis [92].

The study of nonlinear composite materials started later, through the work of Talbot and Willis [84]. The method proposed by these two authors is an extension of Hashin-Shtrikman's procedure, but with the disadvantage of a duality gap between the bounds obtained using the principles of minimum potential energy and minimum complementary energy. This problem is overcome in the work by Castañeda presenting the so-called new variational principle [16, 17], but here the construction of the upper bound is still an open issue.

Finally, recent intensive use of computers has prompted swift development of numerical methods, solving the problems with different ratios of characteristic lengths and simulating materials with different types and geometry of phases. The following methods are worth mentioning in particular: Voronoi cell method [30, 31], secant methods [69, 83], partitioning methods [46]-[48], adaptive hierarchical modeling methods [74, 98], micro-macro domain decomposition methods [99, 100], multiscale method [60]-[64],[79]. Although convenient for a wide range of materials, it is apparent that numerical methods are often time-consuming and demanding in terms of computer capacity.

Comprehensive overviews of important methods for simulating composite materials are provided by Willis [93]-[95], Nemat-Nasser and Hori [72], Mura [70], Torquato [86], Zohdi and Wriggers [101].

2.1 Linear composite materials

2.1.1 Homogenization concept

In order to explain the concept behind the theory of homogenization, first the behavior of a body $\mathcal{B}$ is considered, consisting of a linear composite material with perfect bonding of phases (Fig. 2.1).

The state of deformations and stresses of such a body is governed by the system of equations

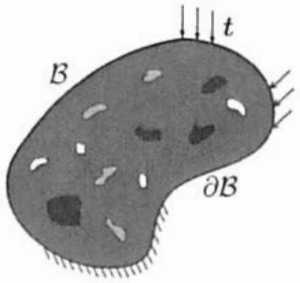

Figure 2.1: A body consisting of a composite material.

$$\nabla \cdot \boldsymbol{\sigma} + \boldsymbol{f} = 0, \tag{2.1}$$

$$\boldsymbol{\sigma} = \boldsymbol{\mathcal{C}} : \boldsymbol{\epsilon}, \tag{2.2}$$

$$\boldsymbol{\epsilon} = \frac{1}{2}(\nabla \boldsymbol{u} + \boldsymbol{u}\nabla), \tag{2.3}$$

$$\boldsymbol{u} = \boldsymbol{u}^* \quad \text{on} \quad \partial\mathcal{B}_u, \qquad \boldsymbol{\sigma} \cdot \boldsymbol{n} = \boldsymbol{t} \quad \text{on} \quad \partial\mathcal{B}_t, \tag{2.4}$$

where the equilibrium equation (2.1) is followed by the constitutive law (2.2), definition of strain (2.3), kinematic boundary conditions on a boundary part $\partial\mathcal{B}_u$ and static boundary conditions on a boundary part $\partial\mathcal{B}_t$ (2.4). According to the standard notation, $\boldsymbol{\sigma}$ represents the stress tensor, $\boldsymbol{\epsilon}$ is the strain tensor, $\boldsymbol{u}$ the displacement field, $\boldsymbol{f}$ the vector of volume forces, $\boldsymbol{t}$ denotes the tractions, $\boldsymbol{u}^*$ the prescribed displacements and $\boldsymbol{n}$ the normal vector on the boundary. The only property to distinguish the system (2.1)-(2.4) from one describing the behavior of a homogeneous body is the elasticity tensor $\boldsymbol{\mathcal{C}}$, which for a heterogeneous material becomes dependent on coordinates due to different material properties of the phases. This can be written

$$\boldsymbol{\mathcal{C}} = \boldsymbol{\mathcal{C}}(\boldsymbol{x}) = \sum_{i=1}^{n} f_i(\boldsymbol{x})\, \boldsymbol{\mathcal{C}}_i, \qquad f_i(\boldsymbol{x}) = \begin{cases} 1 & \boldsymbol{x} \text{ is inside phase } i, \\ 0 & \boldsymbol{x} \text{ is not inside phase } i, \end{cases} \tag{2.5}$$

where f_i represents the indicator function, and a material with n different phases is taken as an example. The specific form of the elasticity tensor (2.5) causes many difficulties in solving the system (2.1)-(2.4) so that the idea of the homogenization method is to replace the original constitutive law (2.2) by the constitutive law corresponding to the homogeneous material whose behavior is equivalent or most similar to the behavior of the original material. The properties of such a material are called effective or overall properties and the replacing constitutive law

$$\boldsymbol{\sigma} = \bar{\boldsymbol{\mathcal{C}}} : \boldsymbol{\epsilon} \tag{2.6}$$

depends on the effective elasticity tensor $\bar{\boldsymbol{\mathcal{C}}}$. Already an intuitive guess indicates that the described substitution does not always apply. The homogenization procedure is only admissible in the case of statistically uniform materials with the specific attribute of having a volume element whose examination yields the same effective material properties, independent of position and shape. This element is called the representative volume element (RVE) and in the rest of this chapter it will be denoted by Ω in contrast to the macroscopic body $\mathcal{B}$. The condition for applicability of the homogenization method is that the ratio of characteristic lengths corresponding to the size of heterogeneities and to the size of the real specimen must tend to zero. This is usually written as

$$\varepsilon = \frac{l}{L} \to 0 \tag{2.7}$$

where L represents a characteristic size at the structural and l at microstructural level. In this limiting case it is reasonable to expect that the type of the boundary conditions used for the analysis of an RVE should not have any influence on the calculated effective values [16, 41].

2.1.2 Volume average concept

Apart from the RVE concept, another important point of the homogenization method is to define the effective properties, which necessitates the volume or ensemble average concept. The volume average, shown in the example of an arbitrary quantity a, is defined as

$$\bar{a} = (\bar{a})_\Omega = \frac{1}{V}\int_\Omega a\, dV \tag{2.8}$$

where it is important to remember that the overbar symbol is used only for volume average over the RVE and not over an arbitrary volume. Such notation is valid for all quantities except the elasticity tensor $\boldsymbol{C}$ and the compliance tensor $\boldsymbol{M}$ where $\bar{\boldsymbol{C}}$ and $\bar{\boldsymbol{M}}$ represent effective values, whose definition can be given in two different ways. According to a mechanical formulation, the effective elasticity tensor $\bar{\boldsymbol{C}}$ is defined as the tensor relating the volume averages of stress $\bar{\boldsymbol{\sigma}}$ and strain $\bar{\boldsymbol{\epsilon}}$

$$\bar{\boldsymbol{\sigma}} = \bar{\boldsymbol{C}} : \bar{\boldsymbol{\epsilon}}, \tag{2.9}$$

whereas, assuming the energetic formulation, the effective elasticity tensor allows for a relation between the average of potential energy $\bar{W}(\bar{\boldsymbol{\epsilon}})$ and the volume average of strain $\bar{\boldsymbol{\epsilon}}$

$$\bar{W}(\bar{\boldsymbol{\epsilon}}) = \frac{1}{2}\bar{\boldsymbol{\epsilon}} : \bar{\boldsymbol{C}} : \bar{\boldsymbol{\epsilon}}. \tag{2.10}$$

This definition is more general than the previous one with the possibility of determining bounds, which will be explained in chapters 2.2.2 and 2.2.3. If the effective compliance tensor is required, definitions analogous to (2.9) and (2.10) are valid

$$\bar{\boldsymbol{\epsilon}} = \bar{\boldsymbol{M}} : \bar{\boldsymbol{\sigma}}, \qquad \bar{U}(\bar{\boldsymbol{\sigma}}) = \frac{1}{2}\bar{\boldsymbol{\sigma}} : \bar{\boldsymbol{M}} : \bar{\boldsymbol{\sigma}}, \tag{2.11}$$

where $U(\boldsymbol{\sigma})$ is the conjugate energy with respect to $W(\boldsymbol{\epsilon})$. Comparing (2.9) and (2.10) with (2.11) it becomes clear that the effective elasticity and compliance tensors must be the inverses of each other $\bar{\boldsymbol{M}} = \bar{\boldsymbol{C}}^{-1}$. Finally, two definitions are required to eliminate any ambiguity concerning the idea of volume average and effective values of material tensors. The volume average of the elasticity tensor

$$\boldsymbol{C}_V = \frac{1}{V}\int_\Omega \boldsymbol{C}(\boldsymbol{x})\, d\boldsymbol{x} = \sum_{i=1}^{n} c_i \boldsymbol{C}_i, \qquad \boldsymbol{M}_V = (\boldsymbol{C}_V)^{-1} \tag{2.12}$$

is known as the Voigt elasticity tensor, while the volume average of the compliance tensor is the Reuss compliance tensor whose inverse is the Reuss elasticity tensor

$$\boldsymbol{M}_R = \frac{1}{V}\int_\Omega \boldsymbol{M}(\boldsymbol{x})\, d\boldsymbol{x} = \sum_{i=1}^{n} c_i \boldsymbol{M}_i, \qquad \boldsymbol{C}_R = (\boldsymbol{M}_R)^{-1}. \tag{2.13}$$

Here c_i represents the volume fraction of a phase i defined as $c_i = V_i/V$ and V_i is the volume of phase i in an RVE of volume V. The difference between the effective and the Voigt elasticity tensor is more obvious from the formulation of the average stress

$$\bar{\boldsymbol{\sigma}} = \boldsymbol{C}_V : \bar{\boldsymbol{\epsilon}} + \overline{(\boldsymbol{C}' : \boldsymbol{\epsilon}')} = \bar{\boldsymbol{C}} : \bar{\boldsymbol{\epsilon}} \tag{2.14}$$

where the quantities with a prime symbol denote the fluctuations around the corresponding volume average.

2.1.3 Ensemble average concept

Elementary relations needed for working with the statistical average will be shown in the example of an arbitrary quantity $\rho(\boldsymbol{x})$, depending on the indicator function f_i

$$\rho(\boldsymbol{x}) = \sum_{r=1}^{n} \rho_r f_r(\boldsymbol{x}). \tag{2.15}$$

The statistical average of such quantity $\langle\rho(\boldsymbol{x})\rangle$ has the form

$$\langle\rho(\boldsymbol{x})\rangle = \sum_{r=1}^{n} \rho_r P_r(\boldsymbol{x}) \tag{2.16}$$

where function $P_r(\boldsymbol{x})$ is the probability of finding a phase r at a chosen point $\boldsymbol{x}$. It can be shown that it is equal to the volume fraction of the corresponding phase $P_r(\boldsymbol{x}) = c_r$. The statistical average can also be calculated for the product of functions of the type (2.15)

$$\langle\rho(\boldsymbol{x})\rho(\boldsymbol{x}')\rangle = \sum_{r=1}^{n}\sum_{s=1}^{n} \rho_r \rho_s P_{rs}(\boldsymbol{x}, \boldsymbol{x}'). \tag{2.17}$$

Here $P_{rs}(\boldsymbol{x}, \boldsymbol{x}')$ is a two-point probability function, representing the probability that phase r is at the point $\boldsymbol{x}$ and phase s is at the point $\boldsymbol{x}'$. Function $\langle\rho(\boldsymbol{x})\rho(\boldsymbol{x}')\rangle$ is called a two-point correlation or coherence function. Correlation and probability functions involving more than two points are difficult to estimate and only some special simple cases can be studied analytically [8]. Definitions of the effective values according to the concept of ensemble average are analogous to those ones based on the concept of volume average and will therefore only be looked at briefly:

- mechanical formulation

$$\langle\boldsymbol{\sigma}\rangle = \hat{\boldsymbol{C}} : \langle\boldsymbol{\epsilon}\rangle\,, \qquad \langle\boldsymbol{\epsilon}\rangle = \hat{\boldsymbol{M}} : \langle\boldsymbol{\sigma}\rangle\,, \tag{2.18}$$

- energetic formulation

$$\langle W\rangle = \frac{1}{2}\,\langle\boldsymbol{\epsilon}\rangle : \hat{\boldsymbol{C}} : \langle\boldsymbol{\epsilon}\rangle\,, \qquad \langle U\rangle = \frac{1}{2}\,\langle\boldsymbol{\sigma}\rangle : \hat{\boldsymbol{M}} : \langle\boldsymbol{\sigma}\rangle\,. \tag{2.19}$$

To distinguish the type of the applied concept, the effective values are denoted by symbol with overhat and not with overbar.

2.1.4 Hill's macrohomogeneity condition

In order to check if the mechanical and the energetic definition provide the same effective values, which is quite natural to expect, the average of strain energy is written using the mechanical formulation of the effective values

$$\bar{W} = \frac{1}{2}\overline{(\boldsymbol{\epsilon} : \boldsymbol{\sigma})} = \frac{1}{2}\,\bar{\boldsymbol{\varepsilon}} : \bar{\boldsymbol{\sigma}} + \frac{1}{2}\overline{(\boldsymbol{\epsilon}' : \boldsymbol{\sigma}')} = \frac{1}{2}\,\bar{\boldsymbol{\varepsilon}} : \bar{\boldsymbol{C}} : \bar{\boldsymbol{\varepsilon}} + \frac{1}{2}\overline{(\boldsymbol{\epsilon}' : \boldsymbol{\sigma}')}. \tag{2.20}$$

This is also compared with the energetic definition (2.10), yielding the conclusion that the volume average of the product of stress and strain fluctuations is equal to zero

$$\frac{1}{2}\,\bar{\boldsymbol{\varepsilon}} : \bar{\boldsymbol{C}} : \bar{\boldsymbol{\varepsilon}} = \frac{1}{2}\,\bar{\boldsymbol{\varepsilon}} : \bar{\boldsymbol{C}} : \bar{\boldsymbol{\varepsilon}} + \frac{1}{2}\overline{(\boldsymbol{\epsilon}' : \boldsymbol{\sigma}')} \qquad \Rightarrow \qquad \overline{(\boldsymbol{\epsilon}' : \boldsymbol{\sigma}')} = 0 \tag{2.21}$$

so that (2.20) reduces to the expression known as Hill's condition [41]

$$\overline{(\boldsymbol{\sigma} : \boldsymbol{\epsilon})} = \bar{\boldsymbol{\sigma}} : \bar{\boldsymbol{\epsilon}}. \tag{2.22}$$

This condition means that the mean value of internal work must be equal to the product of mean stress and strain and the same result could be obtained starting from the dual formulation or using the concept of the statistical average. Condition (2.22) is automatically satisfied in the case of several types of boundary conditions intensively used in the investigation of RVEs. The first type of such boundary conditions are the kinematic ones

$$\boldsymbol{u} = \boldsymbol{\epsilon}^* \cdot \boldsymbol{x}, \quad \boldsymbol{x} \in \partial\Omega \tag{2.23}$$

where $\boldsymbol{\epsilon}^*$ is a prescribed value on the boundary and where Gauss' theorem can be used to show that the volume average of strain tensor $\boldsymbol{\epsilon}$ has exactly the same value as that prescribed on the boundary $\bar{\boldsymbol{\epsilon}} = \boldsymbol{\epsilon}^*$. The other type of boundary conditions assuring that Hill's condition is satisfied are the static ones

$$\boldsymbol{\sigma} \cdot \boldsymbol{n} = \boldsymbol{\sigma}^* \cdot \boldsymbol{n}, \quad \boldsymbol{x} \in \partial\Omega, \tag{2.24}$$

where $\boldsymbol{\sigma}^*$ is prescribed stress on the boundary of RVE. Here again, Gauss' theorem can be used to show that $\bar{\boldsymbol{\sigma}} = \boldsymbol{\sigma}^*$. In the case of periodic boundary conditions, Hill's condition is also automatically satisfied, which will be explained in greater detail in chapter 3.3.2.

2.2 Calculation of effective material properties of linear composites

The calculation of the effective material properties, which is the essential step in the homogenization theory, can be achieved in many ways but this thesis briefly considers only the most important ones:

- perturbation method,
- standard variational method,
- Hashin-Shtrikman variational principle,
- methods based on the application of the strain concentration tensor: dilute dispersion, self-consistent and Mori-Tanaka method.

2.2.1 Perturbation method

The perturbation method is convenient for solving problems which in fact cannot be solved exactly, but their approximative solution can be expressed dependent on the exact solution of an auxiliary problem. This only applies if the original problem can be expressed by adding a small perturbation term to the formulation of the auxiliary problem. Accordingly, for the purposes of the theory of homogenization, it is assumed that the elasticity tensor of a heterogeneous material $\boldsymbol{C}$ can be written as

$$\boldsymbol{C} = \boldsymbol{C}_0 + \delta\boldsymbol{C} \tag{2.25}$$

where $\delta\boldsymbol{C}$ represents a small perturbation and $\boldsymbol{C}_0$ is the material tensor of a homogeneous comparison material. Using such assumption and choosing pure kinematic boundary conditions, the original problem (2.1)-(2.4) becomes

$$\begin{aligned} &\nabla \cdot (\mathcal{C}_0 : \epsilon) + \nabla \cdot (\delta\mathcal{C} : \epsilon) + \boldsymbol{f} = 0, \quad \boldsymbol{x} \in \Omega, \\ &\epsilon = \frac{1}{2}(\nabla \boldsymbol{u} + \boldsymbol{u}\nabla), \\ &\boldsymbol{u} = \boldsymbol{u}_0, \quad \boldsymbol{x} \in \partial\Omega \end{aligned} \tag{2.26}$$

while the corresponding auxiliary problem is obtained from (2.26) for $\delta\mathcal{C} = 0$

$$\begin{aligned} &\nabla \cdot (\mathcal{C}_0 : \epsilon) + \boldsymbol{f} = 0, \quad \boldsymbol{x} \in \Omega, \\ &\epsilon = \frac{1}{2}(\nabla \boldsymbol{u} + \boldsymbol{u}\nabla), \\ &\boldsymbol{u} = \boldsymbol{u}_0, \quad \boldsymbol{x} \in \partial\Omega. \end{aligned} \tag{2.27}$$

The previous system corresponds to the boundary value problem describing the behavior of a homogeneous body and can be solved by any of the standard methods for this kind of problems. In the following, the Green function method is used, which leads to the final solution of (2.26) in the form

$$\epsilon = \epsilon_0 - \Gamma\, \delta\mathcal{C}\epsilon \tag{2.28}$$

where Γ represents a linear operator dependent on the Green function and ϵ_0 is a solution of (2.27). Details about derivations will be left out as they are of purely mathematical nature [93]. The transformation of solution (2.28) permits the calculation of the mean stress and strain, using the concept of the statistical average firstly

$$\epsilon = [\boldsymbol{I} + \Gamma\, \delta\mathcal{C}]^{-1}\, \epsilon_0 \quad \Rightarrow \quad \langle\epsilon\rangle = \left\langle [\boldsymbol{I} + \Gamma\, \delta\mathcal{C}]^{-1} \right\rangle \epsilon_0. \tag{2.29}$$

Furthermore, starting with the definition

$$\sigma = (\mathcal{C}_0 + \delta\mathcal{C}) : \epsilon = (\mathcal{C}_0 + \delta\mathcal{C}) : [\boldsymbol{I} + \Gamma\, \delta\mathcal{C}]^{-1}\, \epsilon^0 \tag{2.30}$$

the statistical average of the stress is obtained in the form

$$\langle\sigma\rangle = \left\langle (\mathcal{C}_0 + \delta\mathcal{C}) : [\boldsymbol{I} + \Gamma\, \delta\mathcal{C}]^{-1} \right\rangle \left\langle [\boldsymbol{I} + \Gamma\, \delta\mathcal{C}]^{-1} \right\rangle^{-1} \langle\epsilon\rangle\,. \tag{2.31}$$

A comparison of the assembling average counterpart of (2.9) and (2.31) indicates that the multiplier in front of $\langle\epsilon\rangle$ in (2.31) represents the statistical effective elasticity tensor $\hat{\mathcal{C}}$

$$\hat{\mathcal{C}} = \mathcal{C}_0 + \left\langle \delta\mathcal{C} : [\boldsymbol{I} + \Gamma\, \delta\mathcal{C}]^{-1} \right\rangle \left\langle [\boldsymbol{I} + \Gamma\, \delta\mathcal{C}]^{-1} \right\rangle^{-1} \tag{2.32}$$

which can also be written as an expansion

$$\hat{\mathcal{C}} = \mathcal{C}_0 + \langle\delta\mathcal{C}\rangle + \langle\delta\mathcal{C}\rangle : \Gamma\, \langle\delta\mathcal{C}\rangle - \langle\delta\mathcal{C} : \Gamma\, \delta\mathcal{C}\rangle + \cdots\,. \tag{2.33}$$

Assuming the concept of mean strain, which means that $\langle\epsilon\rangle = \bar{\epsilon}$, a similar procedure yields the effective elasticity tensor based on the concept of volume average

$$\bar{\mathcal{C}} = \mathcal{C}_0 + \langle\delta\mathcal{C}\rangle - \langle\delta\mathcal{C} : \Gamma_1\, \delta\mathcal{C}\rangle + \cdots \tag{2.34}$$

and consideration of the dual problem provides the effective compliance tensor

$$\bar{\boldsymbol{M}} = \boldsymbol{M}_0 + \langle\delta\boldsymbol{M}\rangle - \langle\delta\boldsymbol{M} : \Delta_1 \delta\boldsymbol{M}\rangle + \cdots\,. \tag{2.35}$$

Operators Γ_1 in (2.34) and Δ_1 in (2.35) are again the linear operators dependent on the Green function [93]. As shown further on, the truncation of an expansion obtained using solution (2.28) is an initial assumption of some other methods.

2.2.2 Standard variational method

The standard variational method is based on applying the principles of minimum potential and conjugate energy, which state that actual deformations and stresses minimize the corresponding energy functional. A direct consequence of such principles is that for each admissible approximation of strain ϵ^a or stress σ^a the energy potential is greater than the actual solution

$$\bar{W}(\bar{\epsilon}) = \frac{1}{2}\bar{\epsilon} : \bar{\boldsymbol{C}} : \bar{\epsilon} \leq \frac{1}{2V}\int_{\Omega} \epsilon^a : \boldsymbol{C} : \epsilon^a d\boldsymbol{x}, \tag{2.36}$$

$$\bar{U}(\bar{\sigma}) = \frac{1}{2}\bar{\sigma} : \bar{\boldsymbol{M}} : \bar{\sigma} \leq \frac{1}{2V}\int_{\Omega} \sigma^a : \boldsymbol{M} : \sigma^a d\boldsymbol{x}, \tag{2.37}$$

where the term "admissible" means that approximative strains and stresses have to belong to the corresponding sets

$$\epsilon^a \in \boldsymbol{E}, \quad \boldsymbol{E} = \{\epsilon \,|\, \epsilon = \frac{1}{2}(\nabla \boldsymbol{u} + \boldsymbol{u}\nabla) \text{ in } \Omega, \text{ and } \boldsymbol{u} = \epsilon^* \cdot \boldsymbol{x} \text{ on } \partial\Omega\}, \tag{2.38}$$

$$\sigma^a \in \boldsymbol{S}, \quad \boldsymbol{S} = \{\sigma \,|\, \nabla \cdot \sigma = 0 \text{ in } \Omega, \text{ and } \sigma \cdot \boldsymbol{n} = \sigma^* \cdot \boldsymbol{n} \text{ on } \partial\Omega\}. \tag{2.39}$$

In these expressions volume forces are neglected and specific boundary conditions are chosen so that Hill's condition (2.22) is satisfied. The method is illustrated firstly by choosing the simplest approximation in the form $\epsilon^a = \epsilon^*$, $\epsilon^a \in \boldsymbol{E}$ where ϵ^* is the strain prescribed on the boundary (2.23). As in this case it applies that $\bar{\epsilon} = \epsilon^*$, the approximation becomes equal to the mean strain value, $\epsilon^a = \epsilon^* = \bar{\epsilon}$, and the corresponding energy potential is

$$\frac{1}{2V}\int_{\Omega} \epsilon^a : \boldsymbol{C} : \epsilon^a \, d\boldsymbol{x} = \frac{1}{2V}\,\bar{\epsilon} : \int_{\Omega} \boldsymbol{C}(\boldsymbol{x}) d\boldsymbol{x} \; : \bar{\epsilon} = \frac{1}{2}\,\bar{\epsilon} : \boldsymbol{C}_V : \bar{\epsilon}. \tag{2.40}$$

Having in mind (2.36), this means that the Voigt elasticity tensor $\boldsymbol{C}_V$ is just the upper bound of the actual effective elasticity tensor

$$\bar{\epsilon} : \bar{\boldsymbol{C}} : \bar{\epsilon} \leq \bar{\epsilon} : \boldsymbol{C}_V : \bar{\epsilon}, \qquad \boldsymbol{C}_V = \sum_{i=1}^{n} c_i \boldsymbol{C}_i. \tag{2.41}$$

The similar can be shown for uniform static boundary conditions (2.24) where, using the volume average of stress $\bar{\sigma} = \sigma^*$, an adequate assumption for the approximative solution becomes $\sigma^a = \sigma^* = \bar{\sigma}$, leading to the volume average of the conjugate energy

$$\frac{1}{2V}\int_{\Omega} \sigma^a : \boldsymbol{M} : \sigma^a \, d\boldsymbol{x} = \frac{1}{2V}\,\bar{\sigma} : \int_{\Omega} \boldsymbol{M} \, d\boldsymbol{x} \; : \bar{\sigma} = \frac{1}{2}\,\bar{\sigma} \; : \boldsymbol{M}_R \; : \bar{\sigma} \tag{2.42}$$

and to the conclusion that the Reuss effective elasticity tensor represents the lower bound for the actual effective elasticity tensor

$$\bar{\sigma} : \bar{\boldsymbol{M}} : \bar{\sigma} \leq \bar{\sigma} : \boldsymbol{M}_R : \bar{\sigma}, \qquad \boldsymbol{C}_R = (\boldsymbol{M}_R)^{-1} = \left[\sum_{i=1}^{n} c_i \boldsymbol{M}_i\right]^{-1}. \tag{2.43}$$

The idea of bounds (2.41),(2.43) was first introduced by Hill [40], but as the approximations $\epsilon^a = \epsilon^*$ and $\sigma^a = \sigma^*$ can be very distinct from the exact solution these bounds are often not sufficiently accurate. The procedure mostly used for their improvement is to apply the perturbation and variational method together, taking the truncated solution from the perturbation method as the approximative solution in the variational method. For example, using the fact that for boundary conditions (2.23) it is valid that

$\bar{\epsilon} = \epsilon^* = \epsilon^0$, where ϵ_0 is the solution of system (2.27) corresponding to the homogeneous body, a reformulation of (2.28) yields the series

$$\epsilon = \sum_{k=0}^{\infty} (-\Gamma \, \delta C)^k \bar{\epsilon}, \tag{2.44}$$

whose truncation after m terms is an admissible approximation

$$\epsilon^a = B_m \bar{\epsilon}, \quad B_m = \sum_{k=0}^{m} (-\Gamma \, \delta C)^k. \tag{2.45}$$

In such a case the upper bound $\tilde{C}$ becomes

$$\tilde{C} = C_0 + \langle \delta C B_{2m} \rangle . \tag{2.46}$$

This solution coincides with that obtained by the perturbation method (2.34) if the first $2m + 1$ terms are considered, but it must also be recalled that this requires a $(2m + 1)$-point correlation function.

2.2.3 Hashin-Shtrikman variational method

The Hashin-Shtrikman method resolves the main difficulty of the standard variational method, which is the problem of finding an admissible approximation for the construction of the bounds. The method considers initially a standard boundary value problem for a heterogeneous RVE Ω

$$\begin{aligned} &\nabla \cdot \sigma = 0, \\ &\epsilon = \frac{1}{2}(\nabla u + u \nabla), \\ &u = u^*, \quad x \in \partial\Omega, \end{aligned} \tag{2.47}$$

where the kinematic boundary conditions dependent on displacements are prescribed. In order to complete the problem description, the potential energy of the heterogeneous material is assumed in the form

$$W(\epsilon) = \frac{1}{2} \epsilon : C : \epsilon. \tag{2.48}$$

The same boundary value problem (2.47) is considered, assuming that the RVE Ω consists of the arbitrarily chosen homogeneous comparison material with elasticity tensor C_0 and with the potential energy in the form

$$W_0(\epsilon_0) = \frac{1}{2} \epsilon_0 : C_0 : \epsilon_0 \tag{2.49}$$

where the subscript "0" emphasizes the use of a simplified type of material. A comparison of the defined problems leads to the alternative form of the energy functional of the original material (2.48), which is the main result of the work of Hashin and Shtrikman

$$W(\epsilon) = W_p(\epsilon', p) = W_0 - \frac{1}{2} \int (p : \delta C^* : p - p : \epsilon' - 2\, p : \epsilon_0) dV. \tag{2.50}$$

Here u', ϵ', p represent displacement, strain and stress perturbation defined by

$$u' = u - u_0, \quad \epsilon' = \epsilon - \epsilon_0, \tag{2.51}$$

$$\sigma = C_0 : \epsilon + p \tag{2.52}$$

and $\delta\mathcal{C}^*$ is a fourth-order tensor defined by the relation $\delta\mathcal{C}^* : \delta\mathcal{C} = \boldsymbol{I}$. Expression (2.50) applies if the following subsidiary conditions are satisfied

$$\begin{aligned} &\nabla \cdot (\mathcal{C}_0 : \epsilon' + \boldsymbol{p}) = 0, \\ &\boldsymbol{u}' = 0 \quad \boldsymbol{x} \in \partial\Omega \end{aligned} \tag{2.53}$$

and it can be shown that (2.50) is stationary in the case that

$$\boldsymbol{p} = (\mathcal{C} - \mathcal{C}_0) : \epsilon = \delta\mathcal{C} : \epsilon. \tag{2.54}$$

A useful property of the new formulation of the energy density (2.50) is that the stress polarization $\boldsymbol{p}$ can be assumed without any limitations, in contrast to the standard method where approximations must belong to sets $\boldsymbol{E}$ or $\boldsymbol{S}$ defined by (2.38) and (2.39). An approximation for ϵ' is not necessary as it can be calculated from (2.53) dependent on the approximation for $\boldsymbol{p}$. A further advantage of expression (2.50) is that depending on the choice of the comparison homogeneous material, this functional can have an absolute minimum or absolute maximum which means that the same expression can be used for the upper and lower bound. Furthermore, it can be shown that if:

$\delta\mathcal{C}$ is positive definite $\Rightarrow$ $W_p(\epsilon', \boldsymbol{p})$ has an absolute maximum,

$\delta\mathcal{C}$ is negative definite $\Rightarrow$ $W_p(\epsilon', \boldsymbol{p})$ has an absolute minimum.

The application of this method can again be illustrated by using results of the perturbation method. It has already been shown that truncation of series (2.44) after m terms represents a possible approximation of strain

$$\epsilon = \sum_{k=0}^{m} (-\Gamma\,\delta\mathcal{C})^k \bar{\epsilon} = \boldsymbol{B}_m \bar{\epsilon}. \tag{2.55}$$

Using this and (2.54), the approximation of the stress polarization can be written as

$$\boldsymbol{p}^a = \delta\mathcal{C} \sum_{k=0}^{m} (-\Gamma\,\delta\mathcal{C})^k \bar{\epsilon}, \tag{2.56}$$

which finally yields the expression for the bounds of the effective elasticity tensor

$$\tilde{\mathcal{C}} = \mathcal{C}_0 + \langle \delta\mathcal{C}\boldsymbol{B}_{2m-1} \rangle \tag{2.57}$$

where $\tilde{\mathcal{C}}$ is the upper bound if $\delta\mathcal{C}$ is negative definite and it is the lower bound if $\delta\mathcal{C}$ is positive definite. Bounds (2.57) can be obtained from expression (2.34) by assuming only its first $2m$ terms of the perturbation series. In the simplest case, this procedure leads to the so-called second-order estimates in contrast to the values obtained by Voigt and Reuss, which are first order estimates.

2.2.4 Methods based on applying the strain concentration tensor

This group of methods is often used because of their simplicity, but the range of application is limited by the requirement that the concentration of inclusions and consequently their interactions have to be small. For their study it is convenient to analyze a composite material with n different kinds of inclusions embedded in a matrix which is itself treated as a phase with index $n + 1$. Here, the stress inside phase r and the effective stress have the form

$$\sigma_r = \mathcal{C}_r : \epsilon_r, \qquad \bar{\sigma} = \sum_{r=1}^{n+1} c_r \mathcal{C}_r : \epsilon_r \tag{2.58}$$

and the contribution of strain in the matrix to the mean strain can be explicitly expressed as

$$\bar{\epsilon} = \sum_{r=1}^{n+1} c_r \epsilon_r \;\Rightarrow\; c_{n+1}\epsilon_{n+1} = \bar{\epsilon} - \sum_{r=1}^{n} c_r \epsilon_r \tag{2.59}$$

yielding the effective stress in the form

$$\bar{\sigma} = \boldsymbol{C}_{n+1} : \bar{\epsilon} + \sum_{r=1}^{n} c_r (\boldsymbol{C}_r - \boldsymbol{C}_{n+1}) : \epsilon_r. \tag{2.60}$$

This can be further transformed by introducing the concept of the strain concentration tensor $\boldsymbol{A}_r$ which relates the strain in a phase r and the mean strain

$$\epsilon_r = \boldsymbol{A}_r : \bar{\epsilon}, \quad \Rightarrow \quad \bar{\sigma} = \boldsymbol{C}_{n+1} : \bar{\epsilon} + \sum_{r=1}^{n} c_r (\boldsymbol{C}_r - \boldsymbol{C}_{n+1}) : \boldsymbol{A}_r : \bar{\epsilon} \tag{2.61}$$

so that by comparison with the definition $\bar{\sigma} = \bar{\boldsymbol{C}} : \bar{\epsilon}$, the effective elasticity tensor becomes

$$\bar{\boldsymbol{C}} = \boldsymbol{C}_{n+1} + \sum_{r=1}^{n} c_r (\boldsymbol{C}_r - \boldsymbol{C}_{n+1}) : \boldsymbol{A}_r. \tag{2.62}$$

There are many concepts for calculating the strain concentration tensor $\boldsymbol{A}_r$, but only two will be mentioned here. According to the dilute distribution theory, specifying that the interaction of inclusions is completely excluded, this tensor has the form

$$\boldsymbol{A}_r^{dil} = [\boldsymbol{I} + \boldsymbol{S}_r : \boldsymbol{M}_{n+1} : (\boldsymbol{C}_r - \boldsymbol{C}_{n+1})]^{-1}, \qquad r = 1, ..., n, \tag{2.63}$$

where $\boldsymbol{S}_r$ represents the Eshelby tensor for an inclusion of type r in a matrix [25]. For materials with a greater concentration of inclusions, it is more convenient to apply the self-consistent method where the strain concentration tensor

$$\boldsymbol{A}_r^{sc} = \left[\boldsymbol{I} + \bar{\boldsymbol{S}}_r : \bar{\boldsymbol{M}} : (\boldsymbol{C}_r - \bar{\boldsymbol{C}})\right]^{-1}, \qquad r = 1, ..., n, \tag{2.64}$$

depends on $\bar{\boldsymbol{S}}_r$ which is the Eshelby tensor of an inclusion of type r embedded in the effective material and no longer in the original matrix. Here, one needs to use tensors corresponding to the effective material instead of tensors corresponding to the matrix. Introduction of (2.63) or (2.64) in (2.62) yields the final expression for the effective elasticity tensor $\bar{\boldsymbol{C}}$. An important difference is that the dilute dispersion method leads to the explicit expression and the self-consistent method to the implicit expression for effective elasticity tensor so that the latter requires an iterative procedure.
In the end, a mention is given to the idea of the mean field method proposed by Mori and Tanaka. In contrast to (2.61)a, this proposes that strain in the inclusions depends on strain in the matrix, while the strain in the matrix itself depends on the effective strain

$$\epsilon_i = \boldsymbol{A}_i^{dil} : \bar{\epsilon}^m = \boldsymbol{A}_i^{dil} : (\bar{\boldsymbol{A}}^m : \bar{\epsilon}), \qquad i = 1, ..., n. \tag{2.65}$$

$\boldsymbol{A}_i^{dil}$ is already defined by (2.63) and the formulation used most for the matrix strain concentration tensor is the one proposed by Benveniste [7]

$$\bar{\boldsymbol{A}}^m = \left[c_2 \boldsymbol{I} + c_1 \boldsymbol{A}_1^{dil}\right]^{-1}, \qquad c_1 + c_2 = 1. \tag{2.66}$$

This applies to a two-phase material where inclusions are denoted by index "1" and the matrix is denoted by index "2". The other different assumptions for strain concentration tensor are proposed by Hill [42], Budianski [15] and Kröner [54].

2.3 Nonlinear composite materials

2.3.1 Problem formulation

At the beginning of this section, it must be emphasized that here consideration will be given only to the material nonlinearity while geometrical nonlinearity will be the topic in some of the later chapters. The study of this kind of composites is based on estimating the bounds of effective energy functionals, for which the potential or conjugate energy has to be minimized, depending on the type of the boundary conditions. In the case of kinematic boundary conditions it is more convenient to consider the strain energy density which for the original composite has the form

$$W(\epsilon, \boldsymbol{x}) = \sum_{r=1}^{n} f_r(\boldsymbol{x}) W_r(\epsilon), \tag{2.67}$$

where $W_r(\epsilon)$ represents the strain potential of phase r and at least one of all of the potentials $W_r(\epsilon)$, $r = 1, \ldots, n$ corresponds to the nonlinear material. The potential energy of the effective material in this case is defined as a result of a minimization problem

$$\tilde{W}(\bar{\epsilon}) = \min_{\epsilon \in \boldsymbol{E}} \frac{1}{V} \int_{\Omega} W(\boldsymbol{x}, \epsilon) d\boldsymbol{x}, \tag{2.68}$$

$$\boldsymbol{E} = \{\epsilon \mid \epsilon = \frac{1}{2}(\nabla \boldsymbol{u} + \boldsymbol{u}\nabla) \text{ in } \Omega, \text{ and } \boldsymbol{u} = \epsilon^{*} \cdot \boldsymbol{x} \text{ on } \partial\Omega\}, \tag{2.69}$$

and it is the stress potential at the same time

$$\bar{\sigma} = \frac{\partial \tilde{W}}{\partial \bar{\epsilon}}(\bar{\epsilon}). \tag{2.70}$$

Analogous relations are valid for the dual formulation considering the conjugate energy

$$U(\sigma, \boldsymbol{x}) = \sum_{r=1}^{n} f_r(\boldsymbol{x})\, U_r(\sigma), \tag{2.71}$$

where the conjugate energy of effective material

$$\tilde{U}(\bar{\sigma}) = \min_{\sigma \in \boldsymbol{S}} \frac{1}{V} \int_{\Omega} U(\boldsymbol{x}, \sigma)\, d\boldsymbol{x}, \tag{2.72}$$

$$\boldsymbol{S} = \{\sigma \mid \nabla \cdot \sigma = 0 \text{ in } \Omega, \text{ and } \sigma \cdot \boldsymbol{n} = \sigma^{*} \cdot \boldsymbol{n} \text{ on } \partial\Omega\}, \tag{2.73}$$

can be used to calculate the effective strain

$$\bar{\epsilon} = \frac{\partial \tilde{U}}{\partial \bar{\sigma}}(\bar{\sigma}). \tag{2.74}$$

Concerning the primary and dual formulations presented here, two remarks must be made. Firstly, the boundary conditions in (2.69) and (2.73) are chosen to coincide with those explained in section 2.1.4 as Hill's condition keeps its form (2.22) due to the geometrical linearity. The relations $\bar{\epsilon} = \epsilon^{*}$ for kinematic and $\bar{\sigma} = \sigma^{*}$ for static boundary conditions also remain valid. Secondly, expressions (2.68) and (2.72) are not independent but related to each other by the Legendre-Fenchel transformation

$$\tilde{U}(\bar{\sigma}) = \tilde{W}^{*}(\bar{\sigma}) = \sup_{\bar{\epsilon}} \left\{ \bar{\epsilon} : \bar{\sigma} - \tilde{W}(\bar{\epsilon}) \right\} \tag{2.75}$$

where the different boundary conditions in (2.69) and (2.73) mean that the Legendre-Fenchel transformation is valid only if the influence of the boundary conditions can be neglected. As the following

discussions concern exclusively the RVE, this requirement is automatically satisfied in accordance with the properties described in section 2.1.1. In his work [96], Willis showed that the complete dualism (2.75) requires the condition that the average stress is equal to the prescribed value, $\bar{\boldsymbol{\sigma}} = \boldsymbol{\sigma}^*$, instead of the uniform boundary conditions given in (2.73).

Due to the complexity of the described minimization problems the approximative solutions have an important role in their study. For example, using the same principles as in chapter 2.2.4, the following inequalities can be written

$$\tilde{W}(\bar{\boldsymbol{\epsilon}}) \leq \frac{1}{V}\int_{\Omega} W(\boldsymbol{x}, \boldsymbol{\epsilon}^a) d\boldsymbol{x}, \tag{2.76}$$

$$\tilde{U}(\bar{\boldsymbol{\sigma}}) \leq \frac{1}{V}\int_{\Omega} U(\boldsymbol{x}, \boldsymbol{\sigma}^a)\, d\boldsymbol{x}, \tag{2.77}$$

where $\boldsymbol{\sigma}^a \in \boldsymbol{S}$ and $\boldsymbol{\epsilon}^a \in \boldsymbol{E}$ are admissible approximative solutions. This means that the standard variational method can be applied here as in the case of linear composite materials, but this time the problem of determining admissible approximations is even more pronounced and a reformulation of bounds is again necessary.

2.3.2 Willis-Talbot variational formulation

Alternative forms of bounds for the energy of nonlinear composite materials were first discussed in the work of Willis and Talbot [84]. The primary problem considered here is the minimization of a functional $F(u)$ where $u \in V$ and V is a closed linear subspace of the Banach space B. This problem is denoted by $\mathcal{P}$ so that it can be written

$$\mathcal{P}: \inf_{u \in V} F(u), \qquad \inf \mathcal{P} = F(\hat{u}) \tag{2.78}$$

where the latter expression means that $\hat{u} \in V$ is a minimizer. Maximization of the negative conjugate functional $-F^*(u^*)$ is taken to be the dual problem

$$\mathcal{P}^*: \sup_{u^* \in V^0} \{-F^*(u^*)\}, \qquad \sup \mathcal{P}^* = F^*(\hat{u}^*) \tag{2.79}$$

where V_0 is a set of annihilators of V, which means that for $u \in V$ and $u^* \in V^0$ it applies that $\langle u, u^* \rangle = 0$. The conjugate functional is defined in the standard way

$$F^*(u^*) = \sup_{u \in B} \{\langle u, u^* \rangle - F(u)\} \tag{2.80}$$

with the symbol $\langle \cdot \rangle$ representing the inner product. The latter expression in (2.79) means that $\hat{u}^* \in V^0$ is the solution of the dual problem. Comparison of the solutions of the described problems also shows that

$$-F^*(u^*) \leq \sup \mathcal{P}^* \leq \inf \mathcal{P} \leq F(u) \tag{2.81}$$

where $u \in V$ and $u^* \in V_0$ are admissible approximations. The sign of equality is valid if $u^* \in \partial F(u)$ or if $u^* = F'(u)$ for a differentiable functional. In this case there is no duality gap, and the primary and dual problem have the same solution. Recall that $\partial F(u)$ represents the subdifferential of a functional $F(u)$.

Relation (2.81) corresponds to the bounds obtained by standard variational principles (2.76) and (2.77), but as stated before, they are not easy to calculate. However, Willis and Talbot proposed alternative bounds depending on the comparison functionals $\overline{F}(u)$ and $\underline{F}(u)$ which can be chosen arbitrarily. In their model, the first step is to form the differences

$$\underline{f}(u) = F(u) - \underline{F}(u), \tag{2.82}$$

$$\overline{f}(u) = F(u) - \overline{F}(u) \tag{2.83}$$

and to subject them to the Legendre-Fenchel transformation

$$\overline{f}_*(v^*) = \inf_{u \in B} \left\{ \langle u, v^* \rangle - \overline{f}(u) \right\}, \tag{2.84}$$

$$\underline{f}^*(v^*) = \sup_{u \in B} \left\{ \langle u, v^* \rangle - \underline{f}(u) \right\}. \tag{2.85}$$

Functionals (2.84),(2.85) depend on the new variable $v^* \in B^*$ where B^* is the dual space of the Banach space B. The final shape of the bounds for the primary problem is

$$\inf_{u \in V} \left\{ \langle u, v^* \rangle + \underline{F}(u) \right\} - \underline{f}^*(v^*) \leq \inf \mathcal{P} \leq \inf_{u \in V} \left\{ \langle u, v^* \rangle + \overline{F}(u) \right\} - \overline{f}_*(v^*) \tag{2.86}$$

where the minimization has to be carried out with respect to $u \in V$ and the comparison functionals $\underline{F}(u)$, $\overline{F}(u)$ are chosen in the form which simplifies the minimization procedure. Additional optimization with respect to v^* gives the best possible bounds for the chosen comparison functionals.
In the same way, for the dual problem based on the comparison functionals $\underline{G}(u^*)$ and $\overline{G}(u^*)$ where $u^* \in B^*$, the needed differences become

$$\underline{g}(u^*) = F^*(u^*) - \underline{G}(u^*), \tag{2.87}$$

$$\overline{g}(u^*) = F^*(u^*) - \overline{G}(u^*), \tag{2.88}$$

the new conjugate functionals dependent on variables $v \in B$ are

$$\overline{g}_*(v) = \inf_{u^* \in B^*} \left\{ \langle v, u^* \rangle - \overline{g}(u^*) \right\}, \tag{2.89}$$

$$\underline{g}^*(v) = \sup_{u^* \in B^*} \left\{ \langle v, u^* \rangle - \underline{g}(u^*) \right\}, \tag{2.90}$$

and the bounds for the dual problem have the form

$$-\inf_{u^* \in V^0} \left\{ \langle v, u^* \rangle + \overline{G}(u^*) \right\} + \overline{g}_*(v) \leq \sup \mathcal{P}^* \leq -\inf_{u^* \in V^0} \left\{ \langle v, u^* \rangle + \underline{G}(u^*) \right\} + \underline{g}^*(v). \tag{2.91}$$

Remarks valid for (2.86) can be repeated here: $\underline{G}(u^*)$ and $\overline{G}(u^*)$ have to be chosen in such a way that the process of minimization is simplified and additional optimization with respect to v is also possible.

The following two application examples present the method of Willis and Talbot. Firstly, it will be shown that the Hashin-Shtrikman procedure for a linear composite material can be derived using this procedure. This considers a homogeneous body with an elasticity tensor $\boldsymbol{C}_0$ and the same boundary conditions as for the composite body. The strain inside the body is $\boldsymbol{\epsilon}_0$ and the stress $\boldsymbol{\sigma}_0 = \boldsymbol{C}_0 : \boldsymbol{\epsilon}_0$. If the strain of the heterogeneous body is expressed as $\boldsymbol{\epsilon} = \boldsymbol{\epsilon}_0 + \boldsymbol{\epsilon}'$, where $\boldsymbol{\epsilon}'$ is strain perturbation, the primary problem consists of minimizing the energy functional of the heterogeneous body

$$\mathcal{P}: \inf_{\boldsymbol{\epsilon}' \in \boldsymbol{E}'} F(\boldsymbol{\epsilon}') = \inf_{\boldsymbol{\epsilon}' \in \boldsymbol{E}'} \int_\Omega \left\{ \boldsymbol{\epsilon}' : \boldsymbol{C} : \boldsymbol{\epsilon}_0 - \boldsymbol{\epsilon}' : \boldsymbol{\sigma}_0 + \frac{1}{2} \boldsymbol{\epsilon}' : \boldsymbol{C} : \boldsymbol{\epsilon}' \right\} d\boldsymbol{x} \tag{2.92}$$

where instead to some general set V, $\boldsymbol{\epsilon}'$ belongs to $\boldsymbol{E}'$ which is

$$\boldsymbol{E}' = \left\{ \boldsymbol{\epsilon} \mid \boldsymbol{\epsilon} = \frac{1}{2} \left[\nabla \boldsymbol{u} + (\nabla \boldsymbol{u})^T \right] \text{ in } \Omega, \text{ and } \boldsymbol{u} = 0 \text{ on } \partial\Omega \right\}. \tag{2.93}$$

The comparison functional has to be assumed in the form

$$F_0(\boldsymbol{\epsilon}') = \frac{1}{2} \int_\Omega \boldsymbol{\epsilon}' : \boldsymbol{C}_0 : \boldsymbol{\epsilon}' \, d\boldsymbol{x} \tag{2.94}$$

and dependent on the choice of C_0 it can be used to calculate the upper or lower bound. Further details of derivation will be left out as the results were already given in chapter 2.2.3.

The second example is the model for nonlinear composite materials proposed by Castañeda and Willis [18]. This looks at a heterogeneous body with kinematic boundary conditions, while the analogous analysis is available for the dual problem. In order to complete the definition of the total potential energy (2.67), the potential corresponding to the nonlinear phases is chosen in the form

$$W_r(\epsilon) = \frac{2}{3}\left(\frac{2n_r}{n_r+1}\right)\mu_r \epsilon_e^{1+\frac{1}{n_r}} + \frac{9}{2}\kappa_r \epsilon_m^2. \tag{2.95}$$

Here $\epsilon_m = \frac{1}{3}\mathrm{tr}\epsilon$ represents the mean strain, $\epsilon_e = \sqrt{3/2\boldsymbol{e} : \boldsymbol{e}}$ is the effective strain, $\boldsymbol{e} = \epsilon - \epsilon_m \boldsymbol{I}$ is the deviatoric strain tensor, μ_r is the shear modulus, and κ_r is the compression modulus of phase r. Dependent on the material, the creep exponent n_r lies in the range $1 \leq n_r \leq \infty$ so that the exponent has the value $1 + 1/n_r \leq 2$ and the functional (2.95) grows slower than the quadratic one. The limiting case $n_r = 1$ corresponds to the linear phase.

In order to construct the bounds defined by (2.86), the idea is to introduce a comparison quadratic functional which corresponds to the linear homogeneous material.

The first part of the problem is to construct the upper bound, which entails the following expressions

$$\overline{F}(u) \quad \leftrightarrow \quad W^0(\epsilon) = \frac{2}{3}\mu_0 \epsilon_e^2 + \frac{9}{2}\kappa_0 \epsilon_m^2, \tag{2.96}$$

$$\overline{f}_*(v^*) \quad \leftrightarrow \quad V^0(\boldsymbol{p}, \boldsymbol{x}) = \inf_{\epsilon}\left\{\boldsymbol{p} : \epsilon - W(\epsilon, \boldsymbol{x}) + W^0(\epsilon)\right\} \tag{2.97}$$

with the new variable $\boldsymbol{p}$ representing stress polarization similarly as in the Hashin-Shtrikman method. Using (2.96) and (2.97), the upper bound becomes

$$\tilde{W}(\epsilon) \leq \inf_{\epsilon \in \boldsymbol{E}} \frac{1}{V}\int_V \left[W^0(\epsilon) + \boldsymbol{p} : \epsilon\right] d\boldsymbol{x} - \frac{1}{V}\int_V V^0(\boldsymbol{p}, \boldsymbol{x})\, d\boldsymbol{x} \tag{2.98}$$

where $\boldsymbol{E}$ is defined by (2.69). The second part of the problem is to construct the lower bound, which has to consider the expression

$$\underline{f}^*(v^*) \quad \leftrightarrow \quad V_0(\boldsymbol{p}, \boldsymbol{x}) = \sup_{\epsilon}\left\{\boldsymbol{p} : \epsilon - W(\epsilon, \boldsymbol{x}) + W_0(\epsilon)\right\}. \tag{2.99}$$

Keeping in mind that $W(\epsilon, \boldsymbol{x})$ depends on (2.95), where the exponent satisfies the relation $1 + 1/n_r \leq 2$, there is only one quadratic functional $W_0(\epsilon)$ so that the difference $W_0(\epsilon) - W(\epsilon, \boldsymbol{x})$ has a maximum. This functional is $W_0(\epsilon) = 0$ and for such a simple assumption, the lower bound of Willis and Talbot is reduced to the classical Reuss bound.

In general, the Willis-Talbot model can only construct one bound which will be a lower or upper bound depending on whether the difference $W_0(\epsilon) - W(\epsilon, \boldsymbol{x})$ is convex or concave. Another disadvantage of this model is that the primary and dual formulations do not yield the same bounds, but this problem has already been resolved in the method proposed by Castañeda.

2.3.3 Ponte Castañeda's new variational formulation

This method is based on transforming the energy functional of the composite material by using the energy functional of the comparison linear composite. The derivations will be shown in the example of static boundary conditions and a convex strain potential, with the nonlinearity stronger than quadratic. For the purpose of derivation, firstly, the strain potential of the comparison linear composite will be written in the form

$$U^0(\boldsymbol{\sigma}, \boldsymbol{x}) = \sum_{r=1}^{n} f_r(\boldsymbol{x})\, U_r^0(\boldsymbol{\sigma}) = \frac{1}{6\mu^0(\boldsymbol{x})}\sigma_e^2 + \frac{1}{2\kappa^0(\boldsymbol{x})}\sigma_m^2, \tag{2.100}$$

where $\sigma_m = \frac{1}{3}\mathrm{tr}\boldsymbol{\sigma}$ represents mean stress, $\sigma_e = \sqrt{\frac{3}{2}\boldsymbol{\sigma}_d : \boldsymbol{\sigma}_d}$ is effective stress, $\boldsymbol{\sigma}_d = \boldsymbol{\sigma} - \sigma_m \boldsymbol{I}$ is deviatoric stress tensor and material parameters are defined as follows

$$\mu^0(\boldsymbol{x}) = \sum_{r=1}^{n} f_r(\boldsymbol{x})\mu_r^0 > 0, \qquad \kappa^0(\boldsymbol{x}) = \sum_{r=1}^{n} f_r(\boldsymbol{x})\kappa_r^0 > 0. \tag{2.101}$$

After introducing the auxiliary notation $\boldsymbol{p} = \{\frac{1}{6\mu_r^0}, \frac{1}{2\kappa_r^0}\}$ and $\boldsymbol{s} = \{\sigma_e^2, \sigma_m^2\}$, the strain potential of one phase can be written as

$$U_r^0(\boldsymbol{\sigma}) = \frac{1}{6\mu_r^0}\sigma_e^2 + \frac{1}{2\kappa_r^0}\sigma_m^2 = \langle \boldsymbol{p}, \boldsymbol{s} \rangle \tag{2.102}$$

and the following Legendre-Fenchel transformation can be applied

$$V_r(\mu_r^0, \kappa_r^0) = \sup_{\boldsymbol{s}}(\langle \boldsymbol{p}, \boldsymbol{s} \rangle - U_r(\boldsymbol{s})) = \sup_{\boldsymbol{\sigma}} \left\{U_r^0(\boldsymbol{\sigma}) - U_r(\boldsymbol{\sigma})\right\} \tag{2.103}$$

where obviously the material parameters μ_r^0 and κ_r^0 become variables of the dual problem. If all of the phases are taken into account, the analogous expression has the form

$$V(\mu^0, \kappa^0) = \sum_{r=1}^{n} f_r(\boldsymbol{x}) V_r(\mu_r^0, \kappa_r^0) = \sup_{\boldsymbol{\sigma}} \left\{U^0(\boldsymbol{\sigma}, \boldsymbol{x}) - U(\boldsymbol{\sigma}, \boldsymbol{x})\right\} \tag{2.104}$$

which yields the inequality

$$U(\boldsymbol{\sigma}, \boldsymbol{x}) \geq U^0(\boldsymbol{\sigma}, \boldsymbol{x}) - V(\mu^0, \kappa^0) \tag{2.105}$$

and the expression for the lower bound

$$\tilde{U}(\bar{\boldsymbol{\sigma}}) \geq \tilde{U}^0(\bar{\boldsymbol{\sigma}}) - \bar{V}(\mu^0, \kappa^0). \tag{2.106}$$

Apart from the definition (2.72), the following notation is used in this inequality

$$\tilde{U}^0(\bar{\boldsymbol{\sigma}}) = \inf_{\boldsymbol{\sigma} \in S} \bar{U}^0(\boldsymbol{\sigma}), \tag{2.107}$$

$$\bar{V}(\mu^0, \kappa^0) = \sum_{r=1}^{n} c_r V_r(\mu_r^0, \kappa_r^0). \tag{2.108}$$

As before, c_r is the concentration of phase r and the overbar symbolizes the volume average over the RVE. Lower bound (2.106) can be further optimized with respect to the new variables μ_r^0, κ_r^0:

$$\tilde{U}(\bar{\boldsymbol{\sigma}}) \geq \tilde{U}_-(\bar{\boldsymbol{\sigma}}), \qquad \tilde{U}_-(\bar{\boldsymbol{\sigma}}) = \sup_{\mu_r^0, \kappa_r^0 > 0} \left\{\tilde{U}^0(\bar{\boldsymbol{\sigma}}) - \bar{V}(\mu^0, \kappa^0)\right\}. \tag{2.109}$$

For the dual case, the comparison strain functional is assumed to be

$$W^0(\boldsymbol{\epsilon}, \boldsymbol{x}) = \sum_{r=1}^{n} f_r(\boldsymbol{x})\; W_r^0(\boldsymbol{\epsilon}) = \frac{3}{2}\mu^0(\boldsymbol{x})\epsilon_e^2 + \frac{9}{2}\kappa^0(\boldsymbol{x})\epsilon_m^2 \tag{2.110}$$

and the final result is the optimized upper boundary in the form

$$\tilde{W}(\bar{\boldsymbol{\epsilon}}) \leq \tilde{W}_+(\bar{\boldsymbol{\epsilon}}), \qquad \tilde{W}_+(\bar{\boldsymbol{\epsilon}}) = \inf_{\mu_r^0, \kappa_r^0 > 0} \left\{\tilde{W}^0(\bar{\boldsymbol{\epsilon}}) + \bar{V}(\mu^0, \kappa^0)\right\} \tag{2.111}$$

where $\tilde{W}(\bar{\epsilon})$ is defined by (2.68) and the used notation is

$$\tilde{W}^0(\bar{\epsilon}) = \inf_{\epsilon \in \boldsymbol{E}} \tilde{W}^0(\epsilon), \tag{2.112}$$

$$V(\mu^0, \kappa^0) = \sup_{\epsilon} \left\{ W(\epsilon, \boldsymbol{x}) - W^0(\epsilon, \boldsymbol{x}) \right\}. \tag{2.113}$$

Bounds obtained by consideration of these two dual problems are conjugate of each other

$$\tilde{U}_-(\bar{\sigma}) = \sup_{\bar{\epsilon}} \left\{ \bar{\sigma} : \bar{\epsilon} + \tilde{W}_+(\bar{\epsilon}) \right\} \tag{2.114}$$

which proves that there is no duality gap between them. Note that here both dual problems are observed and not the upper and lower bound of the same formulation. Note also that, in most cases, $\tilde{U}^0(\bar{\sigma})$ in (2.109) and $\tilde{W}^0(\bar{\epsilon})$ in (2.111) cannot be calculated exactly, but some of the bounds or estimates for linear materials already explained in section 2.2 have to be used.

2.4 Numerical procedures

Because of the complexity of analytical solutions, the numerical modeling of composite materials has recently become particularly intensive. The following methods will be explained to illustrate the main tendencies in this field:

- Huet's partitioning method,
- domain decomposition method,
- adaptive hierarchical modeling method,
- secant method.

2.4.1 Huet's partitioning method

Huet's method is appropriate for cases where data for the complete RVE are not available so that consideration has to be given to a smaller domain D_0 or its uniform partition D_α instead. Recall that the uniform partition D_α of a domain D_0 is a set of its non-overlapping subdomains, which are all of the same form and whose union again builds the domain D_0. In the notation D_α index α represents the number of segments of uniform partition while each particular segment will be denoted by s_i.
Huet's work first generalizes the standard mechanical formulation of the elasticity tensor

$$\bar{\sigma} = \overline{\boldsymbol{C}} : \bar{\epsilon}, \qquad \overline{(\cdot)} = \int_{D_0} (\cdot)\, d\boldsymbol{x}, \qquad D_0 \equiv \text{RVE} \tag{2.115}$$

by introducing new definitions observing the arbitrary domain D_0 instead of the RVE

$$\overline{(\sigma)}_{D_0} = \boldsymbol{C}^{app} : \overline{(\epsilon)}_{D_0}, \qquad \overline{(\cdot)}_{D_0} = \int_{D_0} (\cdot)\, d\boldsymbol{x}, \qquad \forall D_0. \tag{2.116}$$

A similar definition is also introduced for the apparent compliance tensor

$$\overline{(\epsilon)}_{D_0} = \boldsymbol{M}^{app} : \overline{(\sigma)}_{D_0}, \qquad \overline{(\cdot)}_{D_0} = \int_{D_0} (\cdot)\, d\boldsymbol{x}, \qquad \forall D_0. \tag{2.117}$$

In both cases superscript "*app*" symbolizes the "apparent" value in contrast to the effective values $\bar{\boldsymbol{C}}$, $\bar{\boldsymbol{M}}$ and one should recall that $\boldsymbol{C}^{app}$, $\boldsymbol{M}^{app}$ can be different for different domains D_0, even with the same

measure. Furthermore, four types of test are proposed for calculating the apparent values. The first kind of test assumes the kinematic boundary conditions over the complete domain D_0

$$\boldsymbol{u} = \boldsymbol{\epsilon}^* \cdot \boldsymbol{x}, \quad \boldsymbol{x} \in \partial D_0 \tag{2.118}$$

and such a test yields apparent values $\boldsymbol{C}_{\epsilon 0}^{app}$ and $\boldsymbol{M}_{\epsilon 0}^{app}$ defined as follows

$$\overline{(\boldsymbol{\sigma})}_{D_0} = \boldsymbol{C}_{\epsilon 0}^{app} : \overline{(\boldsymbol{\epsilon})}_{D_0}, \qquad \boldsymbol{M}_{\epsilon 0}^{app} = (\boldsymbol{C}_{\epsilon 0}^{app})^{-1}. \tag{2.119}$$

The second type of test prescribes the same kinematic boundary conditions, but this time over the boundary of each segment of uniform partition, which will be written

$$\boldsymbol{u} = \boldsymbol{\epsilon}^* \cdot \boldsymbol{x}, \quad \boldsymbol{x} \in \partial D_\alpha. \tag{2.120}$$

These tests yield values $\boldsymbol{C}_{\epsilon\alpha}^{app}$ and $\boldsymbol{M}_{\epsilon\alpha}^{app}$ such that

$$\boldsymbol{C}_{\epsilon\alpha}^{app} = \left\langle \boldsymbol{C}_{\epsilon s_i}^{app} \right\rangle_{D_\alpha}, \qquad \overline{(\boldsymbol{\sigma})}_{s_i} = \boldsymbol{C}_{\epsilon s_i}^{app} : \overline{(\boldsymbol{\epsilon})}_{s_i}, \qquad \boldsymbol{M}_{\epsilon\alpha}^{app} = (\boldsymbol{C}_{\epsilon\alpha}^{app})^{-1}. \tag{2.121}$$

Here the symbol $\langle \cdot \rangle_{D_\alpha}$ represents the statistical average of the results obtained for individual segments. Two groups of tests still have to be carried out, but in this case for the static boundary conditions over the boundary of the domain D_0 and over the boundary of its uniform partition D_α respectively

$$\boldsymbol{\sigma} \cdot \boldsymbol{n} = \boldsymbol{\sigma}^* \cdot \boldsymbol{n}, \text{ on } \partial D_0, \qquad \text{and} \qquad \boldsymbol{\sigma} \cdot \boldsymbol{n} = \boldsymbol{\sigma}^* \cdot \boldsymbol{n}, \text{ on } \partial D_\alpha. \tag{2.122}$$

According to the definitions analogous to those given by (2.119) and (2.121), such tests yield apparent values $\boldsymbol{C}_{\sigma 0}^{app}$, $\boldsymbol{M}_{\sigma 0}^{app}$, $\boldsymbol{C}_{\sigma\alpha}^{app}$ and $\boldsymbol{M}_{\sigma\alpha}^{app}$. Note that the previous expressions use indices "ϵ" and "σ" in order to distinguish the type of boundary conditions, and "0" and "α" in order to emphasize if the complete domain D_0 or its partition D_α is considered.

The relation between the results obtained using these four different tests represents the essential conclusion of Huet's model, called partitioning theorem

$$\begin{aligned} \boldsymbol{C}_{\sigma\alpha}^{app} &\le \boldsymbol{C}_{\sigma 0}^{app} \le \boldsymbol{C}_{\epsilon 0}^{app} \le \boldsymbol{C}_{\epsilon\alpha}^{app}, \quad \forall D_0, \\ \boldsymbol{M}_{\epsilon\alpha}^{app} &\le \boldsymbol{M}_{\epsilon 0}^{app} \le \boldsymbol{M}_{\sigma 0}^{app} \le \boldsymbol{M}_{\sigma\alpha}^{app}, \quad \forall D_0. \end{aligned} \tag{2.123}$$

There are two important remarks concerning this relation. Firstly, the results obtained for the uniform partition are less precise than for the complete domain D_0 so that they give broader bounds for the actual values. Secondly, the results obtained for the elasticity tensor from the tests with static boundary conditions give the lower bound, and the upper bound with kinematic boundary conditions. The opposite situation applies to the compliance tensor.

The following section makes some interesting observations. Firstly, it should be emphasized that the effective values are obtained instead of the apparent values if the domain D_0 coincides with the RVE. By the definition of the RVE, the effective values are independent of the boundary conditions which means that

$$\boldsymbol{C}_{\sigma 0}^{app} = \boldsymbol{C}_{\epsilon 0}^{app} = \bar{\boldsymbol{C}}, \qquad \boldsymbol{M}_{\sigma 0}^{app} = \boldsymbol{M}_{\epsilon 0}^{app} = \bar{\boldsymbol{M}} \tag{2.124}$$

and consequently the partition theorem reduces to

$$\begin{aligned} \boldsymbol{C}_{\sigma\alpha}^{app} &\le \bar{\boldsymbol{C}} \le \boldsymbol{C}_{\epsilon\alpha}^{app}, \qquad D_0 \equiv \text{RVE}, \\ \boldsymbol{M}_{\epsilon\alpha}^{app} &\le \bar{\boldsymbol{M}} \le \boldsymbol{M}_{\sigma\alpha}^{app}, \qquad D_0 \equiv \text{RVE}. \end{aligned} \tag{2.125}$$

A further observation is that if the tests are carried out for some other uniform partition with greater number of subdomains β, ($\beta > \alpha$), the partition theorem obtains the extended form

$$\begin{aligned} C^{app}_{\sigma\beta} &\leq C^{app}_{\sigma\alpha} \leq C^{app}_{\sigma 0} \leq C^{app}_{\epsilon 0} \leq C^{app}_{\epsilon\alpha} \leq C^{app}_{\epsilon\beta}, \\ M^{app}_{\epsilon\beta} &\leq M^{app}_{\epsilon\alpha} \leq M^{app}_{\epsilon 0} \leq M^{app}_{\sigma 0} \leq M^{app}_{\sigma\alpha} \leq M^{app}_{\sigma\beta}. \end{aligned} \tag{2.126}$$

If the process of increasing the number of segments is continued, in the limiting case the size of subdomains becomes smaller than the size of inhomogeneities. This leads to the well-known Voigt (C_V) and Reuss (M_R) bounds and the partitioning theorem in the form

$$\begin{aligned} (M_R)^{-1} &\leq C^{app}_{\sigma\beta} \leq C^{app}_{\sigma\alpha} \leq C^{app}_{\sigma 0} \leq C^{app}_{\epsilon 0} \leq C^{app}_{\epsilon\alpha} \leq C^{app}_{\epsilon\beta} \leq C_V, \\ (C_V)^{-1} &\leq M^{app}_{\epsilon\beta} \leq M^{app}_{\epsilon\alpha} \leq M^{app}_{\epsilon 0} \leq M^{app}_{\sigma 0} \leq M^{app}_{\sigma\alpha} \leq M^{app}_{\sigma\beta} \leq M_R. \end{aligned}$$

Note that the previous approach does not precisely state how to calculate the apparent material parameters for domain D_0 or segment s_i. Laboratory tests and analytical or numerical procedures can be used to this end. The following sections look at the connection with the numerical procedures.

2.4.2 Domain decomposition method

Both of the methods based on application of the FEM which will be presented here are appropriate for linear heterogeneous materials, where the weak form of the problem for mixed boundary conditions is to determine displacements $\boldsymbol{u}$ satisfying the following conditions

$$\int_{\mathcal{B}} \nabla\delta\boldsymbol{u} : \boldsymbol{C} : \nabla\boldsymbol{u}\, d\boldsymbol{x} = \int_{\mathcal{B}} \boldsymbol{f}\cdot\delta\boldsymbol{u}\, d\boldsymbol{x} + \int_{\partial\mathcal{B}_t} \boldsymbol{t}\cdot\delta\boldsymbol{u}\, ds, \qquad \boldsymbol{u}|_{\partial\mathcal{B}_u} = \boldsymbol{u}^*. \tag{2.127}$$

Note that this expression looks at a body $\mathcal{B}$ and not at the RVE Ω. As stated at the very beginning, the boundary $\partial\mathcal{B}$ consists of two parts, one with prescribed displacements ($\partial\mathcal{B}_u$) and one with prescribed tractions ($\partial\mathcal{B}_t$). For these two parts of the boundary, it is valid that $\partial\mathcal{B}_u \cap \partial\mathcal{B}_t = \emptyset$ and $\partial\mathcal{B}_u \cup \partial\mathcal{B}_t = \partial\mathcal{B}$. $\boldsymbol{u}^*$ are displacements prescribed on the boundary and expression (2.127) must be satisfied for any test function $\delta\boldsymbol{u}$ such that $\delta\boldsymbol{u}|_{\partial\mathcal{B}_u} = \boldsymbol{0}$.

To understand the concept of the domain decomposition method, firstly it will be recalled that the main difficulty concerning the application of FEM in modeling heterogeneous materials is the process of discretization. Namely, it is easy to imagine that very fine meshing is required for materials with highly oscillatory microstructure, yielding a great number of DOFs, and huge systems of equations. Consequently, the main idea of this method is to replace the complex problem (2.127) by a few easily solvable problems. In more detail, the procedure can be described as follows.

- The original problem ($\mathcal{P}1$) is determined by equation (2.127). This defines the exact boundary conditions and material structure. In most cases this problem cannot be solved because of the sheer extent involved.
- The regularized problem ($\mathcal{P}2$) keeps the boundary conditions from the original problem, but assumes a regularized structure instead of the exact material structure. Linear or nonlinear material can be said to replace original material. It can be shown hat the optimal choice is a material with Reuss stiffness so that $\boldsymbol{R} = \left(\overline{\boldsymbol{C}^{-1}}\right)^{-1}$. The problem to be solved, is defined by the conditions

$$\int_{\mathcal{B}} \nabla\delta\boldsymbol{u} : \boldsymbol{R}(\nabla\boldsymbol{u}^R)\, d\boldsymbol{x} = \int_{\mathcal{B}} f\cdot\delta\boldsymbol{u}\, d\boldsymbol{x} + \int_{\partial\mathcal{B}_t} \boldsymbol{t}\cdot\delta\boldsymbol{u}\, ds, \qquad \boldsymbol{u}^R|_{\partial\mathcal{B}_u} = \boldsymbol{u}^*. \tag{2.128}$$

  Here, already a coarse discretization yields good results thanks to the simplicity of this problem. This is important as the results of this step are used as the boundary conditions in the next stage.

- In the decoupled problem $(\mathcal{P}3)$, the initial structure has to be divided into N partitions $\mathcal{B}_k$. The process of partitioning sees the formation of the new boundaries which are named internal boundaries, in contrast to external boundaries already defined in the original problem $(\mathcal{P}1)$. The problem to be solved for each of the partitions is

$$\int_{\mathcal{B}_k} \nabla\delta\boldsymbol{u}_k : \boldsymbol{\mathcal{C}} : \nabla\boldsymbol{u}_k^{R,ID}\, d\boldsymbol{x} = \int_{\mathcal{B}_k} f\cdot\delta\boldsymbol{u}_k\, d\boldsymbol{x} + \int_{\partial\mathcal{B}_k\cap\partial\mathcal{B}_t} \boldsymbol{t}\cdot\delta\boldsymbol{u}_k\, ds,$$

$$\boldsymbol{u}_k^{R,ID}|_{\partial\mathcal{B}_k\cap(\mathcal{B}\cup\partial\mathcal{B}_u)} = \boldsymbol{u}^R.$$

  This retains the material structure and external boundary conditions from the original problem but includes internal boundary conditions depending on the results of the regularized problem. The test function has to fulfill homogeneous boundary conditions $\delta\boldsymbol{u}_K|_{\partial\mathcal{B}_K\cap(\mathcal{B}\cup\partial\mathcal{B}_u)} = \boldsymbol{0}$.

- The final solution is a superposition of the solutions of problems $(\mathcal{P}2)$ and $(\mathcal{P}3)$ and has the form

$$\boldsymbol{u}^{R,ID} = \boldsymbol{u}^R + (\boldsymbol{u}_1^{R,ID} - \boldsymbol{u}^R)|_{\mathcal{B}_1} + \cdots + (\boldsymbol{u}_N^{R,ID} - \boldsymbol{u}^R)|_{\mathcal{B}_N} \tag{2.129}$$

  where the expressions in parenthesis have to be understood as a local perturbation of the regularized solution $\boldsymbol{u}^R$. If the obtained result is not satisfactory, it is advisable to improve partitioning or discretization of partitions while the discretization of the regularized problem should not significantly influence the quality of results. The proof of convergence is given in the original works [99, 100] and is based on Huet's partitioning method.

The previously explained procedure is called the initial displacement approach (superscript "ID") as the weak form of the problem depending on the potential energy is used. The analogous procedure is available for the dual formulation for which it can be shown that optimal choice of regularizing material is a material with Voigt stiffness $\boldsymbol{R} = \bar{\boldsymbol{\mathcal{C}}}$. This procedure is called the internal traction approach. Figure 2.2 shows the idea behind the domain decomposition method, in the example of the cantilever beam with heterogeneous structure.

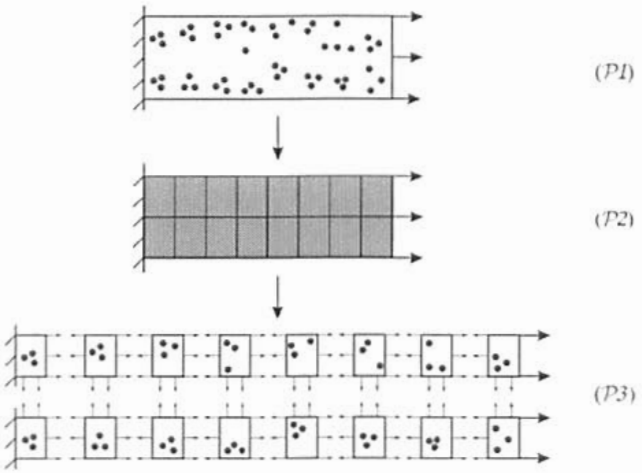

Figure 2.2: Concept of the domain decomposition method.

The advantages of solving regularized and decoupled problems $(\mathcal{P}2)$ and $(\mathcal{P}3)$ instead of the original problem $(\mathcal{P}1)$ are obvious. To solve the regularized problem $(\mathcal{P}2)$, a coarse mesh is already satisfactory while the fluctuation of the elasticity tensor is picked up by solving many small problems instead of the one large $(\mathcal{P}3)$. This procedure requires less time and computer capacity and is suitable for the application of parallel computing.

The domain decomposition method is practically an extension of Huet's partitioning method, with the possibility of calculating deformations of a structural element for any boundary conditions, while Huet's method is limited only to uniform external loading and estimation of the effective elasticity tensor.

2.4.3 Adaptive hierarchical modeling method

Another numerical method based on the application of FEM is the adaptive hierarchical modeling method. Its starting point is to look at a substitution system with an approximative, simple material structure divided into a set of non-overlapping partitions. The modeling error due to simplifying the material is calculated in each of the partitions. If it exceeds the permitted tolerance, this partition is divided into a set of subpartitions where more accurate material parameters have to be calculated. These material parameters replace the old ones and the procedure is repeated with an increasing number of subpartitions until the error tolerance is met everywhere. The number of partitions stays constant during the process.

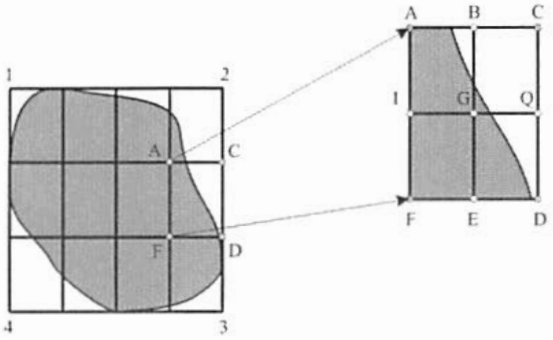

Figure 2.3: Partitioning of an arbitrary curvilinear body.

In order to explain the method in more detail, firstly, a closer look is given to the partitioning process (Fig. 2.3). Here one bounding box $\mathcal{G}$ is circumscribed around the body $\mathcal{B}$ and divided into N partitions

$$\mathcal{G} = \bigcup_{k=1}^{N} \mathcal{G}_k. \tag{2.130}$$

Usually, the partition boundaries do not follow the boundary of the body $\mathcal{B}$ as the body can have an arbitrary curvilinear shape. This means that apart from the partitions $\mathcal{G}_k$, the cells Θ_k have to be defined in the following way

$$\Theta_k = \mathcal{B} \cap \mathcal{G}_k, \qquad \mathcal{B} = \bigcup_{k=1}^{N} \Theta_k. \tag{2.131}$$

If the error bound in some partition k is higher than the permitted limit, this partition has to be divided into N_k^m subpartitions $\mathcal{G}_{k,l}$ and accordingly there will be N_k^m cells $\Theta_{k,l}$ so that

$$\mathcal{G}_k = \bigcup_{l=1}^{N_k^m} \mathcal{G}_{k,l}, \quad \Theta_{k,l} = \mathcal{B} \cap \mathcal{G}_{k,l}, \quad \Theta_k = \bigcup_{l=1}^{N_k^m} \Theta_{k,l}, \tag{2.132}$$

where superscript m represents the level of partitioning. If N_k^m subpartitions still do not provide satisfactory results in the next level, their number has to be increased.
The problem to be solved with respect to displacement $\boldsymbol{u}^m$ in each level of the partitioning is

$$\int_{\mathcal{B}} \nabla \delta \boldsymbol{u} : \boldsymbol{\mathcal{C}}^m : \nabla \boldsymbol{u}^m \, d\boldsymbol{x} = \int_{\mathcal{B}} \boldsymbol{f} \cdot \delta \boldsymbol{u} \, d\boldsymbol{x} + \int_{\Gamma_t} \boldsymbol{t} \cdot \delta \boldsymbol{u} \, ds, \qquad \boldsymbol{u}^m|_{\Gamma_u} = \boldsymbol{u}^*. \tag{2.133}$$

Here $\boldsymbol{\mathcal{C}}^m$ is the elasticity tensor of the substitution material on the level m; and for $m = 0$, $\boldsymbol{\mathcal{C}}^m$ mostly corresponds to the homogeneous isotropic material, but in the later stages it becomes dependent on the

coordinates. For an arbitrary domain $\mathcal{D} \in \mathcal{B}$, the quality of the approximation is estimated according to the condition

$$0 \leq ||\boldsymbol{u} - \boldsymbol{u}^m||_{E(\mathcal{D})} \leq \Psi_{\mathcal{D}}(\nabla \boldsymbol{u}^m) \tag{2.134}$$

where the symbol $||\cdot||^2_{E(\mathcal{D})}$ represents the energy norm, which is defined in the following manner for an arbitrary vector function $\boldsymbol{w}$

$$||\boldsymbol{w}||^2_{E(\mathcal{D})} = \int_{\mathcal{D}} \nabla \boldsymbol{w} : \boldsymbol{C} : \nabla \boldsymbol{w}\, d\boldsymbol{x}. \tag{2.135}$$

The term $||\boldsymbol{u} - \boldsymbol{u}^m||_{E(\mathcal{D})}$ is the exact error due to simplifying the material properties but it cannot be calculated as the exact solution $\boldsymbol{u}$ is not known. Instead, its bound $\Psi_{\mathcal{B}}(\nabla \boldsymbol{u}^m)$ can be calculated

$$\Psi_{\mathcal{B}}(\nabla \boldsymbol{u}^m) = \int_{\mathcal{B}} (\boldsymbol{I} - \boldsymbol{C}^{-1}\boldsymbol{C}^m)\nabla \boldsymbol{u}^m : \boldsymbol{C}(\boldsymbol{I} - \boldsymbol{C}^{-1}\boldsymbol{C}^m)\nabla \boldsymbol{u}^m d\boldsymbol{x}. \tag{2.136}$$

The important steps of the procedure can be reviewed as follows.

- **Step 1.** Error tolerance δ is prescribed so that it should be $||\boldsymbol{u} - \boldsymbol{u}^m||_{E(\mathcal{B})} \leq \delta$.
- **Step 2.** After defining the partitions, the error tolerance is distributed to the specific partitions according to the expression

$$\delta_k = \delta \frac{|\Theta_k|}{|\mathcal{B}|} \quad \forall k = 1, 2, \ldots, N. \tag{2.137}$$

- **Step 3.** The initial material parameters have to be chosen for the substitution material. The most frequent assumption here is that this is homogeneous isotropic material with material parameters calculated using the volume average

$$\kappa^0 = \frac{1}{|\mathcal{B}|}\int_{\mathcal{B}} \kappa\, d\boldsymbol{x} \qquad \mu^0 = \frac{1}{|\mathcal{B}|}\int_{\mathcal{B}} \mu\, d\boldsymbol{x}. \tag{2.138}$$

- **Step 4.** Solution of the problem (2.133) provides approximative displacements $\boldsymbol{u}^m$.
- **Step 5.** Error bound $\Psi_{\Theta_{k,l}}(\nabla \boldsymbol{u}^m)$ is calculated and compared with tolerance δ_k

$$\Psi_{\Theta_{k,l}}(\nabla \boldsymbol{u}^m) \leq \delta_k \quad \forall k = 1, 2, \ldots, N. \tag{2.139}$$

- **Step 6.** Subpartitioning is necessary with the calculation of new parameters in the partitions where condition (2.139) is not satisfied

$$\kappa^m|_{\Theta_{k,l}} = \frac{1}{|\Theta_{k,l}|}\int_{\Theta_{k,l}} \kappa\, d\boldsymbol{x}, \qquad \mu^m|_{\Theta_{k,l}} = \frac{1}{|\Theta_{k,l}|}\int_{\Theta_{k,l}} \mu\, d\boldsymbol{x}. \tag{2.140}$$

  Here the symbol $(\cdot)|_{\Theta_{k,l}}$ means inside the partition $\Theta_{k,l}$. New material parameters are introduced in the elasticity tensor, which becomes

$$\boldsymbol{C}^m(\boldsymbol{x})|_{\Theta_{k,l}} = \boldsymbol{C}^m_{k,l} \quad \boldsymbol{x} \in \Theta_{k,l}. \tag{2.141}$$

- **Step 7.** Steps 4-6 have to be repeated for the new elasticity tensor until the error tolerance has been met everywhere (Fig. 2.4, 2.5). If this is achieved in stage M, the final parameters are

$$\kappa^M|_{\Theta_{k,l}} = \frac{1}{|\Theta_{k,l}|}\int_{\Theta_{k,l}} \kappa\, d\boldsymbol{x} \qquad \mu^M|_{\Theta_{k,l}} = \frac{1}{|\Theta_{k,l}|}\int_{\Theta_{k,l}} \mu\, d\boldsymbol{x} \tag{2.142}$$

  and the final elasticity tensor becomes

$$\boldsymbol{C}^M(\boldsymbol{x})|_{\Theta_{k,l}} = \boldsymbol{C}^M_{k,l} \quad \boldsymbol{x} \in \Theta_{k,l}. \tag{2.143}$$

The disadvantage of this method is that in spite of constructing higher-level partitions, it cannot catch the influences of a fine microstructure. Consequently, it is mostly used only as a preprocessing procedure, for example in combination with the domain decomposition method. In this case, the adaptive hierarchical modeling method is used to solve the auxiliary problem ($\mathcal{P}2$) and the obtained results are introduced as a boundary condition in problem ($\mathcal{P}3$).

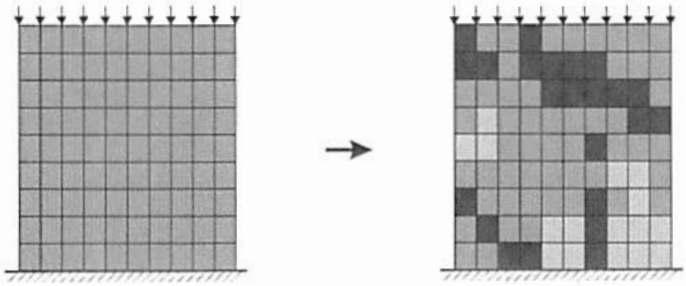

Figure 2.4: Reaverage of each high error cell.

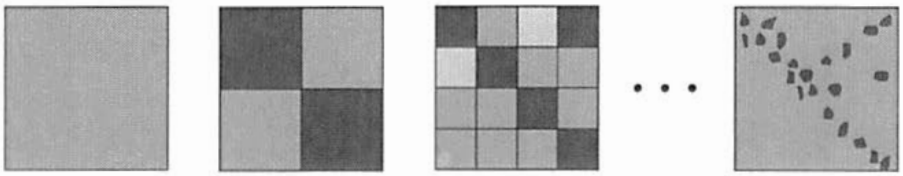

Figure 2.5: Refinement of individual cells with high error.

2.4.4 Secant method of Moulinec and Suquet

The last method to be mentioned here, is appropriate for nonlinear composites and is based on the secant theory, according to which the constitutive law for homogeneous materials has the form

$$\boldsymbol{\sigma} = \boldsymbol{\mathcal{C}}_0^s(\boldsymbol{\epsilon}) : \boldsymbol{\epsilon}, \tag{2.144}$$

$$\boldsymbol{\mathcal{C}}_0^s(\boldsymbol{\epsilon}) = 3k\boldsymbol{J} + 2\mu^s(\epsilon_e)\boldsymbol{K}, \tag{2.145}$$

$$J_{ijkl} = \frac{1}{3}\delta_{ij}\delta_{kl}, \quad K_{ijkl} = \frac{1}{2}(\delta_{ik}\delta_{jl} + \delta_{il}\delta_{jk}) - J_{ijkl}, \tag{2.146}$$

where the nonlinearity of the problem is caused by the dependence of the secant shear modulus μ^s on strains. In the case of heterogeneous materials with n-phases, the elasticity tensor becomes dependent on coordinates, which is written

$$\boldsymbol{\sigma}(\boldsymbol{x}) = \boldsymbol{\mathcal{C}}^s(\boldsymbol{x}) : \boldsymbol{\epsilon}(\boldsymbol{x}), \tag{2.147}$$

$$\boldsymbol{\mathcal{C}}^s(\boldsymbol{x}) = 3k(\boldsymbol{x})\,\boldsymbol{J} + 2\mu^s(\boldsymbol{x})\,\boldsymbol{K}, \tag{2.148}$$

$$k(\boldsymbol{x}) = \sum_{r=1}^{n} f_r(\boldsymbol{x})k_r, \quad \mu^s(\boldsymbol{x}) = \sum_{r=1}^{n} f_r(\boldsymbol{x})\mu_r^s(\epsilon_e(\boldsymbol{x})). \tag{2.149}$$

For modeling such materials, Moulinec and Suquet [69] proposed an iterative procedure which uses the strain from the previous step to calculate the elasticity tensor $\boldsymbol{\mathcal{C}}$ in the current step. Consequently, the material can be treated in each of the steps as a linear composite with an infinite number of phases as $\boldsymbol{\epsilon}$ is different in each point. In order to avoid this difficulty, Moulinec and Suquet assumed that the elasticity tensor does not depend on the exact strain, but rather on the effective strain of each phase

$$\mu_r^s = \mu^s(\boldsymbol{E}_r), \quad \boldsymbol{\mathcal{C}}_r = \boldsymbol{\mathcal{C}}_r^s(\boldsymbol{E}_r). \tag{2.150}$$

In this way, a linear composite material with a finite number of phases becomes the comparison material, and the methods described in section 2.2 can be applied to solve the problem. Different variants of the Moulinec-Suquet procedure are developed depending on the definition of E_r.
The classic secant theory is based on the assumption that the effective strain of phase r is the volume average of the strain over that phase

$$\boldsymbol{E}_r = (\bar{\boldsymbol{\epsilon}})_{(r)} \tag{2.151}$$

where, as usual, notation $(\bar{\cdot})_{(r)}$ represents the volume average over a phase r. The illustration of this method assumes that overall strain $\bar{\boldsymbol{\epsilon}}$ is prescribed and that the strain concentration tensor $\boldsymbol{A}(\boldsymbol{x})$ is applied for the calculation of the strain in each point

$$\boldsymbol{\epsilon}(\boldsymbol{x}) = \boldsymbol{A}(\boldsymbol{x}) : \bar{\boldsymbol{\epsilon}}. \tag{2.152}$$

Here the volume average over one phase yields

$$\boldsymbol{E}_r = \boldsymbol{A}_r : \bar{\boldsymbol{\epsilon}}, \quad \boldsymbol{A}_r = (\tilde{\boldsymbol{A}})_{(r)} \tag{2.153}$$

so that the whole procedure consists of three steps:

- the linear theory provides the expressions for the effective elasticity tensor $\bar{\boldsymbol{C}} = \bar{\boldsymbol{C}}(\boldsymbol{C}_i \,|\, i = 1, ..., n)$ and the strain concentration tensor $\boldsymbol{A}_r = \boldsymbol{A}_r(\boldsymbol{C}_i \,|\, i = 1, ..., n)$,
- the nonlinear system of equations has to be solved

$$\boldsymbol{C}_r = \boldsymbol{C}_r^s(\boldsymbol{E}_r), \quad \boldsymbol{E}_r = \boldsymbol{A}_r : \bar{\boldsymbol{\epsilon}}, \quad \boldsymbol{A}_r = \boldsymbol{A}_r(\boldsymbol{C}_i \,|\, i = 1, ... n), \tag{2.154}$$

- the effective stiffness tensor $\bar{\boldsymbol{C}} = \bar{\boldsymbol{C}}(\boldsymbol{C}_i \,|\, i = 1, ..., n)$ and the stress $\bar{\boldsymbol{\sigma}} = \bar{\boldsymbol{C}} : \bar{\boldsymbol{\epsilon}}$ have to be calculated for final $\boldsymbol{C}_i$, $i = 1, ..., n$.

There are significant disadvantages regarding the classic secant method, as the volume average of strain cannot include the influence of shear fluctuations which are responsible for the nonlinear behavior. Consequently, the modified secant method defines the effective strain as a second-order moment of strain

$$\boldsymbol{E}_r = \bar{\bar{\boldsymbol{\epsilon}}}_{eq}^{(r)} = (\bar{\epsilon}_e^2)_{(r)}^{1/2} \tag{2.155}$$

and the properties of the comparison material become

$$\mu_r^s = \mu^s(\bar{\bar{\epsilon}}_{eq}^{(r)}), \quad \boldsymbol{C}_r = \boldsymbol{C}_r^s(\bar{\bar{\boldsymbol{\epsilon}}}_{eq}^{(r)}). \tag{2.156}$$

Besides better results, one further useful property of this method is that effective strains in particular phases can be calculated directly from the expression for the effective elasticity tensor $\bar{\boldsymbol{C}}$ which is, as before, taken from the linear theory

$$\bar{\bar{\epsilon}}_{eq}^{(r)^2} = (\bar{\epsilon}_e^2)_{(r)} = \frac{1}{3c_r}\, \bar{\boldsymbol{\epsilon}} : \frac{\partial \bar{\boldsymbol{C}}}{\partial \mu_r}(k, \mu) : \bar{\boldsymbol{\epsilon}}. \tag{2.157}$$

This method obviously does not need the strain concentration tensors but expression (2.157) can be used instead. Once again, the procedure consists of three steps:

- the expression for the effective elasticity tensor $\bar{\boldsymbol{C}} = \bar{\boldsymbol{C}}(\boldsymbol{C}_i \,|\, i = 1, ..., n)$ is taken from the linear theory,
- the subsequent nonlinear system has to be solved

$$\bar{\boldsymbol{C}} = \bar{\boldsymbol{C}}(\boldsymbol{C}_i \,|\, i = 1, ..., n), \quad \boldsymbol{C}_r = \boldsymbol{C}_r^s(\bar{\bar{\boldsymbol{\epsilon}}}_{eq}^{(r)}), \quad \bar{\bar{\boldsymbol{\epsilon}}}_{eq}^{(r)} = \left(\frac{1}{3c_r}\, \bar{\boldsymbol{\epsilon}} : \frac{\partial \bar{\boldsymbol{C}}}{\partial \mu_r}(k, \mu) : \bar{\boldsymbol{\epsilon}}\right)^{1/2},$$

- the effective stiffness tensor $\bar{\boldsymbol{C}}$ and the stress $\bar{\boldsymbol{\sigma}} = \bar{\boldsymbol{C}} : \bar{\boldsymbol{\epsilon}}$ have to be calculated.

One important aspect of the modified secant method is that it has a variational structure, which means that the constitutive law of the effective material obtained in this way can be derived from a potential functional. This functional coincides with the potential based on the linear heterogeneous comparison composite proposed by Castañeda (Ch. 2.3.3).

In the end it can be summed up that the previous chapter has looked at some of the main methods for simulating heterogeneous material. They are classified into three groups: analytical procedures related to linear heterogeneous materials, analytical solutions in the case of material nonlinearity, and numerical solutions. In the last group, two of the methods are based on FEM, but they are appropriate for modeling heterogeneous materials where the size of inhomogeneities is finite compared to the size of a simulated body. This thesis will proceed to present a numerical method which applies when the ratio of the characteristic lengths of the scale tends to zero and influences of finite deformations have to be taken into consideration.

3 Theory of the multiscale method

3.1 Introduction

Following the overview of alternative methods, the rest of the work will focus on simulating the behavior of composite materials, using multiscale FEM in particular. As this is a homogenization method its application is limited to the group of materials whose microstructure can be satisfactorily described by an RVE. In this context, "micro/macro" expressions are often used with "micro" referring to the RVE problem while "macro" relates to the simulation of the real body (Fig. 3.1). The method requires considering of both scales simultaneously, so that the thesis introduces a notation where the overbar symbol distinguishes quantities related to macroscale from those related to microscale:

$\bar{\mathcal{B}},\ \bar{\boldsymbol{X}},\ \bar{\boldsymbol{x}},\ \bar{\boldsymbol{F}},\ \bar{\boldsymbol{P}},\ \bar{\boldsymbol{\sigma}}$ - macrocontinuum,

$\mathcal{B},\ \boldsymbol{X},\ \boldsymbol{x},\ \boldsymbol{F},\ \boldsymbol{P},\ \boldsymbol{\sigma}$ - microcontinuum.

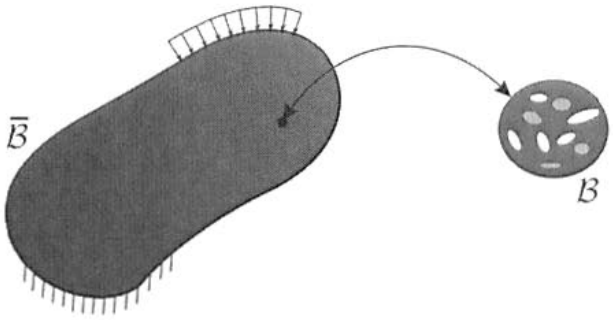

Figure 3.1: Connection of the scales.

The described setting of the problem permits the definition of two coupled boundary value problems, which is the essential property of the method. For the boundary value problem related to macroscale geometry, load and boundary conditions are prescribed while the constitutive law

$$\bar{\boldsymbol{P}} = \frac{\partial \bar{\Psi}}{\partial \bar{\boldsymbol{F}}} \tag{3.1}$$

is not available. For the microscale on the other hand, material parameters are known, the boundary conditions are derived from Hill's condition and micro- and macrostress tensors $\boldsymbol{P}, \bar{\boldsymbol{P}}$ can be calculated for the deformation taken from the macroscale, as a substitution for the missing constitutive law (3.1). The complete procedure can be summarized as follows:

- macrolevel computation provides macrodeformation tensor $\bar{\boldsymbol{F}}$,
- for the provided $\bar{\boldsymbol{F}}$, microscale calculations yield stress tensors $\boldsymbol{P}$ and $\bar{\boldsymbol{P}}$,
- the solution of the problem can be continued at macrolevel.

The following sections look initially at the main quantities in the theory of finite deformations, together with further definitions of the effective values and an explanation for the transformation of Hill's macrohomogeneity condition. For additional reading see Miehe and Schröder [60]-[64],[79].

3.2 Basic quantities in the theory of finite deformations

Considering the finite deformations starts with the observation of the body motion shown in the Figure 3.2. Here $\mathcal{B} \subset \mathcal{R}^3$ represents the body at some moment t_0 usually taken to be the initial moment $t_0 = 0$ and $\mathcal{B}_t \subset \mathcal{R}^3$ represents the body at some other time $t > 0$. These configurations are called reference and current configuration respectively and for the purpose of this short overview it is assumed that they are presented in an unique coordinate system (system $E_1E_2E_3$ coincides with $e_1e_2e_3$).

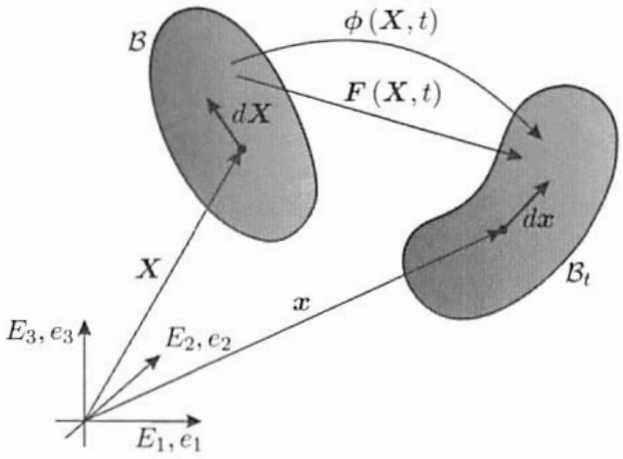

Figure 3.2: Reference and current configuration of the body $\mathcal{B}$.

According to standard notation, quantities describing the state of deformations or forces in the reference configuration are denoted by capital letters, and quantities related to the current configuration are denoted by lowercase letters. For example, $\boldsymbol{X}, \boldsymbol{V}, \boldsymbol{B}, \boldsymbol{T}$ represent position-vector, volume, body forces and tractions related to the reference configuration and $\boldsymbol{x}, \boldsymbol{v}, \boldsymbol{b}, \boldsymbol{t}$ are the corresponding quantities related to the current configuration. Exceptions are especially pronounced. The same principle of notation is valid for operators. These begin with a capital letter if defined in the reference coordinate system (Div, Grad), while the corresponding operators in the current system begin with a lowercase letter (div, grad). For more concise notation, in some cases the symbols " ∇ " and " $\nabla_{\boldsymbol{x}}$" can be used for the reference and the current configuration, respectively.

The choice of a configuration does not influence the results, but rather how the problem is described. Considering the reference configuration leads to the Lagrangian description and considering the current configuration leads to the Eulerian description, which can also be called the material and spatial description, depending on whether consideration is given to the motion of a material point or the spatial position.

The mathematical description of the body motion is given by the deformation $\phi(\boldsymbol{X},t)$ such that

$$\phi(\boldsymbol{X},t) : \mathcal{B} \rightarrow \mathcal{B}_t. \tag{3.2}$$

This mapping relates the points of the reference configuration $\boldsymbol{X} \in \mathcal{B}$ with the points of the current configuration $\boldsymbol{x} \in \mathcal{B}_t$ according to

$$\boldsymbol{x} = \phi(\boldsymbol{X},t). \tag{3.3}$$

The same can be expressed using the displacement function $\boldsymbol{u}(\boldsymbol{X})$:

$$\boldsymbol{x} = \boldsymbol{X} + \boldsymbol{u}(\boldsymbol{X},t) = \boldsymbol{X} + \boldsymbol{u} \tag{3.4}$$

which further yields the following definition of the deformation gradient $\boldsymbol{F}$

$$\boldsymbol{F} = \nabla \boldsymbol{x} = \frac{\partial \boldsymbol{x}(\boldsymbol{X}, t)}{\partial \boldsymbol{X}} = \boldsymbol{I} + \nabla \boldsymbol{u}. \tag{3.5}$$

This gradient, among others, enables transformations of quantities corresponding to the different configurations called push-forward and pull-back transformations. The illustration considers the change in geometry during the deformation process, where the transformation of material and spatial vectors $d\boldsymbol{X}$ and $d\boldsymbol{x}$ can be written as

$$d\boldsymbol{x} = \boldsymbol{F} \cdot d\boldsymbol{X}, \tag{3.6}$$

the deformation of the element area $d\boldsymbol{A}$ with normal $\boldsymbol{N}$ is given by Nanson's formula,

$$d\boldsymbol{a} = J\boldsymbol{F}^{-T} \cdot d\boldsymbol{A}, \qquad d\boldsymbol{A} = dA\,\boldsymbol{N}, \qquad d\boldsymbol{a} = da\,\boldsymbol{n} \tag{3.7}$$

and the volume change can be calculated according to

$$dv = JdV, \qquad J = \det \boldsymbol{F} > 0 \tag{3.8}$$

with J representing the Jacobian. The other quantities describing deformations are the right and left Cauchy deformation tensors $\boldsymbol{C}$ and $\boldsymbol{b}$

$$\boldsymbol{C} = \boldsymbol{F}^T \cdot \boldsymbol{F}, \qquad \boldsymbol{b} = \boldsymbol{F} \cdot \boldsymbol{F}^T \tag{3.9}$$

and the Green and Almansi strain tensors $\boldsymbol{E}$ and $\boldsymbol{e}$

$$\boldsymbol{E} = \frac{1}{2}(\boldsymbol{C} - \boldsymbol{I}), \qquad \boldsymbol{e} = \frac{1}{2}(\boldsymbol{I} - \boldsymbol{b}^{-1}), \tag{3.10}$$

relating the undeformed and deformed line elements $d\boldsymbol{X}_1$, $d\boldsymbol{X}_2$, $d\boldsymbol{x}_1$, $d\boldsymbol{x}_2$ in the following way:

$$d\boldsymbol{x}_1 \cdot d\boldsymbol{x}_2 = d\boldsymbol{X}_1 \cdot \boldsymbol{C} \cdot d\boldsymbol{X}_2, \qquad d\boldsymbol{X}_1 \cdot d\boldsymbol{X}_2 = d\boldsymbol{x}_1 \cdot (\boldsymbol{b}^{-1}) \cdot d\boldsymbol{x}_2,$$

$$\frac{1}{2}(d\boldsymbol{x}_1 \cdot d\boldsymbol{x}_2 - d\boldsymbol{X}_1 \cdot d\boldsymbol{X}_2) = d\boldsymbol{X}_1 \cdot \boldsymbol{E} \cdot d\boldsymbol{X}_2, \qquad \frac{1}{2}(d\boldsymbol{x}_1 \cdot d\boldsymbol{x}_2 - d\boldsymbol{X}_1 \cdot d\boldsymbol{X}_2) = d\boldsymbol{x}_1 \cdot \boldsymbol{e} \cdot d\boldsymbol{x}_2.$$

The extension of the analysis to the time-dependent processes requires the introduction of at least two types of time derivatives: the material time derivative, where reference coordinates are kept constant, and the spatial derivative, where current coordinates are fixed

$$D_t = \left.\frac{\partial}{\partial t}\right|_{\boldsymbol{X}=\text{const}}, \qquad \text{material time derivative,} \tag{3.11}$$

$$\partial_t = \left.\frac{\partial}{\partial t}\right|_{\boldsymbol{x}=\text{const}}, \qquad \text{spatial time derivative.} \tag{3.12}$$

Bearing in mind that the material time derivative of a quantity related to the reference configuration can also be denoted by the dot symbol, the basic time derivatives, velocity $\boldsymbol{V}(\boldsymbol{X}, t)$ and acceleration $\boldsymbol{A}(\boldsymbol{X}, t)$, become

$$\boldsymbol{V}(\boldsymbol{X}, t) = \dot{\boldsymbol{\phi}}(\boldsymbol{X}, t) = \boldsymbol{v}(\boldsymbol{\phi}^{-1}(\boldsymbol{x}, t), t), \tag{3.13}$$

$$\boldsymbol{A}(\boldsymbol{X}, t) = \ddot{\boldsymbol{\phi}}(\boldsymbol{X}, t) = \boldsymbol{a}(\boldsymbol{\phi}^{-1}(\boldsymbol{x}, t), t), \tag{3.14}$$

while the material strain rate $\boldsymbol{D}$ and the rate of deformation tensor $\boldsymbol{d}$ are defined by the expressions

$$\boldsymbol{D} = \dot{\boldsymbol{E}} = \frac{1}{2}(\dot{\boldsymbol{F}}^T \cdot \boldsymbol{F} + \boldsymbol{F}^T \cdot \dot{\boldsymbol{F}}), \qquad \boldsymbol{d} = \boldsymbol{F}^{-T} \cdot \boldsymbol{D} \cdot \boldsymbol{F}^{-1} = \frac{1}{2}(\boldsymbol{l}^T + \boldsymbol{l}). \tag{3.15}$$

Here the last term depends on the so-called spatial velocity gradient $\boldsymbol{l}$

$$\boldsymbol{l} = \operatorname{div} \boldsymbol{v} = \dot{\boldsymbol{F}} \cdot \boldsymbol{F}^{-1}. \tag{3.16}$$

Finally, the stress can also be described using several quantities. The stress state in the current configuration is represented by the true Cauchy stress tensor $\boldsymbol{\sigma}$ whose multiplication by the Jacobian yields the Kirchhoff stress tensor

$$\boldsymbol{\tau} = J\boldsymbol{\sigma}. \tag{3.17}$$

The derivation based on the assumption that the force $d\boldsymbol{p}$ acting on the surface element before and after deformation must remain unchanged, yields the definition of the two-point unsymmetric first Piola Kirchhoff stress tensor $\boldsymbol{P}$

$$d\boldsymbol{p} = \boldsymbol{\sigma} \cdot d\boldsymbol{a} = J\boldsymbol{\sigma} \cdot \boldsymbol{F}^{-T} \cdot d\boldsymbol{A}, \tag{3.18}$$

$$\boldsymbol{P} = J\boldsymbol{\sigma} \cdot \boldsymbol{F}^{-T}, \tag{3.19}$$

whose symmetric counterpart is the second Piola Kirchhoff stress tensor $\boldsymbol{S}$

$$\boldsymbol{S} = J\boldsymbol{F}^{-1} \cdot \boldsymbol{\sigma} \cdot \boldsymbol{F}^{-T} = \boldsymbol{F}^{-1} \cdot \boldsymbol{P}. \tag{3.20}$$

The described kinematic and kinetic quantities form the following power conjugate pairs

$$\mathcal{E} = \boldsymbol{P} : \dot{\boldsymbol{F}} = \boldsymbol{S} : \dot{\boldsymbol{E}} = \boldsymbol{\tau} : \boldsymbol{d} \tag{3.21}$$

where $\mathcal{E}$ represents elastic power. Note that in this short overview, only the most important definitions and relations needed for the formulation of multiscale FEM are presented, while for further reading Ciarlet [19], Ogden [73] and Marsden and Hughes [58] are recommended.

3.3 Main characteristics of the multiscale method

3.3.1 Definition of the macrovariables

The relationship between the quantities characteristic for the different scales of the multiscale method are established according to Hill's assumption that macroquantities have to be expressed dependent on the microquantities acting on the boundary of RVE. This is motivated by the observation that, if laboratory tests are carried out, all quantities necessary for calculation of the effective material properties must be measured on the surface and not inside the sample. A further advantage is that such formulation yields a simple connection of the scales.

Initially, the definition of the relations requires considering an arbitrary RVE $\mathcal{B}$ with one or more cavities and singular surfaces. Such an RVE is shown in Figure 3.3 where the boundaries of the cavities are denoted by $\mathcal{G}$ and the singular surfaces by Γ.

As the multiscale method is based on the concept of the volume average, two general relations are used to define the macrovariables. Firstly, the following is valid for any vector field $\boldsymbol{A}$ defined in the described domain $\mathcal{B}$

$$\int_{\mathcal{B}} \operatorname{Grad} \boldsymbol{A}\, dV = \int_{\partial\mathcal{B}} \boldsymbol{A} \otimes \boldsymbol{N}\, dA + \int_{\mathcal{G}} \boldsymbol{A} \otimes \boldsymbol{N}\, dA - \int_{\Gamma} [\![\boldsymbol{A}]\!] \otimes \boldsymbol{N}\, dA. \tag{3.22}$$

Here $\boldsymbol{N}$ is normal to the surface, $\otimes$ represents the dyadic product and $[\![\boldsymbol{A}]\!]$ in $\boldsymbol{X} \in \Gamma$ is the jump of vector field $\boldsymbol{A}$ on the singular surface. Secondly, for tensor fields $\boldsymbol{M}$ and $\boldsymbol{Q}$ such that

$$\begin{aligned} \operatorname{Div}\boldsymbol{M} &= \boldsymbol{0} \quad \text{in } \mathcal{B}, \\ [\![\boldsymbol{M}]\!] \cdot \boldsymbol{N} &= \boldsymbol{0} \quad \text{on } \Gamma, \\ \boldsymbol{M} \cdot \boldsymbol{N} &= \boldsymbol{0} \quad \text{on } \mathcal{G}, \\ \boldsymbol{Q} &= (\operatorname{Grad} \boldsymbol{R})^T \end{aligned} \tag{3.23}$$

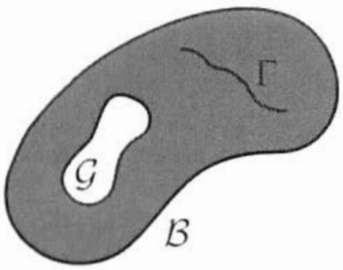

Figure 3.3: An arbitrary RVE with cavities and singular surfaces.

where $\boldsymbol{R}$ is a vector field, the volume average of the product can be directly transformed into a surface integral

$$\left(\overline{\boldsymbol{M}\cdot\boldsymbol{Q}}\right) = \frac{1}{V}\int_{\mathcal{B}} \boldsymbol{M}\cdot\boldsymbol{Q}\, dV = \frac{1}{V}\int_{\partial\mathcal{B}} (\boldsymbol{M}\cdot\boldsymbol{N})\otimes\boldsymbol{R}\, dA. \tag{3.24}$$

Using the fact that the first Piola Kirchhoff stress tensor satisfies the expressions (3.23)

$$\begin{aligned} \mathrm{Div}\boldsymbol{P} &= \boldsymbol{0} \quad \text{in} \quad \mathcal{B}, \\ [\![\boldsymbol{P}]\!]\cdot\boldsymbol{N} &= \boldsymbol{0} \quad \text{on} \quad \Gamma, \\ \boldsymbol{P}\cdot\boldsymbol{N} &= \boldsymbol{0} \quad \text{on} \quad \mathcal{G}, \end{aligned} \tag{3.25}$$

and that unit tensor $\boldsymbol{I} = \mathrm{Grad}\boldsymbol{X}$ can be observed instead of an arbitrary tensor $\boldsymbol{Q}$, the first Piola Kirchhoff macrostress tensor can be defined as

$$\bar{\boldsymbol{P}} := \frac{1}{V}\int_{\mathcal{B}} \boldsymbol{P} dV = \frac{1}{V}\int_{\partial\mathcal{B}} (\boldsymbol{P}\cdot\boldsymbol{N})\otimes\boldsymbol{X}\, dA = \frac{1}{V}\int_{\partial\mathcal{B}} \boldsymbol{T}\otimes\boldsymbol{X}\, dA, \quad \boldsymbol{T} = \boldsymbol{P}\cdot\boldsymbol{N} \tag{3.26}$$

and the Kirchhoff macro-stress tensor becomes

$$\bar{\boldsymbol{\tau}} := \frac{1}{V}\int_{\mathcal{B}} \boldsymbol{P}\cdot\boldsymbol{F}^T dV = \frac{1}{V}\int_{\mathcal{B}} \boldsymbol{\tau}\, dV = \frac{1}{V}\int_{\partial\mathcal{B}} \boldsymbol{T}\otimes\boldsymbol{x}\, dA. \tag{3.27}$$

Furthermore using the following definition for the Jacobian,

$$\bar{J} := \frac{1}{V}\int_{\mathcal{B}} J\, dV = \frac{1}{V}\int_{\mathcal{B}_t} dv = v/V, \tag{3.28}$$

the Cauchy macro-stress tensor can be expressed as

$$\bar{\boldsymbol{\sigma}} := \frac{1}{\bar{J}}\int_{\mathcal{B}} \boldsymbol{\tau}\, dV = \frac{1}{v}\int_{\partial\mathcal{B}_t} \boldsymbol{t}\otimes\boldsymbol{x}\, da, \qquad \boldsymbol{t} = \boldsymbol{\sigma}\cdot\boldsymbol{n}. \tag{3.29}$$

Finally, the definition of the macrodeformation gradient $\bar{\boldsymbol{F}}$ has to be discussed. The microdeformation gradient $\boldsymbol{F}$ itself does not fulfill conditions (3.23) but is defined as $\boldsymbol{F} = \mathrm{Grad}\,\boldsymbol{x}$. Consequently, relation (3.22) can be directly applied to calculate its volume average

$$\frac{1}{V}\int_{\mathcal{B}} \boldsymbol{F}\, dV = \frac{1}{V}\left[\int_{\partial\mathcal{B}} \boldsymbol{x}\otimes\boldsymbol{N}\, dA + \int_{\mathcal{G}} \boldsymbol{x}\otimes\boldsymbol{N}\, dA - \int_{\Gamma} [\![\boldsymbol{x}]\!]\otimes\boldsymbol{N}\, dA\right]. \tag{3.30}$$

Given that macroquantities depend only on values on the boundary of the RVE and assuming that there are no singular surfaces, $[\![\boldsymbol{x}]\!] = 0$, the first term in the right-hand side of (3.30) will be chosen as the definition of the macrodeformation gradient

$$\bar{\boldsymbol{F}} := \frac{1}{V}\int_{\partial\mathcal{B}} \boldsymbol{x}\otimes\boldsymbol{N}\, dA = \frac{1}{V}\left[\int_{\mathcal{B}} \boldsymbol{F}\, dV - \int_{\mathcal{G}} \boldsymbol{x}\otimes\boldsymbol{N}\, dA\right]. \tag{3.31}$$

Clearly, the macrodeformation gradient only coincides with the volume average of the microdeformation gradient for an RVE without cavities or singular surfaces.

3.3.2 Transformation of Hill's macrohomogeneity condition

In order to equate the mechanical and energetic formulation in addition to the definitions explained in the last section, micro- and macroquantities also have to satisfy Hill's macrohomogeneity condition (Ch. 2.1.4). In the case of geometrical nonlinearity, the initial form of this condition states that macropower has to be equal to the volume average of micropower [43]:

$$\bar{\boldsymbol{P}} : \dot{\bar{\boldsymbol{F}}} = \frac{1}{V} \int_{\mathcal{B}} \boldsymbol{P} : \dot{\boldsymbol{F}} \, dV. \tag{3.32}$$

However, this expression needs to be reformulated as it does not tell us much about the state of the microdeformations. To this end, firstly, Gauss' theorem is applied to transform the right-hand side of (3.32) into a surface integral

$$\frac{1}{V} \int_{\mathcal{B}} \boldsymbol{P} : \dot{\boldsymbol{F}} \, dV = \frac{1}{V} \int_{\partial\mathcal{B}} \boldsymbol{T} \cdot \dot{\boldsymbol{x}} \, dA \tag{3.33}$$

and the substitution of (3.33) into (3.32) then yields an expression which can still be extended by adding and subtracting the same term $\bar{\boldsymbol{P}} : \dot{\bar{\boldsymbol{F}}}$

$$\frac{1}{V} \int_{\partial\mathcal{B}} \boldsymbol{T} \cdot \dot{\boldsymbol{x}} \, dA - \bar{\boldsymbol{P}} : \dot{\bar{\boldsymbol{F}}} - \bar{\boldsymbol{P}} : \dot{\bar{\boldsymbol{F}}} + \bar{\boldsymbol{P}} : \dot{\bar{\boldsymbol{F}}} = 0. \tag{3.34}$$

Additionally, the transformations depending on boundary integrals

$$\begin{aligned}
\bar{\boldsymbol{P}} : \dot{\bar{\boldsymbol{F}}} &= \bar{\boldsymbol{P}} : \tfrac{1}{V} \textstyle\int_{\partial\mathcal{B}} \dot{\boldsymbol{x}} \otimes \boldsymbol{N} \, dA &&= \tfrac{1}{V} \textstyle\int_{\partial\mathcal{B}} (\bar{\boldsymbol{P}}\boldsymbol{N}) \cdot \dot{\boldsymbol{x}} \, dA, \\
\bar{\boldsymbol{P}} : \dot{\bar{\boldsymbol{F}}} &= \tfrac{1}{V} \textstyle\int_{\partial\mathcal{B}} \boldsymbol{T} \otimes \boldsymbol{X} \, dA : \dot{\bar{\boldsymbol{F}}} &&= \tfrac{1}{V} \textstyle\int_{\partial\mathcal{B}} \boldsymbol{T} \cdot (\dot{\bar{\boldsymbol{F}}}\boldsymbol{X}) \, dA, \\
\bar{\boldsymbol{P}} : \dot{\bar{\boldsymbol{F}}} &= \bar{\boldsymbol{P}} \tfrac{1}{V} \textstyle\int_{\mathcal{B}} (\mathrm{Grad}\boldsymbol{X})^T \, dV \dot{\bar{\boldsymbol{F}}} &&= \tfrac{1}{V} \textstyle\int_{\partial\mathcal{B}} (\bar{\boldsymbol{P}}\boldsymbol{N}) \cdot (\dot{\bar{\boldsymbol{F}}}\boldsymbol{X}) \, dA,
\end{aligned} \tag{3.35}$$

have to be used for derivation of the alternative form of Hill's condition

$$\frac{1}{V} \int_{\partial\mathcal{B}} (\boldsymbol{T} - \bar{\boldsymbol{P}}\boldsymbol{N}) \cdot (\dot{\boldsymbol{x}} - \dot{\bar{\boldsymbol{F}}}\boldsymbol{X}) \, dA = 0. \tag{3.36}$$

Two solutions of this condition are obvious; they are obtained if the expressions in parenthesis are equal to zero. This directly defines the static and kinematic type of boundary conditions for the RVE

$$\boldsymbol{T} = \bar{\boldsymbol{P}} \cdot \boldsymbol{N} \quad \text{on } \partial\mathcal{B} \qquad \text{- static b.c.} \tag{3.37}$$

$$\boldsymbol{x} = \bar{\boldsymbol{F}} \cdot \boldsymbol{X} \quad \text{on } \partial\mathcal{B} \qquad \text{- kinematic b.c.} \tag{3.38}$$

An additional solution of (3.36) is valid only in the case of a periodic microstructure, with the specific property that each boundary part $\partial\mathcal{B}^+$ of the RVE with normal $\boldsymbol{N}^+$ has its counterpart $\partial\mathcal{B}^-$ with normal $\boldsymbol{N}^-$, so that $\boldsymbol{N}^+ = -\boldsymbol{N}^-$ (Fig. 3.4).

For such a solution, deformation has to be assumed in the form dependent on microfluctuations $\tilde{\boldsymbol{w}}$

$$\boldsymbol{x} = \bar{\boldsymbol{F}}\boldsymbol{X} + \tilde{\boldsymbol{w}} \tag{3.39}$$

so that introducing this assumption in (3.33) yields

$$\bar{\boldsymbol{P}} : \dot{\bar{\boldsymbol{F}}} = \frac{1}{V} \int_{\partial\mathcal{B}} \boldsymbol{T} \cdot (\dot{\bar{\boldsymbol{F}}}\boldsymbol{X}) \, dA + \frac{1}{V} \int_{\partial\mathcal{B}^+} \boldsymbol{T}^+ \cdot \dot{\tilde{\boldsymbol{w}}}^+ \, dA + \frac{1}{V} \int_{\partial\mathcal{B}^-} \boldsymbol{T}^- \cdot \dot{\tilde{\boldsymbol{w}}}^- \, dA. \tag{3.40}$$

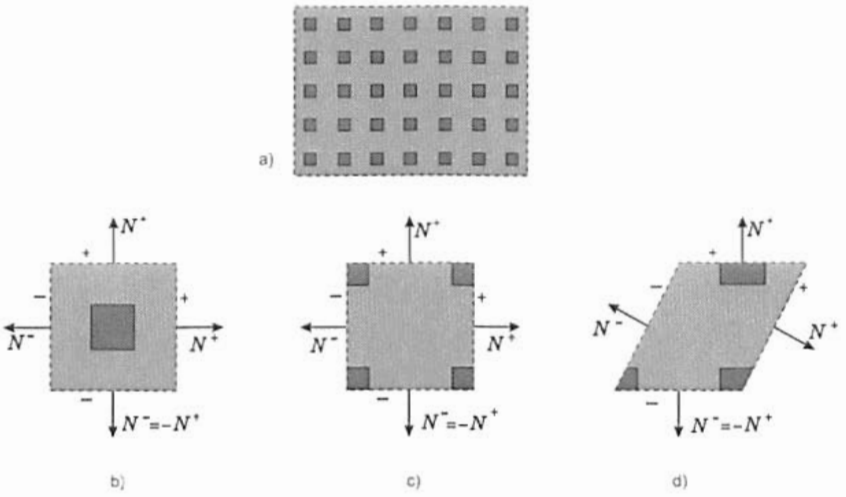

Figure 3.4: Various RVEs of a material with periodic microstructure.

Here $\boldsymbol{w}^+, \boldsymbol{T}^+$ represent microfluctuations and tractions in a point $\boldsymbol{X}^+ \in \partial\mathcal{B}^+$, and $\boldsymbol{w}^-, \boldsymbol{T}^-$ microfluctuations and tractions in a corresponding point $\boldsymbol{X}^- \in \partial\mathcal{B}^-$. Assuming periodic deformations and antiperiodic tractions on the boundary (Fig. 3.5)

$$\boldsymbol{w}^+ = \boldsymbol{w}^- = \boldsymbol{w}, \quad \boldsymbol{T}^+ = -\boldsymbol{T}^-, \qquad \text{on } \partial\mathcal{B}, \tag{3.41}$$

it can be shown that the sum of the last two terms in (3.40) is equal to zero

$$\frac{1}{V}\int_{\partial\mathcal{B}^+} \boldsymbol{T}^+ \cdot \dot{\boldsymbol{w}}^+ \, dA + \frac{1}{V}\int_{\partial\mathcal{B}^-} \boldsymbol{T}^- \cdot \dot{\boldsymbol{w}}^- \, dA = \frac{1}{V}\int_{\partial\mathcal{B}^+} \left(\boldsymbol{T}^+ + \boldsymbol{T}^-\right) \cdot \dot{\boldsymbol{w}} \, dA = 0. \tag{3.42}$$

The remaining part of (3.40) is the second expression in (3.35), which means that Hill's condition is identically satisfied.

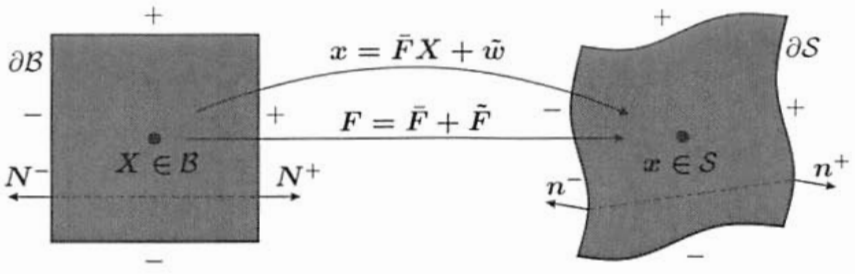

Figure 3.5: Deformation of RVE with periodic boundary conditions.

An important consequence of the assumption (3.39) is that the microdeformation gradient can be written as a sum of the macrodeformation gradient $\bar{\boldsymbol{F}}$ and the microfluctuations gradient $\tilde{\boldsymbol{F}}$

$$\boldsymbol{F} = \operatorname{Grad} \boldsymbol{x} = \bar{\boldsymbol{F}} + \operatorname{Grad} \tilde{\boldsymbol{w}} = \bar{\boldsymbol{F}} + \tilde{\boldsymbol{F}}. \tag{3.43}$$

In the remaining part of the thesis, analysis will focus primarily on materials with a periodic microstructure or consisting of parts with a periodic structure, making intensive use of the latter type of boundary conditions.

4 Coupling of the homogenization theory and FEM

The previous chapter explained the concept of the multiscale FEM, emphasizing that, typical for that method, one boundary value problem has to be solved on each of the levels. The relations between macro- and microquantities are assumed in accordance with the concept of the volume average, and the boundary conditions at microlevel are derived from Hill's macrohomogeneity condition. The only point which has not been considered yet, is the method of solving the mentioned boundary value problems. The FEM is used to this end in the framework of this thesis. Later on, various examples will show that this particular choice makes possible to model a wide spectrum of materials with very different microstructures.

For a simple explanation of how the methods are coupled, the main idea in this chapter is to stress the differences between standard and multiscale formulation. To this end, two cases are chosen: the standard form of the energy and the mixed formulation applicable to nearly incompressible materials. The chapter is organized as follows:

- the first part presents the standard FEM formulation for both types of the energy potential,
- the second part extends this formulation to the case where both scales are included.

4.1 FEM application for modeling of nonlinear elastic materials

4.1.1 Standard variational principle

In this introductory example, it is assumed that the body consists of a hyperelastic material with the free energy $\Psi(\boldsymbol{F})$ depending only on the deformation $\boldsymbol{F}$, so that the total potential of the body Π has the form

$$\Pi = \int_{\mathcal{B}} \Psi(\boldsymbol{F})\, dV + \Pi^{ext}, \qquad \boldsymbol{u} = \boldsymbol{u}^* \quad \text{on} \quad \partial\mathcal{B}_u \tag{4.1}$$

where Π^{ext} represents the potential of the external load, and the kinematic boundary conditions are prescribed on $\mathcal{B}_u$. As the actual deformation minimizes the potential, displacements can be calculated from the condition that the first variation of potential (4.1) is equal to zero

$$\delta\Pi(\boldsymbol{u}, \delta\boldsymbol{u}) = \int_{\mathcal{B}} \delta\boldsymbol{F} : \boldsymbol{P}\, dV - \int_{\mathcal{B}} \delta\boldsymbol{u} \cdot \boldsymbol{B}\, dV - \int_{\partial\mathcal{B}_t} \delta\boldsymbol{u} \cdot \boldsymbol{T}\, dA = 0, \tag{4.2}$$

$$\boldsymbol{u} = \boldsymbol{u}^*, \quad \delta\boldsymbol{u} = 0, \quad \text{on } \partial\mathcal{B}_u.$$

The previous problem is nonlinear and in the frame of this work for its solution the Newton-Raphson iteration procedure is used. According to this method a new displacement increment $\Delta\boldsymbol{u}$ is calculated in each step so that the following condition is satisfied

$$\text{Lin}\,\delta\Pi\,(\boldsymbol{u}^c, \delta\boldsymbol{u}, \Delta\boldsymbol{u}) = \delta\Pi\,(\boldsymbol{u}^c, \delta\boldsymbol{u}) + \Delta\delta\Pi\,(\boldsymbol{u}^c, \delta\boldsymbol{u}, \Delta\boldsymbol{u}) = 0. \tag{4.3}$$

This expression represents the linearization of (4.2) where $\boldsymbol{u}^c$ is the current value of displacement, updated at the end of each step according to

$$\boldsymbol{u}^c \leftarrow \boldsymbol{u}^c + \Delta\boldsymbol{u}. \tag{4.4}$$

The whole proceeding is continued until the prescribed error tolerance for a criterion mostly based on applying the energy norm is reached. The first term in (4.3) can be calculated using (4.2), but the second variation of the potential

$$\Delta\delta\Pi\left(\boldsymbol{u}, \delta\boldsymbol{u}, \Delta\boldsymbol{u}\right) = \Delta\left[\int_{\mathcal{B}} \delta\boldsymbol{F} : \boldsymbol{P}\, dV - \int_{\mathcal{B}} \delta\boldsymbol{u} \cdot \boldsymbol{B}\, dV - \int_{\partial\mathcal{B}_t} \delta\boldsymbol{u} \cdot \boldsymbol{T}\, dA\right] \tag{4.5}$$

still has to be determined. For that purpose it should be emphasized that only the conservative loads are considered in the following and that in such a case the increment of the last two terms in (4.5) is equal to zero, as this type of load is deformation independent. Based on this assumption, the reduction of (4.5) yields

$$\Delta\delta\Pi\left(\boldsymbol{u}, \delta\boldsymbol{u}, \Delta\boldsymbol{u}\right) = \int_{\mathcal{B}} \Delta\left(\delta\boldsymbol{F} : \boldsymbol{P}\right) dV = \int_{\mathcal{B}} \delta\boldsymbol{F} : \Delta\boldsymbol{P}\, dV \tag{4.6}$$

and applying the transformation

$$\Delta\boldsymbol{P} = \boldsymbol{\mathcal{C}} : \Delta\boldsymbol{F}, \qquad \boldsymbol{\mathcal{C}} = \frac{\partial\boldsymbol{P}}{\partial\boldsymbol{F}} = \frac{\partial^2\psi\left(\boldsymbol{F}\right)}{\partial\boldsymbol{F}^2}, \tag{4.7}$$

where $\boldsymbol{\mathcal{C}}$ represents the elasticity tensor, the second variation of the potential becomes

$$\Delta\delta\Pi\left(\boldsymbol{u}, \delta\boldsymbol{u}, \Delta\boldsymbol{u}\right) = \int_{\mathcal{B}} \delta\boldsymbol{F} : \boldsymbol{\mathcal{C}} : \Delta\boldsymbol{F}\, dV. \tag{4.8}$$

Finally, after introducing (4.2) and (4.8) into (4.3), the linearized problem takes the form

$$\begin{aligned} &\mathrm{Lin}\,\delta\Pi\left(\boldsymbol{u}^c, \delta\boldsymbol{u}, \Delta\boldsymbol{u}\right) = \\ &\underbrace{\int_{\mathcal{B}} \delta\boldsymbol{F} : \boldsymbol{P}\, dV - \int_{\mathcal{B}} \delta\boldsymbol{u} \cdot \boldsymbol{B}\, dV - \int_{\delta\mathcal{B}_t} \delta\boldsymbol{u} \cdot \boldsymbol{T}\, dA}_{\delta\Pi\left(\boldsymbol{u}^c, \delta\boldsymbol{u}\right)} + \underbrace{\int_{\mathcal{B}} \delta\boldsymbol{F} : \boldsymbol{\mathcal{C}} : \Delta\boldsymbol{F}\, dV}_{\Delta\delta\Pi\left(\boldsymbol{u}^c, \delta\boldsymbol{u}, \Delta\boldsymbol{u}\right)} = 0. \end{aligned} \tag{4.9}$$

which is also appropriate for introducing FEM approximation [6, 49, 53]. To illustrate the complete procedure, a four-node discretization and isoparametric bilinear shape functions are assumed:

$$N^i = \frac{1}{4}\left(1 + \xi\xi_i\right)\left(1 + \eta\eta_i\right), \quad i = 1, .., 4 \tag{4.10}$$

with ξ, η being natural coordinates such that $\xi \in [-1, 1]$ and $\eta \in [-1, 1]$. ξ_i, η_i are coordinates of node i in the natural coordinate system (ξ, η), which is shown in Figure 4.1.

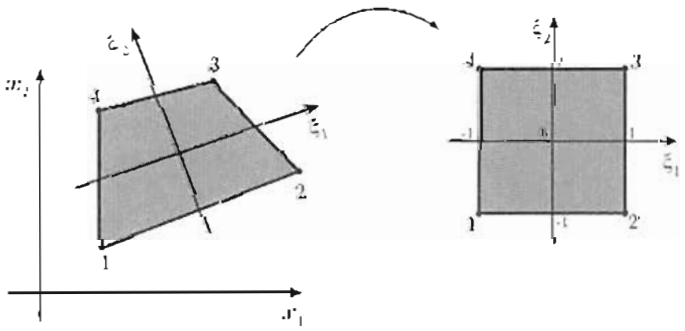

Figure 4.1: Physical and natural coordinate system.

Shape functions (4.10) permit to express the coordinates in both configurations dependent on the nodal coordinates X_i and x_i as follows

$$X \approx \sum_{i=1}^{4} N^i\left(\xi, \eta\right) X_i, \qquad x \approx \sum_{i=1}^{4} N^i\left(\xi, \eta\right) x_i \tag{4.11}$$

and in the same way, the quantities related to the displacements become

$$\boldsymbol{u} \approx \sum_{i=1}^{4} N^i(\xi,\eta)\,\boldsymbol{u}_i\,, \quad \delta\boldsymbol{u} \approx \sum_{i=1}^{4} N^i(\xi,\eta)\,\delta\boldsymbol{u}_i, \quad \Delta\boldsymbol{u} \approx \sum_{i=1}^{4} N^i(\xi,\eta)\,\Delta\boldsymbol{u}_i. \tag{4.12}$$

Here $\boldsymbol{u}_i$, $\delta\boldsymbol{u}_i$ and $\Delta\boldsymbol{u}_i$ represent again the nodal values. Relations (4.11) and (4.12) can also be written in the matrix notation

$$\boldsymbol{X} \approx \boldsymbol{N}\cdot\boldsymbol{X}^e, \qquad \boldsymbol{x} \approx \boldsymbol{N}\cdot\boldsymbol{x}^e, \tag{4.13}$$

$$\boldsymbol{u} \approx \boldsymbol{N}\cdot\boldsymbol{u}^e, \qquad \delta\boldsymbol{u} \approx \boldsymbol{N}\cdot\delta\boldsymbol{u}^e, \qquad \Delta\boldsymbol{u} \approx \boldsymbol{N}\cdot\Delta\boldsymbol{u}^e, \tag{4.14}$$

where the vector $\boldsymbol{u}^e$ consists of the nodal vectors

$$\boldsymbol{u}^{eT} = \left\{ \begin{array}{cccc} \boldsymbol{u}_1^T & \boldsymbol{u}_2^T & \boldsymbol{u}_3^T & \boldsymbol{u}_4^T \end{array} \right\}, \qquad \boldsymbol{u}_i^T = \left\{ \begin{array}{ccc} u_i^1 & u_i^2 & u_i^3 \end{array} \right\}. \tag{4.15}$$

In the notation u_i^j the lower index represents the node and the upper index represents the degree of freedom. The vectors $\boldsymbol{X}^e$, $\boldsymbol{x}^e$, $\delta\boldsymbol{u}^e$, $\Delta\boldsymbol{u}^e$ are defined analogous to $\boldsymbol{u}^e$, and the terms of matrix $\boldsymbol{N}$ are shape functions ordered as follows

$$\boldsymbol{N} = \left\{ \begin{array}{cccc} \boldsymbol{N}^1 & \boldsymbol{N}^2 & \boldsymbol{N}^3 & \boldsymbol{N}^4 \end{array} \right\}, \qquad \boldsymbol{N}^i = \left\{ \begin{array}{ccc} N^i & 0 & 0 \\ 0 & N^i & 0 \\ 0 & 0 & N^i \end{array} \right\}. \tag{4.16}$$

(4.15) and (4.16) are presumed to describe a 3D problem. Substituting (4.13), (4.14) into (4.9) together with the assembling process yield the approximation

$$\int_{\mathcal{B}} \delta\boldsymbol{F} : \boldsymbol{P}\,dV - \int_{\mathcal{B}} \delta\boldsymbol{u}\cdot\boldsymbol{B}\,dV - \int_{\partial\mathcal{B}_t} \delta\boldsymbol{u}\cdot\boldsymbol{T}\,dA \;\approx\; \delta\boldsymbol{U}^T\cdot\boldsymbol{R} \tag{4.17}$$

$$\int_{\mathcal{B}} \delta\boldsymbol{F} : \boldsymbol{C} : \Delta\boldsymbol{F}\,dV \;\approx\; \delta\boldsymbol{U}^T\cdot\boldsymbol{K}\cdot\Delta\boldsymbol{U} \tag{4.18}$$

so that problem (4.9) obtains the new form

$$\delta\boldsymbol{U}^T\cdot\{\boldsymbol{K}\cdot\Delta\boldsymbol{U} + \boldsymbol{R}\} = \boldsymbol{0} \tag{4.19}$$

where $\boldsymbol{K}$ is the stiffness matrix, $\boldsymbol{R}$ is the residual vector, and $\Delta\boldsymbol{U}$ is a vector of unknown displacement increments for the whole system. As the values of the test function $\delta\boldsymbol{U}$ can be arbitrary, the expression in parenthesis must be equal to zero, yielding an algebraic system of equations in the unknown $\Delta\boldsymbol{U}$

$$\boldsymbol{K}\cdot\Delta\boldsymbol{U} + \boldsymbol{R} = \boldsymbol{0}. \tag{4.20}$$

The new current value of the displacements of all nodal points $\boldsymbol{U}$ has to be calculated by superposition

$$\boldsymbol{U} \leftarrow \boldsymbol{U} + \Delta\boldsymbol{U}. \tag{4.21}$$

4.1.2 The mixed variational principle and the derivation of the P0Q1 element

In the case of incompressible or nearly incompressible materials, the standard variational formulation shows the effect of volume locking which is manifested by obtaining the results corresponding to the behavior of a much stiffer material than is actually the case. To improve the results, a few mixed methods are developed with the three-field variational description proposed by Simo, Taylor and Pister [80] being presented here. In this method, in addition to the displacements, two new variables, hydrostatic pressure

p and volume change Θ, are introduced to decouple the volumetric and deviatoric parts of the potential. Accordingly, the total potential has the form

$$\Pi(\boldsymbol{u},\Theta,p)=\int_V\left[\Psi_{vol}(\Theta)+\Psi_{dev}(\bar{\boldsymbol{C}}(\boldsymbol{u}))+p(J(\boldsymbol{u})-\Theta)\right]dV+\Pi^{ext}, \tag{4.22}$$

where $\bar{\boldsymbol{C}}$ is the right Cauchy Green deformation tensor corresponding to a pure distortion as its determinant is equal to one

$$\bar{\boldsymbol{C}}=J^{-\frac{2}{3}}\boldsymbol{C},\qquad \det\bar{\boldsymbol{C}}=1. \tag{4.23}$$

Analogous expressions for the deformation gradient $\bar{\boldsymbol{F}}$ are often necessary, too,

$$\bar{\boldsymbol{F}}=J^{-\frac{1}{3}}\boldsymbol{F},\qquad \det\bar{\boldsymbol{F}}=1. \tag{4.24}$$

The minimization of (4.22) yields three conditions

$$\delta_u\Pi=\delta_u\Pi^{int}+\delta_u\Pi^{ext}=\int_V\left[(\frac{\partial\Psi_{dev}}{\partial\boldsymbol{C}}+p\frac{\partial J}{\partial\boldsymbol{C}})\delta\boldsymbol{C}(\boldsymbol{u})\right]dV+\delta_u\Pi^{ext}=0, \tag{4.25}$$

$$\delta_\Theta\Pi=\int_V\left[(\frac{\partial\Psi_{vol}}{\partial\Theta}-p)\delta\Theta\right]dV=0, \tag{4.26}$$

$$\delta_p\Pi=\int_V[(J-\Theta)\delta p]\,dV=0 \tag{4.27}$$

which can be additionally reformulated. Firstly, for the transformation of (4.25), it is convenient to introduce the following brief notation

$$\boldsymbol{S}_{dev}=2\frac{\partial\Psi_{dev}}{\partial\boldsymbol{C}},\qquad \boldsymbol{S}_{vol}=2p\frac{\partial J}{\partial\boldsymbol{C}}=pJ\boldsymbol{C}^{-1} \tag{4.28}$$

and to write the variation of the Cauchy Green deformation tensor in the form

$$\delta\boldsymbol{C}=\boldsymbol{F}^{\mathrm{T}}\cdot\mathrm{Grad}\,\delta\boldsymbol{u}+\mathrm{Grad}^{\mathrm{T}}\delta\boldsymbol{u}\cdot\boldsymbol{F}. \tag{4.29}$$

In this way, the variation of internal potential becomes

$$\delta_u\Pi^{int}=\int_V\left[(\mathrm{Grad}^{\mathrm{T}}\delta\boldsymbol{u}\cdot\boldsymbol{F}):(\boldsymbol{S}_{dev}+\boldsymbol{S}_{vol})\right]dV \tag{4.30}$$

and the linearization of condition (4.25) reads

$$\begin{aligned}&\int_V\mathrm{Grad}\,\delta\boldsymbol{u}:[\mathrm{Grad}\Delta\boldsymbol{u}\cdot(\boldsymbol{S}_{dev}+\boldsymbol{S}_{vol})]dV\\&+\int_V(\mathrm{Grad}^{\mathrm{T}}\delta\boldsymbol{u}\cdot\boldsymbol{F}):\left(2\frac{\partial\boldsymbol{S}_{dev}}{\partial\boldsymbol{C}}+2\frac{\partial\boldsymbol{S}_{vol}}{\partial\boldsymbol{C}}\right):(\boldsymbol{F}^{\mathrm{T}}\cdot\mathrm{Grad}\,\Delta\boldsymbol{u})dV\\&+\int_V(\mathrm{Grad}^{\mathrm{T}}\delta\boldsymbol{u}\cdot\boldsymbol{F}):\left(\frac{\partial\boldsymbol{S}_{vol}}{\partial p}\Delta p\right)dV+\Delta\delta_u\Pi^{ext}=-\delta\Pi^{res}(\boldsymbol{u})\end{aligned} \tag{4.31}$$

where $\delta\Pi^{res}(\boldsymbol{u})$ represents the value of the variation of potential (4.22) for the current $\boldsymbol{u}$. Furthermore, expressions (4.26) and (4.27) can be reformulated in the following way

$$p=\frac{\partial\psi_{vol}}{\partial\Theta}\qquad\Rightarrow\qquad\Delta p=\frac{\partial^2\psi_{vol}}{\partial^2\Theta}\Delta\Theta, \tag{4.32}$$

$$\Theta=\frac{1}{V}\int_V JdV\qquad\Rightarrow\qquad\Delta\Theta=\frac{1}{V}\int_V J\mathbf{C}^{-1}:(\boldsymbol{F}^{\mathrm{T}}\cdot\mathrm{Grad}\,\Delta\boldsymbol{u})dV \tag{4.33}$$

where the latter is obtained using the assumption that the volume change Θ is the volume average of the Jacobian J instead of the strong form $J = \Theta$. The implementation of the obtained increments in (4.31) results in the alternative form of the linearized problem

$$\begin{aligned}
&\int_V \mathrm{Grad}\,\delta\boldsymbol{u} : [\mathrm{Grad}\Delta\boldsymbol{u} \cdot (\boldsymbol{S}_{dev} + \boldsymbol{S}_{vol})]dV \\
&+ \int_V (\mathrm{Grad}^{\mathrm{T}}\delta\boldsymbol{u} \cdot \boldsymbol{F}) : \boldsymbol{C} : (\boldsymbol{F}^{\mathrm{T}} \cdot \mathrm{Grad}\,\Delta\boldsymbol{u})dV \\
&+ \int_V \left[(\mathrm{Grad}^{\mathrm{T}}\delta\boldsymbol{u} \cdot \boldsymbol{F}) : J\boldsymbol{C}^{-1} \left(\frac{1}{V} \frac{\partial^2 \Psi_{vol}}{\partial \Theta^2} \right) \int_V J\boldsymbol{C}^{-1} : (\boldsymbol{F}^{\mathrm{T}} \cdot \mathrm{Grad}\Delta\boldsymbol{u})dV \right] dV \\
&+ \Delta\delta_{\boldsymbol{u}}\Pi^{ext} = -\delta\Pi^{res}(\boldsymbol{u})
\end{aligned} \tag{4.34}$$

where it applies that

$$\frac{\partial \boldsymbol{S}_{vol}}{\partial p} = J\boldsymbol{C}^{-1} \tag{4.35}$$

and the elasticity tensor $\boldsymbol{C}$ is calculated as the following superposition

$$\boldsymbol{C} = \boldsymbol{C}_{dev} + \boldsymbol{C}_{vol}, \qquad \boldsymbol{C}_{dev} = 2\frac{\partial \boldsymbol{S}_{dev}}{\partial \boldsymbol{C}}, \qquad \boldsymbol{C}_{vol} = 2\frac{\partial \boldsymbol{S}_{vol}}{\partial \boldsymbol{C}}. \tag{4.36}$$

Finally, introducing the FEM-approximation (Sec. 4.1.2) into (4.34) yields the system of algebraic equations

$$\boldsymbol{K} \cdot \Delta\boldsymbol{U} + \boldsymbol{R} = 0 \tag{4.37}$$

with a stiffness matrix of the form

$$\begin{aligned}
\boldsymbol{K} &= \int_{V^e} \boldsymbol{G}^{\mathrm{T}} \cdot (\boldsymbol{S}_{dev} + \boldsymbol{S}_{vol}) \cdot \boldsymbol{G}\, dV \\
&+ \int_{V^e} (\boldsymbol{B}^{\mathrm{T}} \cdot \boldsymbol{F}) : \boldsymbol{C} : (\boldsymbol{F}^{\mathrm{T}} \cdot \boldsymbol{B})dV \\
&+ \int_{V^e} \left[(\boldsymbol{B}^{\mathrm{T}} \cdot \boldsymbol{F}) : J\boldsymbol{C}^{-1} \left(\frac{1}{V} \frac{\partial^2 \Psi_{vol}}{\partial \Theta^2} \right) \int_{V^e} J\boldsymbol{C}^{-1} : (\boldsymbol{F}^{\mathrm{T}} \cdot \boldsymbol{B})dV \right] dV.
\end{aligned} \tag{4.38}$$

Here the following notation is used

$$\mathrm{Grad}\Delta\boldsymbol{u} = \boldsymbol{B} \cdot \Delta\boldsymbol{u}^e, \qquad \mathrm{Grad}\,\delta\boldsymbol{u} = \boldsymbol{B} \cdot \delta\boldsymbol{u}^e, \qquad \boldsymbol{B} = \mathrm{Grad}\,\boldsymbol{N}, \tag{4.39}$$

and the matrix $\boldsymbol{G}$ consists of derivatives of shape functions so that the following condition is satisfied

$$\int_{V^e} \mathrm{Grad}\delta\boldsymbol{u} : [\mathrm{Grad}\Delta\boldsymbol{u} \cdot (\boldsymbol{S}_{dev} + \boldsymbol{S}_{vol})]dV = \delta\boldsymbol{u} \cdot \int_{V^e} [\boldsymbol{G}^{\mathrm{T}} \cdot (\boldsymbol{S}_{dev} + \boldsymbol{S}_{vol}) \cdot \boldsymbol{G}]dV \cdot \Delta\boldsymbol{u}. \tag{4.40}$$

Expressions (4.38) and (4.40) depend on the integral over a volume of an element V^e. Except in the case of incompressible materials, the principle of decoupling of deformation into a volumetric and a deviatoric part is often used in plastic deformation modes as they are exclusively deviatoric. In the scope of the FEM, the described derivation corresponds to the so called P0Q1 element.

4.2 Multiscale FEM for modeling of materials with nonlinear microstructure

4.2.1 The standard variational principle

In order to achieve a clear representation of the connection between the homogenization theory and FEM, the strong and the variational form of the problem in the case of the standard form of potential will be

considered separately for each of the scales.

The explanation starts with the strong form of the boundary value problem on the macroscale consisting of the equilibrium equation and the boundary conditions

$$\begin{aligned} &\mathrm{Div}\bar{\boldsymbol{P}}(\bar{\boldsymbol{F}}) + \bar{\boldsymbol{B}} = 0 \quad &&\text{in} \quad &&\bar{\mathcal{B}}, \\ &\bar{\boldsymbol{T}} = \bar{\boldsymbol{P}}\cdot\bar{\boldsymbol{N}} &&\text{on} \quad &&\partial\bar{\mathcal{B}}_t, \\ &\bar{\boldsymbol{u}} = \bar{\boldsymbol{u}}_0 &&\text{on} \quad &&\partial\bar{\mathcal{B}}_u, \end{aligned} \tag{4.41}$$

where the parts of the boundary still have to satisfy the usual conditions

$$\partial\bar{\mathcal{B}} = \partial\bar{\mathcal{B}}_u \cup \partial\bar{\mathcal{B}}_t, \qquad \partial\bar{\mathcal{B}}_u \cap \partial\bar{\mathcal{B}}_t = \emptyset. \tag{4.42}$$

System (4.41) is equal to the problem formulation of any singlescale method except that $\bar{\boldsymbol{P}}$ cannot be calculated directly, but rather using microscale results. The FEM solution of (4.41) has already been studied in section 4.1.1 showing that the weak form corresponding to this system is given by

$$\bar{\Pi} = \int_{\bar{\mathcal{B}}} \bar{\Psi}(\bar{\boldsymbol{F}})\, d\bar{V} + \bar{\Pi}^{ext}, \qquad \bar{\boldsymbol{u}} = \bar{\boldsymbol{u}}_0 \quad \text{on} \quad \partial\bar{\mathcal{B}}_u \tag{4.43}$$

and that its second variation has the form

$$\mathrm{Lin}\,\delta\bar{\Pi} = \underbrace{\int_{\bar{\mathcal{B}}} \delta\bar{\boldsymbol{F}} : \bar{\boldsymbol{P}}\, d\bar{V} - \int_{\bar{\mathcal{B}}} \delta\bar{\boldsymbol{u}}\cdot\bar{\boldsymbol{B}}\, dV - \int_{\partial\bar{\mathcal{B}}_t} \delta\bar{\boldsymbol{u}}\cdot\bar{\boldsymbol{T}}\, d\bar{A}}_{\delta\bar{\Pi}(\bar{\boldsymbol{u}},\delta\bar{\boldsymbol{u}})} + \underbrace{\int_{\bar{\mathcal{B}}} \delta\bar{\boldsymbol{F}} : \bar{\boldsymbol{C}} : \Delta\bar{\boldsymbol{F}}\, d\bar{V}}_{\Delta\delta\bar{\Pi}(\bar{\boldsymbol{u}},\delta\bar{\boldsymbol{u}},\Delta\bar{\boldsymbol{u}})} = 0.$$

The primary variable at this level is the displacement $\bar{\boldsymbol{u}}$ and its approximation

$$\bar{\boldsymbol{u}} = \sum_{i=1}^{4} N^i(\xi,\eta)\,\bar{\boldsymbol{u}}_i\,, \quad \delta\bar{\boldsymbol{u}} = \sum_{i=1}^{4} N^i(\xi,\eta)\,\delta\bar{\boldsymbol{u}}_i, \quad \Delta\bar{\boldsymbol{u}} = \sum_{i=1}^{4} N^i(\xi,\eta)\,\Delta\bar{\boldsymbol{u}}_i, \tag{4.44}$$

yields a linear system of equations in the unknown increment $\Delta\bar{\boldsymbol{U}}$

$$\bar{\boldsymbol{K}}\cdot\Delta\bar{\boldsymbol{U}} + \bar{\boldsymbol{R}} = 0, \tag{4.45}$$

$$\bar{\boldsymbol{U}} = \bar{\boldsymbol{U}}_0 \quad \text{on} \quad \partial\bar{\mathcal{B}}_u \tag{4.46}$$

where $\bar{\boldsymbol{U}}$ is the vector of displacements of all nodes in $\mathcal{B}/\partial\bar{\mathcal{B}}_u$ and $\bar{\boldsymbol{U}}_0$ are the prescribed displacements on the boundary part $\partial\bar{\mathcal{B}}_u$.

The microscale problem is slightly different. Assuming periodic boundary conditions derived from Hill's condition, the strong form of the microscale problem becomes

$$\begin{aligned} &\mathrm{Div}\boldsymbol{P}(\boldsymbol{F}) = 0 \quad &&\text{in} \quad &&\mathcal{B}, \\ &\tilde{\boldsymbol{w}}^{+} = \tilde{\boldsymbol{w}}^{-}, &&\text{on} \quad &&\partial\mathcal{B}, \end{aligned} \tag{4.47}$$

where the connection between stresses and microfluctuations is given according to

$$\boldsymbol{P} = \boldsymbol{P}(\boldsymbol{F}), \qquad \boldsymbol{F} = \mathrm{Grad}\,\boldsymbol{x} = \bar{\boldsymbol{F}} + \tilde{\boldsymbol{F}}, \qquad \boldsymbol{x} = \bar{\boldsymbol{F}}\boldsymbol{X} + \tilde{\boldsymbol{w}}. \tag{4.48}$$

As the body forces are neglected and kinematic boundary conditions are prescribed over the entire boundary, the potential at the microscale has only one term

$$\Pi = \int_{\mathcal{B}} \Psi(\boldsymbol{F}) \tag{4.49}$$

and its first and second variations are

$$\delta\Pi(\tilde{\boldsymbol{w}},\delta\tilde{\boldsymbol{w}}) = \int_{\mathcal{B}} \delta\tilde{\boldsymbol{F}} : \boldsymbol{P}\, dV, \qquad \Delta\delta\Pi(\tilde{\boldsymbol{w}},\delta\tilde{\boldsymbol{w}},\Delta\tilde{\boldsymbol{w}}) = \int_{\mathcal{B}} \delta\tilde{\boldsymbol{F}} : \boldsymbol{C} : \Delta\tilde{\boldsymbol{F}}\, dV \tag{4.50}$$

so that the linearized problem can be described by

$$\text{Lin}\,\delta\Pi = \underbrace{\int_{\mathcal{B}} \delta\tilde{\boldsymbol{F}} : \boldsymbol{P}\, dV}_{\delta\Pi(\tilde{\boldsymbol{w}},\delta\tilde{\boldsymbol{w}})} + \underbrace{\int_{\mathcal{B}} \delta\tilde{\boldsymbol{F}} : \boldsymbol{\mathcal{C}} : \Delta\tilde{\boldsymbol{F}}\, dV}_{\Delta\delta\Pi(\tilde{\boldsymbol{w}},\delta\tilde{\boldsymbol{w}},\Delta\tilde{\boldsymbol{w}})} = 0. \tag{4.51}$$

The approximation of the unknown microfluctuations

$$\tilde{\boldsymbol{w}} = \sum_{i=1}^{n} N^i(\xi,\eta)\,\tilde{\boldsymbol{w}}_i, \quad \delta\tilde{\boldsymbol{w}} = \sum_{i=1}^{n} N^i(\xi,\eta)\,\delta\tilde{\boldsymbol{w}}_i, \quad \Delta\tilde{\boldsymbol{w}} = \sum_{i=1}^{n} N^i(\xi,\eta)\,\Delta\tilde{\boldsymbol{w}}_i \tag{4.52}$$

yields the system of algebraic equations

$$\boldsymbol{K}\cdot\Delta\tilde{\boldsymbol{W}} + \boldsymbol{R} = 0, \tag{4.53}$$

$$\tilde{\boldsymbol{W}}^{+} = \tilde{\boldsymbol{W}}^{-} \quad \text{on } \partial\mathcal{B}. \tag{4.54}$$

Here $\tilde{\boldsymbol{W}}^{+}$ and $\tilde{\boldsymbol{W}}^{-}$ are vectors of microfluctuations in nodes lying on $\partial\mathcal{B}^{+}$ and $\partial\mathcal{B}^{-}$, respectively. Note that the residual $\boldsymbol{R}$ depends on the macrodeformation gradient $\bar{\boldsymbol{F}}$ and microfluctuations $\tilde{\boldsymbol{w}}$ and not, as usual, on external loads and displacements. The final result at this level is the first Piola Kirchhoff stress tensor whose volume average (3.26) is the macrostress tensor $\bar{\boldsymbol{P}}$. This result enables further calculations at the macrolevel.

4.2.2 The mixed variational principle

As a comprehensive derivation for the standard form of the potential has already been given in 4.2.1, here, only the final expressions and the differences between the scales will be pointed out. At the beginning, it can be pointed out that the linearized formulation for the mixed form of the potential presented in chapter 4.1.2 completely corresponds to the macroscale problem, where applying the overbar notation yields the expression

$$\begin{aligned}
&\int_{\bar{V}} \bar{\text{Grad}}\,\delta\bar{\boldsymbol{u}} : [\bar{\text{Grad}}\,\Delta\bar{\boldsymbol{u}}\cdot(\bar{\boldsymbol{S}}_{dev}+\bar{\boldsymbol{S}}_{vol})]d\bar{V}\\
&+\int_{\bar{V}} (\bar{\text{Grad}}^{\mathrm{T}}\delta\bar{\boldsymbol{u}}\cdot\bar{\boldsymbol{F}}) : (\bar{\boldsymbol{\mathcal{C}}}_{dev} + \bar{\boldsymbol{\mathcal{C}}}_{vol}) : (\bar{\boldsymbol{F}}^{\mathrm{T}}\cdot\bar{\text{Grad}}\Delta\bar{\boldsymbol{u}})d\bar{V}\\
&+\int_{\bar{V}} (\bar{\text{Grad}}^{\mathrm{T}}\delta\bar{\boldsymbol{u}}\cdot\bar{\boldsymbol{F}}) : \bar{J}\bar{\boldsymbol{C}}^{-1}d\bar{V}\left(\frac{1}{\bar{V}}\frac{\partial^2\bar{\Psi}_{vol}}{\partial\bar{\Theta}^2}\right)\int_{\bar{V}}\bar{J}\bar{\boldsymbol{C}}^{-1} : (\bar{\boldsymbol{F}}^{\mathrm{T}}\cdot\bar{\text{Grad}}\Delta\bar{\boldsymbol{u}})d\bar{V}\\
&+\Delta\delta_{\bar{\boldsymbol{u}}}\bar{\Pi}^{ext} = -\delta\bar{\Pi}^{res}\\
&\bar{\boldsymbol{u}} = \bar{\boldsymbol{u}}_0,\ \ \delta\bar{\boldsymbol{u}} = 0,\ \ \Delta\bar{\boldsymbol{u}} = 0 \quad \text{on } \partial\bar{\mathcal{B}}_{\bar{u}}; \qquad \bar{\boldsymbol{t}} = \bar{\boldsymbol{t}}_0 \quad \text{on } \partial\bar{\mathcal{B}}_{\bar{t}}.
\end{aligned} \tag{4.55}$$

In contrast to the singlescale formulation, here, the stress tensors $\bar{\boldsymbol{S}}_{vol}$, $\bar{\boldsymbol{S}}_{dev}$ and the second derivatives of potential $\bar{\boldsymbol{\mathcal{C}}}_{vol}$, $\bar{\boldsymbol{\mathcal{C}}}_{dev}$, $\frac{\partial^2\bar{\Psi}_{vol}}{\partial\bar{\Theta}^2}$ cannot be calculated without using the data obtained from the microscale. At microlevel, the variational formulation has a similar form as (4.55), but depends on the microfluctuations

$\tilde{\boldsymbol{w}}$ and the residual part is a function of the macrodeformation gradient $\bar{\boldsymbol{F}}$ and microfluctuations $\tilde{\boldsymbol{w}}$:

$$\begin{aligned}
&\int_V \mathrm{Grad}\,\delta\tilde{\boldsymbol{w}} : [\mathrm{Grad}\,\Delta\tilde{\boldsymbol{w}} \cdot (\boldsymbol{S}_{dev} + \boldsymbol{S}_{vol})]dV \\
&+ \int_V (\mathrm{Grad}^{\mathrm{T}}\delta\tilde{\boldsymbol{w}} \cdot \boldsymbol{F}) : (\boldsymbol{C}_{dev} + \boldsymbol{C}_{vol}) : (\boldsymbol{F}^{\mathrm{T}} \cdot \mathrm{Grad}\Delta\tilde{\boldsymbol{w}})dV \\
&+ \int_V (\mathrm{Grad}^{\mathrm{T}}\delta\tilde{\boldsymbol{w}} \cdot \boldsymbol{F}) : J\boldsymbol{C}^{-1}dV \left(\frac{1}{V}\frac{\partial^2\Psi_{vol}}{\partial\Theta^2}\right) \int_V J\boldsymbol{C}^{-1} : (\boldsymbol{F}^{\mathrm{T}} \cdot \mathrm{Grad}\Delta\tilde{\boldsymbol{w}})dV \\
&= -\delta\Pi^{res} \qquad (4.56) \\
&\tilde{\boldsymbol{w}}^+ = \tilde{\boldsymbol{w}}^-, \quad \delta\tilde{\boldsymbol{w}} = 0, \quad \Delta\tilde{\boldsymbol{w}} = 0 \quad \text{on } \partial\mathcal{B}; \qquad \delta\Pi^{res} = \delta\Pi^{res}(\bar{\boldsymbol{F}}, \tilde{\boldsymbol{w}}).
\end{aligned}$$

The boundary value problem (4.56) is completely solvable as the material structure of the RVE is known. Details about the FEM approximation and derivation of the stiffness matrix and the residual vector on both scales can be left out because similar procedures have already been shown in 4.1.2 and 4.2.1.

To summarize, this and the previous chapter present the theoretical background of multiscale FEM, while the rest of the thesis will concentrate on applying this method to the different fields of mechanics. Thereby, we will use especially the formulation explained in the last section, either directly (Ch. 5) or in the extended form (Ch. 6).

5 Numerical results for nearly incompressible porous materials

The simulation of microporous, nearly incompressible materials is chosen as a first example of applying multiscale FEM [50]. This kind of material requires the mixed variational principle, so that the problem corresponds unambiguously to the situation considered in section 4.2.2.

5.1 The effective behavior of microporous media

5.1.1 Tension test for a plate with random microporous structure

The effective material parameters of the microporous media are estimated by simulating a tension test for a square plate with a side length of 40 cm. The vertical uniform load $p = 1$ kN/cm is applied along the horizontal boundaries of the plate. Thanks to double symmetry, it is sufficient to simulate only one fourth of the plate. In that case, the vertical displacements on the lower boundary and the horizontal displacements on the left boundary are constrained (Fig. 5.1).

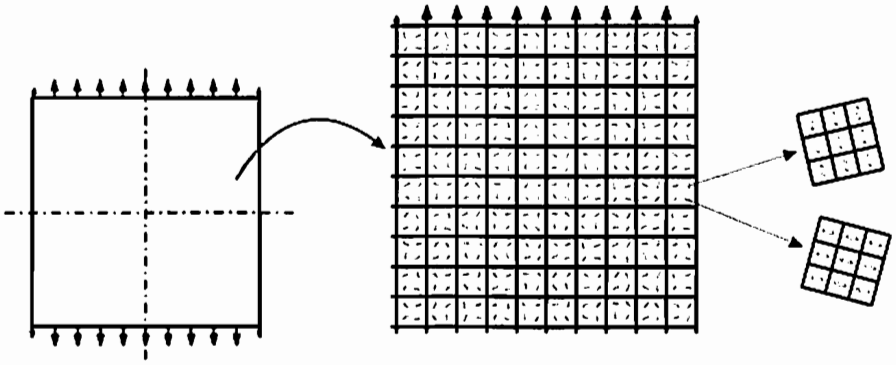

Figure 5.1: Tension test of a plate with random microporous structure.

A periodic microstructure is assumed in the surrounding area of each Gauss point, while the RVEs with different orientations correspond to distinct Gauss points. This simulates a random microporous structure. The RVE is chosen to be a unit square with an elliptical pore and its geometry is shown in Figure 5.2a. Here the side length is denoted by $2d$=1 mm, the major axis of the pore by $2a$ and its minor axis by $2b$.

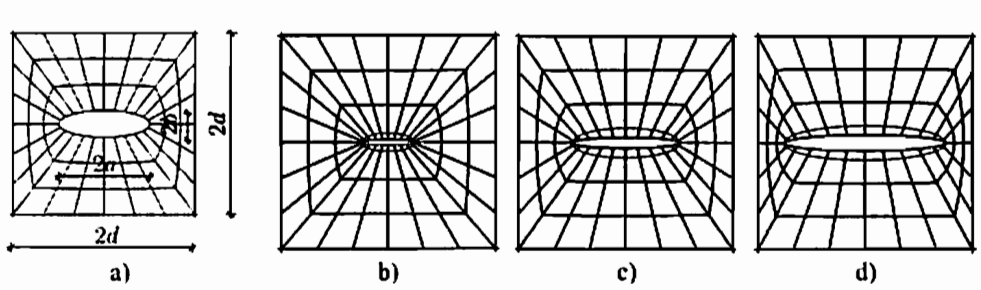

Figure 5.2: a) RVE with an elliptical pore. Three groups of tests with fixed major axis are simulated: b) $a = d/4$, c) $a = 2d/4$, d) $a = 3d/4$. Ellipticity b/a takes values in the interval [0,1] for each group of tests.

The material behavior at microscale is described by the relations

$$\Pi(u,\Theta,p) = \int_V \left[\Psi_{vol}(\Theta) + \Psi_{dev}(\bar{C}(u)) + p(J(u)-\Theta)\right] dV + \Pi^{ext}, \tag{5.1}$$

$$\Psi = \Psi_{dev} + \Psi_{vol} = \underbrace{\frac{1}{2}\mu(\mathrm{tr}\,\bar{C}^c - 3)}_{\Psi_{dev}} + \underbrace{K(J\ln J - J + 1)}_{\Psi_{vol}}, \tag{5.2}$$

where a multi-field description of the potential and the stored energy density of Neo-Hookean material can be recognized. The assumed material parameters are $E = 1000\mathrm{N/mm}^2$, $\nu = 0.3$ in all of the examples. Note that due to (5.1), the formulation presented in section 4.2.2 corresponds directly to the problem of simulating this kind of materials.

The following section discusses the results of three groups of tests with different lengths of the major axis (Fig. 5.2b-d). In the first case, the major axis is fixed as $a = d/4$, $a = 2d/4$ in the second, and $a = 3d/4$ in the last case. Ellipticity b/a changes in each group of tests, taking values from 0 to 1. Ellipticity 0 means that a pore has just appeared and its width is equal to zero, ellipticity 1 corresponds to circular voids. Some of the intermediate results at microscale are shown in Figure 5.3, just as a small illustration.

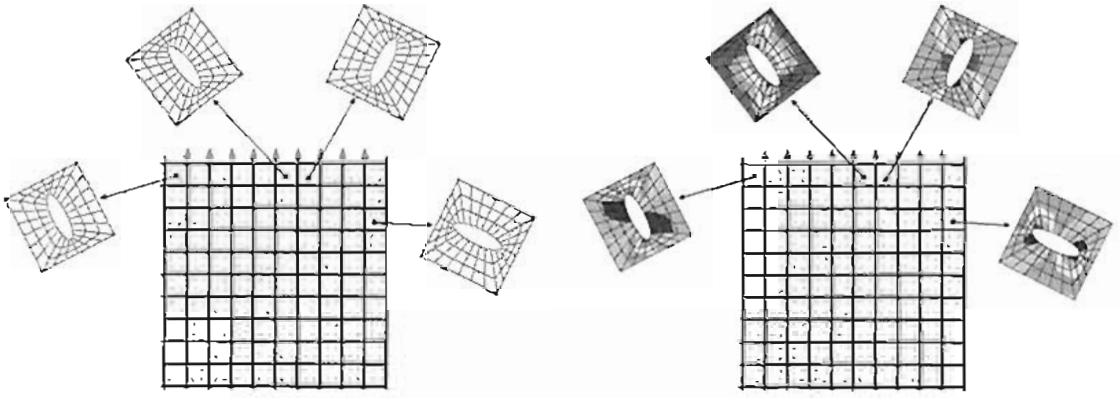

Figure 5.3: Plot of the microfluctuations and of the 11-term of the first Piola Kirchhoff stress tensor. These are intermediate results of a tension test for a plate with random orientation of RVEs.

The final results, the macromaterial parameters E and ν, are calculated using displacements on the boundary of the plate at macrolevel. These results are shown in Figure 5.4, where both of the parameters are seen to decrease with the appearance of pores, while Young's modulus decreases and Poisson's ratio increases with their growth. Naturally the pores with the bigger major axis have more significant influence. The change in parameters is regular.

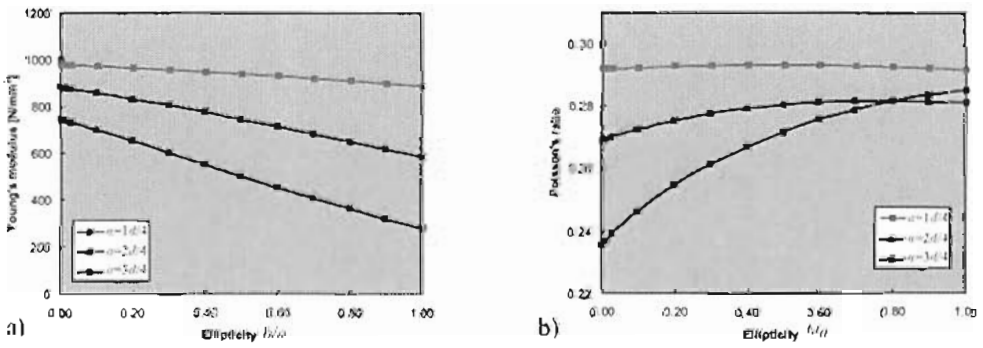

Figure 5.4: Changes in Young's modulus and Poisson's ratio for different pore sizes.

Similar tests are carried out in order to calculate the shear modulus. This time a square plate with side length 20 cm is observed under a horizontal load $p = 1$ kN/cm. Because of horizontal symmetry, simulation suffices with one half of the plate having constrained horizontal and vertical displacements on the lower horizontal boundary. In order to avoid the effects of buckling, vertical displacements are also constrained along all remaining boundaries (Fig. 5.5a). As in the case of the tension test, three groups of tests are simulated for fixed major axis a and changeable ellipticity b/a. Figure 5.5b shows that the shear modulus μ behaves similarly to Young's modulus (Fig. 5.4a). With the appearance of pores it decreases at once and with growing pore size it decreases gradually. The change is regular. The values of the shear modulus obtained by the shear test are compared with the shear modulus calculated with Young's modulus E and Poisson's ratio ν from the tension test. This comparison shows that the departure is almost negligible, for the smallest major axis it is 0.4% and for the longest one 1.5%.

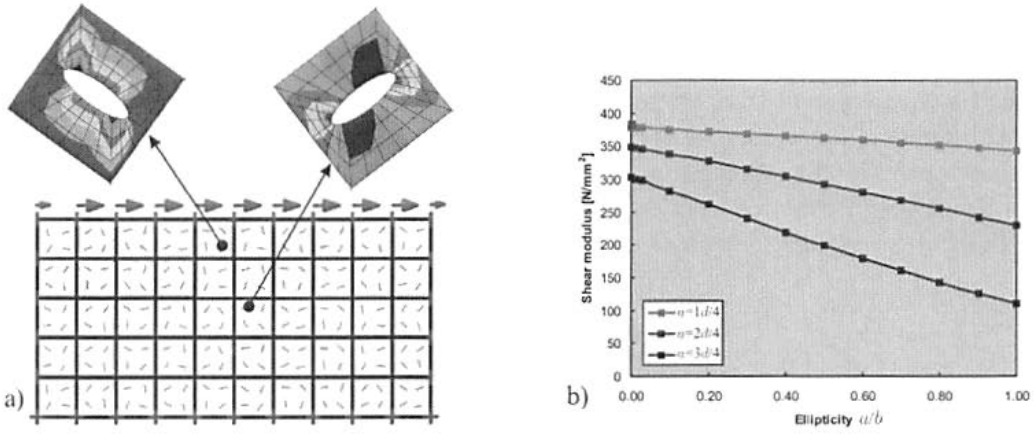

Figure 5.5: a) Plate for the shear test. b) Changes of the shear modulus for the three test groups.

5.1.2 Comparison with Hashin-Shtrikman bounds

In order to check the quality of the simulations, the results shown in Figures 5.4 and 5.5b are compared with the analytical Hashin-Shtrikman bounds. Here it should be pointed out that the load and the parameters in previously described tests were chosen in such a way that the behavior of the structural element stays in the domain of small deformations. In such a case, the results can be compared with analytical solutions for linear materials which are much simpler than those for nonlinear materials.

In contrast to the general form presented in the section 2.2.3, the Hashin-Shtrikman bounds take an explicit form for two-phase materials:

$$K_l = K_1 + \frac{c_2}{\frac{1}{K_2-K_1} + \frac{3c_1}{3K_1+4\mu_1}}, \qquad K_u = K_2 + \frac{c_1}{\frac{1}{K_1-K_2} + \frac{3c_2}{3K_2+4\mu_2}}, \tag{5.3}$$

$$\mu_l = \mu_1 + \frac{c_2}{\frac{1}{\mu_2-\mu_1} + \frac{6(K_1+2\mu_1)c_1}{5\mu_1(3K_1+4\mu_1)}}, \qquad \mu_u = \mu_2 + \frac{c_1}{\frac{1}{\mu_1-\mu_2} + \frac{6(K_2+2\mu_2)c_2}{5\mu_2(3K_2+4\mu_2)}}. \tag{5.4}$$

Here, subscripts l, u denote the lower and upper bound respectively, and phases are chosen so that $K_2 > K_1$ and $\mu_2 > \mu_1$. Their volume concentrations are denoted by c_1 and c_2. The microporous material represents a two-phase material so that the expressions above can be applied directly. However, as the material parameters of voids are equal to zero, the lower bounds (5.3)a and (5.4)a reduce to zero and only the upper bounds remain. Figure 5.6 shows the change in bulk modulus K and shear modulus μ with respect to the porosity p which is equal to the volume faction of voids $p = c_1 = \frac{V_1}{V}$. The diagrams show that the values obtained by the homogenization procedure really lie beneath the upper Hashin-Shtrikman bound, endorsing that the results are in the allowed domain.

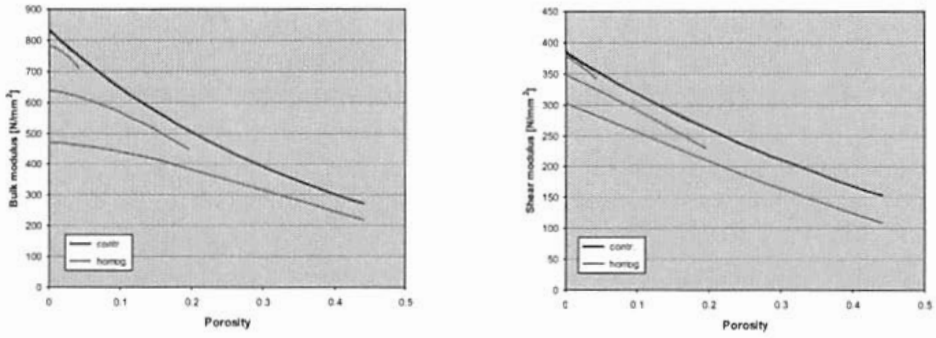

Figure 5.6: Comparison with Hashin-Shtrikman upper bound for the bulk and shear modulus.

In each of the diagrams, the line representing the data obtained by the multiscale method has three branches, one for each group of tests where the major axis a is fixed. The branch on the top corresponds to the RVE with a pore of the width $a = d/4$, the middle one to the RVE with a pore of the width $a = d/2$, and the last one correspond to the case $a = 3d/4$. This shows that materials with the same porosity but different shapes of micropores have different material parameters. More precisely, the strength of materials with the same porosity decreases more significantly for elongated voids than for circular voids.

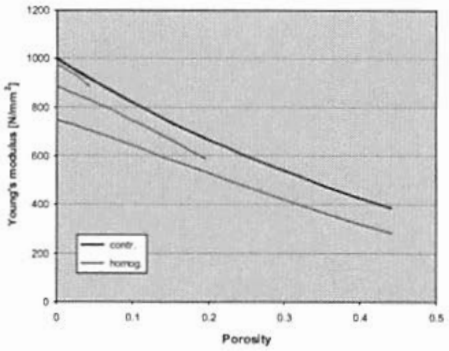

Figure 5.7: Comparison with Hashin-Shtrikman upper bound for the Young modulus.

A diagram for Young's modulus is shown in Figure 5.7, where the lower bound also reduces to zero. Using the Hashin-Shtrikman method, a check only fails in the case of Poisson's ratio, as the standard constraint $0 < \nu < 0.5$ is stricter than the Hashin-Shtrikman bounds.

5.2 Overview of the results concerning the model for microporous media

This section uses multiscale FEM for the estimation of material parameters of microporous media. The results show that, with the appearance of pores with a still negligible width, all material parameters decrease at once. Furthermore, with the growth of the pores Young's modulus and bulk modulus decrease but Poisson's ratio increases. The change in parameters is regular. Tests also show that the elongated narrow pores result in a more significant decrease in the strength of material than for circular voids, even if the porosity is the same. Finally, a comparison with Hashin-Shtrikman bounds shows that the results are inside the permitted domain.

6 Solution-precipitation creep – a deformation process in geomechanics

The model presented in this chapter was developed for the purposes of project D8 of the Collaborative Research Center 526 "Rheology of the Earth – from the Upper Crust to the Subduction Zone." Part of the results has already been published in [34, 51, 52].

6.1 Introduction

6.1.1 Solution-precipitation creep in polycrystalline rocks

In the context of this thesis, solution-precipitation creep is considered to be a geomechanical process occurring in polycrystalline rocks, and it is worth mentioning that similar phenomena also occur in the field of metallurgy. The process has a diffusional character and is based on the particle migration from the compressive to the tensile zone according to the established interpretation. The precipitation phase leads to the extension of existing crystals or to the formation of completely new ones, mostly with a fibrous habit. Frequently, such crystals or crystal parts are full of inclusions and interleaved with thin layers of white mica and chlorite.

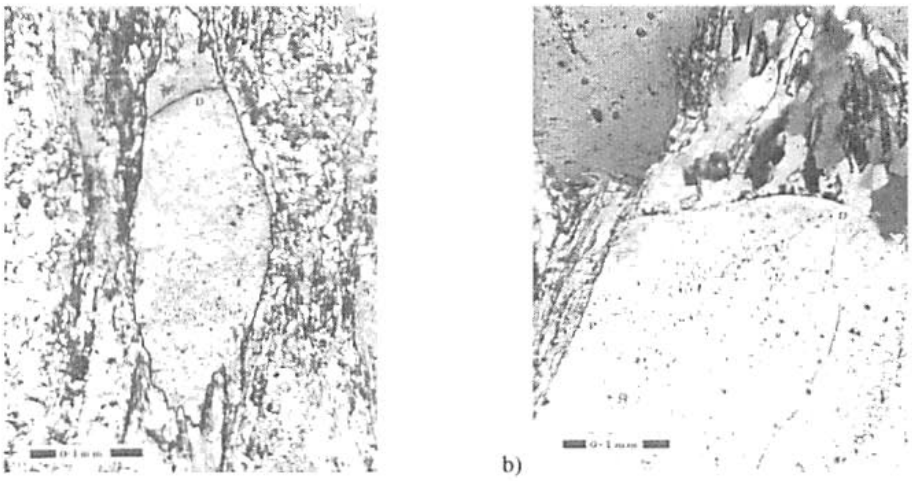

Figure 6.1: Examples of new crystals formed by solution-precipitation creep [23].

One typical example of deformations caused by solution-precipitation creep is shown in Figure 6.1a, where the pressure zone is denoted by P and the tensile zone by D. The active particles are presolved from the P-zone and precipitated outside the boundary of zone D, forming a new crystal. The same labeling is kept in Figure 6.1b, where a new crystal consisting of quartz and white mica is formed outside the D-zone. Both figures were taken from the work of D. Elliott [23].

One of the important properties of solution-precipitation creep is that considered alone it is a "self-exhausting" process. That means that on observing an extended period of time, the grains always become more elongated, which causes a significant decrease in strain rate. Consequently, this deformation type is always accompanied by rotation of the individual grains.

It should be also pointed out that this process is often mistaken for the process of grain boundary migration, although they have a quite distinct nature. While the driving force of solution-precipitation creep is the normal stress gradient, grain migration is a result of the tendency to minimize elastic strain energy stored in the crystal or to minimize the surface energy. In addition, grain boundary migration can never cause the development of the new crystals.

Finally, it is worthy mentioning that this problem has a long history. The investigation of diffusional flows in geology started in the nineteenth century with Sorby [81, 82], but still remains the subject of many new publications [21, 22, 23, 28, 29, 75, 76].

6.1.2 Correns' equation and corresponding expressions customary in metallurgy

The solution-precipitation creep and similar diffusional processes depend on the number of particles, so that some specific quantities need to be introduced for their description. The many models in this field start by defining the partial molar volume ν_i of the phase i which at constant temperature T and number of moles n_i can be written as

$$\nu_i = \left(\frac{\partial \mu_i}{\partial P}\right)_{T,n_i}. \tag{6.1}$$

Here P is pressure and μ_i is the chemical potential of the component i and it has to be understood as a force which, when unbalanced, pushes an exchange of particles, either with the surroundings or between the phases in the system. The expression for chemical potential can be obtained by integrating (6.1) in the form

$$\mu_i^P = \mu_i^0 + \nu_i P \tag{6.2}$$

where the integration constant μ_i^0 represents the chemical potential at the reference pressure $P = 0$, so that for two points with different pressure it can be written

$$\mu_i^{P_1} - \mu_i^{P_2} = \nu_i(P_1 - P_2). \tag{6.3}$$

Solution (6.2) is valid for material transport inside the crystals, while along the diffusional path it can be transformed into an expression dependent on the concentration c, gas constant R and temperature T

$$\mu_i^P = \mu_i' + RT \ln c_i^P \tag{6.4}$$

which again can be used in order to pose the condition for two different points

$$RT \ln c_i^{P_1} - RT \ln c_i^{P_2} = \nu_i^{P_1} - \nu_i^{P_2}. \tag{6.5}$$

Finally, as the equilibrium between material transport inside the crystal and through the intercrystalline space must hold, equating relations (6.3) and (6.5), it can be written:

$$\mu_i^{P_1} - \mu_i^{P_2} = \nu_i(P_1 - P_2) = RT \ln \left(\frac{c_i^{P_1}}{c_i^{P_2}}\right). \tag{6.6}$$

This expression is known as Correns' equation having a simplified form in the case of a single component material and for the specific choice $P_2 = 0$

$$\mu - \mu_0 = \nu\sigma_n = RT \ln \left(\frac{c}{c_0}\right). \tag{6.7}$$

Here μ_0, and c_0 are the chemical potential and concentration corresponding to the reference state ($P_2 = 0$), and P_1 is assumed to be equal to the normal stress σ_n. Equations (6.6) and (6.7) are basic expressions

for treating diffusional flows in geological problems, but only a few steps based on the application of the first Fick's law of diffusion and on the approximation of logarithmic function yield an expression analog to those which are customary in metallurgy

$$\dot{e} \approx \frac{KD\Omega}{X^2kT}\sigma. \tag{6.8}$$

Here $\dot{e}$ is the strain rate, K represents a proportionality coefficient between the normal stress gradient on the local scale and the macroscopic stress σ acting on the polycrystalline sample, D is the diffusion coefficient, Ω the atomic volume, k the Bolzman's constant and X is the diameter of a representative grain. Expression (6.8) can be compared with Nabarro-Herring's equation [39, 71] describing the diffusion process through the bulk crystal lattice

$$\dot{e}_n = \frac{KD_n\Omega}{X^2r^2k^2T}\sigma \tag{6.9}$$

or with Coble's equation [20] corresponding to the diffusion process taking place along the crystal boundary

$$\dot{e}_c = \frac{k\pi D_c h\Omega}{X^3r^{3/2}kT}\sigma. \tag{6.10}$$

In the last two equations, $\dot{e}_n$ and $\dot{e}_c$ are strain rates, D_n and D_c diffusion coefficients, r is the ratio of the longest to the shortest dimension of the grain, and h is the width of the boundary region of a crystal.

6.2 Continuum mechanical model and numerical solutions

It has already been mentioned that according to the established interpretation, the normal stress gradient is the driving force of the process, but recent investigations [57] show that the process actually occurs in the regions of discontinuous stresses (triple points), while no changes occur in the parts with homogeneous stress state. This chapter continues by presenting a continuum mechanical model corresponding to the new interpretation of the process and numerical results, obtained using standard and multiscale FEM.

6.2.1 Continuum mechanical modeling

For the explanation of the model an RVE Ω consisting of disjoint grains Ω_i (Fig. 6.2a) is considered. For

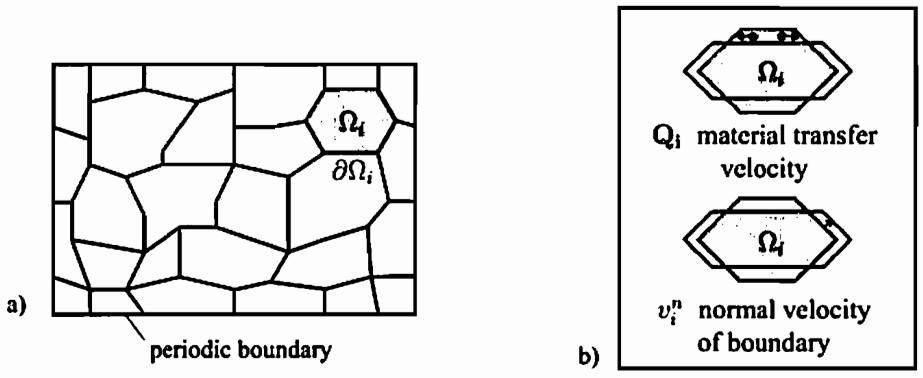

Figure 6.2: a) Representative volume element of polycrystalline material consisting of disjoint grains Ω_i with boundaries $\partial\Omega_i$. b) Types of motion along the boundary of a grain.

each grain Ω_i it is assumed that the deformation has to be decomposed into an elastic and an inelastic part

$$\phi = \phi_i^{\mathrm{E}} \circ \phi_i^{\mathrm{I}} \tag{6.11}$$

leading to a corresponding multiplicative decomposition of the deformation gradients

$$\boldsymbol{F} = \boldsymbol{F}_i^{\mathrm{E}} \cdot \boldsymbol{F}_i^{\mathrm{I}}. \tag{6.12}$$

Note that the inelastic deformation is compatible within individual grains but incompatible at grain-boundaries. Of course $\boldsymbol{\phi}_i^{\mathrm{I}}$ has physical meaning at the grain-boundaries only. In the interior of Ω_i it is just a mathematical tool to describe the change of shape of the grain and does not correspond to an actual deformation.
The material formulation of the problem relies on the functional of total power given as

$$L = \dot{E} + \Delta \tag{6.13}$$

where E denotes stored elastic energy and Δ dissipation [33], [65]-[67]. The stored elastic energy can be expressed via the integral of energy density $\Psi(\boldsymbol{F}^{\mathrm{E}})$ as

$$E = \sum_i \int_{\overline{\Omega}_i} \Psi(\boldsymbol{F}(\boldsymbol{F}_i^{\mathrm{I}})^{-1})\, d\overline{V} = \sum_i \int_{\Omega_i} \Psi(\boldsymbol{F}(\boldsymbol{F}_i^{\mathrm{I}})^{-1})\, J_i^{\mathrm{I}}\, dV. \tag{6.14}$$

Here $\overline{\Omega}_i = \boldsymbol{\phi}_i^{\mathrm{I}}(\Omega_i)$ is the volume of the inelastically deformed grain. With respect to this configuration the material laws have to be formulated. However it turns out to be convenient to transform all expressions to the reference volume Ω_i.
Dissipation is assumed to be caused by two different processes (Fig. 6.2b). Material transport within the grain-interfaces is considered as a major source of dissipation. This can be described by a term of the form $\frac{\gamma}{2}\boldsymbol{Q}_i^2$, where $\boldsymbol{Q}_i$ denotes the velocity of material transport within the grain-boundaries. As a secondary source of dissipation precipitation and solution of material are viewed. They lead to an expression of the form $\frac{\kappa}{2}(v_i^n)^2$. Here

$$v_i^n = \frac{d}{dt}\boldsymbol{\phi}_i^{\mathrm{I}} \cdot \bar{\boldsymbol{n}}_i \tag{6.15}$$

is the normal velocity of grain boundary-movement and $\bar{\boldsymbol{n}}_i$ is the unit-normal to the grain surface in the inelastically deformed configuration. Two constitutive parameters γ and κ are related to the specific mechanism of dissipation. Experimental evidence suggests that $\kappa/\gamma << d^2$, where d corresponds to a characteristic dimension of a grain.
The formulation above leads to a total dissipation of the form

$$\begin{aligned}\Delta &= \sum_i \int_{\partial\overline{\Omega}_i} \left[\frac{\gamma}{2}\boldsymbol{Q}_i^2 + \frac{\kappa}{2}(v_i^n)^2\right] d\overline{S} \\ &= \sum_i \int_{\partial\Omega_i} \left[\frac{\gamma}{2}\boldsymbol{Q}_i^2 + \frac{\kappa}{2}(v_i^n)^2\right] J_i^{\mathrm{I}}\, |(\boldsymbol{F}_i^{\mathrm{I}})^{\mathrm{T}-1} \cdot \boldsymbol{N}_i|\, dS.\end{aligned} \tag{6.16}$$

Here, $J_i^{\mathrm{I}} = \det \boldsymbol{F}_i^{\mathrm{I}}$ denotes the Jacobian and $\boldsymbol{N}_i$ the unit-normal to the grain surface in the undeformed configuration.
It is important to note that the two types of motion within the grain-interfaces are coupled via balance of mass which takes the form

$$v_i^n = \overline{\nabla} \cdot \boldsymbol{Q}_i \tag{6.17}$$

along grain-interfaces and

$$\sum_i \boldsymbol{Q}_i = 0 \tag{6.18}$$

at interface-junctions (triple-points), i.e. points where several grains meet. Here $\overline{\nabla}$ refers to differentiation in the inelastically deformed configuration.

The material formulation is now based on a common assumption in continuum mechanics, namely minimization of energy locally in time. Hence the Lagrangian L introduced above has to be minimized by $\frac{d}{dt}\phi_i^{\mathrm{I}}$, v_i^n and $\boldsymbol{Q}_i$ under the constraint (6.17) and (6.18) for fixed ϕ and ϕ_i^{I}. This leads after the substitution of equations (6.14)-(6.17) in (6.13) to a Lagrangian of the form

$$L = \sum_i \left[\frac{d}{dt} \int_{\Omega_i} \Psi \left[\boldsymbol{F} \left(\boldsymbol{F}_i^{\mathrm{I}} \right)^{-1} \right] J_i^{\mathrm{I}} \, dV \right.$$
$$\left. + \int_{\partial\Omega_i} \left[\frac{\gamma}{2} \boldsymbol{Q}_i^2 + \frac{\kappa}{2} \left(v_i^n \right)^2 + \alpha_i \left(v_i^n - \overline{\nabla} \cdot \boldsymbol{Q}_i \right) \right] J_i^{\mathrm{I}} \left| \left(\boldsymbol{F}_i^{\mathrm{I}} \right)^{\mathrm{T}-1} \cdot \boldsymbol{N}_i \right| \, dS \right], \tag{6.19}$$

where the constraint (6.17) is included using Lagrange-parameters α_i. It should be noted that, contrary to $\frac{d}{dt}\phi_i^{\mathrm{I}}$, v_i^n and $\boldsymbol{Q}_i$, the variable α_i is continuous across interface-junctions.
Variation of L with respect to the variables $\frac{d}{dt}\phi_i^{\mathrm{I}}$, v_i^n and $\boldsymbol{Q}_i$ (for constant ϕ_i^{I} using the standard procedures of partial integration) gives the following Euler-Lagrange equations of the system:

$$\begin{array}{lcll} \nabla \cdot \boldsymbol{b} & = 0 & \text{in} \quad \Omega_i, & \text{a)} \\ \kappa v_i^n + \alpha_i & = \beta_i & \text{on} \quad \partial\Omega_i, & \text{b)} \\ \gamma \boldsymbol{Q}_i + \overline{\nabla} \alpha_i & = 0 & \text{on} \quad \partial\Omega_i, & \text{c)} \end{array} \tag{6.20}$$

where ∇ and $\overline{\nabla}$ denote differentiation with respect to the reference and the inelastically deformed configuration.
The equations involve the Eshelby-tensor given by

$$\boldsymbol{b} = -\frac{\partial}{\partial \boldsymbol{F}_i^{\mathrm{I}}} (J_i^{\mathrm{I}} \Psi)(\boldsymbol{F}_i^{\mathrm{I}})^{\mathrm{T}} = J_i^{\mathrm{I}} \Psi \boldsymbol{I} - \boldsymbol{F}^{\mathrm{T}} \cdot \boldsymbol{P}, \tag{6.21}$$

where $\boldsymbol{P} = \frac{\partial}{\partial \boldsymbol{F}} (J_i^{\mathrm{I}} \Psi)$ is the Piola-stress-tensor, and the normal component of the Eshelby-tensor pushed-forward to the inelastically deformed configuration

$$\beta_i = \bar{\boldsymbol{n}}_i \cdot (\boldsymbol{F}_i^{\mathrm{I}-1})^{\mathrm{T}} \cdot \boldsymbol{b} \cdot (\boldsymbol{F}_i^{\mathrm{I}})^{\mathrm{T}} \cdot \bar{\boldsymbol{n}}_i. \tag{6.22}$$

Equation (6.22) essentially identifies the normal component of the Eshelby-tensor β_i as the thermodynamical driving-force for solution-precipitation creep. This is consistent with the observation made in continuum mechanics, that the Eshelby-tensor is generally responsible for configurational changes, [24, 59]. Note that for small elastic deformations, i.e. if $\boldsymbol{F}_i^{\mathrm{E}}$ is close to a rotation, β_i is well approximated by the normal component of Cauchy-stress, justifying formulations common in geophysics, see for example [28].
Equation (6.20)a can be interpreted as a condition ensuring, that the deformation in the interior of a grain is purely elastic, or otherwise stated, that the material model is independent of the particular choice of ϕ_i^{I}; remember that ϕ_i^{I} has physical meaning only at the surface of the grain.
Finally substitution of equation (6.17) into (6.20)b,c leads to the governing differential equations of the deformation process at the grain boundaries

$$-\frac{\kappa}{\gamma} \Delta \alpha_i + \alpha_i = \beta_i, \tag{6.23}$$

$$v_i^n = -\frac{1}{\gamma} \bar{\nabla} \cdot \bar{\nabla} \alpha_i = -\frac{1}{\gamma} \bar{\Delta} \alpha_i = \frac{1}{\kappa} (\beta_i - \alpha_i). \tag{6.24}$$

The obtained material model allows some interesting interpretations. Equation (6.24) introduces an important modification of the point of view stated above. Not β_i is the actual driving force but rather $\beta_i - \alpha_i$. Whereas β_i is discontinuous at corners and bifurcation-points of the grain-boundaries, equation (6.23) defines α_i as a smooth approximation of β_i (Fig. 6.3). This implies the occurrence of boundary-layer effects at such points which have a strong influence on the mechanical behavior.

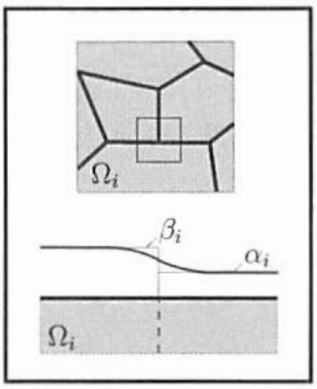

Figure 6.3: α_i is a smooth approximation of β_i.

6.2.2 Single crystal under uniform pressure

The physical meaning of the governing equations is illustrated by considering an idealized case. It is assumed that along the horizontal boundary of a rectangular crystal, the normal component of the Eshelby tensor has a constant value $\beta = 0.1\,\text{kN/mm}^2$. The vertical sides of the crystal are not loaded, so that along them β is equal to zero. The ratio of inelastic constants is taken to be $\frac{\kappa}{\gamma} = 0.002\,\text{mm}^2$ and the length of the loaded side is $l = 2\,\text{mm}$. The solution of differential equation (6.23) for such parameters represents the values of α over the loaded side. Figure 6.4 shows that α is the smooth transition between $\beta = 0.1\,\text{kN/mm}^2$ and $\beta = 0\,\text{kN/mm}^2$ in the edge zones, while elsewhere α and β have the same value. According to the second governing equation (6.24), it means that material motion will occur only at the places where α and β differ. Such expectations have already been proved by the experimental observations. Namely, the results of the test presented in [57] show that homogeneous stress really does not initiate solution-precipitation creep.

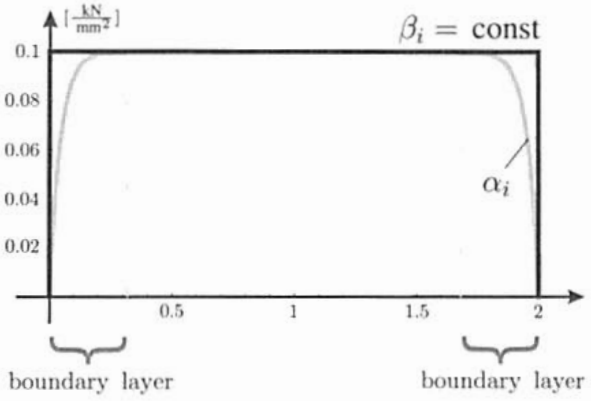

Figure 6.4: Change of α_i and β_i over the loaded side.

The experimental interrogation used a two-part test based on the method of phase shift interference microscope. At the beginning, (first 17 days), a halite crystal (Fig. 6.5A) was observed without any load. The Figure 6.5B shows that no changes occurred in this phase. In the continuation, the same crystal was observed under pressure of 1MPa. This part of the experiment took additional 17 days and the final results showed that the edges of the crystals moved by 1.7 μm (Fig. 6.5C). There was no change at all in the rest of the sample. The experiment was carried out in saturated NaCl solution and under low stresses so that dislocation creep is avoided.

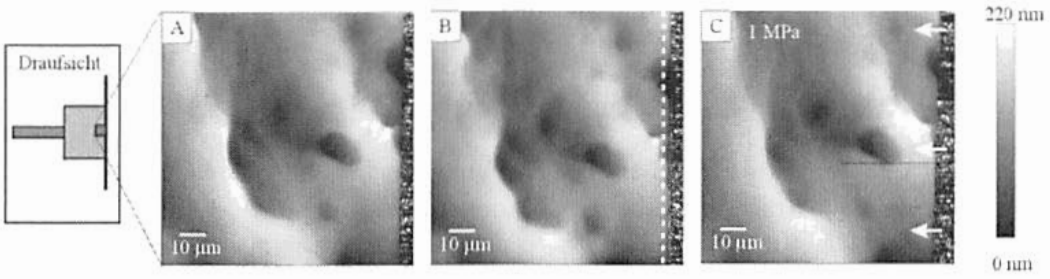

Figure 6.5: Halite crystallite at the beginning of test (A), showing the situation after 17 days without load (B) and 17 days with load (C). Load has caused the crystal edge to move by 1.7 μm. The figure is taken from the work of Lochämper et al. [57].

6.2.3 Micromechanical model

A numerical implementation of the full model presented in the previous section appears to be quite demanding due to its nature of a coupled volumetric and interface problem. Because of that first a simplified model will be observed in order to predict the evolution of the grain shapes and size for moderatory large deformations.
The formulation will be two-dimensional and assume that the polycrystalline material is composed of a set of rectangular particles with aspects a_i, b_i and orientation φ_i (Fig. 6.6a).

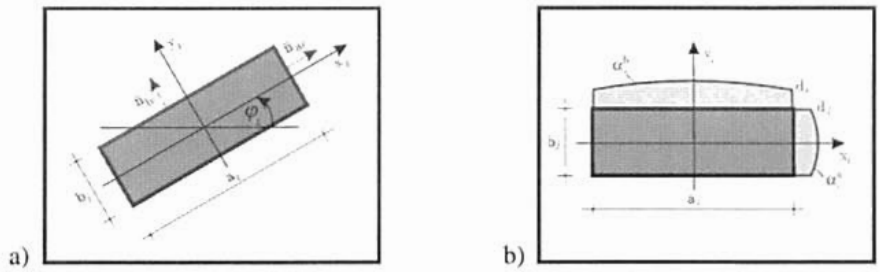

Figure 6.6: a) Single grain in Taylor model. b) Quadratic expression for α_i.

It will be assumed that there is an effective macroscopical inelastic deformation $\boldsymbol{F}^{\mathrm{I}}_{\mathrm{eff}}$ such that there exists a macroscopical stored energy density in the form $\Psi(\boldsymbol{F}(\boldsymbol{F}^{\mathrm{I}}_{\mathrm{eff}})^{-1})$, where $\boldsymbol{F}$ denotes the macroscopical total deformation gradient.
Stored energy density will be specified as that one of a compressible Neo-Hookean material

$$\Psi = U(JJ_{\mathrm{eff}}^{-1}) + \frac{\mu}{2}\,(\boldsymbol{C}^{\mathrm{I}}_{\mathrm{eff}})^{-1} : \boldsymbol{C}, \tag{6.25}$$

$$J_{\mathrm{eff}} = \det \boldsymbol{F}^{\mathrm{I}}_{\mathrm{eff}}, \quad \boldsymbol{C}^{\mathrm{I}}_{\mathrm{eff}} = (\boldsymbol{F}^{\mathrm{I}}_{\mathrm{eff}})^{\mathrm{T}} \cdot \boldsymbol{F}^{\mathrm{I}}_{\mathrm{eff}}$$

where $U(JJ_{\mathrm{eff}}^{-1})$ is a functional representing influence of volume deformations. Individual grains are anisotropic of course. Here it is assumed that the macroscopical energy of the polycrystal has to be isotropic, i.e. the possible influence of texture is disregarded. The specific form of Ψ is of minor importance since only small elastic deformations are envisaged. The expression above turns out to be convenient for calculations.
Next a Taylor's hypothesis is introduced by assuming that the macroscopic Cauchy-stress, given by

$$\boldsymbol{\sigma} = 2\frac{1}{J}\boldsymbol{F}\cdot\frac{\partial\Psi}{\partial\boldsymbol{C}}\cdot\boldsymbol{F}^{\mathrm{T}} = U'(JJ_{\mathrm{eff}}^{-1})\mathbf{I} + \mu\frac{J_{\mathrm{eff}}}{J}\,\boldsymbol{F}\cdot(\boldsymbol{C}^{\mathrm{I}}_{\mathrm{eff}})^{-1}\cdot\boldsymbol{F}^{\mathrm{T}}, \tag{6.26}$$

is also the average Cauchy-stress acting on all grain-interfaces. This implies that the elastic deformation gradient is in an average sense constant on all grains, hence

$$\boldsymbol{F}^{\mathrm{E}}_i = \boldsymbol{F}(\boldsymbol{F}^{\mathrm{I}}_i)^{-1} = \boldsymbol{F}(\boldsymbol{F}^{\mathrm{I}}_{\mathrm{eff}})^{-1}. \tag{6.27}$$

Using (6.21) and (6.22) the average value of the normal component of the Eshelby stress-tensor depending only on J_i^{I} and macroscopical quantities can be obtained

$$\beta_{i,\mathrm{avg}} = -J_i^{\mathrm{I}} \left[\Psi - J J_{\mathrm{eff}}^{-1}\, U'(J J_{\mathrm{eff}}^{-1}) - \mu\, \bar{\boldsymbol{n}}_i \cdot (\mathbf{F}_{\mathrm{eff}}^{\mathrm{I}})^{T-1} \cdot \boldsymbol{C} \cdot (\boldsymbol{F}_{\mathrm{eff}}^{\mathrm{I}})^{-1} \cdot \bar{\boldsymbol{n}}_i\right]. \tag{6.28}$$

The grain-shapes are assumed to remain rectangular which means that the v_i^n are spatially constant. From equation (6.24) follows then that $\bar{\Delta}\alpha_i = \alpha_i''$ is constant and thus α_i, β_i have to be quadratic in x_i and y_i respectively, (Fig. 6.6b). In the following only α_i^a and β_i^a, appearing on one face of the grain i, will be considered (Fig. 6.6a). The case of α_i^b and β_i^b is analogous. The function α_i^a has the following general form

$$\alpha_i^a = \mathrm{c}_i \left[\left(\frac{\mathrm{b}_i}{2}\right)^2 - \mathrm{y}_i^2\right] + \mathrm{d}_i, \tag{6.29}$$

where c_i and d_i are constants. According to (6.23) β_i^a follows in the form

$$\beta_i^a = \alpha_i^a - \frac{\kappa}{\gamma}(\alpha_i^a)'' = \mathrm{c}_i \left[\left(\frac{\mathrm{b}_i}{2}\right)^2 - \mathrm{y}_i^2\right] + \mathrm{d}_i + 2\frac{\kappa}{\gamma}\mathrm{c}_i, \tag{6.30}$$

and from its volume average

$$\beta_{i,\mathrm{avg}}^a = \frac{1}{\mathrm{b}_i} \int_{-\mathrm{b}_i/2}^{\mathrm{b}_i/2} \beta_i^a \, \mathrm{d}y_i = \mathrm{c}_i \left(\frac{\mathrm{b}_i^2}{6} + 2\frac{\kappa}{\gamma}\right) + \mathrm{d}_i \tag{6.31}$$

c_i can be expressed and introduced in (6.24) what yields the velocity

$$\dot{\mathrm{a}}_i = -\frac{1}{\gamma}(\alpha_i^a)'' - \lambda = \frac{2}{\gamma}\mathrm{c}_i - \lambda = \frac{\beta_{i,\mathrm{avg}}^a - \mathrm{d}_i}{\frac{\gamma}{12}\mathrm{b}_i^2 + \kappa} - \lambda. \tag{6.32}$$

Here a Lagrange-parameter λ is introduced which represents a constant field of precipitation/solution over all grains. This parameter is determined via the volume constraint

$$\sum_i \mathrm{a}_i \mathrm{b}_i = \mathrm{const} = V_0 \tag{6.33}$$

which has to be added to the Lagrangian (6.19). This takes care of the obvious fact, that no creep should take place under hydrostatic stress conditions. An analogous expression is valid for the other face of the particle

$$\dot{\mathrm{b}}_i = \frac{\beta_{i,\mathrm{avg}}^b - \mathrm{d}_i}{\frac{\gamma}{12}\mathrm{a}_i^2 + \kappa} - \lambda. \tag{6.34}$$

Finally the effective velocity gradient can be expressed as the average of the inelastic velocity gradients of the single grains, which closes the system

$$\dot{\boldsymbol{F}}_{\mathrm{eff}}^{\mathrm{I}} \cdot (\boldsymbol{F}_{\mathrm{eff}}^{\mathrm{I}})^{-1} = \frac{1}{V_0}\sum_i \dot{\boldsymbol{F}}_i^{\mathrm{I}} (\boldsymbol{F}_i^{\mathrm{I}})^{-1} = \frac{1}{V_0}\sum_i \boldsymbol{R}_i^{\mathrm{T}} \cdot \begin{pmatrix} \dot{\mathrm{a}}_i \mathrm{b}_i & 0 \\ 0 & \mathrm{a}_i \dot{\mathrm{b}}_i \end{pmatrix} \cdot \boldsymbol{R}_i, \tag{6.35}$$

where $\boldsymbol{R}_i$ is the rotation tensor corresponding to a rotation by the angle φ_i.
The complete micromechanical model requires the solution of the system of equations (6.28), (6.32)–(6.35). It allows to calculate the evolution of the distributions of the aspects a_i and b_i as well as macroscopic deformations or stresses respectively, provided stresses or macroscopic deformations respectively are given as functions of time. Initial distributions have to be defined for the variables a_i, b_i, φ_i and d_i, where the d_i can be interpreted as eigenstress inherent in the polycrystal.

Numerical results for a displacement controlled tension test using a sample of 200 grains are shown in Figures 6.7 and 6.8. In Fig. 6.7 the stress-strain behavior is displayed using two different time-scales in order to resolve all features. One can see that the test starts with a transitory regime where the stress rises essentially elastically, i.e. there is only very little creep. Then there is a softening regime, which is due to the fact that the distribution of grain aspects adjusts to the given macroscopical deformation. Finally the system settles into stationary creep.

Figure 6.8 shows the evolution of the distribution of the aspects of the grains. One observes that the grains tend to become more prolongated. Also a certain grain coarsening can be seen due to the fact that small grains are resolved completely.

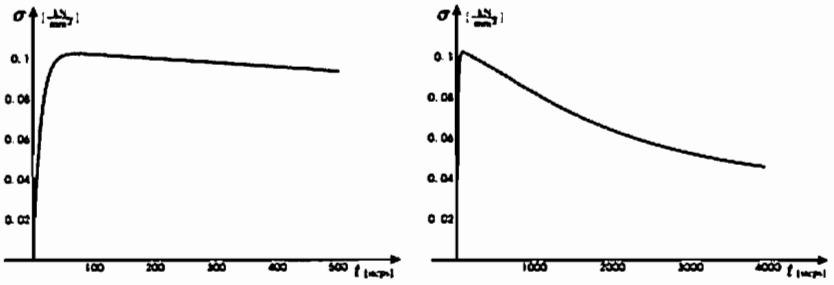

Volumetric part of free energy:
$U = \frac{1}{4}\lambda J_e^2 - \frac{1}{2}(\lambda + 2\mu)\ln J_e - (\mu + \frac{1}{4}\lambda)$
$J_e = JJ_{\text{eff}}^{-1}$
Material parameters:
$\kappa = 10\ \text{kNs/mm}^3$, $\gamma = 100\ \text{kNs/mm}^5$
$\mu = 23\ \text{kN/mm}^2$, $\lambda = 15.5\,\text{kN/mm}^2$

Crystallite aspects:
$a_i \in [0.5, 2.0]$mm, $b_i \in [0.5, 2.0]$mm
Eigenstress: $d_i \in [-0.01, 0.01]\,\text{kN/mm}^2$
Time step: $\Delta t = 0.05$s

Figure 6.7: Stress-strain behavior for tension test.

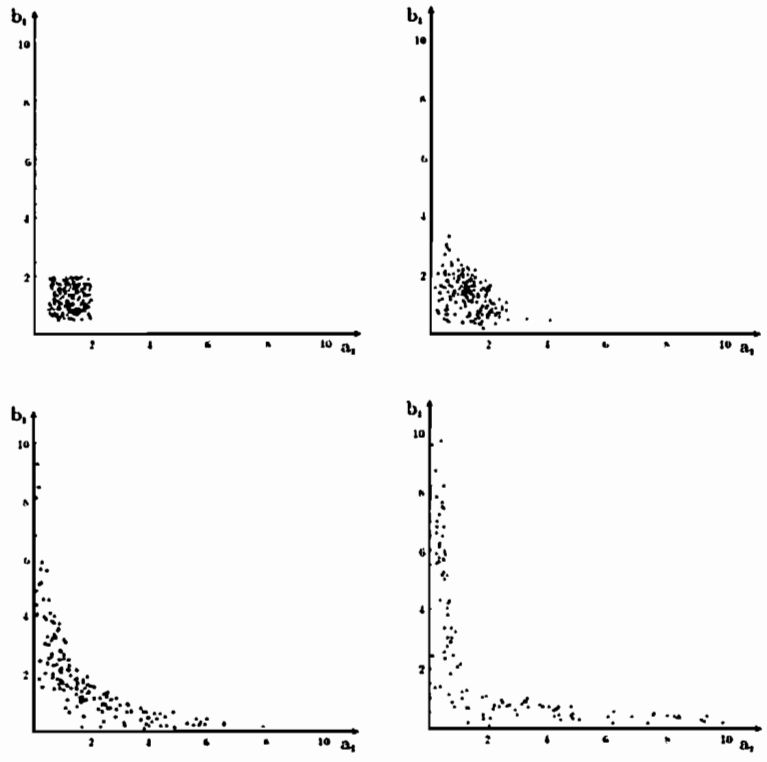

Figure 6.8: Evolution of the grain aspects (values in mm).

6.2.4 Application of FEM for simulating the behavior of polycrystals

The previously described micromechanical model is a simplified version convenient for predicting the behavior of a group of crystals with assumed neglected interaction, while FEM is necessary for a more realistic simulation. This method starts with a Lagrangian functional (6.19) which after introduction of (6.15) and (6.20) becomes

$$
\begin{aligned}
L = \sum_i \Bigg\{ & \frac{d}{dt} \int_{\Omega_i} \psi \left[\boldsymbol{F} \left(\boldsymbol{F}_i^{\mathrm{I}} \right)^{-1} \right] J_i^{\mathrm{I}} \, dV \\
& + \int_{\partial\Omega_i} \left[\frac{1}{2\gamma} (\bar{\nabla}\alpha_i)^2 + \frac{\kappa}{2} (\dot{\boldsymbol{\phi}}_i^{\mathrm{I}} \cdot \bar{\boldsymbol{n}}_i)^2 \right] J_i^{\mathrm{I}} \left| \left(\boldsymbol{F}_i^{\mathrm{I}} \right)^{\mathrm{T}-1} \cdot \boldsymbol{N}_i \right| \, dS \\
& + \int_{\partial\Omega_i} \alpha_i (\dot{\boldsymbol{\phi}}_i^{\mathrm{I}} \cdot \bar{\boldsymbol{n}}_i + \frac{1}{\gamma} \bar{\Delta}\alpha_i) \, J_i^{\mathrm{I}} \left| \left(\boldsymbol{F}_i^{\mathrm{I}} \right)^{\mathrm{T}-1} \cdot \boldsymbol{N}_i \right| \, dS \Bigg\}.
\end{aligned} \tag{6.36}
$$

The previous expression depends on total deformation $\boldsymbol{\phi}$, inelastic deformations $\boldsymbol{\phi}_i^{\mathrm{I}}$ and Lagrange parameter α_i and with respect to these, the variational of the total potential $\Pi = L + \Pi^{ext}$ has to be calculated:

$$\delta_{\boldsymbol{\phi}} \Pi = 0$$

$$
\int_{\Omega} \nabla \delta\boldsymbol{\phi} : \boldsymbol{P} dV = \int_{\Omega} \delta\boldsymbol{\phi} \cdot \boldsymbol{F} dV + \int_{\partial\Omega} \delta\boldsymbol{\phi} \cdot \boldsymbol{T} dS, \tag{6.37}
$$

$$\delta_{\dot{\boldsymbol{\phi}}_i^{\mathrm{I}}} \Pi = 0$$

$$
\begin{aligned}
\sum_i \int_{\partial\Omega_i} & \delta\boldsymbol{\phi}_i^{\mathrm{I}} J_i^{\mathrm{I}} \left| \left(\boldsymbol{F}_i^{\mathrm{I}} \right)^{\mathrm{T}-1} \cdot \boldsymbol{N}_i \right| \left(\kappa \dot{\boldsymbol{\phi}}^{\mathrm{I}} \cdot \bar{\boldsymbol{n}}_i + \alpha_i \right) \cdot \bar{\boldsymbol{n}}_i \, dS = \\
& = \sum_i \int_{\partial\Omega_i} \delta\boldsymbol{\phi}_i^{\mathrm{I}} \cdot \left(\boldsymbol{F}_i^{\mathrm{I}} \right)^{\mathrm{T}-1} \cdot \left(J_i^{\mathrm{I}} \psi \boldsymbol{I} - \boldsymbol{F}^{\mathrm{T}} \cdot \boldsymbol{P} \right) \cdot \boldsymbol{N}_i \, dS,
\end{aligned} \tag{6.38}
$$

$$\delta_{\alpha_i} \Pi = 0$$

$$
\begin{aligned}
\sum_i \int_{\partial\Omega_i} & \delta\alpha_i (\dot{\boldsymbol{\phi}}_i^{\mathrm{I}} \cdot \bar{\boldsymbol{n}}_i) J_i^{\mathrm{I}} \left| \left(\boldsymbol{F}_i^{\mathrm{I}} \right)^{\mathrm{T}-1} \cdot \boldsymbol{N}_i \right| \, dS + \\
& + \left(-\frac{1}{\gamma} \bar{\nabla}\alpha_i \cdot \bar{\nabla}\delta\alpha_i \right) J_i^{\mathrm{I}} \left| \left(\boldsymbol{F}_i^{\mathrm{I}} \right)^{\mathrm{T}-1} \cdot \boldsymbol{N}_i \right| \, dS = 0.
\end{aligned} \tag{6.39}
$$

In Lagrangean (6.36), just the general form of free energy $\psi(\boldsymbol{F}^e)$ is used. For a more precise specification, an elastic potential appropriate for nearly incompressible materials is assumed (Ch. 4.1.2). In that case equation (6.37) has the particular form

$$
\begin{aligned}
& \int_V \mathrm{Grad}\, \delta\boldsymbol{\phi} : [\mathrm{Grad}\, \Delta\boldsymbol{\phi} \cdot (\boldsymbol{S}_{dev} + \boldsymbol{S}_{vol})] dV \\
& + \int_V (\mathrm{Grad}^{\mathrm{T}} \delta\boldsymbol{\phi} \cdot \boldsymbol{F}) : (\boldsymbol{C}_{dev} + \boldsymbol{C}_{vol}) : (\boldsymbol{F}^{\mathrm{T}} \cdot \mathrm{Grad}\Delta\boldsymbol{\phi}) dV \\
& + \int_V (\mathrm{Grad}^{\mathrm{T}} \delta\boldsymbol{\phi} \cdot \boldsymbol{F}) : J\boldsymbol{C}^{-1} dV \left(\frac{1}{V} \frac{\partial^2 \Psi_{vol}}{\partial \Theta^2} \right) \int_V J\boldsymbol{C}^{-1} : (\boldsymbol{F}^{\mathrm{T}} \cdot \mathrm{Grad}\Delta\boldsymbol{\phi}) dV \\
& + \Delta\delta_{\boldsymbol{\phi}} \Pi^{ext} = -\delta\Pi^{res}
\end{aligned} \tag{6.40}
$$

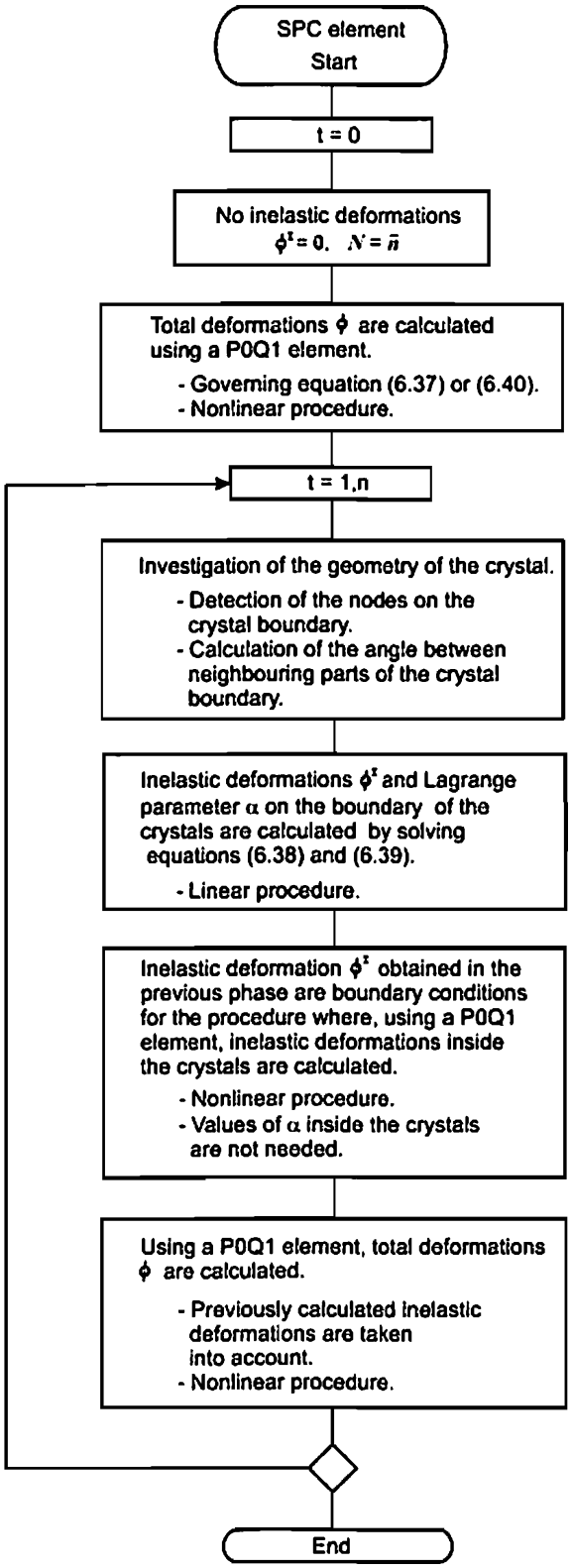

Figure 6.9: Flow chart of the SPC element.

which is identical to (4.34) except that here the second Piola Kirchhoff stress tensor S and elasticity tensor C depend on elastic deformations

$$S = 2\frac{\partial\left(J^{\mathrm{I}}\Psi(C\cdot C^{\mathrm{I}-1})\right)}{\partial C}, \qquad C = 2\frac{\partial^2\left(J^{\mathrm{I}}\Psi(C\cdot C^{\mathrm{I}-1})\right)}{\partial C^2}. \tag{6.41}$$

Such formulation is more general, and the purely elastic case can be derived from it for $C^{\mathrm{I}} = I$.

Equations (6.37)-(6.40) are used as the basis for formulating the solution-precipitation creep element (SPC element) whose most important characteristics are presented in the flow chart (Fig. 6.9). Here it can be seen that in the first time step, inelastic deformations are assumed to be zero, and the total deformations are calculated for such a state. In the further steps, crystal geometry is checked in order to calculate the normal vector on the inelastically deformed surface $\bar{n}$. The inelastic deformations on the boundary of the crystals are calculated by solving the linear problem defined by (6.38) and (6.39) while a nonlinear procedure (P0Q1 element) is applied for calculating inelastic deformations inside the crystals and of the total deformations. Note that total deformations and Lagrange parameter must be compatible everywhere, while the inelastic ones are compatible inside the crystals but not on their boundaries. The total number of DOFs per node in the 2D case is five, and seven in the 3D case which has to give additional consideration to the total and inelastic deformation in the third direction of coordinate system.

In the continuation three examples of applying the model are presented. Each time, it is assumed that the stored energy density Ψ corresponds to Neo-Hook material (5.2).

The first example was chosen to permit comparison with an analytical solution (Fig. 6.10). The observed sample is a rectangular crystal whose upper horizontal boundary is loaded by pressure, with vertical displacements constrained on the lower horizontal boundary. Pressure is chosen to be $p = 0.1\,\mathrm{kN/mm^2}$ for the sample of unit thickness $d = 1\,\mathrm{mm}$. The material parameters $E = 23\,\mathrm{kN/mm^2}$, $\nu = 0.16$ are assumed, corresponding to the characteristics of halite crystal. As the real values of inelastic parameters are unknown, they are chosen arbitrarily in such way that inelastic and total displacements can be monitored in a few time steps. Discretization of the crystal is made by a mesh with 40x20 elements (Fig. 6.10a). Figure 6.10b shows that along the loaded boundary, $\alpha = 0.1\,\mathrm{kN/mm^2}$. On the vertical sides, $\alpha = 0$ as these sides are not loaded. In the edge zones there is a smooth transition of α between 0.1 and 0. These results agree with the analytical ones discussed in section 6.2.2, repeated here in Figure 6.10g. Inelastic deformations ϕ^{I} (Fig. 6.10c,d) are concentrated in the edges, which agrees with the physical interpretation of the second governing equation (6.24). Finally, Figures 6.10e,f show total displacements after 50 time steps, where one time step is taken as one second. Note that subscripts in ϕ^{I} and α can be omitted as the single crystal is observed.

The second example simulates the behavior of a polycrystal consisting of 9 crystals (Fig. 6.11). Each of the crystals is discretized by a mesh with 14x14 elements. A test similar to the one before is carried out. Pressure $p = 0.1\ \mathrm{kN/mm^2}$ is applied on the upper boundary, and vertical displacements on the lower boundary are suppressed. An important observation, not apparent in the case of single crystal is that here total displacements ϕ and Lagrange parameter α_i are continuous everywhere, but inelastic deformations ϕ_i^{I} are discontinuous on the boundaries of the crystals.

Finally, the third example (Fig. 6.12) studies the behavior of a polycrystal consisting of five crystals. Some of these crystals have an arbitrary and not a four-node form, which was a characteristic of previous examples. This ability of the program will be used intensively in the further examples, which simulate some more realistic shapes of crystals.

Crystal of aspects 2x1 (mm)
Discretisation 40x20 elements

Normal pressure $p = 0.1\,\text{kN/mm}$

Neo-Hookean material
$E = 23\,\text{kN/mm}^2$ $\quad \nu = 0.16$
$\gamma = 25000\,\text{kNs/mm}^5$ $\quad \kappa = 500\,\text{kNs/mm}^3$

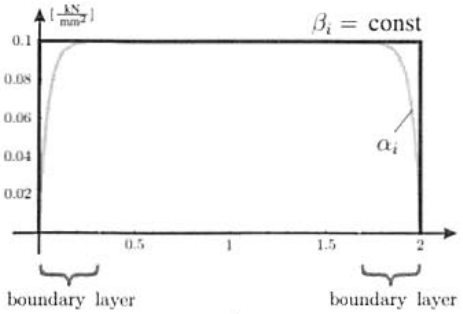

g)

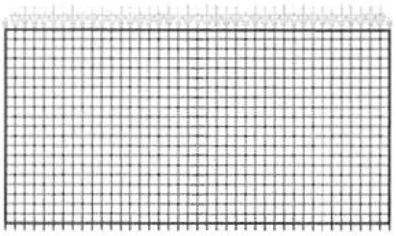

a)

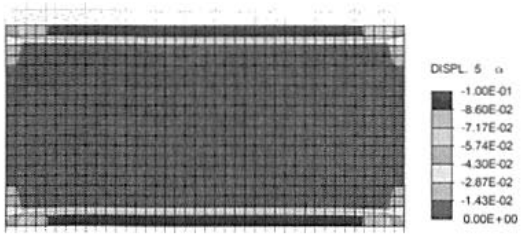

b)

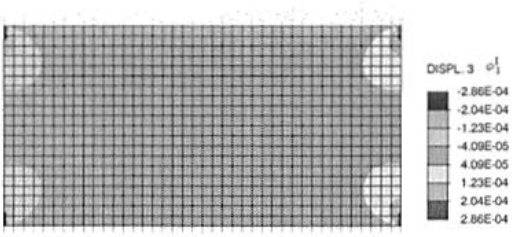

c)

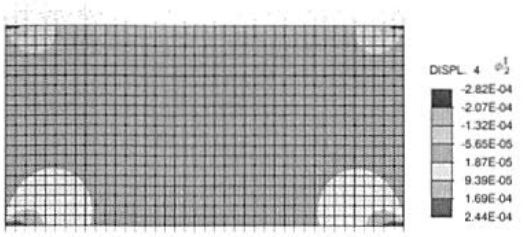

d)

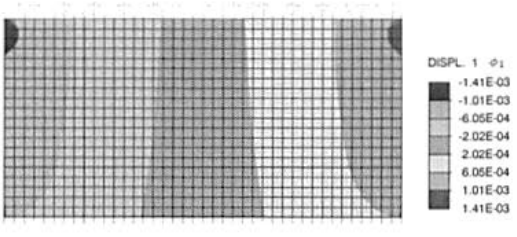

e)

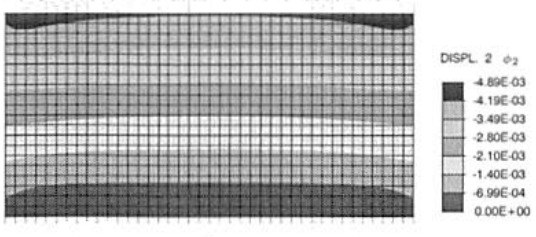

f)

Figure 6.10: Simulation for single rectangular crystal. a) Geometry, discretization and applied load. b)-f) Diagrams of DOFs after 50 time steps $\Delta t = 1$s. g) Analytic solution for Lagrange parameter α.

Four-node crystals
Discretisation of a crystal 14x14
Normal pressure $p = 0.1\,\mathrm{kN/mm}$

Neo-Hookean material
$E = 23\,\mathrm{kN/mm^2}$ $\nu = 0.16$
$\gamma = 25000\ \mathrm{kNs/mm^5}$ $\kappa = 500\,\mathrm{kNs/mm^3}$

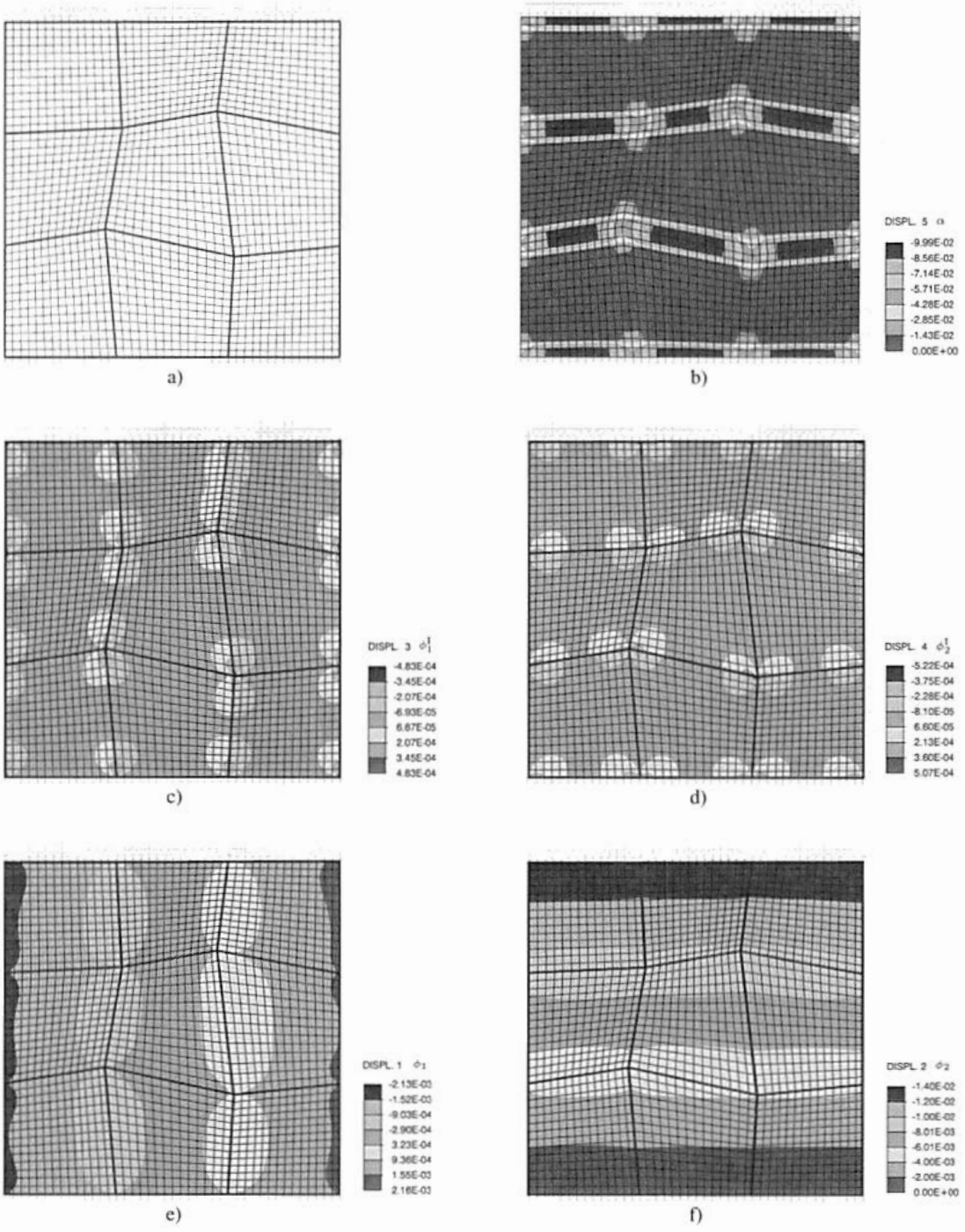

a) b) c) d) e) f)

Figure 6.11: Simulation for polycrystal consisting of four-node crystals. a) Geometry, discretization and applied load. b)-f) Diagrams of DOFs after 50 time steps $\Delta t = 1\mathrm{s}$.

Crystals of arbitrary shape
Four-node part of a crystal: 14x14 elements
Normal pressure $p = 0.1\,\mathrm{kN/mm}$

Neo-Hookean material
$E = 23\,\mathrm{kN/mm^2}$ $\nu = 0.46$
$\gamma = 25000\,\mathrm{kNs/mm^4}$ $\kappa = 500\,\mathrm{kNs/mm^3}$

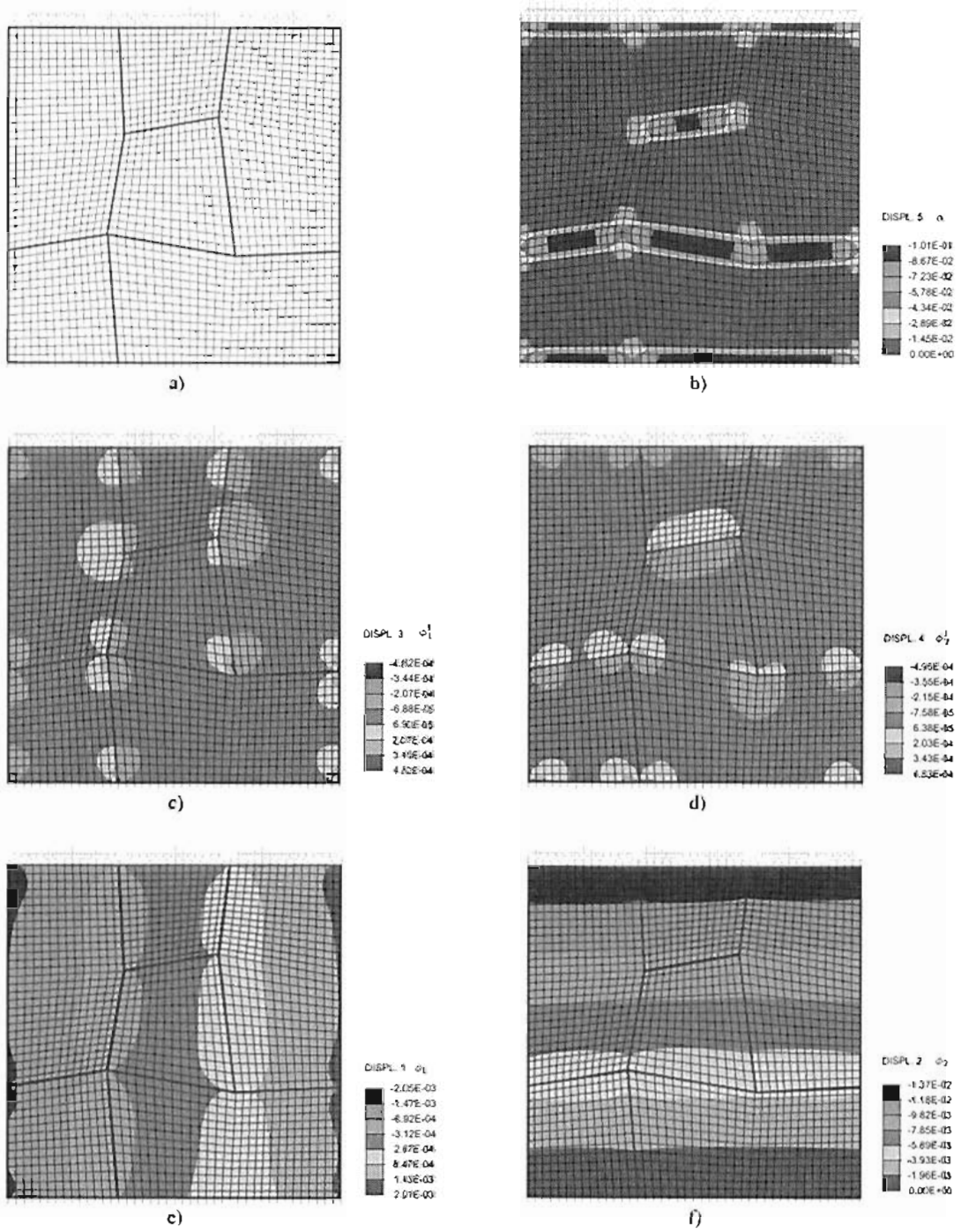

Figure 6.12: Simulation for polycrystal consisting of crystals of arbitrary shape. a) Geometry, discretization and applied load. b)-f) Diagrams of DOFs after 50 time steps $\Delta t = 1\mathrm{s}$.

6.2.5 Using multiscale FEM to estimate the change in elastic material parameters over time

One further step in modeling solution-precipitation creep is to simulate its influence on the deformation of a macroscopic body. To this end, the effective material properties have to be estimated, using the concept described in chapter 3. In contrast to the case of purely elastic material, here the material at macroscale behaves as Neo-Hook nearly incompressible material, while at microscale, the model derived for solution–precipitation creep has to be applied. At microlevel, the problem is time dependent, so that consequently, the calculated effective material parameters are too. The problem to be solved is described by the following system where the overbar symbol in (6.42) denotes macroscale and in (6.45) the operators related to the inelasticaly deformed configuration:

- macroscale:

$$\begin{aligned}
&\int_{\bar{V}} \bar{\mathrm{Grad}}\,\delta\bar{\boldsymbol{\phi}} : [\bar{\mathrm{Grad}}\,\Delta\bar{\boldsymbol{\phi}} \cdot (\bar{\boldsymbol{S}}_{dev} + \bar{\boldsymbol{S}}_{vol})]d\bar{V} \\
&+ \int_{\bar{V}} (\bar{\mathrm{Grad}}^{\mathrm{T}}\delta\bar{\boldsymbol{\phi}} \cdot \bar{\boldsymbol{F}}) : (\bar{\boldsymbol{C}}_{dev} + \bar{\boldsymbol{C}}_{vol}) : (\bar{\boldsymbol{F}}^{\mathrm{T}} \cdot \bar{\mathrm{Grad}}\Delta\bar{\boldsymbol{\phi}})d\bar{V} \\
&+ \int_{\bar{V}} \left[(\bar{\mathrm{Grad}}^{\mathrm{T}}\delta\bar{\boldsymbol{\phi}} \cdot \bar{\boldsymbol{F}}) : \bar{J}\bar{\boldsymbol{C}}^{-1} \left(\frac{1}{\bar{V}} \frac{\partial^2 \bar{\Psi}_{vol}}{\partial \bar{\Theta}^2} \right) \int_{\bar{V}} \bar{J}\bar{\boldsymbol{C}}^{-1} : (\bar{\boldsymbol{F}}^{\mathrm{T}} \cdot \bar{\mathrm{Grad}}\Delta\bar{\boldsymbol{\phi}})d\bar{V} \right] d\bar{V} \\
&+ \Delta\delta_{\bar{\boldsymbol{\phi}}}\bar{\Pi}^{ext} = -\delta\bar{\Pi}^{res}, \\
&\bar{\boldsymbol{\phi}} = \bar{\boldsymbol{\phi}}_0 \quad \text{on } \partial\bar{\mathcal{B}}_{\bar{\phi}}; \qquad \bar{\boldsymbol{t}} = \bar{\boldsymbol{t}}_0 \quad \text{on } \partial\bar{\mathcal{B}}_{\bar{t}},
\end{aligned} \tag{6.42}$$

- microscale:

$$\begin{aligned}
&\int_V \mathrm{Grad}\,\delta\tilde{\boldsymbol{w}} : [\mathrm{Grad}\,\Delta\tilde{\boldsymbol{w}} \cdot (\boldsymbol{S}_{dev} + \boldsymbol{S}_{vol})]dV \\
&+ \int_V (\mathrm{Grad}^{\mathrm{T}}\delta\tilde{\boldsymbol{w}} \cdot \boldsymbol{F}) : (\boldsymbol{C}_{dev} + \boldsymbol{C}_{vol}) : (\boldsymbol{F}^{\mathrm{T}} \cdot \mathrm{Grad}\Delta\tilde{\boldsymbol{w}})dV \\
&+ \int_V \left[(\mathrm{Grad}^{\mathrm{T}}\delta\tilde{\boldsymbol{w}} \cdot \boldsymbol{F}) : J\boldsymbol{C}^{-1} \left(\frac{1}{V} \frac{\partial^2 \Psi_{vol}}{\partial \Theta^2} \right) \int_V J\boldsymbol{C}^{-1} : (\boldsymbol{F}^{\mathrm{T}} \cdot \mathrm{Grad}\Delta\tilde{\boldsymbol{w}})dV \right] dV \\
&= -\delta\Pi^{res}, \\
&\tilde{\boldsymbol{w}}_i^+ = \tilde{\boldsymbol{w}}_i^- \quad \text{on } \partial\mathcal{B}, \\
&\delta\Pi^{res} = \delta\Pi^{res}(\bar{\boldsymbol{F}}, \tilde{\boldsymbol{w}}, \tilde{\boldsymbol{w}}^I, \alpha),
\end{aligned} \tag{6.43}$$

$$\begin{aligned}
&\sum_i \int_{\partial\Omega_i} \delta\tilde{\boldsymbol{w}}_i^{\mathrm{I}} J_i^{\mathrm{I}} \, |(\boldsymbol{F}_i^{\mathrm{I}})^{\mathrm{T}-1} \cdot \boldsymbol{N}_i| (\kappa\dot{\boldsymbol{\phi}}^{\mathrm{I}} \cdot \bar{\boldsymbol{n}}_i + \alpha_i) \cdot \bar{\boldsymbol{n}}_i \, dS = \\
&\qquad \sum_i \int_{\partial\Omega_i} \delta\tilde{\boldsymbol{w}}_i^{\mathrm{I}} \cdot (\boldsymbol{F}_i^{\mathrm{I}})^{\mathrm{T}-1} \cdot (J_i^{\mathrm{I}} \psi \boldsymbol{I} - \boldsymbol{F}^{\mathrm{T}} \cdot \boldsymbol{P}) \cdot \boldsymbol{N}_i \, dS,
\end{aligned} \tag{6.44}$$

$$\begin{aligned}
&\sum_i \int_{\partial\Omega_i} \delta\alpha_i (\dot{\tilde{\boldsymbol{w}}}_i^{\mathrm{I}} \cdot \bar{\boldsymbol{n}}_i) J_i^{\mathrm{I}} \, |(\boldsymbol{F}_i^{\mathrm{I}})^{\mathrm{T}-1} \cdot \boldsymbol{N}_i| \, dS + \\
&\qquad \sum_i \int_{\partial\Omega_i} (-\frac{1}{\gamma} \bar{\nabla}\alpha \cdot \bar{\nabla}\delta\alpha) J_i^{\mathrm{I}} \, |(\boldsymbol{F}_i^{\mathrm{I}})^{\mathrm{T}-1} \cdot \boldsymbol{N}_i| \, dS = 0.
\end{aligned} \tag{6.45}$$

The simplified flow chart of the element corresponding to the problem defined by (6.42)-(6.45) is shown in Figure 6.13. From the diagram it is obvious that the first phase of calculation at macroscale yields the macrodeformation gradient $\bar{\boldsymbol{F}}$, but the terms $\bar{\boldsymbol{S}}_{dev}$, $\bar{\boldsymbol{S}}_{vol}$, $\bar{\boldsymbol{C}}_{dev}$, $\bar{\boldsymbol{C}}_{vol}$, $\frac{\partial^2 \bar{\Psi}_{vol}}{\partial \bar{\Theta}^2}$ in (6.42) must be obtained using the microscale (SPC element). At this level the variables are total microfluctuations $\tilde{\boldsymbol{w}}$ which have

to be calculated according to (6.43), and inelastic microfluctuations and Lagrange parameter $\tilde{w}^1$, α which have to be calculated from (6.44) and (6.45). As the last two equations are defined only on the boundary, inside the crystals $\tilde{w}^1$ are calculated according to the expression (6.42), where macrodeformations $\bar{\phi}$ are replaced by $\tilde{w}^1$ and the solution of (6.44) and (6.45) is taken as the boundary condition (Fig. 6.9). Similarly to the standard formulation, $\tilde{w}$ and α have to be continuous everywhere, but $\tilde{w}^1$ is discontinuous on the crystal boundaries. Additionally, due to the Hill transfer condition, total deformations must be periodic on the periodic boundaries of the RVE. Once the microscale results have been obtained, the calculation can be continued on the macrolevel, also with calculation of the macrodeformations and macrostresses.

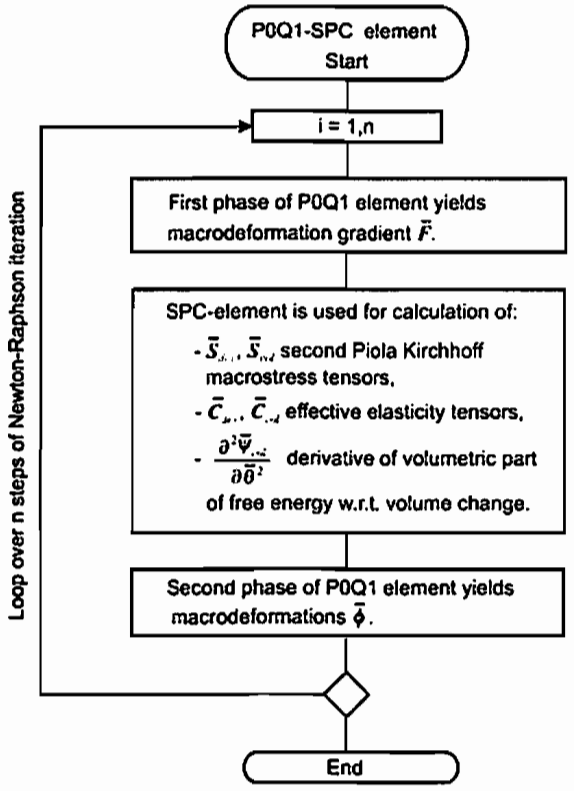

Figure 6.13: Flow chart of the P0Q1-SPC element.

Applying calculations at macroscale is illustrated by studying the change of material parameters over time for three different types of microstructure. Firstly, the tension test is simulated for a square plate similar to the one in section 5. Because of double symmetry, only one fourth of the plate is considered. Again, to simulate the random structure, the orientation of RVE (Fig. 6.14a,b) is taken to be arbitrary in each Gauss' point. The vertical displacements on the upper boundary ($\bar{v}$) and horizontal displacements on the left vertical boundary ($\bar{u}$) are calculated and shown in Figure 6.14c. Corresponding elastic material parameters are shown in Figures 6.14d-g. Inelastic microparameters are arbitrarily chosen so that the change in macromaterial parameters can be obvious in a few time steps.

Randomly oriented RVE consisting of four node crystals

$E = 23\,\mathrm{kN/mm^2}$ $\nu = 0.16$

$\gamma = 50000\,\mathrm{kNs/mm^5}$ $\kappa = 1000\,\mathrm{kNs/mm^3}$

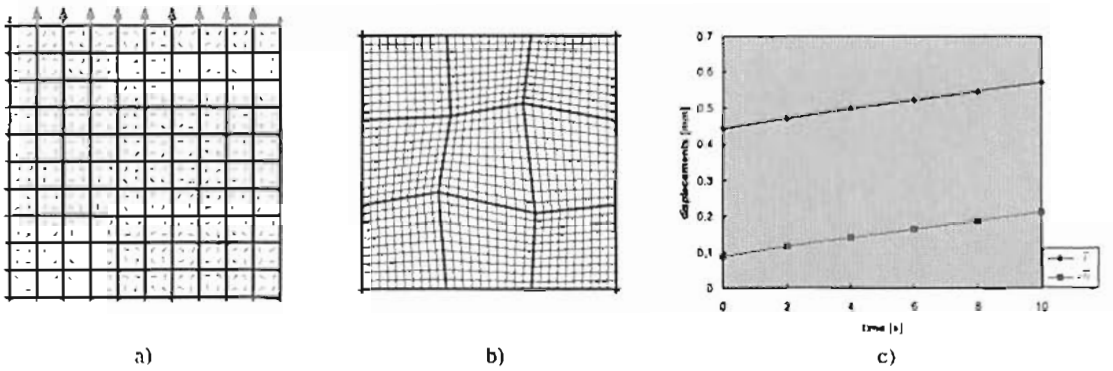

a) b) c)

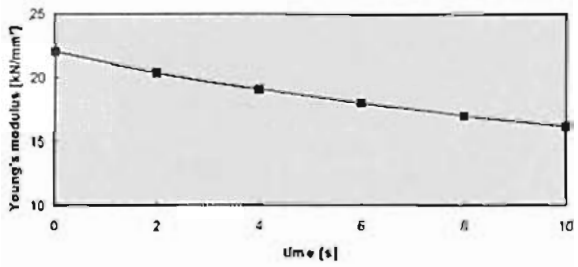

d)

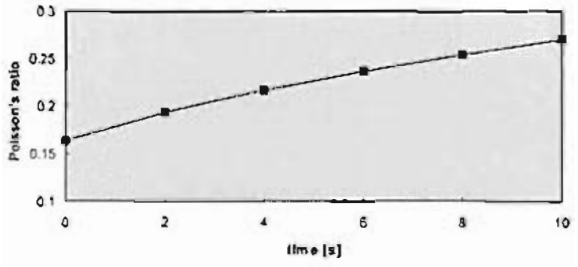

f)

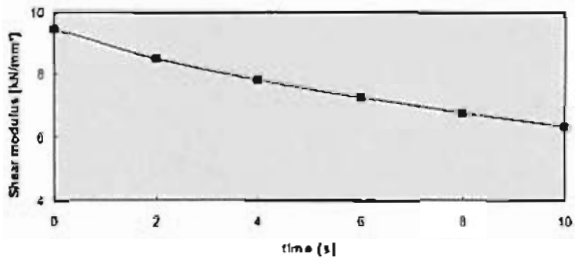

g)

Figure 6.14: Estimation of effective material parameters for random polycrystalline microstructure. a) Macroscale. b) RVE. c) Displacements on the boundaries of the plate. e)-f) Effective material parameters.

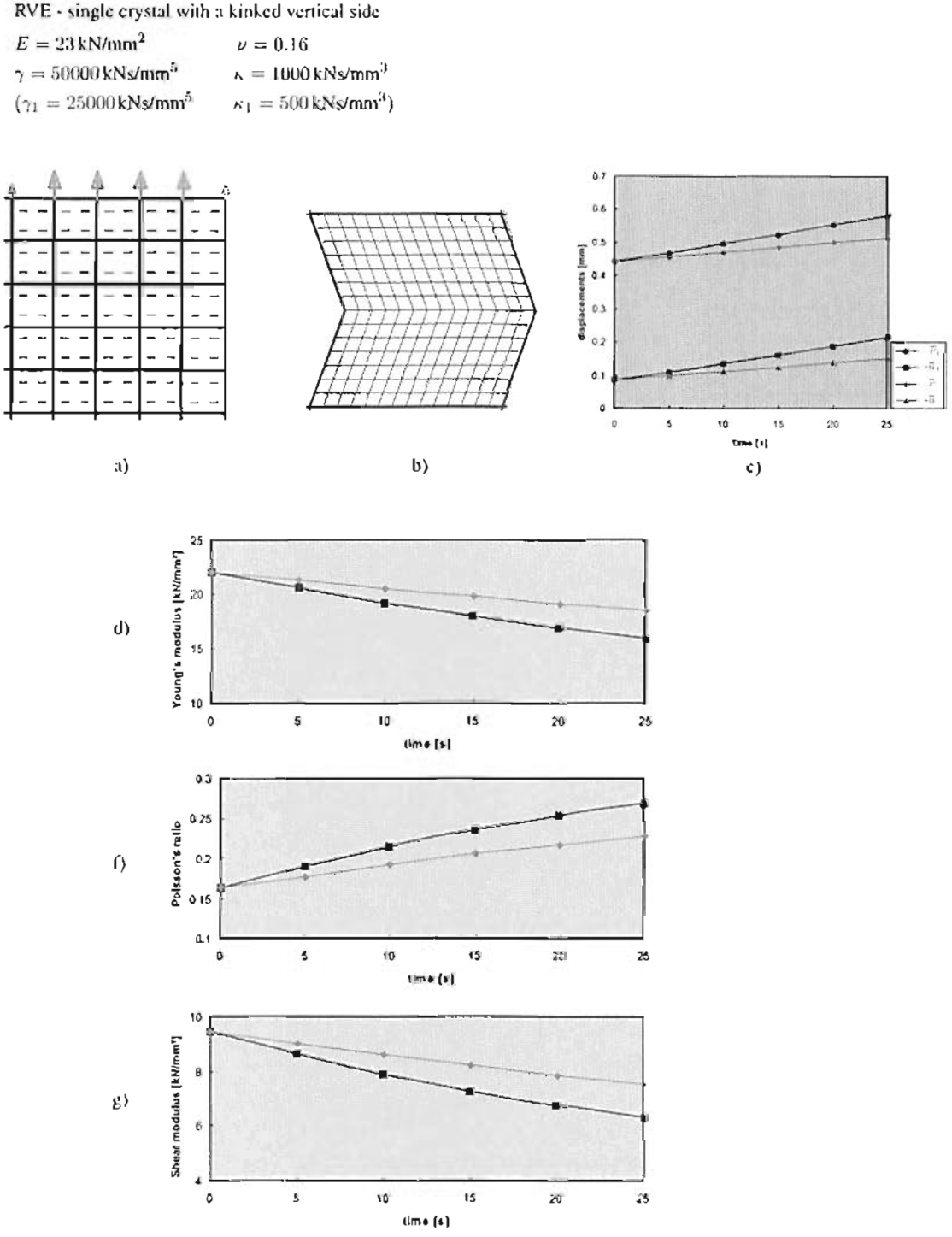

Figure 6.15: Estimation of effective material parameters for regular microstructure consisting of crystals with kinked vertical sides. a) Macroscale. b) RVE. c) Displacements on the boundaries of the plate. e)-f) Effective material parameters.

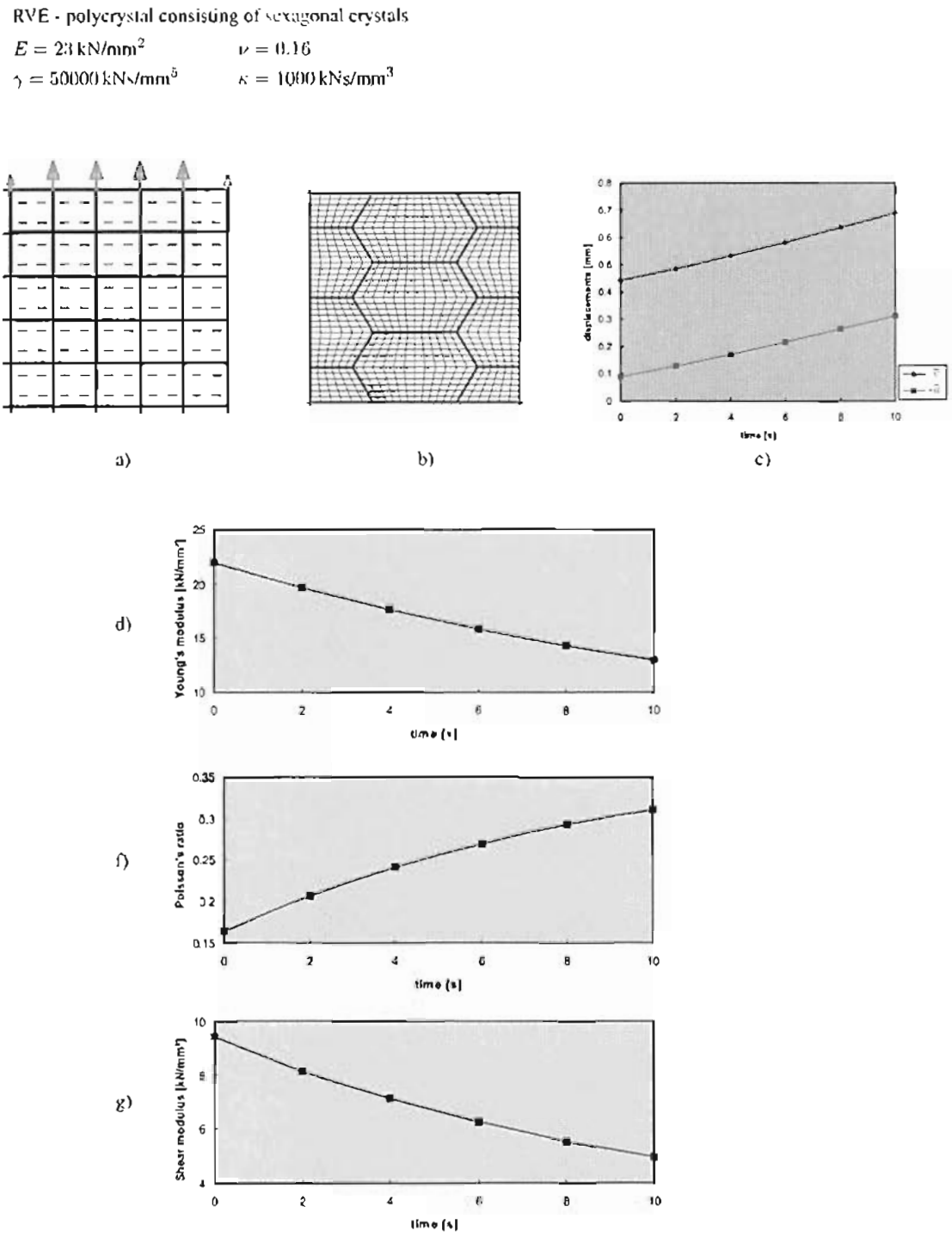

Figure 6.16: Estimation of effective material parameters for regular microstructure consisting of hexagonal crystals. a) Macroscale. b) RVE. c) Displacements on the boundaries of the plate. e)-f) Effective material parameters.

The second case also observes a plate under tension, but this time the orientation of the RVE in Gauss points is taken to be constant. At microscale, one single crystal with kinked vertical side is assumed (Fig. 6.15a,b). Two different sets of inelastic parameters are chosen and the results show that displacements are greater for the smaller inelastic material parameters (Fig. 6.15c). The change in the resulting effective parameters is shown in Figures 6.15d-g.

In the last example, an RVE is chosen to consists of hexagonal crystals, which is actually the most appropriate and consequently the mostly used approximation for the crystal form. The resulting displacements and change of parameters in this case are presented in Figure 6.16d-g, indicating finally that material parameters in all of the three examples behave similarly: Young's modulus and shear modulus decrease over time while Poisson's ratio increases.

6.2.6 Estimation of the inelastic parameters

The previous explanations already mentioned that the method proposed here depends on two inelastic constants κ and γ whose values are not known. The investigation of these constants is the next task in the frame of work in project D8 of the SFB 526 "Rheology of the Earth - from the Upper Crust to the Subduction Zone". To this end, experimental results obtained by an indentation test will be combined with some of the methods for parameter identification. Parameter identification belongs to the group of inverse problems where four different spaces have to be considered:

$\mathcal{P}$ – space of all admissible parameters $\boldsymbol{p}$,

$\mathcal{F}$ – space of all input variables $\boldsymbol{f}$,

$\mathcal{U}$ – space of all output variables $\boldsymbol{u}$,

$\tilde{\mathcal{U}}$ – space of all experimental results $\tilde{\boldsymbol{u}}$.

So, for example, the direct problem for the process presented in this chapter is

$$\text{find } \boldsymbol{u} \in \mathcal{U}, \text{ such that } g(\boldsymbol{p}, \boldsymbol{f}, \boldsymbol{u}) = 0 \text{ for given } \boldsymbol{f} \in \mathcal{F} \text{ and } \boldsymbol{p} \in \mathcal{P} \tag{6.46}$$

and its corresponding inverse problem has the form

$$\text{find } \boldsymbol{p}^* \in \mathcal{P}, \text{ such that } \boldsymbol{u}(\boldsymbol{p}^*, \boldsymbol{f}) = \tilde{\boldsymbol{u}}, \text{ for given } \boldsymbol{f} \in \mathcal{F} \text{ and } \tilde{\boldsymbol{u}} \in \tilde{\mathcal{U}}. \tag{6.47}$$

Bearing in mind that according to Hadamard [35], all problems are classified as well- or ill-posed, thereby the conditions for classification are the existence, the stability and the uniqueness of the solution, it can be easily recognized that the problem of parameter identification is ill-posed. Namely, given that typically there are more experimental data available than unknown parameters, the problem is overdetermined and in general the single solution does not exist. In order to overcome this difficulty, the most often used approach is the least square minimization method where (6.47) is transformed into an optimization problem

$$\begin{aligned} &\text{find } \boldsymbol{p}^* \in \mathcal{P}, \text{ such that for given } \boldsymbol{f} \in \mathcal{F} \text{ and } \tilde{\boldsymbol{u}} \in \tilde{\mathcal{U}} \\ &\boldsymbol{p}^* = \operatorname{argmin} \left\{ \chi^2(\boldsymbol{p}) = \frac{1}{2} \|\tilde{\boldsymbol{u}} - \boldsymbol{u}(\boldsymbol{p}, \boldsymbol{f})\|^2 \right\}. \end{aligned} \tag{6.48}$$

This also can be solved using some of the standard minimization procedures [4]. As (6.48) is not satisfactory in some cases, many modified procedures are developed, such as the weighted least square functional and the Levenberg-Marquardt method.

6.3 Overview of the results concerning the model for solution-precipitation creep

This chapter presented a continuum-mechanical model for solution–precipitation creep. In contrast to the other models where the well-posedness of the problem requires continuous stress in triple points, in this model stress is discontinuous at these points, which is expected as being more natural. The driving force of the process is the difference between the normal component of the Eshelby stress tensor and its smooth approximation, which agrees with experimental results showing that solution-precipitation creep does not occur at the places with homogeneous stress but at the places with a jump of stresses.

Preliminary results obtained by observing a set of mutually independent crystals show that the process of solution-precipitation creep yields the elongation of crystal shape, but a more precise study of realistic polycrystals was possible when just using the FEM. For a comparison with the analytical solution, the FEM was used initially to simulate a single crystal behavior. Subsequently the same method was used for simulating polycrystals with four-node and arbitrarily shaped crystals. Furthermore, the model is included in multiscale FEM which made it possible to study the change in the material parameters over time. The results obtained in this way show that Young's and shear modulus decrease gradually while Poisson's ratio increases.

At the end of the chapter, attention is drawn to two inelastic parameters κ and γ. Their real physical values are not known but they should be the subject of the future research work in the scope of subproject D8 of SFB 526 "Rheology of the Earth - from the Upper Crust to the Subduction Zone".

7 Cancellous bone – effective behavior and ultrasonic test

The model presented in this chapter was produced in the collaboration with Professor Robert Gilbert from the University of Delaware who has has worked on this field for a long time [12, 13, 14, 26, 27]. In contrast to the previous examples, the model considers small deformations caused by dynamic excitation.

7.1 Properties of cancellous bone

Cancellous bone is a two-component structure consisting of the bone frame and interstitial blood marrow. The study of its properties has recently become particularly intensive as it can lead to early detection of osteoporosis which is mainly manifested by a weakening of the bone through increased resorption and decreased production of solid phase. In other words, the general indications of this disease are that bone frame gets thinner and partially disappears, with increasing spacing between the remaining solid parts. Material porosity can increase from the normal value of 72% up to 95%. Figure 7.1 shows samples of healthy bone and of bone in the late stage of osteoporosis. The decrease in solid volume and even the disappearance of complete walls due to the process of osteoporosis are quite obvious.

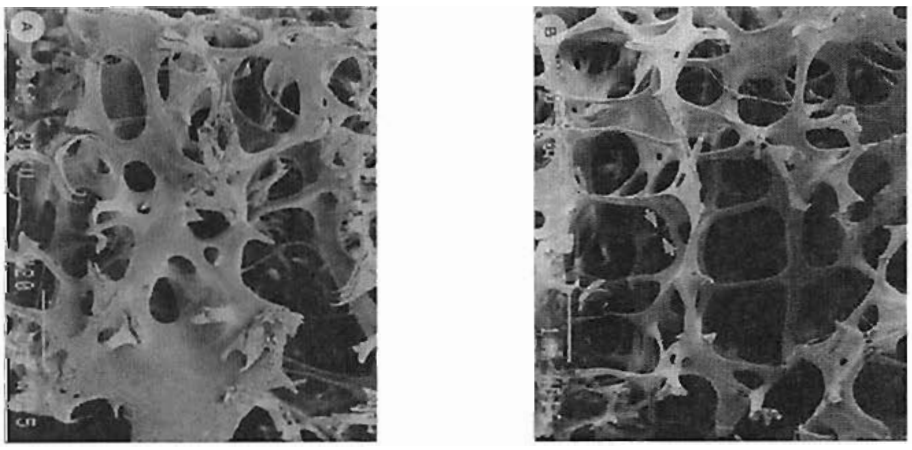

Figure 7.1: A) Healthy bone. B) Bone in the late stage of osteoporosis.

As the simulation of laboratory interrogation of the bone structure will be one of the major topics of the further work, one example will be briefly described here. This example considers an experiment based on the ultrasonic technique, carried out by A. Hosokawa and T. Otani [45]. In this test (Fig. 7.2), transmitter and hydrophone are submerged in distilled water at 23 ± 0.5°C and bone specimen is placed between them. The chosen frequency bandwidth of excitation waves is 0.5-5 MHz. The test uses samples measuring 20-30mm with two different thicknesses d_1=9mm and d_2=7mm. The samples are chosen to represent the different types of cancellous bone whose densities vary in the range 1120-1200 kg/m^3. Before the experiments, the samples are saturated with water in order to remove air bubbles formed in the process of preparation. The final results of the ultrasonic test are wave speed v and attenuation α. Using the properties of waves emitted through the samples of different thicknesses these have to be

calculated according to the expressions

$$v = \frac{\Delta d\, v_0}{\Delta d - (\Delta\phi/\omega)v_0}, \tag{7.1}$$

$$\alpha = (\ln \Delta V)/\Delta d. \tag{7.2}$$

Here Δd represents the difference in thickness $\Delta d = d_1 - d_2$, v_0 is the propagating speed of the wave in water, $\Delta\phi$ is the phase difference, ω the frequency of initial signals and ΔV is the ratio of amplitude spectra. Together with the diagram of the experiment in Figure 7.2, the original appearance of a similar setup in the laboratory at Ruhr University Bochum can be seen in Figure 7.3.

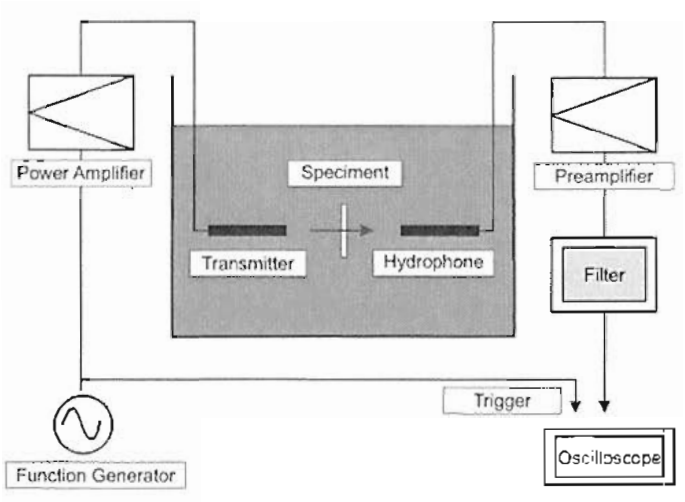

Figure 7.2: Laboratory test of A. Hosokawa and T. Otani [45].

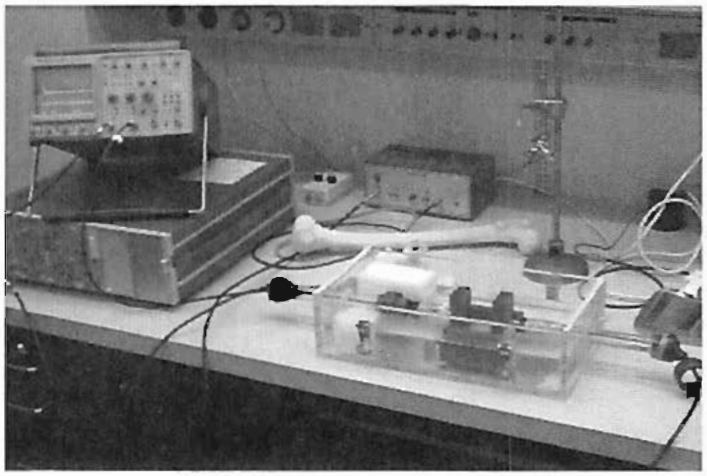

Figure 7.3: Experimental setup of the ultrasonic test. (Institute of High Frequency Engineering, Ruhr University Bochum).

7.2 Biot's model

Biot's model [10, 11] is used mostly for studying of cancellous bone, although it was originally developed for saturated porous soils and rocks in geomechanics. The constitutive equations proposed by this author

are those of linear elastic material, extended to include the influence of the interaction of solid and fluid

$$\begin{aligned} \sigma_{ii} &= 2\mu\epsilon_{ii} + \lambda\epsilon + Qe, \\ \sigma_{ij} &= 2\mu\epsilon_{ij}, \qquad i \neq j, \\ s &= Qe + R\epsilon. \end{aligned} \tag{7.3}$$

Here σ represents stress in the solid phase while s denotes stress in the fluid phase. Strain in solid part is defined in the classic manner

$$\epsilon_{ij} = \frac{1}{2}\left(\frac{\partial u_i}{\partial x_j} + \frac{\partial u_j}{\partial x_i}\right) \tag{7.4}$$

and the volumetric part of the deformation is denoted by

$$\epsilon = \nabla \cdot \boldsymbol{u}, \qquad e = \nabla \cdot \boldsymbol{U}. \tag{7.5}$$

Note that in the previous expressions, $\boldsymbol{u}$ and $\boldsymbol{U}$ are used to denote displacements in the solid and the fluid phase respectively. One particular property of this model consists in the so-called Biot's constants λ, R, Q, which have to be calculated according to the expressions

$$\lambda = K_b - \frac{2}{3}\mu + \frac{(K_s - K_b)^2 - 2\beta K_s (K_s - K_b) + \beta^2 K_s^2}{D - K_b} \tag{7.6}$$

$$R = \frac{\beta^2 K_s^2}{D - K_b} \tag{7.7}$$

$$Q = \frac{\beta K_s ((1-\beta) K_s - K_b)}{D - K_b} \tag{7.8}$$

$$D = K_s (1 + \beta (K_s/K_f - 1)) \tag{7.9}$$

and which depend on the material and structural parameters listed in the following table:

Symbol	Parameter
ρ_f	Density of the pore fluid
ρ_s	Density of the frame material
K_b	Complex frame bulk modulus
μ	Complex frame shear modulus
K_f	Fluid bulk modulus
K_s	Frame material bulk modulus
β	Porosity
η	Viscosity of pore fluid
k	Permeability
α	Structure constant
a	Pore size parameters

Table 7.1: Parameters in the Biot model

To study dynamic problems, the model is extended by introducing kinetic energy E_k and dissipation D in the form

$$2E_k = \rho_{11}\, \dot{\boldsymbol{u}} \cdot \dot{\boldsymbol{u}} + 2\rho_{12}\, \dot{\boldsymbol{u}} \cdot \dot{\boldsymbol{U}} + \rho_{22}\, \dot{\boldsymbol{U}} \cdot \dot{\boldsymbol{U}}, \tag{7.10}$$

$$2D = b(\dot{\boldsymbol{u}} - \dot{\boldsymbol{U}}) \cdot (\dot{\boldsymbol{u}} - \dot{\boldsymbol{U}}), \tag{7.11}$$

where ρ_{11} and ρ_{22}, are density parameters of the solid and fluid, ρ_{12} is the density coupling parameter, b is a dissipation parameter, and all of them again depend on the parameters given in Table (7.1). Their

exact definitions will not be given here, but can be found in standard literature [10, 11]. Finally, using the principles of Lagrangean mechanics,

$$\frac{\partial}{\partial t}\left(\frac{\partial E_k}{\partial \dot{\boldsymbol{u}}}\right)+\frac{\partial D}{\partial \dot{\boldsymbol{u}}}=\nabla\cdot\boldsymbol{\sigma} \tag{7.12}$$

$$\frac{\partial}{\partial t}\left(\frac{\partial E_k}{\partial \dot{\boldsymbol{U}}}\right)+\frac{\partial D}{\partial \dot{\boldsymbol{U}}}=\nabla s \tag{7.13}$$

equations of motion describing the behavior of saturated porous media and here in particular of cancellous bone become

$$\begin{aligned}\mu\nabla^2\boldsymbol{u}+\nabla\left[(\lambda+\mu)\,e+Q\epsilon\right] &= \left(\rho_{11}\ddot{\boldsymbol{u}}+\rho_{12}\ddot{\boldsymbol{U}}\right)+b\left(\dot{\boldsymbol{u}}-\dot{\boldsymbol{U}}\right),\\ \nabla\left[Qe+R\epsilon\right] &= \left(\rho_{12}\ddot{\boldsymbol{u}}+\rho_{22}\ddot{\boldsymbol{U}}\right)-b\left(\dot{\boldsymbol{u}}-\dot{\boldsymbol{U}}\right).\end{aligned} \tag{7.14}$$

For sound excitation, which is often the considered case, using the fact that excitation and deformations are time harmonic functions,

$$\boldsymbol{u}(\boldsymbol{x},t)=\boldsymbol{u}(\boldsymbol{x})\,e^{-i\omega t},\qquad \boldsymbol{U}(\boldsymbol{x},t)=\boldsymbol{U}(\boldsymbol{x})\,e^{-i\omega t} \tag{7.15}$$

equations of motion (7.14) acquire the simpler from,

$$\begin{aligned}\mu\nabla^2\boldsymbol{u}+\nabla\left[(\lambda+\mu)\,e+Q\epsilon\right] &= -\omega^2\left(\rho_{11}\boldsymbol{u}+\rho_{12}\boldsymbol{U}\right)-ib\left(\boldsymbol{u}-\boldsymbol{U}\right),\\ \nabla\left[Qe+R\epsilon\right] &= -\omega^2\left(\rho_{12}\boldsymbol{u}+\rho_{22}\boldsymbol{U}\right)+ib\left(\boldsymbol{u}-\boldsymbol{U}\right).\end{aligned} \tag{7.16}$$

The serious disadvantage of Biot's method and simultaneously a good reason to look for another solution is the fact that this method depends on a large number of material and structural parameters (Tab. 7.1), only some of which can be determined precisely (Tab. 7.2). Here, one additional remark must be made: even in the case of the parameters listed in Table 7.2, the various authors still do not agree. The cited values are taken from the work of Williams and Johnson [90].

Parameter	Symbol	Value	Unity
Pore fluid density	ρ_f	950	kg m^{-3}
Fluid bulk modulus	K_f	2.00×10^9	Pa
Pore fluid viscosity	η	1.5	Ns m^{-2}
Frame material density	ρ_s	1960	kg m^{-3}
Frame material Young's modulus	E_s	2.20×10^{10}	Pa
Frame material Poisson's ratio	ν_s	0.32	-

Table 7.2: Parameters for cancellous bone according to Williams and Johnson [90].

7.3 Some characteristics of modeling the fluid phase

7.3.1 Constitutive law of the Newtonian fluid

Concerning a constitutive law of a fluid, firstly it must be recalled that in the static case, by this sort of materials, the stress tensor $\boldsymbol{\sigma}_0$ depends on hydrostatic pressure p_0 and it has the diagonal form

$$\boldsymbol{\sigma}_0=-p_0\boldsymbol{I} \tag{7.17}$$

while the shear stresses are activated only in the dynamic case and they depend on strain rate $\dot{\epsilon}$ and indirectly on velocity v

$$\dot{\epsilon} = \frac{1}{2}(\nabla v + v\nabla). \tag{7.18}$$

The simplest relation between stress and strain rate corresponds to Newtonian fluids where deviatoric stress depends linearly on deviatoric strain rate

$$\sigma^{dev} = \sigma - \frac{1}{3}\operatorname{tr}\sigma\, I = 2\eta\left(\dot{\epsilon} - \frac{1}{3}\operatorname{tr}\dot{\epsilon}\, I\right) \tag{7.19}$$

and proportion coefficient η represents the shear viscosity. The volumetric stress depends on volumetric strain rate and hydrostatic pressure. Using the coefficient of volumetric viscosity κ, this can be written

$$p = -\frac{\operatorname{tr}\sigma}{3} = -\kappa \operatorname{tr}\dot{\epsilon} + p_0. \tag{7.20}$$

According to (7.19) and (7.20), the expression for the total stress obtained by superposing the deviatoric and volumetric part becomes

$$\sigma = \sigma^{dev} - pI = 2\eta\,\dot{\epsilon} + \left(\kappa - \frac{2}{3}\eta\right)\operatorname{tr}\dot{\epsilon}\, I - pI \tag{7.21}$$

where the term inside parentheses is often taken to be a new viscosity coefficient ξ. Given the requirement for original material parameters $\eta > 0$, $\kappa > 0$, this must satisfy the condition

$$\frac{\eta}{\xi} > -\frac{2}{3}. \tag{7.22}$$

Omitting the zero index in term p_0 constitutive law of Newtonian fluid obtains the form

$$\sigma = 2\eta\,\dot{\epsilon} + \xi \operatorname{tr}\dot{\epsilon} I - pI \tag{7.23}$$

where it is important to distinguish one part due to velocities (σ^v) and one part due to pressure p

$$\sigma = \sigma^v - pI. \tag{7.24}$$

Note that in the case of more complicated constitutive laws, viscosity coefficients become dependent on strain rates, which correspond to the nonlinear or non-Newtonian fluids, but such kinds of materials will not be considered in this thesis.

7.3.2 Conservative and nonconservative form of the balance laws

The application of balance laws in Eulerian description is typical for fluid mechanics. Here, for the purposes of our model, only continuity equation, dynamic equilibrium and energy balance will be recalled

$$\begin{aligned}
&\partial_t \rho + \nabla\cdot(\rho v) = 0, && \text{a)}\\
&\rho D_t v - \nabla\cdot\sigma - \rho b = 0, && \text{b)}\\
&\rho D_t e_t + \nabla\cdot q - \nabla\cdot(\sigma\cdot v) - \rho b\cdot v - \rho r = 0, && \text{c).}
\end{aligned} \tag{7.25}$$

In these equations, ρ represents the material density, q is the heat flux, r the heat source and e_t is the total energy defined as the sum of internal energy e and kinetic energy $e_k = \frac{1}{2}v\cdot v$. Note that elementary

rules of differentiation and the continuity equation (7.25)a can be used to reformulate the material time derivatives in equation (7.25)b and (7.25)c in such way that the previous system becomes

$$\begin{aligned} &\partial_t \rho + \nabla \cdot (\rho \boldsymbol{v}) = 0, && \text{a)} \\ &\partial_t (\rho \boldsymbol{v}) + (\rho \boldsymbol{v} \otimes \boldsymbol{v}) \cdot \nabla - \nabla \cdot \boldsymbol{\sigma} - \rho \boldsymbol{b} = \boldsymbol{0}, && \text{b)} \\ &\partial_t (\rho e_t) + \nabla \cdot (\rho \boldsymbol{v} e_t) + \nabla \cdot \boldsymbol{q} - \nabla \cdot (\boldsymbol{\sigma} \cdot \boldsymbol{v}) - \rho \boldsymbol{b} \cdot \boldsymbol{v} - \rho r = 0. && \text{c).} \end{aligned} \tag{7.26}$$

In the context of fluid mechanics, the first system (7.25) is referred to as the nonconservative and the second one (7.26) as the conservative description of the problem, but due to the fact that they can be derived from each other, in most cases it is irrelevant which formulation is used. The only exception is the propagation of shock waves through compressible fluids, where it is advisable to consider conservative formulation [89, 97]. The difference in the physical interpretation of these two descriptions is shown in Figure 7.4. Here the nonconservative formulation is seen to correspond to the case of the control volume moving together with the fluid (Fig. 7.4a), while the conservative formulation corresponds to observing the fluid motion through the fixed control volume (Fig. 7.4b). Systems (7.25) and (7.26) are often referred to in the literature as Navier-Stockes equation. For perfect fluids where viscosity becomes equal to zero, these equations reduces to the Euler equation.

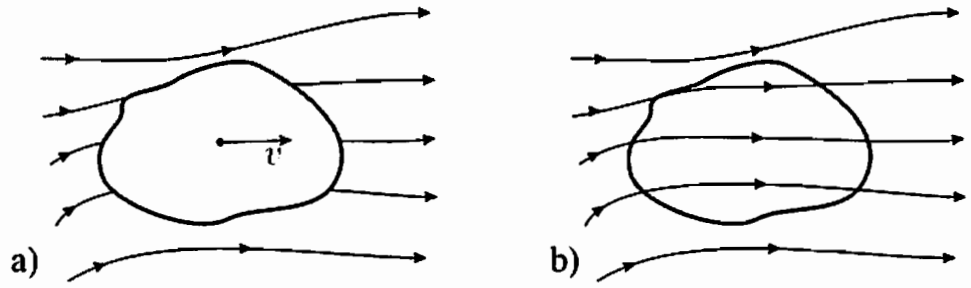

Figure 7.4: a) Moving control volume. b) Fixed control volume.

It is also worth mentioning that systems (7.25) and (7.26) can be reduced in some special cases. The illustration considers the balance of momentum (7.26)b in the case of a Newtonian fluid (7.24)

$$\partial_t (\rho \boldsymbol{v}) + (\rho \boldsymbol{v} \otimes \boldsymbol{v}) \cdot \nabla - \nabla \cdot \boldsymbol{\sigma}' + \nabla p - \rho \boldsymbol{b} = \boldsymbol{0}. \tag{7.27}$$

This equation alone represents an under-determined system so that it cannot be solved independently of the rest of the problem. Another obligatory condition that also has to be considered is the state equation relating density ρ, pressure p and temperature T

$$\rho = \rho(p, T). \tag{7.28}$$

The shape of the state equation significantly influences the solution method, because if it really depends on all three variables (ρ, p, T), then continuity equation and energy balance also have to be considered as well as (7.27), while in the event that only density and pressure are related to each other,

$$\rho = \rho(p) \tag{7.29}$$

the balance of energy must not be considered. Note that this special case when temperature is not included in the state equation corresponds to so-called barotropic fluids.

7.3.3 Nearly incompressible flow

Nearly incompressible flows are observed as the isothermal processes where the change of density ρ with pressure p is very small, so that in their product terms, the latter can be treated as a constant. Due to the first assumption (isothermal process), the state equation becomes dependent only on pressure and density, and can be expressed in the form

$$d\rho = \frac{1}{c^2}\,dp \tag{7.30}$$

where $c = \sqrt{K/\rho}$ is a sound wave velocity dependent on elastic bulk modulus K. Such a state equation obviously corresponds to a barotropic fluid, and its time derivative can be used for transformation of the balance of mass

$$\frac{\partial \rho}{\partial t} = \frac{1}{c^2}\frac{\partial p}{\partial t} \quad \Rightarrow \quad \frac{1}{c^2}\frac{\partial p}{\partial t} + \rho\frac{\partial u_i}{\partial x_i} = 0 \tag{7.31}$$

which also yields the expression for the pressure p depending on displacements and not on velocities

$$p = -c^2\rho\frac{\partial u_i}{\partial x_i} = -c^2\rho\,\nabla\cdot\boldsymbol{u} = -K\,\nabla\cdot\boldsymbol{u}. \tag{7.32}$$

Using this, the constitutive law (7.23) becomes:

$$\boldsymbol{\sigma} = c^2\rho\,\nabla\cdot\boldsymbol{u}\boldsymbol{I} + 2\eta\,\dot{\boldsymbol{\epsilon}} + \xi\,\mathrm{tr}\,\dot{\boldsymbol{\epsilon}}\boldsymbol{I}. \tag{7.33}$$

Due to the second assumption for modeling incompressible fluids (the change in pressure causes a small change in density), the conservation of momentum (7.26)b can be written as

$$\partial_t\boldsymbol{v} + (\boldsymbol{v}\otimes\boldsymbol{v})\cdot\nabla - \frac{1}{\rho}\nabla\cdot\boldsymbol{\sigma} - \boldsymbol{b} = \boldsymbol{0}. \tag{7.34}$$

while the nonconservative formulation apparently stays unchanged:

$$\rho\,D_t\boldsymbol{v} - \nabla\cdot\boldsymbol{\sigma} - \rho\,\boldsymbol{b} = \boldsymbol{0}. \tag{7.35}$$

It should not be forgotten that in both equations (7.34) and (7.35), density has to be treated as a constant. Final observation is that the constitutive law (7.33) depends only on displacements and velocities so that the conservation of momentum (7.34) or (7.35) followed by boundary and initial conditions completely defines the problem of the motion of a Newtonian incompressible fluid.

7.4 RVE for cancellous bone

7.4.1 Concept of the model

As the RVE for cancellous bone contains a fluid phase for the activation of the viscous phenomena in it, consideration is given to the behavior of a sample under sound excitation. Due to the small velocities, it is assumed that the linearized form of the equation of motion (7.34) or (7.35) describes the state in a point of the RVE. This can be written

$$\rho\,\ddot{\boldsymbol{u}} - \nabla\cdot\boldsymbol{\sigma} = \rho\,\boldsymbol{b}(t) \tag{7.36}$$

where term $\boldsymbol{b}(t)$ denotes harmonic excitation force with frequency ω

$$\boldsymbol{b}(t) = \boldsymbol{b}e^{i\omega t}. \tag{7.37}$$

The steady state solution of equation (7.36) is a complex time harmonic function

$$\boldsymbol{u} = \boldsymbol{u}(\boldsymbol{x})e^{i\omega t} = \left(\boldsymbol{u}^R(\boldsymbol{x}) + i\boldsymbol{u}^I(\boldsymbol{x})\right) e^{i\omega t}, \tag{7.38}$$

so that due to the standard properties of the exponential function for time derivatives of this function, it applies that

$$\ddot{\boldsymbol{u}} = -\omega^2 \boldsymbol{u}, \qquad \dot{\boldsymbol{u}} = i\omega \boldsymbol{u}. \tag{7.39}$$

Bearing in mind that the equation of motion (7.36) requires a complementary constitutive law, the following section describes both of the phases of RVE separately. Starting with the solid phase Ω_s, it can be pointed out that the state of deformations and stresses in it is determined by the system

$$-\omega^2 \rho_s \boldsymbol{u} - \nabla \cdot \boldsymbol{\sigma}_s = \rho_s \boldsymbol{b}(\boldsymbol{x}), \tag{7.40}$$

$$\boldsymbol{\sigma}_s = \boldsymbol{C} : \boldsymbol{\epsilon} \tag{7.41}$$

where the index s is used to denote the solid phase and the constitutive law (7.41) is written in the general form dependent on the complex elasticity tensor $\boldsymbol{C}$ which will be defined precisely later in section 7.4.4. In contrast to the solid phase, the state of deformation and stress inside the fluid Ω_f is defined by

$$-\omega^2 \rho_f \boldsymbol{u} - \nabla \cdot \boldsymbol{\sigma}_f = \rho_f \boldsymbol{b}(\boldsymbol{x}), \tag{7.42}$$

$$\boldsymbol{\sigma}_f = c^2 \rho_f \nabla \cdot \boldsymbol{u}\, \boldsymbol{I} + 2i\omega\eta\, \boldsymbol{\epsilon} + i\omega\xi \nabla \cdot \boldsymbol{u}\, \boldsymbol{I}, \tag{7.43}$$

where the constitutive law (7.33) is applied and index f denotes the fluid phase. Furthermore, the deformations in different phases must satisfy a coupling condition which requires that there is no jump of displacements on the interface of phases

$$\boldsymbol{u}_s = \boldsymbol{u}_f \quad \text{on} \quad \Gamma = \Omega_s \cap \Omega_f. \tag{7.44}$$

Together with the material behavior, one additional property important for modeling the RVE is the geometry of the microstructure. This property particularly influences the choice of the type of elements needed for FE simulation. The following chapter uses shell elements to simulate the solid walls of cancellous bone, due to their thin structure, while the eight-node cubic element is applied for modeling the fluid phase. For an analysis in the complex domain, the standard formulation of these elements has to be extended and the number of DOFs has to be doubled.

7.4.2 Formulation of the shell element

In order to develop an element appropriate to simulating the solid phase of the RVE, the standard shell element of the finite element program FEAP is taken as a starting point [5, 88, 97].

The formulation of this element is based on the theory of small deformations for shallow shells, where the complete structure is treated as an assembly of the plate elements simultaneously loaded by bending load and load in their own plane. If the elements are flat, different load cases are completely decoupled problems, while elements with curvature need additional corrections causing the coupling.

Figure 7.5 shows a shell element and its local coordinate system xyz. In each node of the element six DOFs are needed for approximation of deformation: three displacements in the directions of coordinate axis u_i, v_i, w_i and three rotations around these axis $\theta_{xi}, \theta_{yi}, \theta_{zi}$. System $\bar{x}\bar{y}\bar{z}$ represents the global coordinate system.

For a precise description of the used element, firstly it is pointed out that the formulation is based on discrete Kirchhoff theory where shear deformations γ are neglected due to the thin structure of plate elements

$$\gamma = 0. \tag{7.45}$$

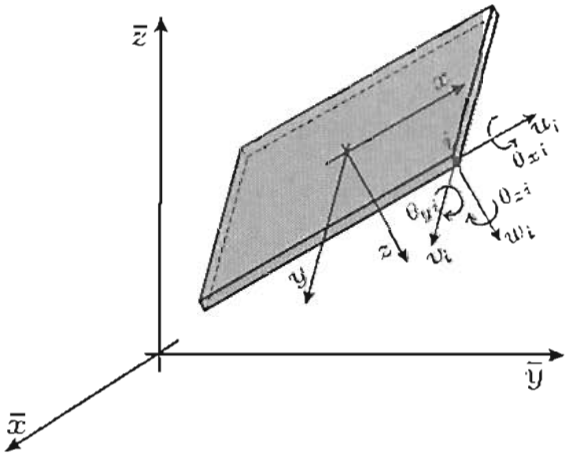

Figure 7.5: Shell element and its DOFs.

This assumption yields the following relation between the deflection w and vector of rotations θ'

$$\nabla w = \theta', \qquad \theta' = \{\theta_y \ -\theta_x\}^T \tag{7.46}$$

and consequently the expression for the potential of an plate element in the form

$$\Pi_b^e = \Pi_b^{e,int} + \Pi_b^{e,ext} = \frac{1}{2}\int_{\mathcal{A}^e} \theta^T \cdot \boldsymbol{L}_b^T \cdot \boldsymbol{\mathcal{C}}_b \cdot \boldsymbol{L}_b \cdot \theta \, da + \Pi_b^{e,ext}. \tag{7.47}$$

Note that literature focusing only on the plate theory often uses different notation for the rotations so that condition (7.46) is written in a slightly different form [97]. In expression (7.47), the superscript e denotes that an element is considered and the index b denotes the bending case. Integration is carried out over the middle surface of element $\mathcal{A}^e$, $\boldsymbol{L}_b$ represents the differential operator and $\boldsymbol{\mathcal{C}}_b$ is the bending stiffness matrix dependent on the thickness of plate t, Young's modulus E and Poisson's ratio ν. The matrix $\boldsymbol{\mathcal{C}}_b$ and the operator $\boldsymbol{L}_b$ are defined by

$$\boldsymbol{\mathcal{C}}_b = \frac{Et^3}{12(1-\nu^2)}\begin{bmatrix} 1 & \nu & 0 \\ \nu & 1 & 0 \\ 0 & 0 & (1-\nu)/2 \end{bmatrix}, \qquad \boldsymbol{L}_p = \begin{bmatrix} 0 & -\frac{\partial}{\partial x} \\ \frac{\partial}{\partial y} & 0 \\ \frac{\partial}{\partial x} & -\frac{\partial}{\partial y} \end{bmatrix}. \tag{7.48}$$

Potential (7.47) depends on the vector of rotations $\theta = \{\theta_x \, \theta_y\}^T$ which can be approximated using nodal values of deflection w and rotations θ_x, θ_y

$$\theta = \boldsymbol{N}_b^m \cdot \hat{\mathbf{a}}_b^{m\,e}, \qquad \theta = \begin{Bmatrix} \theta_x \\ \theta_y \end{Bmatrix}, \qquad \hat{\mathbf{a}}_{bi}^m = \begin{Bmatrix} \hat{w}_i \\ \hat{\theta}_{xi} \\ \hat{\theta}_{yi} \end{Bmatrix}, \qquad \hat{\mathbf{a}}_b^{m\,e} = \mathrm{A}^e \hat{\mathbf{a}}_{bi}^m. \tag{7.49}$$

Here the vector $\hat{\mathbf{a}}_b^{m\,e}$ is a vector of DOFs of an element consisting of the vectors of nodal DOFs $\hat{\mathbf{a}}_{bi}^m$, and the index m means that a mixed or modified approximation is applied. The notation A^e is introduced for the element assembling operator. Using (7.49) and (7.47), the variation of the potential of the plate under bending load becomes

$$\begin{aligned} \delta\Pi_b^e &= (\delta\hat{\mathbf{a}}_b^e)^T \cdot \left(\int_{\mathcal{A}^e} (\boldsymbol{N}_b^m)^T \cdot \boldsymbol{L}_b^T \cdot \boldsymbol{\mathcal{C}}_b \cdot \boldsymbol{L}_b \cdot \boldsymbol{N}_b^m \, da \right) \cdot \hat{\mathbf{a}}_b^e + \delta\Pi_b^{e,ext} \\ &= (\delta\hat{\mathbf{a}}_b^e)^T \cdot \left(\int_{\mathcal{A}^e} (\boldsymbol{B}_b^m)^T \cdot \boldsymbol{\mathcal{C}}_b \cdot \boldsymbol{B}_b^m \, da \right) \cdot \hat{\mathbf{a}}_b^e + \delta\Pi_b^{e,ext}. \end{aligned} \tag{7.50}$$

In the opposite case, if the plate is loaded only in its own plane from the standard form of the potential

$$\Pi = \frac{1}{2}\int_{\Omega} \epsilon : \boldsymbol{C} : \epsilon dv, \tag{7.51}$$

an alternative expression can easily be obtained using the relation between strains and displacements

$$\Pi_p^e = \Pi_p^{e,int} + \Pi_p^{e,ext} = \frac{1}{2}\int_{\mathcal{A}^e} \boldsymbol{u}^T \cdot \boldsymbol{L}_p^T \cdot \boldsymbol{C}_p \cdot \boldsymbol{L}_p \cdot \boldsymbol{u}\, da + \Pi_p^{e,ext}, \tag{7.52}$$

$$\boldsymbol{C}_p = \frac{E}{(1-\nu^2)}\begin{bmatrix} 1 & \nu & 0 \\ \nu & 1 & 0 \\ 0 & 0 & (1-\nu)/2 \end{bmatrix}, \qquad \boldsymbol{L}_p = \begin{bmatrix} \frac{\partial}{\partial x} & 0 \\ 0 & \frac{\partial}{\partial y} \\ \frac{\partial}{\partial y} & \frac{\partial}{\partial x} \end{bmatrix}. \tag{7.53}$$

Relation (7.52) depends only on the displacements in the plane of plate $\boldsymbol{u}_p = \{u\ v\}^T$. In the context of FEM, again a mixed approximation is used

$$\boldsymbol{u}_p = \boldsymbol{N}_p^m \cdot \hat{\boldsymbol{a}}_p^{me}, \qquad \boldsymbol{u}_p = \begin{Bmatrix} u \\ v \end{Bmatrix}, \qquad \hat{\boldsymbol{a}}_{pi}^m = \begin{Bmatrix} \hat{u}_i \\ \hat{v}_i \\ \hat{\theta}_{zi} \end{Bmatrix}, \qquad \hat{\boldsymbol{a}}_p^{me} = \mathrm{A}^e \hat{\boldsymbol{a}}_{pi}^m, \tag{7.54}$$

where the reasons for introducing drilling DOF θ_{zi} have a purely numerical character [85]. The approximation (7.54) leads to the variation of the potential (7.52) in the form

$$\begin{aligned} \delta\Pi_p^e &= (\delta\hat{\boldsymbol{a}}_p^{me})^T \cdot \left(\int_{\mathcal{A}^e} (\boldsymbol{N}_p^m)^T \cdot \boldsymbol{L}_p^T \cdot \boldsymbol{C}_p \cdot \boldsymbol{L}_p \cdot \boldsymbol{N}_p^m\, da \right) \cdot \hat{\boldsymbol{a}}_p^{me} + \delta\Pi_p^{e,ext} \\ &= (\delta\hat{\boldsymbol{a}}_p^{me})^T \cdot \left(\int_{\mathcal{A}^e} (\boldsymbol{B}_p^m)^T \cdot \boldsymbol{C}_p \cdot \boldsymbol{B}_p^m\, da \right) \cdot \hat{\boldsymbol{a}}_p^{me} + \delta\Pi_p^{e,ext} \end{aligned} \tag{7.55}$$

so that when using (7.50) and (7.55), the final expression for the variation of the potential of the flat shell element becomes

$$\begin{aligned} \delta\Pi_p^e &= (\delta\hat{\boldsymbol{a}}^{me})^T \cdot \left(\int_{\mathcal{A}^e} (\boldsymbol{N}^m)^T \cdot \boldsymbol{L}^T \cdot \boldsymbol{C} \cdot \boldsymbol{L} \cdot \boldsymbol{N}^m\, da \right) \cdot \hat{\boldsymbol{a}}^{me} + \delta\Pi^{e,ext} \\ &= (\delta\hat{\boldsymbol{a}}^{me})^T \cdot \left(\int_{\mathcal{A}^e} (\boldsymbol{B}^m)^T \cdot \boldsymbol{C} \cdot \boldsymbol{B}^m\, da \right) \cdot \hat{\boldsymbol{a}}^{me} + \delta\Pi^{e,ext}. \end{aligned} \tag{7.56}$$

Here the separated approximations (7.49) and (7.54) are replaced by the unique one

$$\begin{aligned} &\boldsymbol{u}^m = \boldsymbol{N}^m \cdot \hat{\boldsymbol{a}}^{me}, \\ &\boldsymbol{u}^m = \{\ u\ \ v\ \ \theta_x\ \ \theta_y\ \}^T, \qquad \hat{\boldsymbol{a}}_i^m = \{\ \hat{u}_i\ \ \hat{v}_i\ \ \hat{\theta}_{zi}\ \ \hat{w}_i\ \ \hat{\theta}_{xi}\ \ \hat{\theta}_{yi}\ \}^T, \end{aligned} \tag{7.57}$$

and the following notation is introduced

$$\boldsymbol{N}^m = \begin{bmatrix} \boldsymbol{N}_p^m & 0 \\ 0 & \boldsymbol{N}_b^m \end{bmatrix}, \qquad \boldsymbol{L} = \begin{bmatrix} \boldsymbol{L}_p & 0 \\ 0 & \boldsymbol{L}_b \end{bmatrix}, \tag{7.58}$$

$$\boldsymbol{B}^m = \begin{bmatrix} \boldsymbol{B}_p^m & 0 \\ 0 & \boldsymbol{B}_b^m \end{bmatrix}, \qquad \boldsymbol{C} = \begin{bmatrix} \boldsymbol{C}_p & 0 \\ 0 & \boldsymbol{C}_b \end{bmatrix}. \tag{7.59}$$

Expression (7.56) yields the system of equations customary in FEM

$$\boldsymbol{K}^e \cdot \hat{\boldsymbol{a}}^{me} = \boldsymbol{f}^e. \tag{7.60}$$

where the stiffness matrix is defined as the integral

$$\boldsymbol{K}^e = \int_{\mathcal{A}^e} (\boldsymbol{B}^m)^T \cdot \boldsymbol{C} \cdot \boldsymbol{B}^m\, da \tag{7.61}$$

and the vector of external load is obtained from $\delta\Pi^{e,ext}$ in the form

$$\boldsymbol{f}_i^e = \{\ F_{xi}\ \ F_{yi}\ \ M_{zi}\ \ F_{zi}\ \ M_{xi}\ \ M_{yi}\ \}^T. \tag{7.62}$$

7.4.3 Dynamic excitation

In order to extend the formulation of the shell element to the case where dynamic excitation occurs, it is necessary to consider the full Lagrangean

$$L = E_k - \Pi^{int} - \Pi^{ext} \tag{7.63}$$

whose minimization yields the equation of motion

$$\delta \int_t L\,dt = \delta \int_t \left(E_k - \Pi^{int} - \Pi^{ext}\right) dt = 0. \tag{7.64}$$

In the general case, the kinetic energy $E_k = E_k(q, \dot{q})$ depends on some arbitrary variable q and its time derivative $\dot{q}$ so that using partial integration it can be shown that its variation has the form

$$\delta \int_t E_k(q, \dot{q})\,dt = \int_t \delta q \left(-\frac{\partial}{\partial t}\left(\frac{\partial E_k}{\partial \dot{q}}\right) + \frac{\partial E_k}{\partial q}\right) dt \tag{7.65}$$

while for the standard type of kinetic energy and its derivatives

$$E_k = \frac{1}{2}\int_\Omega \rho\,\dot{\boldsymbol{u}}^T\cdot\dot{\boldsymbol{u}}\,dv, \qquad \frac{\partial}{\partial t}\left(\frac{\partial E_k}{\partial \dot{\boldsymbol{u}}}\right) = \int_\Omega \rho\,\ddot{\boldsymbol{u}}\,dv, \qquad \frac{\partial E_k}{\partial \boldsymbol{u}} = 0, \tag{7.66}$$

variation (7.65) becomes

$$\delta \int_t E_k(\dot{\boldsymbol{u}})\,dt = -\int_t\int_\Omega \rho\,\delta\boldsymbol{u}^T\cdot\ddot{\boldsymbol{u}}\,dv\,dt = \omega^2 \int_t\int_\Omega \rho\,\delta\boldsymbol{u}^T\cdot\boldsymbol{u}\,dv\,dt. \tag{7.67}$$

Note that in the case of harmonic excitation, which only will be considered in the rest of the work, each of the terms of (7.64) contains the exponential function $e^{i\omega t}$ as a multiplier. Consequently this function and the complete time integration in (7.64) can be canceled. Assuming that kinetic energy depends only on translatory and not on angular velocities, a reduced approximation can be used instead of approximation (7.57)

$$\begin{aligned} &\boldsymbol{u} = \boldsymbol{N}\cdot\hat{\boldsymbol{a}}^{me}, \quad \boldsymbol{u} = \left\{\begin{array}{cc} u & v \quad w \end{array}\right\}^T, \\ &\hat{\boldsymbol{a}}_i^m = \left\{\begin{array}{ccccc} \hat{u}_i & \hat{v}_i & \hat{\theta}_{zi} & \hat{w}_i & \hat{\theta}_{xi} \quad \hat{\theta}_{yi} \end{array}\right\}^T. \end{aligned} \tag{7.68}$$

After substitution in (7.67) this yields

$$\int_{\Omega^e} \rho(\delta\boldsymbol{u}^e)^T\cdot\ddot{\boldsymbol{u}}^e\,dv = -\omega^2(\delta\hat{\boldsymbol{a}}^e)^T\cdot\left(\int_{\Omega^e}\rho\,\boldsymbol{N}^T\cdot\boldsymbol{N}dv\right)\cdot\hat{\boldsymbol{a}}^e, \tag{7.69}$$

where Ω^e is the volume of an element, and the integral expression represents a consistent mass matrix

$$\boldsymbol{M}^e = \int_{\Omega^e}\rho\,\boldsymbol{N}^T\cdot\boldsymbol{N}dv. \tag{7.70}$$

Taking into account the results from section 7.4.2 considering the potential energy, the equation of motion for one shell element becomes

$$\left(-\omega^2\boldsymbol{M}^e + \boldsymbol{K}^e\right)\cdot\hat{\boldsymbol{a}}^{me} = \boldsymbol{f}^e. \tag{7.71}$$

7.4.4 Extension to the complex domain

Chapter 7.4.1 already mentioned the need for analysis in the complex domain due to the periodic excitation and the influence of damping. It has also already been mentioned that the solution (7.38) belongs to this domain so that, in the scope of FEM, instead of (7.57) and (7.68), an extended approximation is needed

$$\boldsymbol{u}_c^m = \boldsymbol{N}_c^m \cdot \hat{\boldsymbol{a}}_c^{me}, \qquad \boldsymbol{u}_c^m = \boldsymbol{u}^{mR} + i\boldsymbol{u}^{mI}, \tag{7.72}$$

$$\boldsymbol{u}_c = \boldsymbol{N}_c \cdot \hat{\boldsymbol{a}}_c^{me}, \qquad \boldsymbol{u}_c = \boldsymbol{u}^R + i\boldsymbol{u}^I, \tag{7.73}$$

Here the index c is taken to emphasize that the search is now for the complex solution, and the following notation is introduced

$$\boldsymbol{N}_c^m = \begin{bmatrix} \boldsymbol{N}^m & 0 \\ 0 & \boldsymbol{N}^m \end{bmatrix}, \qquad \boldsymbol{N}_c = \begin{bmatrix} \boldsymbol{N} & 0 \\ 0 & \boldsymbol{N} \end{bmatrix} \tag{7.74}$$

$$\hat{\boldsymbol{a}}_c^{me} = \left\{ \; (\hat{\boldsymbol{a}}^{eR})^T \quad i(\hat{\boldsymbol{a}}^{eI})^T \; \right\}^T, \tag{7.75}$$

$$\begin{aligned} \hat{\boldsymbol{a}}_i^R \;\in\; \hat{\boldsymbol{a}}^{eR}, \quad (\hat{\boldsymbol{a}}_i^R)^T &= \{\, \hat{u}_i^R \;\; \hat{v}_i^R \;\; \hat{\theta}_{zi}^R \;\; \hat{w}_i^R \;\; \hat{\theta}_{xi}^R \;\; \hat{\theta}_{yi}^R \,\}, \\ \hat{\boldsymbol{a}}_i^I \;\in\; \hat{\boldsymbol{a}}^{eI}, \quad (\hat{\boldsymbol{a}}_i^I)^T &= \{\, \hat{u}_i^I \;\; \hat{v}_i^I \;\; \hat{\theta}_{zi}^I \;\; \hat{w}_i^I \;\; \hat{\theta}_{xi}^I \;\; \hat{\theta}_{yi}^I \,\}. \end{aligned} \tag{7.76}$$

Another important observation is that the parameters of viscoelastic materials also belong to the complex domain (Ch.7.2), and that they can be written in the form

$$K = K^R + iK^I, \qquad \mu = \mu^R + i\mu^I \tag{7.77}$$

where the imaginary parts in the case of bone material have to be calculated dependent on logarithmic decrement δ according to

$$K^I = \frac{\delta}{\pi} K^R, \qquad \mu^I = \frac{\delta}{\pi} \mu^R. \tag{7.78}$$

Using standard relations between the material parameters and the previous definitions of bulk and shear modulus, it is easy to show that similar expressions are valid for Young's modulus

$$E = E^R + iE^I, \qquad E^I = \frac{\delta}{\pi} E^R \tag{7.79}$$

while in this special case, Poisson's ratio only has the real part $\nu = \nu^R$. The complex form of the material parameters also yields the complex form of the elasticity tensor

$$\boldsymbol{C}_c = \begin{bmatrix} \boldsymbol{C}^R & i\boldsymbol{C}^I \\ i\boldsymbol{C}^I & \boldsymbol{C}^R \end{bmatrix} \tag{7.80}$$

whose submatrices $\boldsymbol{C}^R, \boldsymbol{C}^I$ have to be calculated using (7.48)a, (7.53)a, (7.59)b

$$\boldsymbol{C}^R = \boldsymbol{C}(E^R, \nu), \qquad \boldsymbol{C}^I = \boldsymbol{C}(E^I, \nu). \tag{7.81}$$

Bearing in mind (7.72)-(7.81), a procedure similar to that described in the previous sections leads to the equation of motion

$$\left(-\omega^2 \boldsymbol{M}_c^e + \boldsymbol{K}_c^e\right) \cdot \hat{\boldsymbol{a}}_c^{me} = \boldsymbol{f}_c^e, \tag{7.82}$$

where consistent mass matrix M_c^e and stiffness matrix K_c^e are

$$M_c^e = \int_{\Omega^e} \rho N_c^T \cdot N_c \, dv = \begin{bmatrix} M^{eR} & 0 \\ 0 & M^{eI} \end{bmatrix}, \tag{7.83}$$

$$K_c^e = \int_{\mathcal{A}^e} (B_c^m)^T \cdot \mathcal{C} \cdot B_c^m \, da = \begin{bmatrix} K^{eR} & iK^{eI} \\ iK^{eI} & K^{eR} \end{bmatrix} \tag{7.84}$$

and where the extended operator B_c^m is used

$$B_c^m = \begin{bmatrix} B^m & 0 \\ 0 & B^m \end{bmatrix}. \tag{7.85}$$

Interchanging the position of rows and columns, DOFs belonging to the same node can be merged so that the element vector of DOFs $\hat{a}^{*e}$ consists of nodal vectors

$$\hat{a}_i^* = \left\{ (\hat{a}^{eR})^T \quad i(\hat{a}^{eI})^T \right\}^T, \tag{7.86}$$

$$(\hat{a}_i^R)^T = \{ \hat{u}_i^R \;\; \hat{v}_i^R \;\; \hat{w}_i^R \;\; \hat{\theta}_{xi}^R \;\; \hat{\theta}_{yi}^R \;\; \hat{\theta}_{zi}^R \}, \qquad (\hat{a}_i^I)^T = \{ \hat{u}_i^I \;\; \hat{v}_i^I \;\; \hat{w}_i^I \;\; \hat{\theta}_{xi}^I \;\; \hat{\theta}_{yi}^I \;\; \hat{\theta}_{zi}^I \}.$$

This is the standard way of arranging DOFs of an element, in which case (7.82) becomes

$$\left(-\omega^2 M^{*e} + K^{*e}\right) \cdot \hat{a}^{*e} = f^{*e}, \tag{7.87}$$

and the process of assembling over all of the elements leads to the complete system of algebraic equations

$$\left(-\omega^2 M^* + K^*\right) \cdot a^* = f^*. \tag{7.88}$$

7.4.5 Modeling of the fluid phase

In contrast to the solid part of the RVE where the application of shell elements was appropriate due to the the thin-wall structure, a cubic element with eight nodes is assumed for modeling the fluid phase (Fig. 7.6).

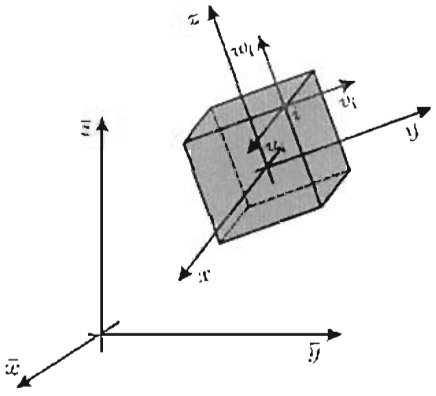

Figure 7.6: Standard eight-node cubic element.

The standard DOFs of this element are displacements in the directions of the axis of the local coordinate system xyz, and the FEM approximation is defined in the form

$$u = N \cdot \hat{a}, \quad u = \{u \quad v \quad w\}^T, \quad \hat{a}_i = \{\hat{u}_i \quad \hat{v}_i \quad \hat{w}_i\}^T, \tag{7.89}$$

where N is a matrix dependent on shape functions of the cubic element [6, 49, 53]. As this again requires an analysis in the complex domain, the approximation (7.89) has to be extended. Assuming that the real and imaginary DOFs of an element are grouped together, this can be done as follows

$$\boldsymbol{u}_c = \boldsymbol{N}_c \cdot \hat{\boldsymbol{a}}_c^e, \qquad \boldsymbol{u}_c = \boldsymbol{u}^R + i\boldsymbol{u}^I, \tag{7.90}$$

$$\boldsymbol{N}_c = \begin{bmatrix} \boldsymbol{N} & 0 \\ 0 & \boldsymbol{N} \end{bmatrix}, \qquad \hat{\boldsymbol{a}}_c^e = \left\{ \; (\hat{\boldsymbol{a}}^{eR})^T \quad i(\hat{\boldsymbol{a}}^{eI})^T \; \right\}^T, \tag{7.91}$$

$$\begin{aligned} \hat{\boldsymbol{a}}_i^R \;\in\; \hat{\boldsymbol{a}}^{eR}, \qquad & \hat{\boldsymbol{a}}_i^R \;=\; \{\, \hat{u}_i^R \quad \hat{v}_i^R \quad \hat{w}_i^R \,\}^T, \\ \hat{\boldsymbol{a}}_i^I \;\in\; \hat{\boldsymbol{a}}^{eI}, \qquad & \hat{\boldsymbol{a}}_i^I \;=\; \{\, \hat{u}_i^I \quad \hat{v}_i^I \quad \hat{w}_i^I \,\}^T. \end{aligned} \tag{7.92}$$

Furthermore, if the constitutive law (7.43) is written in the matrix form

$$\boldsymbol{\sigma}_c = \boldsymbol{C}_c \cdot \boldsymbol{\epsilon}_c \tag{7.93}$$

where $\boldsymbol{C}_c$ denotes complex elasticity matrix of the type (7.80) with submatrices

$$\boldsymbol{C}^R = \begin{bmatrix} c^2\rho & c^2\rho & c^2\rho & 0 & 0 & 0 \\ c^2\rho & c^2\rho & c^2\rho & 0 & 0 & 0 \\ c^2\rho & c^2\rho & c^2\rho & 0 & 0 & 0 \\ 0 & 0 & 0 & 0 & 0 & 0 \\ 0 & 0 & 0 & 0 & 0 & 0 \\ 0 & 0 & 0 & 0 & 0 & 0 \end{bmatrix}, \tag{7.94}$$

$$\boldsymbol{C}^I = \begin{bmatrix} 2\omega\eta + \omega\xi & \omega\xi & \omega\xi & 0 & 0 & 0 \\ \omega\xi & 2\omega\eta + \omega\xi & \omega\xi & 0 & 0 & 0 \\ \omega\xi & \omega\xi & 2\omega\eta + \omega\xi & 0 & 0 & 0 \\ 0 & 0 & 0 & \omega\eta & 0 & 0 \\ 0 & 0 & 0 & 0 & \omega\eta & 0 \\ 0 & 0 & 0 & 0 & 0 & \omega\eta \end{bmatrix} \tag{7.95}$$

the Lagrangean of the cubic element becomes

$$L = \frac{1}{2}\int_\Omega \rho\, \dot{\boldsymbol{u}}_c^T \cdot \dot{\boldsymbol{u}}_c \, dv - \frac{1}{2}\int_\Omega \boldsymbol{\epsilon}_c \cdot \boldsymbol{C}_c \cdot \boldsymbol{\epsilon}_c \, dv - \Pi^{ext} \tag{7.96}$$

and its minimization (see chapter 7.4.3) yields the equation

$$-\omega^2 \int_\Omega \rho\, \delta\boldsymbol{u}_c^T \cdot \boldsymbol{u}_c \, dv + \int_\Omega \delta\boldsymbol{u}_c^T \cdot \boldsymbol{L}_c^T \cdot \boldsymbol{C}_c \cdot \boldsymbol{L}_c \cdot \boldsymbol{u}_c \; dv + \delta\Pi^{ext} = 0, \tag{7.97}$$

where $\boldsymbol{L}_c$ represents the differential operator for the three-dimensional case

$$\boldsymbol{L}_c = \begin{bmatrix} \boldsymbol{L} & 0 \\ 0 & \boldsymbol{L} \end{bmatrix}, \qquad \boldsymbol{L} = \begin{bmatrix} \partial_x & 0 & 0 & \partial_y & 0 & \partial_z \\ 0 & \partial_y & 0 & \partial_x & \partial_z & \partial_x \\ 0 & 0 & \partial_z & 0 & \partial_y & 0 \end{bmatrix}^T. \tag{7.98}$$

The relation (7.97) for one element and after introduction of approximation (7.90) becomes

$$-\omega^2(\delta\hat{\boldsymbol{a}}_c^e)^T \cdot \left(\int_{\Omega^e} \rho \boldsymbol{N}_c^T \cdot \boldsymbol{N}_c \, dv \right) \cdot \hat{\boldsymbol{a}}_c^e + (\delta\hat{\boldsymbol{a}}_c^e)^T \cdot \left(\int_{\Omega^e} \boldsymbol{N}_c^T \cdot \boldsymbol{L}_c^T \cdot \boldsymbol{C}_c \cdot \boldsymbol{L}_c \cdot \boldsymbol{N}_c \, dv \right) \cdot \hat{\boldsymbol{a}}_c^e + \delta\Pi^{e,ext} = 0$$

yielding complex equation of motion

$$(-\omega^2 \boldsymbol{M}_c^e + \boldsymbol{K}_c^e) \cdot \hat{\boldsymbol{a}}_c^e = \boldsymbol{f}_c^e \tag{7.99}$$

with mass and stiffness matrix of the form

$$\boldsymbol{M}_c^e = \int_{\Omega^e} \rho \boldsymbol{N}_c^T \cdot \boldsymbol{N}_c \, dv = \begin{bmatrix} \boldsymbol{M}^e & 0 \\ 0 & \boldsymbol{M}^e \end{bmatrix}, \tag{7.100}$$

$$\boldsymbol{K}_c^e = \int_{\Omega^e} \boldsymbol{N}_c^T \cdot \boldsymbol{L}_c^T \cdot \boldsymbol{C}_c \cdot \boldsymbol{L}_c \cdot \boldsymbol{N}_c \, dv = \begin{bmatrix} \boldsymbol{K}^{eR} & i\boldsymbol{K}^{el} \\ i\boldsymbol{K}^{el} & \boldsymbol{K}^{eR} \end{bmatrix}. \tag{7.101}$$

By rearranging the order of DOFs and by the process of assembling, the final system of equations becomes

$$\left(-\omega^2 \boldsymbol{M}^* + \boldsymbol{K}^*\right) \cdot \boldsymbol{a}^* = \boldsymbol{f}^* \tag{7.102}$$

where the real and imaginary DOFs of one node are grouped together

$$\boldsymbol{a}_j \in \boldsymbol{a}, \quad \boldsymbol{a}_i = \left\{ \hat{u}_j^R \quad \hat{v}_j^R \quad \hat{w}_j^R \quad i\hat{u}_j^I \quad i\hat{v}_j^I \quad i\hat{w}_i^I \right\}^T. \tag{7.103}$$

In the end it is important to stress that although this section partly uses the same notation as before, the meaning of the symbols for cubic elements differs mostly from those for shell elements.

For the sake of clarity the equations (7.88) and (7.102), necessary for later work, will be written in the form

$$\left(-\omega^2 \boldsymbol{M}_s^* + \boldsymbol{K}_s^*\right) \cdot \boldsymbol{a}_s^* = \boldsymbol{f}_s^*, \tag{7.104}$$

$$\left(-\omega^2 \boldsymbol{M}_f^* + \boldsymbol{K}_f^*\right) \cdot \boldsymbol{a}_f^* = \boldsymbol{f}_f^*, \tag{7.105}$$

where indices s and f are taken to distinguish expressions related to the solid and fluid phases respectively.

7.4.6 Problem formulation at microlevel

Typically for a homogenization method, the purpose of the computations at microscale is to determine effective material tensor of heterogeneous material $\bar{\boldsymbol{C}}$ in which case the effective constitutive law can be written as follows

$$\bar{\boldsymbol{\sigma}} = \bar{\boldsymbol{C}} : \bar{\boldsymbol{\epsilon}}. \tag{7.106}$$

In the comparison with standard formulation described in the previous chapters, the difference is that equations defining the problem at microlevel depend on microfluctuations $\tilde{\boldsymbol{u}}_c$ and consequently on nodal microvariables $\tilde{\boldsymbol{a}}^*$, and that the residual depends on strain tensor $\bar{\boldsymbol{\epsilon}}$ calculated at macrolevel

$$\left(-\omega^2 \boldsymbol{M}_s^* + \boldsymbol{K}_s^*\right) \cdot \tilde{\boldsymbol{a}}_s^* = \boldsymbol{f}_s^*(\bar{\boldsymbol{\epsilon}}), \tag{7.107}$$

$$\left(-\omega^2 \boldsymbol{M}_f^* + \boldsymbol{K}_f^*\right) \cdot \tilde{\boldsymbol{a}}_f^* = \boldsymbol{f}_f^*(\bar{\boldsymbol{\epsilon}}). \tag{7.108}$$

The coupling condition on the interface of materials affects the microfluctuations

$$[\tilde{\boldsymbol{u}}] = 0 \quad \text{on} \quad \Gamma = \Omega_s \cup \Omega_f \tag{7.109}$$

and on the surface of RVE additionally periodic boundary conditions on the periodic boundary $\partial\Omega$ have to be satisfied

$$\tilde{\boldsymbol{u}}^+ = \tilde{\boldsymbol{u}}^- \quad \text{on} \quad \partial\Omega. \tag{7.110}$$

Recall that all of the previous equations deal with complex quantities. The final results at microscale are stresses whose average over the volume of RVE yields macroscopic stress $\bar{\boldsymbol{\sigma}}$ necessary for the numerical calculation of elasticity tensor defined by the expression

$$\bar{\boldsymbol{C}} = \frac{\partial \bar{\boldsymbol{\sigma}}}{\partial \bar{\boldsymbol{\epsilon}}}. \tag{7.111}$$

7.5 Effective behavior of cancellous bone

7.5.1 Calculation of the effective elasticity tensors

The interrogation of the material properties of the cancellous bone assumes the RVE shown in Figure 7.7. Its size is in the order of millimeters and its geometry is determined by three parameters: side length a, wall width b and wall thickness d presented in Figure 7.7a. Figures 7.7b,c show the geometry and discretization of the fluid phase and of the complete RVE.

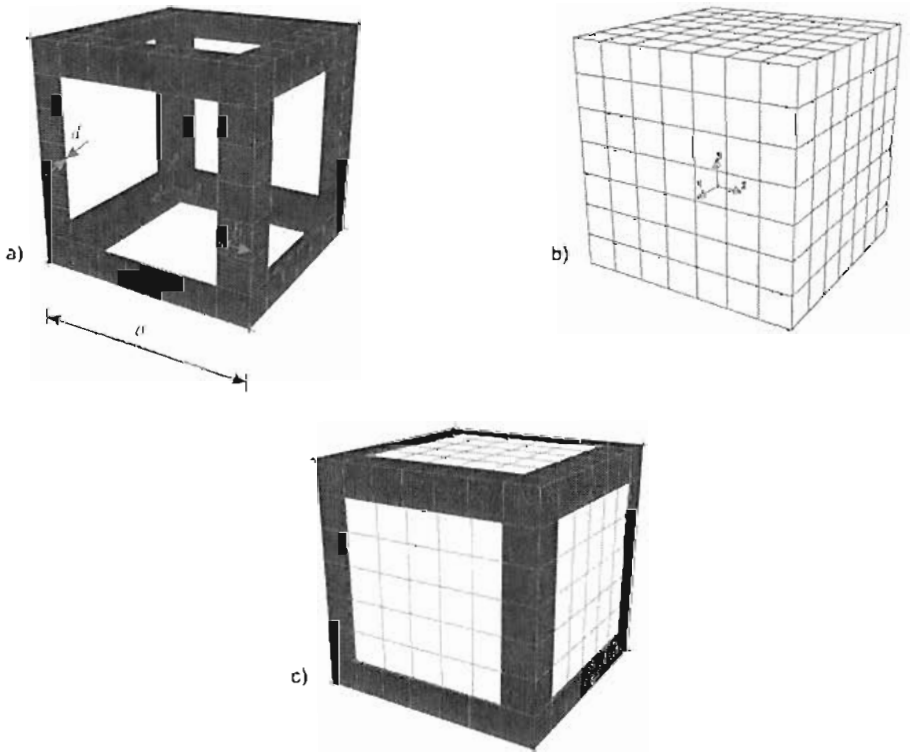

Figure 7.7: Geometry and discretization of: a) solid phase, b) fluid phase, c) complete RVE.

The material behavior of both phases is determined by the parameters given in Table 7.2 and by the constitutive laws explained in chapter 7.4.1. Additionally, the logarithmic decrement $\delta = 0.1$ is chosen corresponding to the motion of sound through the bone material. As the volume strain rate of the fluid can be neglected, the viscosity coefficient ξ is taken as zero. In this stage for all of the calculations, it is assumed that sound excitation has a frequency $\omega = 100\text{kHz}$.

As the process of osteoporosis manifests itself through the loss of solid material, the idea of the analysis is to study the change in effective material tensor of cancellous bone dependent on change in the width and thickness of the solid wall. To this end, two series of tests are carried out for the RVE in the form of unit cube. In one series, the thickness of the solid wall is fixed at $d = 0.1\text{mm}$, and in the second one at $d = 0.05\text{mm}$. In both series, the width of the wall decreases from 0.25 to 0.125mm. According to the procedure summarized in 7.4.6, the effective elasticity tensors for materials with different microstructures are calculated and some illustrative examples are listed below.

a=1mm d=0.1mm b=a/4 V=1.45mm^3
material tensor [N/mm^2]

5162.17	1874.21	1874.21	0.00	0.00	0.00	117.241	13.641	13.641	0.001	0.001	0.001
1874.21	5162.17	1874.21	0.00	0.00	0.00	13.641	117.241	13.641	0.001	0.001	0.001
1874.21	1874.21	5162.17	0.00	0.00	0.00	13.641	13.641	117.241	0.001	0.001	0.001
0.00	0.00	0.00	477.82	0.00	0.00	0.001	0.001	0.001	15.201	0.001	0.001
0.00	0.00	0.00	0.00	477.82	0.00	0.001	0.001	0.001	0.001	15.201	0.001
0.00	0.00	0.00	0.00	0.00	477.82	0.001	0.001	0.001	0.001	0.001	15.201
117.241	13.641	13.641	0.001	0.001	0.001	5162.17	1874.21	1874.21	0.00	0.00	0.00
13.641	117.241	13.641	0.001	0.001	0.001	1874.21	5162.17	1874.21	0.00	0.00	0.00
13.641	13.641	117.241	0.001	0.001	0.001	1874.21	1874.21	5162.17	0.00	0.00	0.00
0.001	0.001	0.001	15.201	0.001	0.001	0.00	0.00	0.00	477.82	0.00	0.00
0.001	0.001	0.001	0.001	15.201	0.001	0.00	0.00	0.00	0.00	477.82	0.00
0.001	0.001	0.001	0.001	0.001	15.201	0.00	0.00	0.00	0.00	0.00	477.82

a=1mm d=0.1mm b=a/5 V=1.384mm^3
material tensor [N/mm^2]

4470.27	1753.46	1753.46	0.00	0.00	0.00	93.621	7.821	7.821	0.001	0.001	0.001
1753.46	4470.27	1753.46	0.00	0.00	0.00	7.821	93.621	7.821	0.001	0.001	0.001
1753.46	1753.46	4470.27	0.00	0.00	0.00	7.821	7.821	93.621	0.001	0.001	0.001
0.00	0.00	0.00	261.28	0.00	0.00	0.001	0.001	0.001	8.461	0.001	0.001
0.00	0.00	0.00	0.00	261.28	0.00	0.001	0.001	0.001	0.001	8.461	0.001
0.00	0.00	0.00	0.00	0.00	261.28	0.001	0.001	0.001	0.001	0.001	8.461
93.621	7.821	7.821	0.001	0.001	0.001	4470.27	1753.46	1753.46	0.00	0.00	0.00
7.821	93.621	7.821	0.001	0.001	0.001	1753.46	4470.27	1753.46	0.00	0.00	0.00
7.821	7.821	93.621	0.001	0.001	0.001	1753.46	1753.46	4470.27	0.00	0.00	0.00
0.001	0.00	0.001	8.461	0.001	0.001	0.00	0.00	0.00	261.28	0.00	0.00
0.001	0.00	0.001	0.001	8.461	0.001	0.00	0.00	0.00	0.00	261.28	0.00
0.001	0.00	0.001	0.001	0.001	8.461	0.00	0.00	0.00	0.00	0.00	261.28

a=1mm d=0.1mm b=a/6 V=1.3333mm^3
material tensor [N/mm^2]

4039.85	1717.16	1717.16	0.00	0.00	0.00	78.881	5.341	5.341	0.001	0.001	0.001
1717.16	4039.85	1717.16	0.00	0.00	0.00	5.341	78.881	5.341	0.001	0.001	0.001
1717.16	1717.16	4039.85	0.00	0.00	0.00	5.341	5.341	78.881	0.001	0.001	0.001
0.00	0.00	0.00	160.92	0.00	0.00	0.001	0.001	0.001	5.331	0.001	0.001
0.00	0.00	0.00	0.00	160.92	0.00	0.001	0.001	0.001	0.001	5.331	0.001
0.00	0.00	0.00	0.00	0.00	160.92	0.001	0.001	0.001	0.001	0.001	5.331
78.881	5.341	5.341	0.001	0.001	0.001	4039.85	1717.16	1717.16	0.00	0.00	0.00
5.341	78.881	5.341	0.001	0.001	0.001	1717.16	4039.85	1717.16	0.00	0.00	0.00
5.341	5.341	78.881	0.001	0.001	0.001	1717.16	1717.16	4039.85	0.00	0.00	0.00
0.001	0.001	0.001	5.331	0.001	0.001	0.00	0.00	0.00	160.92	0.00	0.00
0.001	0.001	0.001	0.001	5.331	0.001	0.00	0.00	0.00	0.00	160.92	0.00
0.001	0.001	0.001	0.001	0.001	5.331	0.00	0.00	0.00	0.00	0.00	160.92

a=1mm d=0.1mm b=a/7 V=1.294mm^3
material tensor [N/mm^2]

3741.16	1706.47	1706.47	0.00	0.00	0.00	68.421	3.861	3.861	0.001	0.001	0.001
1706.47	3741.16	1706.47	0.00	0.00	0.00	3.861	68.421	3.861	0.001	0.001	0.001
1706.47	1706.47	3741.16	0.00	0.00	0.00	3.861	3.861	68.421	0.001	0.001	0.001
0.00	0.00	0.00	110.41	0.00	0.00	0.001	0.001	0.001	3.761	0.001	0.001
0.00	0.00	0.00	0.00	110.41	0.00	0.001	0.001	0.001	0.001	3.761	0.001
0.00	0.00	0.00	0.00	0.00	110.41	0.001	0.001	0.001	0.001	0.001	3.761
68.421	3.861	3.861	0.00	0.001	0.001	3741.16	1706.47	1706.47	0.00	0.00	0.00
3.861	68.421	3.861	0.001	0.001	0.001	1706.47	3741.16	1706.47	0.00	0.00	0.00
3.861	3.861	68.421	0.001	0.001	0.001	1706.47	1706.47	3741.16	0.00	0.00	0.00
0.001	0.001	0.001	3.761	0.001	0.001	0.00	0.00	0.00	110.41	0.00	0.00
0.001	0.001	0.001	0.001	3.761	0.001	0.00	0.00	0.00	0.00	110.41	0.00
0.001	0.001	0.001	0.001	0.001	3.761	0.00	0.00	0.00	0.00	0.00	110.41

a=1mm d=0.1mm b=a/8 V=1.262mm^3
material tensor [N/mm^2]

3521.68	1708.14	1708.14	0.00	0.00	0.00	60.581	2.941	2.941	0.001	0.001	0.001
1708.14	3521.68	1708.14	0.00	0.00	0.00	2.941	60.581	2.941	0.001	0.001	0.001
1708.14	1708.14	3521.68	0.00	0.00	0.00	2.941	2.941	60.581	0.001	0.001	0.001
0.00	0.00	0.00	81.84	0.00	0.00	0.001	0.001	0.001	2.871	0.001	0.001
0.00	0.00	0.00	0.00	81.84	0.00	0.001	0.001	0.001	0.001	2.871	0.001
0.00	0.00	0.00	0.00	0.00	81.84	0.001	0.001	0.001	0.001	0.001	2.871
60.581	2.941	2.941	0.001	0.001	0.001	3521.68	1708.14	1708.14	0.00	0.00	0.00
2.941	60.581	2.941	0.001	0.001	0.001	1708.14	3521.68	1708.14	0.00	0.00	0.00
2.941	2.941	60.581	0.001	0.001	0.001	1708.14	1708.14	3521.68	0.00	0.00	0.00
0.001	0.001	0.001	2.871	0.001	0.001	0.00	0.00	0.00	81.84	0.00	0.00
0.001	0.001	0.001	0.001	2.871	0.001	0.00	0.00	0.00	0.00	81.84	0.00
0.001	0.001	0.001	0.001	0.001	2.871	0.00	0.00	0.00	0.00	0.00	81.84

Figure 7.8: Effective elasticity tensors for the RVE with unity side length and wall thickness 0.1mm. The width of the wall is in the range 0.25-0.125mm.

a=1mm d=0.05mm b=a/4 V=1.225mm^3
material tensor [N/mm^2]

3927.95	1959.50	1959.50	0.00	0.00	0.00	70.00i	8.49i	8.49i	0.00i	0.00i	0.00i
1959.50	3927.95	1959.50	0.00	0.00	0.00	8.49i	70.00i	8.49i	0.00i	0.00i	0.00i
1959.50	1959.50	3927.95	0.00	0.00	0.00	8.49i	8.49i	70.00i	0.00i	0.00i	0.00i
0.00	0.00	0.00	272.98	0.00	0.00	0.00i	0.00i	0.00i	8.73i	0.00i	0.00i
0.00	0.00	0.00	0.00	272.98	0.00	0.00i	0.00i	0.00i	0.00i	8.73i	0.00i
0.00	0.00	0.00	0.00	0.00	272.98	0.00i	0.00i	0.00i	0.00i	0.00i	8.73i
70.00i	8.49i	8.49i	0.00i	0.00i	0.00i	3927.95	1959.50	1959.50	0.00	0.00	0.00
8.49i	70.00i	8.49i	0.00i	0.00i	0.00i	1959.50	3927.95	1959.50	0.00	0.00	0.00
8.49i	8.49i	70.00i	0.00i	0.00i	0.00i	1959.50	1959.50	3927.95	0.00	0.00	0.00
0.00i	0.00i	0.00i	8.73i	0.00i	0.00i	0.00	0.00	0.00	272.98	0.00	0.00
0.00i	0.00i	0.00i	0.00i	8.73i	0.00i	0.00	0.00	0.00	0.00	272.98	0.00
0.00i	0.00i	0.00i	0.00i	0.00i	8.73i	0.00	0.00	0.00	0.00	0.00	272.98

a=1mm d=0.05mm b=a/5 V=1.192mm^3
material tensor [N/mm^2]

3883.07	1889.93	1889.93	0.00	0.00	0.00	54.84i	4.85i	4.85i	0.00i	0.00i	0.00i
1889.93	3883.07	1889.93	0.00	0.00	0.00	4.85i	54.84i	4.85i	0.00i	0.00i	0.00i
1889.93	1889.93	3883.07	0.00	0.00	0.00	4.85i	4.85i	54.84i	0.00i	0.00i	0.00i
0.00	0.00	0.00	136.42	0.00	0.00	0.00i	0.00i	0.00i	4.53i	0.00i	0.00i
0.00	0.00	0.00	0.00	136.42	0.00	0.00i	0.00i	0.00i	0.00i	4.53i	0.00i
0.00	0.00	0.00	0.00	0.00	136.42	0.00i	0.00i	0.00i	0.00i	0.00i	4.53i
54.84i	4.85i	4.85i	0.00i	0.00i	0.00i	3883.07	1889.93	1889.93	0.00	0.00	0.00
4.85i	54.84i	4.85i	0.00i	0.00i	0.00i	1889.93	3883.07	1889.93	0.00	0.00	0.00
4.85i	4.85i	54.84i	0.00i	0.00i	0.00i	1889.93	1889.93	3883.07	0.00	0.00	0.00
0.00i	0.00i	0.00i	4.53i	0.00i	0.00i	0.00	0.00	0.00	136.42	0.00	0.00
0.00i	0.00i	0.00i	0.00i	4.53i	0.00i	0.00	0.00	0.00	0.00	136.42	0.00
0.00i	0.00i	0.00i	0.00i	0.00i	4.53i	0.00	0.00	0.00	0.00	0.00	136.42

a=1mm d=0.05mm b=a/6 V=1.167mm^3
material tensor [N/mm^2]

3203.35	1865.10	1865.10	0.00	0.00	0.00	45.43i	3.25i	3.25i	0.00i	0.00i	0.00i
1865.10	3203.35	1865.10	0.00	0.00	0.00	3.25i	45.43i	3.25i	0.00i	0.00i	0.00i
1865.10	1865.10	3203.35	0.00	0.00	0.00	3.25i	3.25i	45.43i	0.00i	0.00i	0.00i
0.00	0.00	0.00	76.09	0.00	0.00	0.00i	0.00i	0.00i	2.68i	0.00i	0.00i
0.00	0.00	0.00	0.00	76.09	0.00	0.00i	0.00i	0.00i	0.00i	2.68i	0.00i
0.00	0.00	0.00	0.00	0.00	76.09	0.00i	0.00i	0.00i	0.00i	0.00i	2.68i
45.43i	3.25i	3.25i	0.00i	0.00i	0.00i	3203.35	1865.10	1865.10	0.00	0.00	0.00
3.25i	45.43i	3.25i	0.00i	0.00i	0.00i	1865.10	3203.35	1865.10	0.00	0.00	0.00
3.25i	3.25i	45.43i	0.00i	0.00i	0.00i	1865.10	1865.10	3203.35	0.00	0.00	0.00
0.00i	0.00i	0.00i	2.68i	0.00i	0.00i	0.00	0.00	0.00	76.09	0.00	0.00
0.00i	0.00i	0.00i	0.00i	2.68i	0.00i	0.00	0.00	0.00	0.00	76.09	0.00
0.00i	0.00i	0.00i	0.00i	0.00i	2.68i	0.00	0.00	0.00	0.00	0.00	76.09

a=1mm d=0.05mm b=a/7 V=1.147mm^3
material tensor [N/mm^2]

3011.36	1855.72	1855.72	0.00	0.00	0.00	38.88i	2.31i	2.31i	0.00i	0.00i	0.00i
1855.72	3011.36	1855.72	0.00	0.00	0.00	2.31i	38.88i	2.31i	0.00i	0.00i	0.00i
1855.72	1855.72	3011.36	0.00	0.00	0.00	2.31i	2.31i	38.88i	0.00i	0.00i	0.00i
0.00	0.00	0.00	47.68	0.00	0.00	0.00i	0.00i	0.00i	1.81i	0.00i	0.00i
0.00	0.00	0.00	0.00	47.68	0.00	0.00i	0.00i	0.00i	0.00i	1.81i	0.00i
0.00	0.00	0.00	0.00	0.00	47.68	0.00i	0.00i	0.00i	0.00i	0.00i	1.81i
38.88i	2.31i	2.31i	0.00i	0.00i	0.00i	3011.36	1855.72	1855.72	0.00	0.00	0.00
2.31i	38.88i	2.31i	0.00i	0.00i	0.00i	1855.72	3011.36	1855.72	0.00	0.00	0.00
2.31i	2.31i	38.88i	0.00i	0.00i	0.00i	1855.72	1855.72	3011.36	0.00	0.00	0.00
0.00i	0.00i	0.00i	1.81i	0.00i	0.00i	0.00	0.00	0.00	47.68	0.00	0.00
0.00i	0.00i	0.00i	0.00i	1.81i	0.00i	0.00	0.00	0.00	0.00	47.68	0.00
0.00i	0.00i	0.00i	0.00i	0.00i	1.81i	0.00	0.00	0.00	0.00	0.00	47.68

a=1mm d=0.05mm b=a/8 V=1.131mm^3
material tensor [N/mm^2]

2872.28	1854.45	1854.45	0.00	0.00	0.00	34.05i	1.74i	1.74i	0.00i	0.00i	0.00i
1854.45	2872.28	1854.45	0.00	0.00	0.00	1.74i	34.05i	1.74i	0.00i	0.00i	0.00i
1854.45	1854.45	2872.28	0.00	0.00	0.00	1.74i	1.74i	34.05i	0.00i	0.00i	0.00i
0.00	0.00	0.00	32.55	0.00	0.00	0.00i	0.00i	0.00i	1.33i	0.00i	0.00i
0.00	0.00	0.00	0.00	32.55	0.00	0.00i	0.00i	0.00i	0.00i	1.33i	0.00i
0.00	0.00	0.00	0.00	0.00	32.55	0.00i	0.00i	0.00i	0.00i	0.00	1.33i
34.05i	1.74i	1.74i	0.00i	0.00i	0.00i	2872.28	1854.45	1854.45	0.00	0.00	0.00
1.74i	34.05i	1.74i	0.00i	0.00i	0.00i	1854.45	2872.28	1854.45	0.00	0.00	0.00
1.74i	1.74i	34.05i	0.00i	0.00i	0.00i	1854.45	1854.45	2872.28	0.00	0.00	0.00
0.00i	0.00i	0.00i	1.33i	0.00i	0.00i	0.00	0.00	0.00	32.55	0.00	0.00
0.00i	0.00i	0.00i	0.00i	1.33i	0.00i	0.00	0.00	0.00	0.00	32.55	0.00
0.00i	0.00i	0.00i	0.00i	0.00i	1.33i	0.00	0.00	0.00	0.00	0.00	32.55

Figure 7.9: Effective elasticity tensors for the RVE with unity side length and wall thickness 0.05mm. The width of the wall is in the range 0.25-0.125mm.

The calculated material tensors belong to the complex domain (7.80), which means that they correspond to the effective viscoelastic behavior. Figure 7.10 shows the change in two terms of elasticity tensor (C_{11}, C_{12}) with respect to porosity $\beta = V_f/V$ where V_f represents the volume of fluid and V the total volume of RVE. A comparison of the same type is carried out for two terms of imaginary block of elasticity tensor which is shown in Figure 7.11. Similar behavior is noted in all cases: the terms of elasticity tensor gradually decrease with increasing porosity.

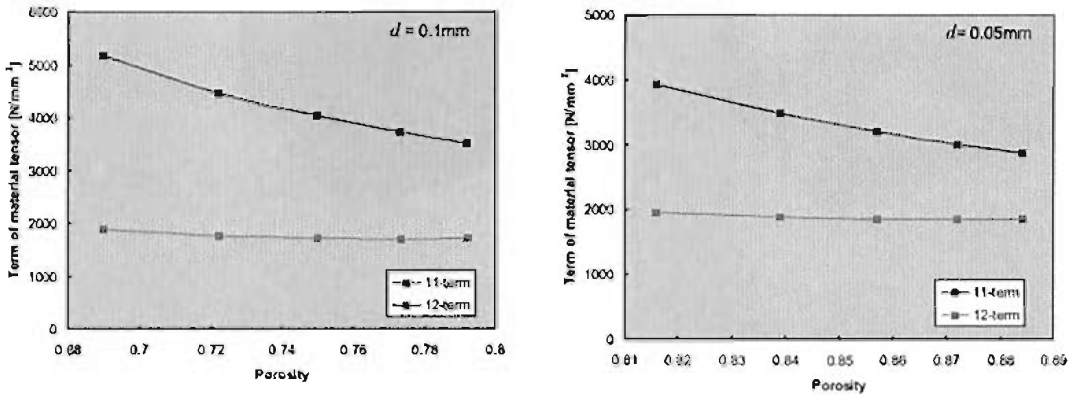

Figure 7.10: Change in the real terms C_{11} and C_{12} of the elasticity tensor with respect to increasing porosity. The solid wall thickness takes the values 0.1 and 0.05mm.

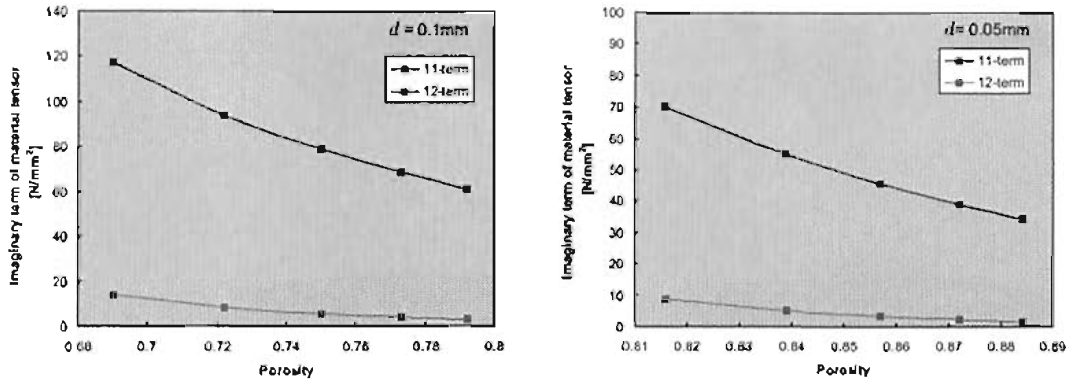

Figure 7.11: Change in the imaginary terms of the elasticity tensor C_{71} and C_{81} with respect to the increasing porosity for different thicknesses of the solid wall.

To digress slightly, it is recalled that an intermediate result of the calculations at microlevel is a distribution of the microfluctuations caused by macrostrain tensor $\bar{\varepsilon}$. Several examples of that distribution are shown in Figure 7.12, where it is interesting to note that Hill's periodic boundary conditions and coupling conditions between the phases are satisfied.

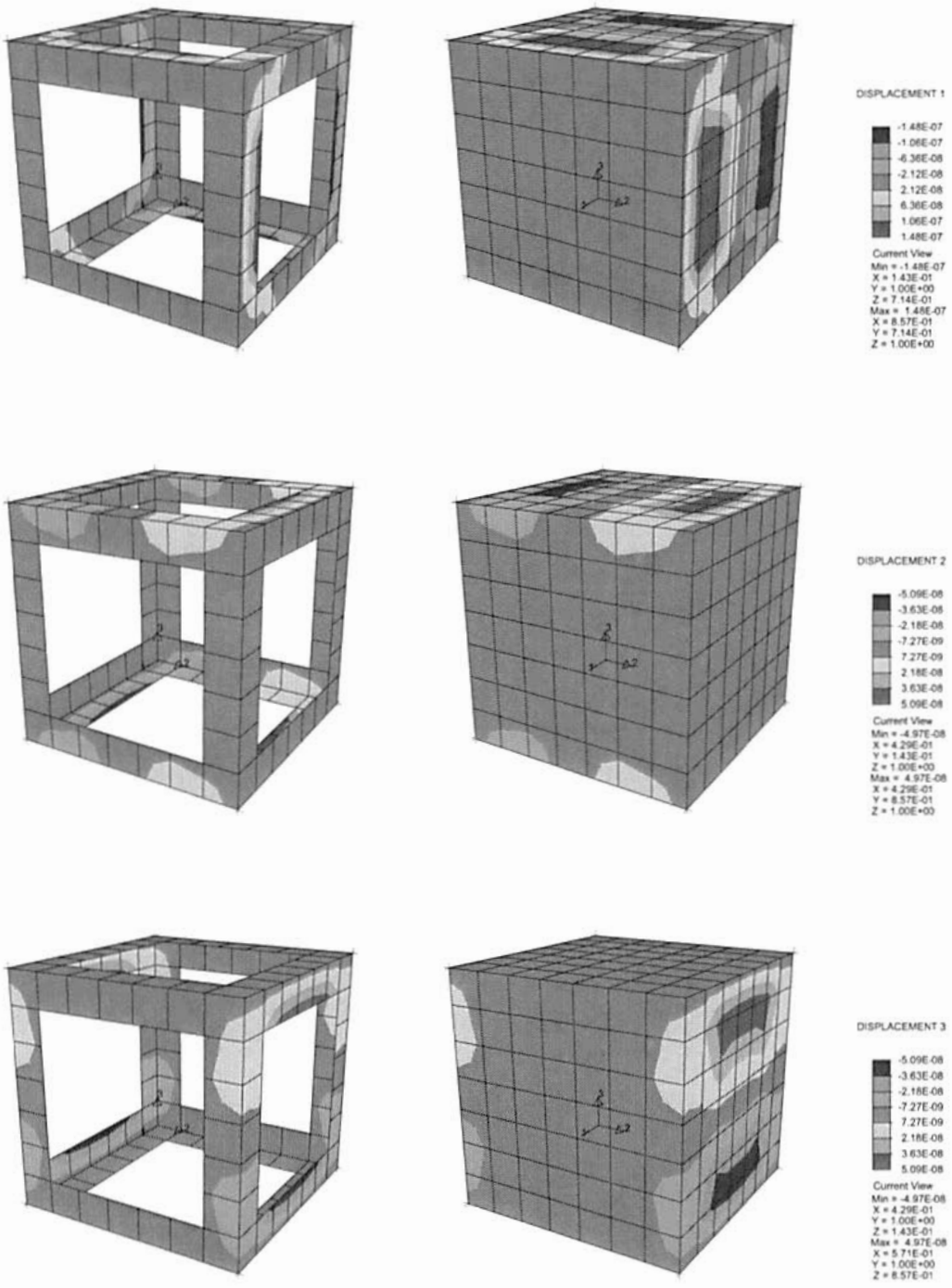

Figure 7.12: Distribution of the microfluctuations - examples of resulting calculations at microscale. Coupling conditions on the interface of phases and Hill's conditions on the boundary are satisfied.

Together with the already considered cases assuming that only the change in thickness and width of the wall influence the effective bone behavior, recent laboratory investigations have shown that one of the main reasons for decreasing bone strength is the disappearance of the complete solid walls (Fig. 7.13). This process automatically leads to increasing spans between the remaining walls, so that instead of a porosity of 72% and an average span of 0.47 mm, typical for the healthy bone, in the late stage of osteoporosis, the corresponding values reach 95% for porosity and 2.2 mm for average span.

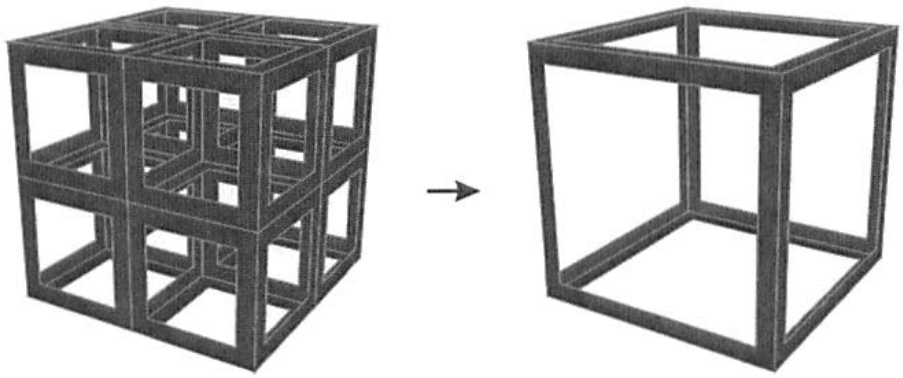

Figure 7.13: Strong bone resorption causes some walls to disappear, while increasing the span between remaining walls.

When interrogating the influence of the size of average span on the strength of the bone, a cubic RVE is again observed, but this time its side length is variable and has values in the range 0.47-2.2mm. The wall thickness is fixed at $d = 0.05$ mm and two cases of the wall width are considered. In one case its relation with the side length is given by $b = a/6$, and in the other case by $b = a/7$.

The change in two terms of elasticity tensor over side length and porosity is shown in Figure 7.14. Here, obviously, $\mathcal{C}_{11}$ gradually decreases and $\mathcal{C}_{12}$ gradually increases, but both of these values tend to the value $\mathcal{C}_{11} = \mathcal{C}_{12} = 2000\text{N/mm}^2$, which exactly corresponds to the case of pure marrow.

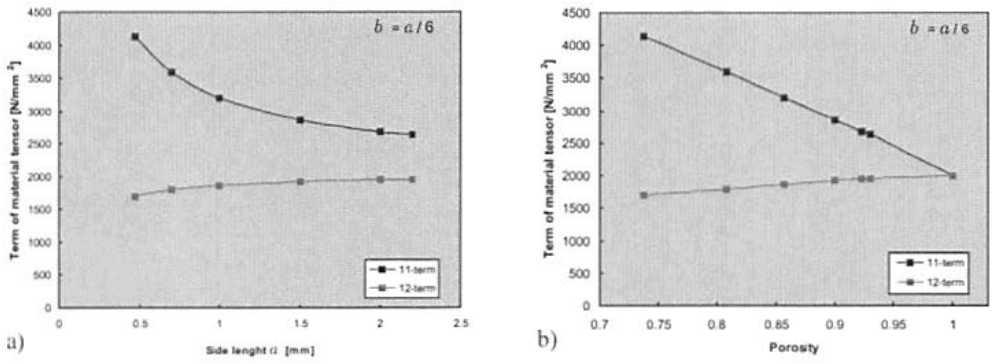

Figure 7.14: Change in terms $\mathcal{C}_{11}$ and $\mathcal{C}_{12}$ with increasing spans and corresponding porosity. The width of solid wall $b = a/6$.

The following section lists the effective elasticity tensors as the main results of calculations at microscale and for the case of increase in the side length of RVE.

a=0.470mm d=0.05mm b=a/6 V=0.1406mm^3 Vf=0.104mm^3 Vs=0.037mm^3
material tensor [N/mm^2]

4132.75	1701.13	1701.13	0.00	0.00	0.00	82.581	5.571	5.571	0.001	0.001	0.001
1701.13	4132.75	1701.13	0.00	0.00	0.00	5.571	82.581	5.571	0.001	0.001	0.001
1701.13	1701.13	4132.75	0.00	0.00	0.00	5.571	5.571	82.581	0.001	0.001	0.001
0.00	0.00	0.00	172.71	0.00	0.00	0.001	0.001	0.001	5.701	0.001	0.001
0.00	0.00	0.00	0.00	172.71	0.00	0.001	0.001	0.001	0.001	5.701	0.001
0.00	0.00	0.00	0.00	0.00	172.71	0.001	0.001	0.001	0.001	0.001	5.701
82.581	5.571	5.571	0.001	0.001	0.001	4132.75	1701.13	1701.13	0.00	0.00	0.00
5.571	82.581	5.571	0.001	0.001	0.001	1701.13	4132.75	1701.13	0.00	0.00	0.00
5.571	5.571	82.581	0.001	0.001	0.001	1701.13	1701.13	4132.75	0.00	0.00	0.00
0.001	0.001	0.001	5.701	0.001	0.001	0.00	0.00	0.00	172.71	0.00	0.00
0.001	0.001	0.001	0.001	5.701	0.001	0.00	0.00	0.00	0.00	172.71	0.00
0.001	0.001	0.001	0.001	0.001	5.701	0.00	0.00	0.00	0.00	0.00	172.71

a=0.700mm d=0.05mm b=a/6 V=0.4247mm^3 Vf=0.343mm^3 Vs=0.082mm^3
material tensor [N/mm^2]

3589.79	1797.35	1797.35	0.00	0.00	0.00	60.841	4.201	4.201	0.001	0.001	0.001
1797.35	3589.79	1797.35	0.00	0.00	0.00	4.201	60.841	4.201	0.001	0.001	0.001
1797.35	1797.35	3589.79	0.00	0.00	0.00	4.201	4.201	60.841	0.001	0.001	0.001
0.00	0.00	0.00	110.70	0.00	0.00	0.001	0.001	0.001	3.761	0.001	0.001
0.00	0.00	0.00	0.00	110.70	0.00	0.001	0.001	0.001	0.001	3.761	0.001
0.00	0.00	0.00	0.00	0.00	110.70	0.001	0.001	0.001	0.001	0.001	3.761
60.841	4.201	4.201	0.001	0.001	0.001	3589.79	1797.35	1797.35	0.00	0.001	0.00
4.201	60.841	4.201	0.001	0.001	0.001	1797.35	3589.79	1797.35	0.00	0.00	0.00
4.201	4.201	60.841	0.001	0.001	0.001	1797.35	1797.35	3589.79	0.00	0.00	0.00
0.001	0.001	0.001	3.761	0.001	0.001	0.00	0.00	0.00	110.70	0.00	0.00
0.001	0.001	0.001	0.001	3.761	0.001	0.00	0.00	0.00	0.00	110.70	0.00
0.001	0.001	0.001	0.001	0.001	3.761	0.00	0.00	0.00	0.00	0.00	110.70

a=1.000mm d=0.05mm b=a/6 V=1.167mm^3 Vf=1.000mm^3 Vs=0.167mm^3
material tensor [N/mm^2]

3203.35	1865.10	1865.10	0.00	0.00	0.00	45.431	3.251	3.251	0.001	0.001	0.001
1865.10	3203.35	1865.10	0.00	0.00	0.00	3.251	45.431	3.251	0.001	0.001	0.001
1865.10	1865.10	3203.35	0.00	0.00	0.00	3.251	3.251	45.431	0.001	0.001	0.001
0.00	0.00	0.00	76.10	0.00	0.00	0.001	0.001	0.001	2.681	0.001	0.001
0.00	0.00	0.00	0.00	76.10	0.00	0.001	0.001	0.001	0.001	2.681	0.001
0.00	0.00	0.00	0.00	0.00	76.10	0.001	0.001	0.001	0.001	0.001	2.681
45.431	3.251	3.251	0.001	0.001	0.001	3203.35	1865.10	1865.10	0.00	0.00	0.00
3.251	45.431	3.251	0.001	0.001	0.001	1865.10	3203.35	1865.10	0.00	0.00	0.00
3.251	3.251	45.431	0.001	0.001	0.001	1865.10	1865.10	3203.35	0.00	0.00	0.00
0.001	0.001	0.001	2.681	0.001	0.001	0.00	0.00	0.00	76.10	0.00	0.00
0.001	0.001	0.001	0.001	2.681	0.001	0.00	0.00	0.00	0.00	76.10	0.00
0.001	0.001	0.001	0.001	0.001	2.681	0.00	0.00	0.00	0.00	0.00	76.10

a=1.500mm d=0.05mm b=a/6 V=3.7525mm^3 Vf=3.375mm^3 Vs=0.3775mm^3
material tensor [N/mm^2]

2864.25	1920.41	1920.41	0.00	0.00	0.00	32.101	2.471	2.471	0.001	0.001	0.001
1920.41	2864.25	1920.41	0.00	0.00	0.00	2.471	32.101	2.471	0.001	0.001	0.001
1920.41	1920.41	2864.25	0.00	0.00	0.00	2.471	2.471	32.101	0.001	0.001	0.001
0.00	0.00	0.00	50.94	0.00	0.00	0.001	0.001	0.001	1.901	0.001	0.001
0.00	0.00	0.00	0.00	50.94	0.00	0.001	0.001	0.001	0.001	1.901	0.001
0.00	0.00	0.00	0.00	0.00	50.94	0.001	0.001	0.001	0.001	0.001	1.901
32.101	2.471	2.471	0.001	0.001	0.001	2864.25	1920.41	1920.41	0.00	0.001	0.00
2.471	32.101	2.471	0.001	0.001	0.001	1920.41	2864.25	1920.41	0.00	0.00	0.00
2.471	2.481	32.101	0.001	0.001	0.001	1920.41	1920.41	2864.25	0.00	0.00	0.00
0.001	0.001	0.001	1.901	0.001	0.001	0.00	0.00	0.00	50.94	0.00	0.00
0.001	0.001	0.001	0.001	1.901	0.001	0.00	0.00	0.00	0.00	50.94	0.00
0.001	0.001	0.001	0.001	0.001	1.901	0.00	0.00	0.00	0.00	0.00	50.94

a=2.200mm d=0.05mm b=a/6 V=11.455mm^3 Vf=10.648mm^3 Vs=0.806mm^3
material tensor [N/mm^2]

2630.74	1958.30	1958.30	0.00	0.00	0.00	22.971	1.951	1.951	0.001	0.001	0.001
1958.30	2630.74	1958.30	0.00	0.00	0.00	1.951	22.971	1.951	0.001	0.001	0.001
1958.30	1958.30	2630.74	0.00	0.00	0.00	1.951	1.951	22.971	0.001	0.001	0.001
0.00	0.00	0.00	35.55	0.00	0.00	0.001	0.001	0.001	1.421	0.001	0.001
0.00	0.00	0.00	0.00	35.55	0.00	0.001	0.001	0.001	0.001	1.421	0.001
0.00	0.00	0.00	0.00	0.00	35.55	0.001	0.001	0.001	0.001	0.001	1.421
22.971	1.951	1.951	0.001	0.001	0.001	2630.74	1958.30	1958.30	0.00	0.00	0.00
1.951	22.971	1.951	0.001	0.001	0.001	1958.30	2630.74	1958.30	0.00	0.00	0.00
1.951	1.951	22.971	0.001	0.001	0.001	1958.30	1958.30	2630.74	0.00	0.00	0.00
0.001	0.001	0.001	1.421	0.001	0.001	0.00	0.00	0.00	35.55	0.00	0.00
0.001	0.001	0.001	0.001	1.421	0.001	0.00	0.00	0.00	0.00	35.55	0.00
0.001	0.001	0.001	0.001	0.001	1.421	0.00	0.00	0.00	0.00	0.00	35.55

••• pure fluid•••
material tensor [N/mm^2]

2000.00	2000.00	2000.00	0.00	0.00	0.00	0.301	0.001	0.001	0.001	0.001	0.001
2000.00	2000.00	2000.00	0.00	0.00	0.00	0.001	0.301	0.001	0.001	0.001	0.001
2000.00	2000.00	2000.00	0.00	0.00	0.00	0.001	0.001	0.301	0.001	0.001	0.001
0.00	0.00	0.00	0.00	0.00	0.00	0.001	0.001	0.001	0.301	0.001	0.001
0.00	0.00	0.00	0.00	0.00	0.00	0.001	0.001	0.001	0.001	0.301	0.001
0.00	0.00	0.00	0.00	0.00	0.00	0.001	0.001	0.001	0.001	0.001	0.301
0.301	0.001	0.001	0.00	0.001	0.001	2000.00	2000.00	2000.00	0.00	0.00	0.00
0.001	0.301	0.001	0.001	0.001	0.001	2000.00	2000.00	2000.00	0.00	0.00	0.00
0.301	0.001	0.301	0.001	0.001	0.001	2000.00	2000.00	2000.00	0.00	0.00	0.00
0.001	0.001	0.001	0.301	0.001	0.001	0.00	0.00	0.00	0.00	0.00	0.00
0.001	0.001	0.001	0.001	0.301	0.001	0.00	0.00	0.00	0.00	0.00	0.00
0.001	0.001	0.001	0.001	0.001	0.301	0.00	0.00	0.00	0.00	0.00	0.00

Figure 7.15: Effective elasticity tensors for the RVE with the width of the solid wall $b=a/6$ and constant wall thickness 0.1mm. The side length of the RVE is in the range 0.47-2.2mm.

```
a=0.470mm   d=0.05mm   b=a/7   V=0.136mm^3   Vf=0.104mm^3   Vs=0.033mm^3
material tensor [N/mm^2]
  3822.45   1689.68   1689.68      0.00      0.00      0.00     71.721     4.041     4.041     0.001     0.001     0.001
  1689.68   3822.45   1689.68      0.00      0.00      0.00      4.041    71.721     4.041     0.001     0.001     0.001
  1689.68   1689.68   3822.45      0.00      0.00      0.00      4.041     4.041    71.721     0.001     0.001     0.001
     0.00      0.00      0.00    119.51      0.00      0.00      0.001     0.001     0.001     4.041     0.001     0.001
     0.00      0.00      0.00      0.00    119.51      0.00      0.001     0.001     0.001     0.001     4.041     0.001
     0.00      0.00      0.00      0.00      0.00    119.51      0.001     0.001     0.001     0.001     0.001     4.041
   71.721     4.041     4.041     0.001     0.001     0.001   3822.45   1689.68   1689.68      0.00      0.00      0.00
    4.041    71.721     4.041     0.001     0.001     0.001   1689.68   3822.45   1689.68      0.00      0.00      0.00
    4.041     4.041    71.721     0.001     0.001     0.001   1689.68   1689.68   3822.45      0.00      0.00      0.00
    0.001     0.001     0.001     4.041     0.001     0.001      0.00      0.00      0.00    119.51      0.00      0.00
    0.001     0.001     0.001     0.001     4.041     0.001      0.00      0.00      0.00      0.00    119.51      0.00
    0.001     0.001     0.001     0.001     0.001     4.041      0.00      0.00      0.00      0.00      0.00    119.51

a=0.700mm   d=0.05mm   b=a/7   V=0.415mm^3   Vf=0.343mm^3   Vs=0.072mm^3
material tensor [N/mm^2]
  3346.27   1787.75   1787.75      0.00      0.00      0.00     52.411    3.011     3.011     0.001     0.001     0.001
  1787.75   3346.27   1787.75      0.00      0.00      0.00      3.011   52.411     3.011     0.001     0.001     0.001
  1787.75   1787.75   3346.27      0.00      0.00      0.00      3.011    3.011    52.411     0.001     0.001     0.001
     0.00      0.00      0.00     72.44      0.00      0.00      0.001     0.001     0.001     2.581     0.001     0.001
     0.00      0.00      0.00      0.00     72.44      0.00      0.001     0.001     0.001     0.001     2.581     0.001
     0.00      0.00      0.00      0.00      0.00     72.44      0.001     0.001     0.001     0.001     0.001     2.581
   52.411     3.011     3.011     0.001     0.001     0.001   3346.27   1787.75   1787.75      0.00      0.00      0.00
    3.011    52.411     3.011     0.001     0.001     0.001   1787.75   3346.27   1787.75      0.00      0.00      0.00
    3.011     3.011    52.411     0.001     0.001     0.001   1787.75   1787.75   3346.27      0.00      0.00      0.00
    0.001     0.001     0.001     2.581     0.001     0.001      0.00      0.00      0.00     72.44      0.00      0.00
    0.001     0.001     0.001     0.001     2.581     0.001      0.00      0.00      0.00      0.00     72.44      0.00
    0.001     0.001     0.001     0.001     0.001     2.581      0.00      0.00      0.00      0.00      0.00     72.44

a=1.000mm   d=0.05mm   b=a/7   V=1.147mm^3   Vf=1.000mm^3   Vs=0.147mm^3
material tensor [N/mm^2]
  3011.36   1855.72   1855.72      0.00      0.00      0.00     38.881    2.311     2.311     0.001     0.001     0.001
  1855.72   3011.36   1855.72      0.00      0.00      0.00      2.311   38.881     2.311     0.001     0.001     0.001
  1855.72   1855.72   3011.36      0.00      0.00      0.00      2.311    2.311    38.881     0.001     0.001     0.001
     0.00      0.00      0.00     47.68      0.00      0.00      0.001     0.001     0.001     1.811     0.001     0.001
     0.00      0.00      0.00      0.00     47.68      0.00      0.001     0.001     0.001     0.001     1.811     0.001
     0.00      0.00      0.00      0.00      0.00     47.68      0.001     0.001     0.001     0.001     0.001     1.811
   38.881     2.311     2.311     0.001     0.001     0.001   3011.36   1855.72   1855.72      0.00      0.00      0.00
    2.311    38.881     2.311     0.001     0.001     0.001   1855.72   3011.36   1855.72      0.00      0.00      0.00
    2.311     2.311    38.881     0.001     0.001     0.001   1855.72   1855.72   3011.36      0.00      0.00      0.00
    0.001     0.001     0.001     1.811     0.001     0.001      0.00      0.00      0.00     47.68      0.00      0.00
    0.001     0.001     0.001     0.001     1.811     0.001      0.00      0.00      0.00      0.00     47.68      0.00
    0.001     0.001     0.001     0.001     0.001     1.811      0.00      0.00      0.00      0.00      0.00     47.68

a=1.500mm   d=0.05mm   b=a/7   V=3.706mm^3   Vf=3.375mm^3   Vs=0.331mm^3
material tensor [N/mm^2]
  2722.70   1912.47   1912.47      0.00      0.00      0.00     27.311    1.741     1.741     0.001     0.001     0.001
  1912.47   2722.70   1912.47      0.00      0.00      0.00      1.741   27.311     1.741     0.001     0.001     0.001
  1912.47   1912.47   2722.70      0.00      0.00      0.00      1.741    1.741    27.311     0.001     0.001     0.001
     0.00      0.00      0.00     30.80      0.00      0.00      0.001     0.001     0.001     1.291     0.001     0.001
     0.00      0.00      0.00      0.00     30.80      0.00      0.001     0.001     0.001     0.001     1.291     0.001
     0.00      0.00      0.00      0.00      0.00     30.80      0.001     0.001     0.001     0.001     0.001     1.291
   27.311     1.741     1.741     0.001     0.001     0.001   2722.70   1912.47   1912.47      0.00      0.00      0.00
    1.741    27.311     1.741     0.001     0.001     0.001   1912.47   2722.70   1912.47      0.00      0.00      0.00
    1.741     1.741    27.311     0.001     0.001     0.001   1912.47   1912.47   2722.70      0.00      0.00      0.00
    0.001     0.001     0.001     1.291     0.001     0.001      0.00      0.00      0.00     30.80      0.00      0.00
    0.001     0.001     0.001     0.001     1.291     0.001      0.00      0.00      0.00      0.00     30.80      0.00
    0.001     0.001     0.001     0.001     0.001     1.291      0.00      0.00      0.00      0.00      0.00     30.80

a=2.200mm   d=0.05mm   b=a/7   V=11.360mm^3   Vf=10.648mm^3   Vs=0.711mm^3
material tensor [N/mm^2]
  2523.97   1950.04   1950.04      0.00      0.00      0.00     19.441    1.371     1.371     0.001     0.001     0.001
  1950.04   2523.97   1950.04      0.00      0.00      0.00      1.371   19.441     1.371     0.001     0.001     0.001
  1950.04   1950.04   2523.97      0.00      0.00      0.00      1.371    1.371    19.441     0.001     0.001     0.001
     0.00      0.00      0.00     21.00      0.00      0.00      0.001     0.001     0.001     0.991     0.001     0.001
     0.00      0.00      0.00      0.00     21.00      0.00      0.001     0.001     0.001     0.001     0.991     0.001
     0.00      0.00      0.00      0.00      0.00     21.00      0.001     0.001     0.001     0.001     0.001     0.991
   19.441     1.371     1.371     0.001     0.001     0.001   2523.97   1950.04   1950.04      0.00      0.00      0.00
    1.371    19.441     1.371     0.001     0.001     0.001   1950.04   2523.97   1950.04      0.00      0.00      0.00
    1.371     1.371    19.441     0.001     0.001     0.001   1950.04   1950.04   2523.97      0.00      0.00      0.00
    0.001     0.001     0.001     0.991     0.001     0.001      0.00      0.00      0.00     21.00      0.00      0.00
    0.001     0.001     0.001     0.001     0.991     0.001      0.00      0.00      0.00      0.00     21.00      0.00
    0.001     0.001     0.001     0.001     0.001     0.991      0.00      0.00      0.00      0.00      0.00     21.00

*** pure fluid***
material tensor [N/mm^2]
  2000.00   2000.00   2000.00      0.00      0.00      0.00     0.301     0.001     0.001     0.001     0.001     0.001
  2000.00   2000.00   2000.00      0.00      0.00      0.00     0.001     0.301     0.001     0.001     0.001     0.001
  2000.00   2000.00   2000.00      0.00      0.00      0.00     0.001     0.001     0.301     0.001     0.001     0.001
     0.00      0.00      0.00      0.00      0.00      0.00     0.001     0.001     0.001     0.301     0.001     0.001
     0.00      0.00      0.00      0.00      0.00      0.00     0.001     0.001     0.001     0.001     0.301     0.001
     0.00      0.00      0.00      0.00      0.00      0.00     0.001     0.001     0.001     0.001     0.001     0.301
    0.301     0.001     0.001      0.00     0.001     0.001  2000.00   2000.00   2000.00      0.00      0.00      0.00
    0.001     0.301     0.001     0.001     0.001     0.001  2000.00   2000.00   2000.00      0.00      0.00      0.00
    0.301     0.001     0.301     0.001     0.001     0.001  2000.00   2000.00   2000.00      0.00      0.00      0.00
    0.001     0.001     0.001     0.301     0.001     0.001     0.00      0.00      0.00      0.00      0.00      0.00
    0.001     0.001     0.001     0.001     0.301     0.001     0.00      0.00      0.00      0.00      0.00      0.00
    0.001     0.001     0.001     0.001     0.001     0.301     0.00      0.00      0.00      0.00      0.00      0.00
```

Figure 7.16: Effective elasticity tensors for the RVE with the width of the solid wall $b=a/7$ and constant wall thickness 0.1mm. The side length of the RVE is in the range 0.47-2.2mm.

7.5.2 Effective material properties

The effective elasticity tensors obtained as the results of macroscale calculations yield some additional information about the bone material. Although the obtained results have the same form as the elasticity tensors of an isotropic material, due to the missing connection between the shear modulus and Young's modulus and Poisson's ratio ($G=\frac{E}{2(1+\nu)}$), they correspond to the group of orthotropic materials which characteristically have three mutually orthogonal symmetry planes and the compliance matrix in the form

$$\boldsymbol{N} = \begin{bmatrix} \frac{1}{E_1} & -\frac{\nu_{21}}{E_2} & -\frac{\nu_{31}}{E_3} & 0 & 0 & 0 \\ -\frac{\nu_{12}}{E_1} & \frac{1}{E_2} & -\frac{\nu_{32}}{E_3} & 0 & 0 & 0 \\ -\frac{\nu_{13}}{E_1} & -\frac{\nu_{23}}{E_2} & \frac{1}{E_3} & 0 & 0 & 0 \\ 0 & 0 & 0 & \frac{1}{G_{23}} & 0 & 0 \\ 0 & 0 & 0 & 0 & \frac{1}{G_{31}} & 0 \\ 0 & 0 & 0 & 0 & 0 & \frac{1}{G_{12}} \end{bmatrix}. \tag{7.112}$$

The concrete examples listed in chapter 7.5.1 can be taken to show that for bone material with the RVE presented in Figure 7.7, material parameters in all of the directions have the same values $E_1 = E_2 = E_3 = E$; $G_{23} = G_{31} = G_{12} = G$; $\nu_{21} = \nu_{31} = \nu_{12} = \nu_{32} = \nu_{13} = \nu_{23} = \nu$; and that their values can be directly calculated from the terms N_{11}, N_{12}, N_{44}. The change in material parameters dependent on the geometry of RVE is shown in Figures 7.17 and 7.18.

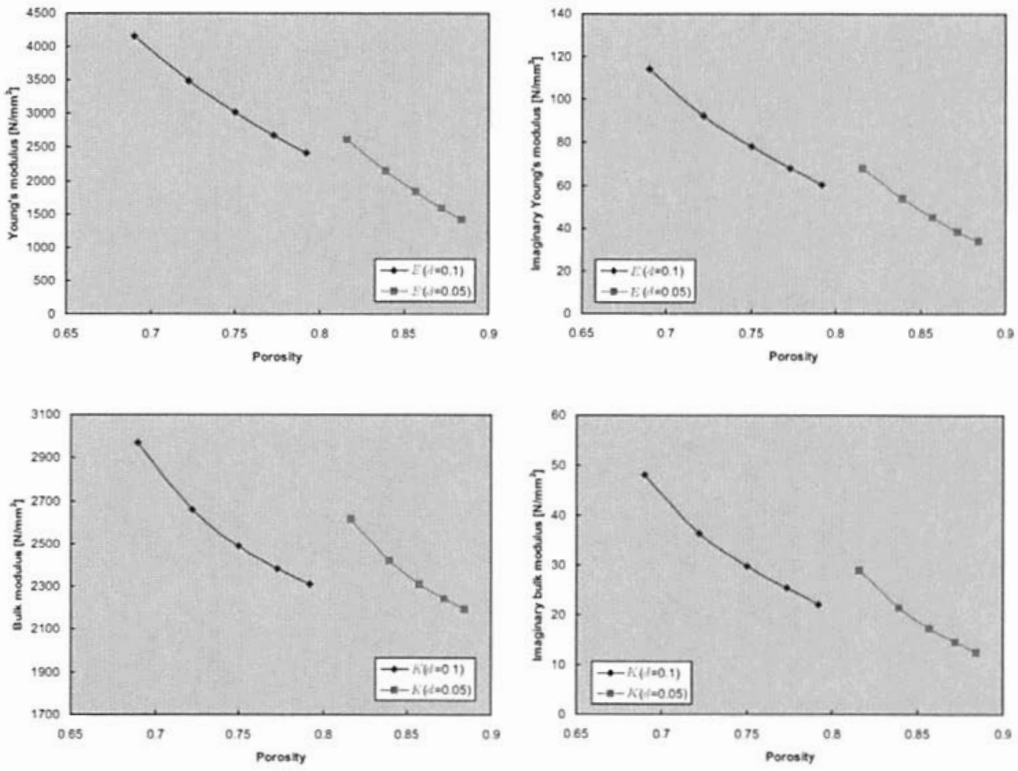

Figure 7.17: Change in the real and imaginary parts of Young's and bulk modulus versus porosity.

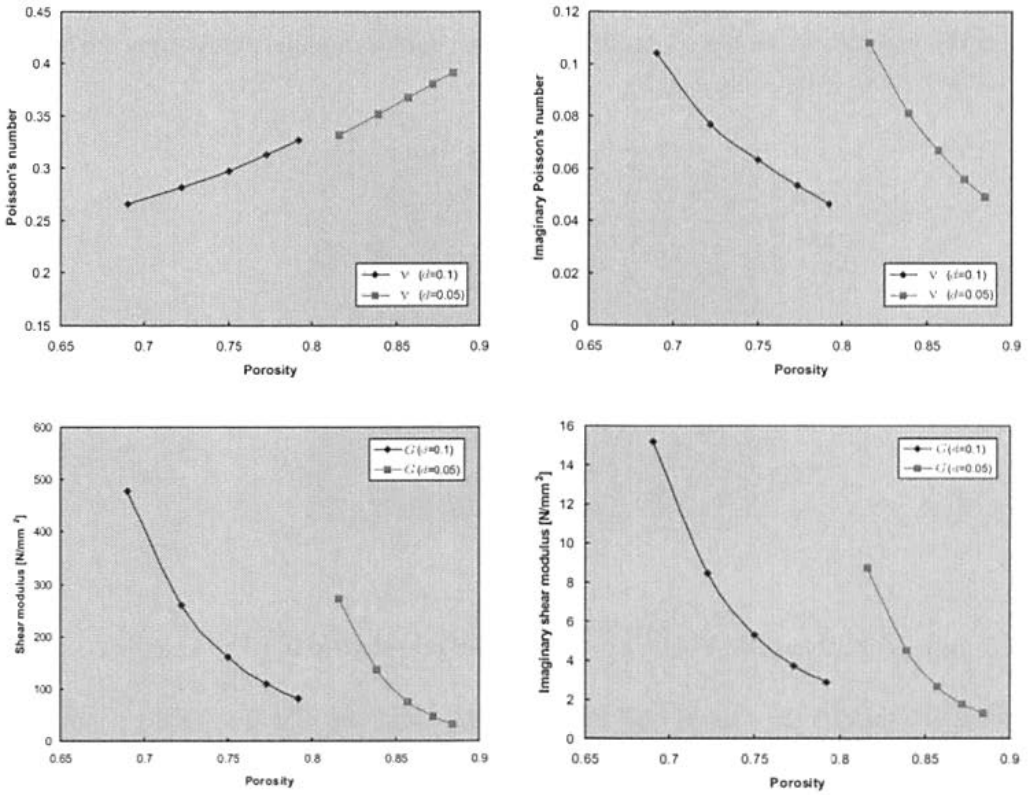

Figure 7.18: Change in the real and imaginary parts of Poisson's ratio and shear modulus with respect to the porosity.

Each of the diagrams presented in Figures 7.17 and 7.18 have two branches corresponding to the cases where the thickness of the solid wall is fixed. The analysis presumes that the volume fraction of the solid phase decreases due to the change in thickness and width of the solid wall, while the case of increasing wall spans is not considered; however, this can be analyzed in the same way. Results show that imaginary material parameters have the same behavior as the real ones, except in the case of Poisson's ratio where the real parameter increases with increasing porosity but the imaginary part decreases.

7.5.3 Results concerning the dry skeleton

Standard literature [1, 2, 3, 78, 90, 102, 103, 44] mostly investigates the effective elasticity parameters of the pure solid phase. For the purpose of comparison, the calculations described in 7.4 are repeated for the RVE without marrow core (Fig. 7.7a). In this case, the problem is determined by the equation of motion for the solid phase and Hill's condition

$$(-\omega^2 \boldsymbol{M}_s^* + \boldsymbol{K}_s^*) \cdot \tilde{\boldsymbol{a}}_s^* = \boldsymbol{f}_s^*(\bar{\epsilon}), \tag{7.113}$$

$$\tilde{\boldsymbol{u}}^+ = \tilde{\boldsymbol{u}}^- \quad \text{on} \quad \partial\Omega, \tag{7.114}$$

while in the comparison with the system (7.107)-(7.110), the equation of motion for the fluid phase and coupling condition are left out.

As in the case of interrogating the complete RVE, the final results at microlevel are effective elasticity tensors and material parameters but here only the change in Young's modulus with respect to the porosity will be considered in more detail (Fig. 7.19).

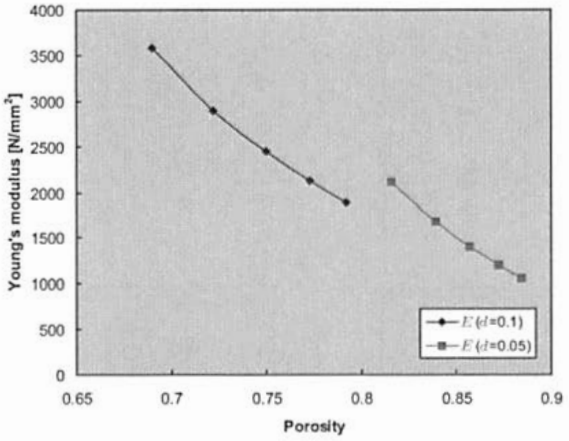

Figure 7.19: Change in Young's modulus over porosity for the dry skeleton.

The calculations show that for the case of wall thickness of 0.1mm, the effective Young's modulus takes the values 3576-1883 N/mm^2 while for a wall thickness of 0.05mm, the values are between 2114-1050 N/mm^2. These results agree well with the results obtained by Ashman [3], who found using the ultrasonic tests that the structural elasticity modulus of cancellous bone has the values in the interval 2110-985 N/mm^2. A consideration of the pure solid phase yields the small values of Poisson's ratio, leading to the conclusion that the fluid phase has a significant influence on this material parameter.

7.6 Simulation of the ultrasonic test

7.6.1 Problem formulation at macroscale

The effective elasticity tensor and material parameters calculated at microlevel also permit a definition of the problem at macroscale with a simulation of the behavior of the complete bone or some of its parts. The problem at macroscale is described by the equation of motion followed by the constitutive law and the boundary and initial conditions

$$\bar{\rho}\,\ddot{\bar{\boldsymbol{u}}} - \bar{\nabla}\cdot\bar{\boldsymbol{\sigma}} = \bar{\rho}\,\bar{\boldsymbol{b}}, \tag{7.115}$$

$$\bar{\boldsymbol{\sigma}} = \bar{\boldsymbol{C}} : \bar{\boldsymbol{\epsilon}}, \tag{7.116}$$

$$\bar{\boldsymbol{u}} = \bar{\boldsymbol{u}}^* \quad \text{on} \quad \partial\bar{\mathcal{B}}_u, \qquad \bar{\boldsymbol{\sigma}}\cdot\bar{\boldsymbol{n}} = \bar{\boldsymbol{t}} \quad \text{on} \quad \partial\bar{\mathcal{B}}_t, \tag{7.117}$$

$$\bar{\boldsymbol{u}}(\bar{\boldsymbol{x}}, t=0) = \boldsymbol{0}, \qquad \dot{\bar{\boldsymbol{u}}}(\bar{\boldsymbol{x}}, t=0) = \boldsymbol{0}, \tag{7.118}$$

where the body is chosen to be initially undeformed and at rest (7.118). The constitutive law (7.116) depends on the effective elasticity tensor $\bar{\boldsymbol{C}}$ whose form corresponds to the viscoelastic material behavior, according to the results shown in chapter 7.5.1.

For the special case where the body forces are neglected and periodic excitation $\bar{\boldsymbol{p}} = \bar{\boldsymbol{p}}(\boldsymbol{x})e^{i\omega t}$ is assumed, the problem becomes dependent on periodic displacements $\bar{\boldsymbol{u}}(\boldsymbol{x}, t) = \bar{\boldsymbol{u}}(\boldsymbol{x})e^{i\omega t}$ and indirectly only on the amplitudes $\bar{\boldsymbol{u}}(\boldsymbol{x})$

$$-\omega^2\bar{\rho}\,\bar{\boldsymbol{u}} - \bar{\nabla}\cdot\bar{\boldsymbol{\sigma}} = 0, \tag{7.119}$$

$$\bar{\sigma} = \bar{\mathbf{C}} : \bar{\epsilon} \tag{7.120}$$

$$\bar{u} = \bar{u}^* \quad \text{on} \quad \partial\bar{\mathcal{B}}_u, \qquad \bar{\sigma} \cdot \bar{n} = \bar{p} \quad \text{on} \quad \partial\bar{\mathcal{B}}_p. \tag{7.121}$$

Note that for further work, the formulation (7.119)-(7.121) is of the interest, as consideration is only given to the sound excitation on the bone sample.

7.6.2 FEM model of the ultrasonic test

An example of the calculations at macroscale consists in simulating the ultrasonic test already described in 7.1. To this end, it should be recalled that during the experiment the bone specimen is immersed in the water in the middle between the piezoelectric pulser and hydrophone. The pulser emits the sound signal which is received by the hydrophone after propagation through the water and the specimen. According to the difference between the original and recorded signal, the attenuation coefficient can be calculated. Its value regularly depends on the excitation frequency and microstructure of the sample. As the sound wave is of the longitudinal type, particles of the water and of the sample oscillate in the same direction as the wave propagates. The amplitudes of oscillations are of the small order and they cause the small change in the pressure in the surrounding medium. These two quantities are related to each other according to the expression

$$u = \frac{v}{2\pi f} = \frac{p}{2\pi f c \rho} \tag{7.122}$$

where u and v are the displacement and velocity of the particle, f and c are the frequency and velocity of the wave propagating through the medium of the density ρ and p is the change in pressure.

The previously described properties of the real laboratory test significantly influence the choice of convenient FE model and enable the introduction of a few important simplifications. Firstly, as the water in the original test is used only as a transmitter whose attenuation can be neglected in the FEM model, consideration only has to be given to the behavior of the sample. Secondly, as the sound wave is longitudinal, the whole simulation can be considered as a 2D problem of wave propagation through the thin slice of the sample (Fig. 7.20). Moreover, the displacements in the y direction in all of the points have to be suppressed, while the results will show that displacements in the z direction are of the order smaller than those in the x direction, which fits in with the nature of sound waves.

The remaining properties of the model can be described and motivated as follows. The dimension of the sample transversal to the direction of the wave propagation is assumed to be 50 mm, which in any case is greater than the wavelength of the excitation sound waves (see Ch. 7.6.3). Two kinds of boundary conditions are simulated on the top and the bottom of the specimen. In the first case, it is presumed that all the displacements in all the points on these two boundaries are constrained. In the second case, only the middle points on the top and bottom boundary are supported. The results show that the type of boundary conditions on these two boundaries does not influence the results, which can be expected as they are only responsible for suppression of the rigid body motion.

The size of the specimen in the direction of wave propagation is chosen as 30mm. This dimension does not correspond to the size of the specimens used in the real tests, but it is more appropriate for the necessary calculations and in some cases it permits a simulation of the wave propagation until its complete attenuation.

The discretization of the sample and applied load are shown in Figure 7.20. Here the number of elements is 100x50. The thickness in the direction "2" is 0.5mm. The sound pressure p=8kPa acts on the left boundary of the sample. The diameter of the pulser is assumed to be 10mm. The last few parameters (thickness, pressure and diameter) are chosen arbitrarily as they do not have any qualitative influence on the simulation.

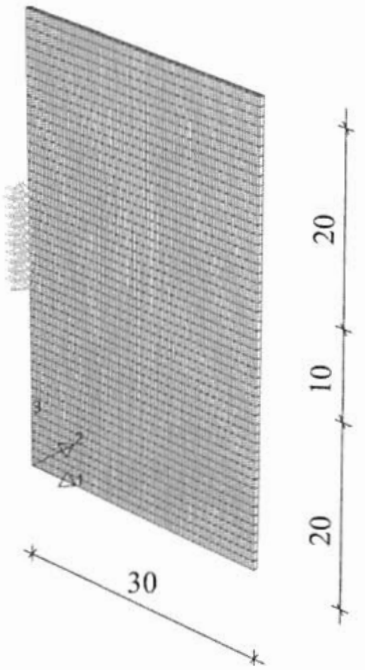

Figure 7.20: Model for FEM simulation of wave propagation through cancellous bone.

7.6.3 Expected properties of wave propagation through the homogenized medium

The main properties characterizing wave propagation through a medium are velocity, frequency and wavelength, and all are dependent on the properties of the particle oscillations mentioned in the previous section. Wave velocity is a particularly important quality in the laboratory tests as it is easily measured. It can be observed as a material property of the medium through which the wave propagates, but in the case of solid materials it also depends on the shape and especially on the dimensions of the body affected by the wave. For example, in the case of bounded medium, the wave moves with so-called bar velocity defined by the expression which depends on the Young's modulus

$$c_e = c(E) = \sqrt{E/\rho}. \tag{7.123}$$

In the practical sense, the term "bounded" means that cross-sectional dimensions of the sample, transverse to the direction of wave motion, have to be smaller than the wavelength. On the other hand, if the unbounded medium is considered, the wave velocity becomes greater and it can be calculated according to the expression dependent on plane wave modulus M

$$c_m = c(M) = \sqrt{M/\rho}, \qquad M = E\frac{1-\nu}{1-\nu-2\nu^2}. \tag{7.124}$$

Bearing in mind that the excitation frequency is the same with the wave frequency and frequency of the particle oscillations, and taking into account that properties of the medium are known, including the wave velocity, the wavelength can be calculated according to the expression

$$\lambda = c/f \tag{7.125}$$

where obviously, for the same velocity a shorter wavelength corresponds to the higher frequency.

In the case of the laboratory interrogation of Young's modulus, experiments are mostly carried out so that the expression (7.123) is valid and E can be calculated directly. For example, in the work of Ashman [3], a cylinder with radius 5mm and length 15mm is tested for estimating the structural effective Young's modulus. This uses sound excitation with frequency 50 kHz and expected wavelength of 20 mm. By

contrast, estimating the elasticity modulus of an individual trabecula with a radius of 0.1-0.5mm uses excitation of 2.25 MHz and a wavelength of approximately 1mm. The attenuation tests mostly use higher frequencies, so that it is more realistic to expect the case of "unbounded" medium.

Regarding the numerical model of cancellous bone proposed in this chapter, the previous discussion means that the wave velocities for that material can be calculated, because its effective material parameters are known (Ch. 7.5.2). The values obtained in this way are presented in the following table. Assuming that excitation frequency is in the range 0.5-2MHz, wavelengths for unbounded medium are calculated with the values 4.04-0.82mm, and with 3.63-0.58mm for bounded medium. The values presented here, can also be used to check the results obtained numerically, using FEM.

a=1mm, d=0.1mm						
Quantity		b=0.250mm	b=0.200mm	b=0.167mm	b=0.143mm	b=0.125mm
E	N/mm^2	4163.74	3482.24	3015.49	2672.06	2405.87
M	N/mm^2	5162.17	4470.27	4039.85	3741.16	3521.68
ρ	kg/m^3	1263.00	1230.00	1202.00	1179.00	1160.00
c_e	m/s	1815.68	1682.58	1583.90	1504.81	1440.15
c_m	m/s	2021.69	1906.40	1833.29	1781.04	1742.39
a=1mm, d=0.05mm						
Quantity		b=0.250mm	b=0.200mm	b=0.167mm	b=0.143mm	b=0.125mm
E	N/mm^2	2623.00	2153.50	1830.70	1596.00	1417.17
M	N/mm^2	3927.95	3483.07	3203.35	3011.36	2872.28
ρ	kg/m^3	1136.00	1113.00	1094.00	1097.00	1067.00
c_e	m/s	1520.74	1391.00	1293.60	1216.30	1152.46
c_m	m/s	1859.49	1769.02	1711.17	1670.59	1640.71

Figure 7.21: Material parameters and corresponding wave velocities for different types of cancellous bone.

7.6.4 Check of the results at the macrolevel

Two examples will be shown to illustrate simulation of the wave propagation and to check the results. Firstly, consideration is given to the wave propagation through the homogenized bone with an RVE geometry determined by the parameters a=1mm, d=0.1mm and b=0.25mm. The model shown in Figure 7.20 corresponds to the case of unbounded medium, so that the expected wave velocity amounts to c_m = 2021.69 m/s. For an arbitrarily chosen excitation frequency f=0.6 MHz, the expected wavelength is 3.37mm. The results of the FEM simulation shown in Figure 7.22a endorse such expectations as the resulting wavelength is approximately 3.24mm (9.25 wavelengths on the length of sample which amounts to 30mm). An additional check looks at the magnitude of particle displacements. Namely, relation (7.122) can be used to calculate that approximate particle displacement for the problem discussed here has the value $8.32 \cdot 10^{-7}$mm, which agrees with the displacement values shown in Figure 7.22a.

Wave propagation through water is simulated as a second example, to illustrate that the developed procedure also applies to the case of pure fluid. For this medium, wave velocity has to be calculated according to the expression

$$c_k = c(K) = \sqrt{K/\rho} \tag{7.126}$$

where K represents the standard bulk modulus. The properties of water are well known and they amount to K=2.2 GPa, ρ=1000kg/m^3, $\eta = 10^{-3}$Pa s, so that the bulk wave velocity has the value c_k=1481m/s. If the excitation frequency is assumed to be 0.1 MHz, the expected wavelength becomes 14.83mm. The results of the FEM simulation are shown in Figure 7.22b, where it is easy to see that there are two full wavelengths on the length of 30mm.

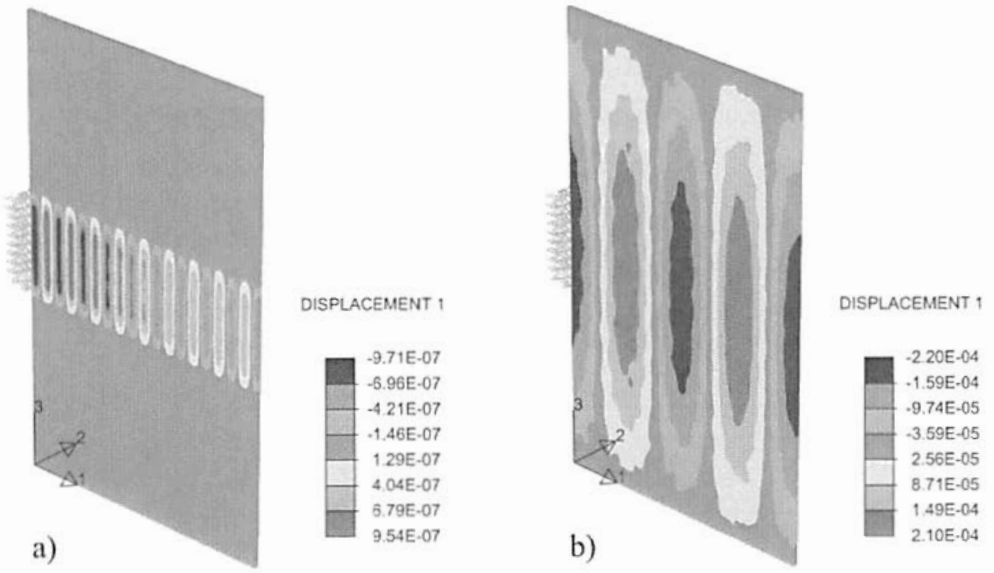

Figure 7.22: a) Wave propagation through cancellous bone with an RVE geometry determined by the parameters a=1mm, d=0.1mm, b=0.25mm. Assumed excitation frequency 0.6MHz. b) Wave propagation through water. Assumed excitation frequency 0.1MHz.

7.6.5 Dependence of the attenuation on the excitation frequency and material density

The results of the laboratory attenuation tests show that increasing excitation frequencies and increasing bone material density (BMD) lead to an increase in wave attenuation. Using the information about emitted and received signal, this permits a non-destructive estimate of the internal structure of the cancellous bone. The same principle apply to numerical tests. The results of simulated attenuation tests should show if the assumed bone structure corresponds to the real one.

In order to check if the numerical simulations are adequate substitution of the real attenuation tests, firstly consideration is given to the influence of increasing excitation frequency on bone behavior. To this end the type of material microstructure in the simulations is fixed, and sound excitation of different frequencies is applied. As the influence of attenuation is more noticeable in the case of higher frequencies, excitation is simulated in the domain 0.9-1.7 MHz. The microstructure is chosen corresponding to the geometry of the RVE determined by the parameters a=1mm, b=0.25mm and d=0.05mm. The results of the simulations are shown in Figure 7.23, where the stronger attenuation obviously corresponds to the higher frequencies.

The study of the relationship between attenuation and BMD is a rather more complicated than the influence of the excitation frequency. This can be expected, as the change in density is a consequence of the change in RVE geometry, which mostly depends on many parameters. In the case of the model proposed in chapter 7.4, the RVE geometry is determined by three parameters (wall thickness d, wall width b and side length a) so that three different types of tests are carried out in order to study the influence of BMD on attenuation. In each group of tests, two of the geometrical parameters previously mentioned are kept constant and the remaining one is observed as a variable.

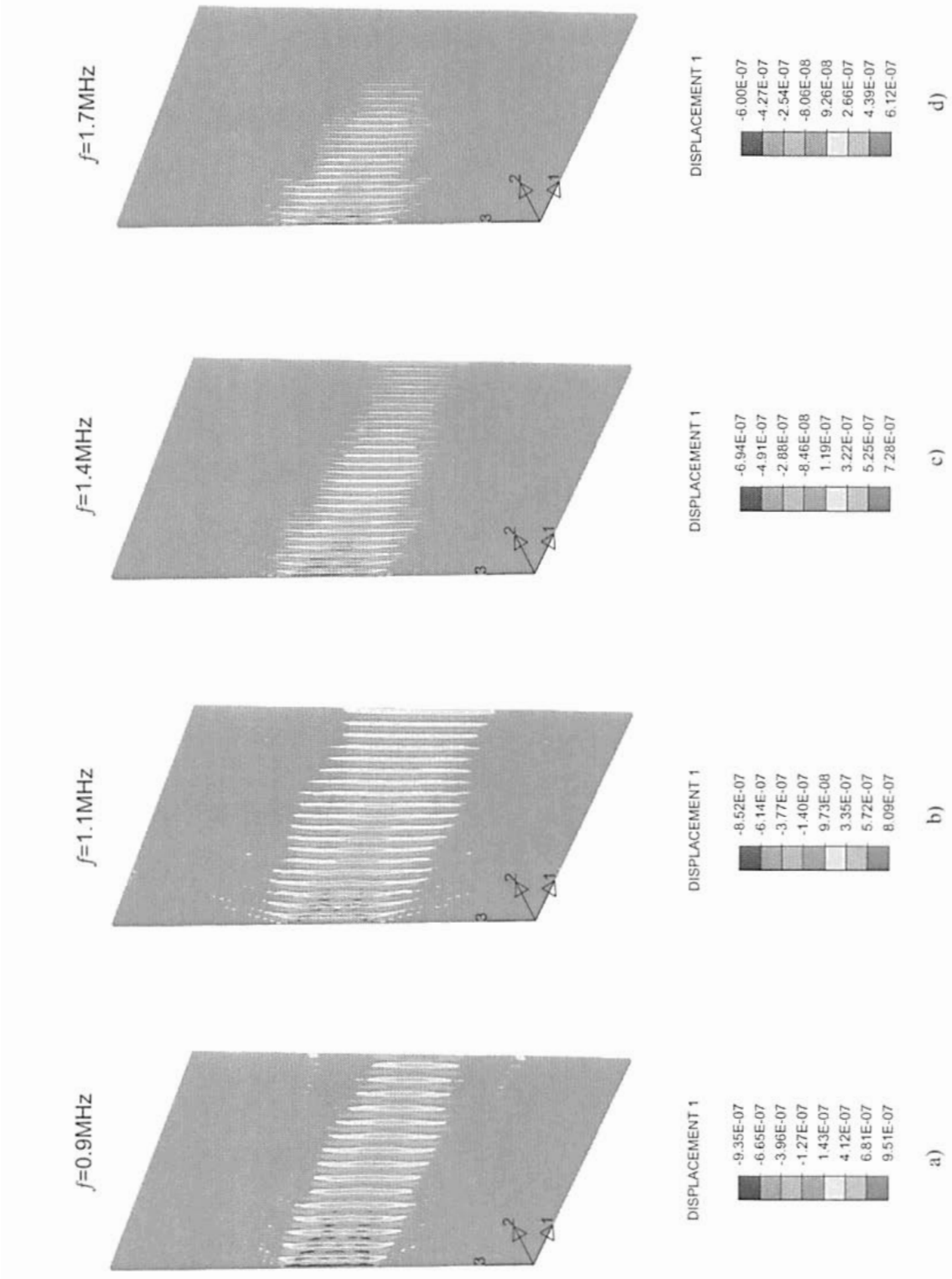

Figure 7.23: Wave propagation of the sound waves of the different frequencies through the bone whose geometry of RVE is determined by the parameters a=1mm, b=0.25mm and d=0.05mm.

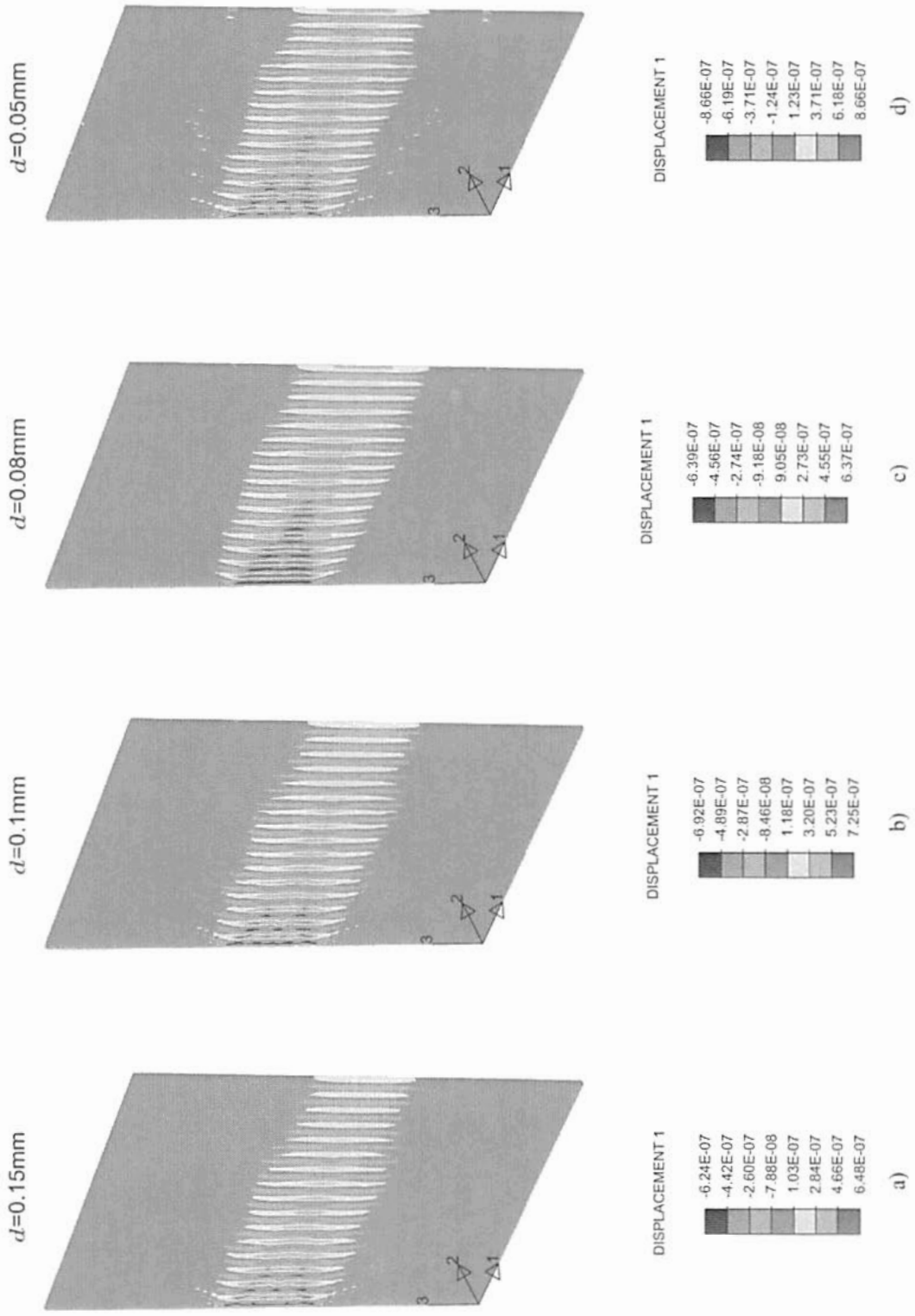

Figure 7.24: Wave propagation of the wave of frequency 1MHz through the material whose microstructure is determined by the parameters a=1mm, b=0.25mm. The thickness of the solid wall is variable and it takes the values 0.15, 0.1, 0.08 and 0.05mm.

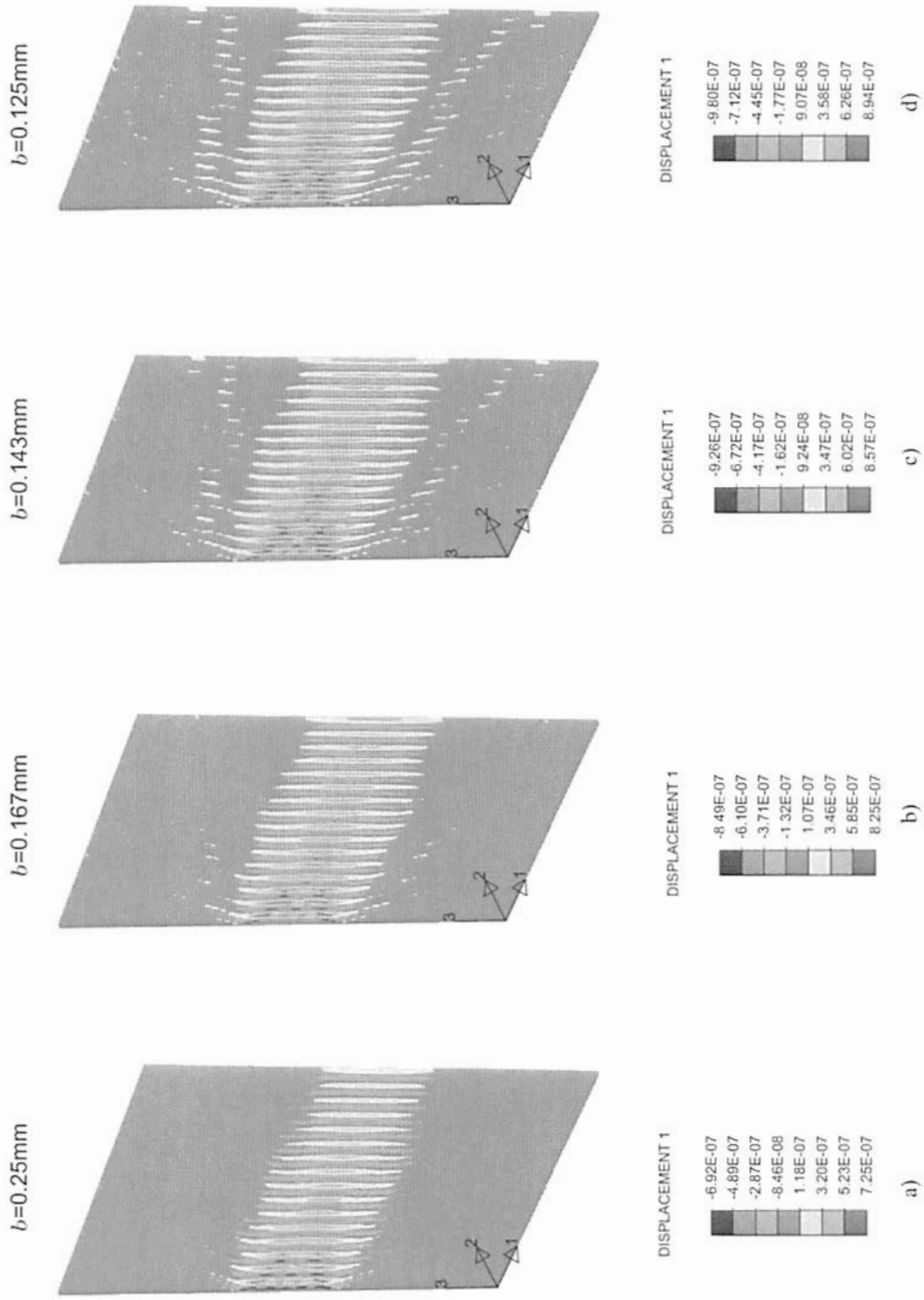

Figure 7.25: Wave propagation of the wave of frequency 1MHz in the case that material microstructure is determined by the parameters a=1mm and d=0.05mm. The width of the solid wall is changeable and it takes the values 0.25, 0.1667, 0.143 and 0.125mm.

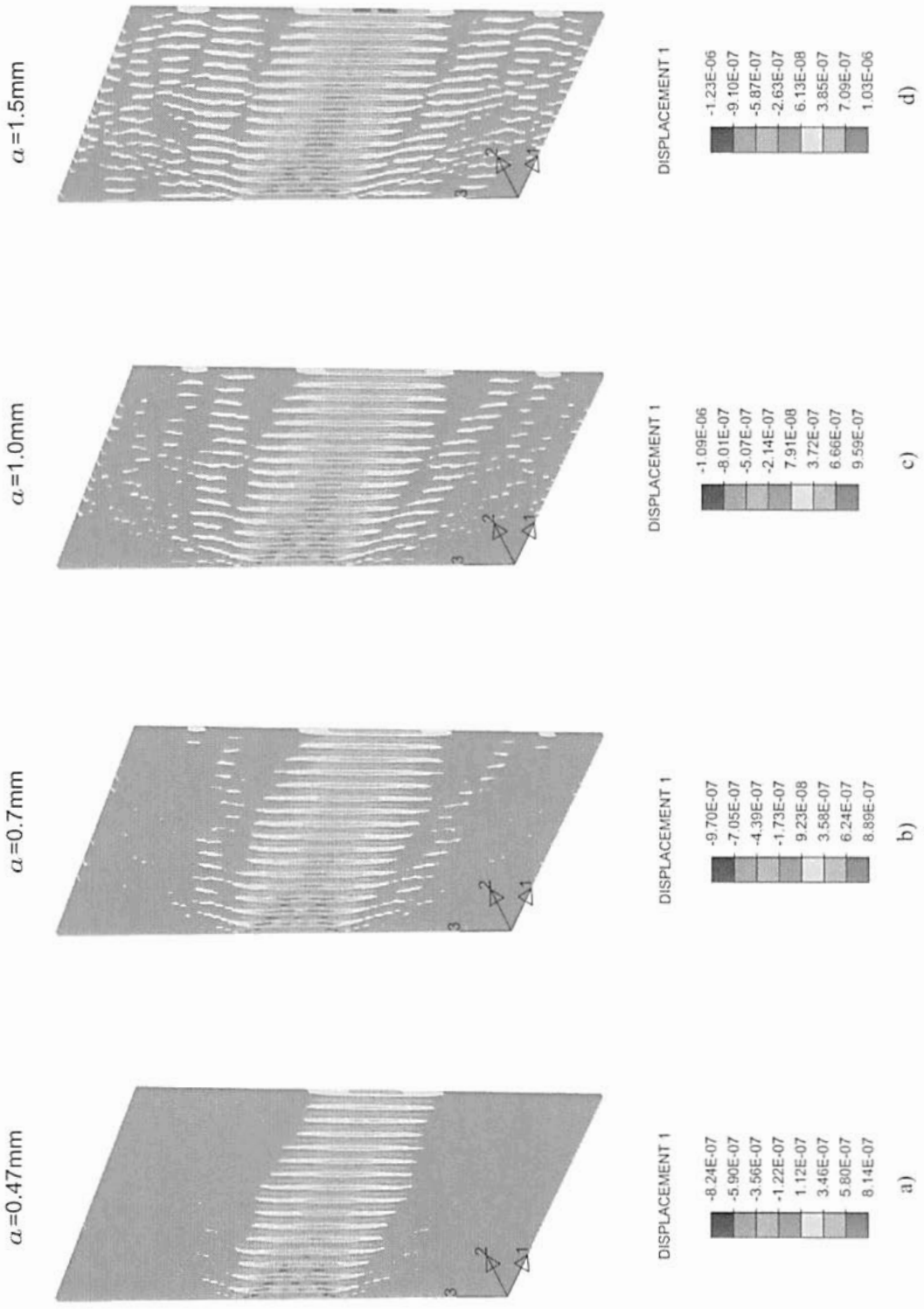

Figure 7.26: Wave propagation of the wave of frequency 1MHz. Material microstructure is determined by the parameter d=0.05mm and relation b=0.167a. The side length of the cube is variable and it takes the values 0.47, 0.7, 1.0 and 1.5mm respectively.

The influence of wall thickness on attenuation is examined on the basis of the effective elasticity tensors of the materials with RVE which is a unity cube and with wall width b=0.25mm. The wall thickness is assumed to be 0.15, 0.1, 0.08 and 0.05mm respectively. Wave propagation through the macrosample is shown in Figure 7.24. The influence of the width of the wall is investigated using materials with RVE which is a unity cube and thickness of the wall 0.05mm. The results for this case are shown in Figure 7.25, where the width of the wall takes the values 0.25-0.125mm. Finally, the influence of the side length is studied by simulating wave propagation through the sample with material structure determined by the parameters d=0.05mm and relation $b = a/6$ (Fig. 7.26). In the examples, the side length increases from 0.47 up to 1.50mm.

The results presented in Figures 7.23-7.26 show that numerical simulations similar to those in laboratory yield the conclusion that increasing frequency and density cause an increase in attenuation; but it also transpires that numerical values obtained in this way are much smaller than those obtained by the laboratory tests. Note that for calculating the attenuation expression (7.2) and amplitudes of the oscillations of particles whose distance is the integer number of wavelengths ($n\lambda$) were used. The obtained values amount on average to 1-2 bB/(MHz cm), so that it can be supposed that the model presented here leads to an attenuation coefficient originating mainly from attenuation of the solid phase, while the laboratory tests show that homogenized material has far greater attenuation than its component materials. A value of 20 bB/(MHz cm) is often taken for the illustration.

At the moment, there are two main proposals for resolving the problem of calculating the attenuation coefficient: reconsidering the geometry of RVE, and introducing wave scattering. With regard to the geometry of RVE, one possible alternative to the model presented here is to observe such RVE where the thin wall structure is replaced by the beam structure, or a combination of both is used [90]. The idea of studying wave scattering on the interface of the solid and fluid phases is motivated by the laboratory results obtained by Laugier [55, 56] indicating a very strong influence of this phenomenon on the cancellous bone attenuation.

7.7 Conclusions concerning the model of cancellous bone

This chapter looked at calculating the material parameters for cancellous bone using a procedure based on the multiscale FEM. Its main advantages compared to Biot's theory are its simplicity and the smaller number of material parameters required. At microscale, the method yields effective elasticity tensor and material parameters, so that changing the RVE geometry is used to study the influence of increasing porosity on the strength of material. At macroscale, the ultrasonic laboratory test is simulated as an elucidating example. These results agree well with the real values except in the domain of attenuation, so that a reconsideration of the model is being envisaged. Some possible improvements include changing the RVE geometry, or introducing the influence of scattering the sound waves on the interface of the solid and fluid phases.

8 Conclusions

The multiscale FEM is a numerical method based on the theory of homogenization, with the specific principle that real material properties have to be replaced by effective ones obtained by the examination of a RVE. The terminology "macro" relates to the examined body, while "micro" relates to the RVE describing the material structure thereby the macroquantities are defined using the concept of the volume average and the coupling of the scales requires Hill's macrohomogeneity condition to be satisfied. Transformation of the latter condition leads to the definition of the boundary conditions at microscale and in that way to the closed formulation of the boundary value problem related to this level. The work examines materials with periodic and random microstructure, explaining three examples in detail.

The first example simulates the behavior of microporous nonlinear material. Here, a tension test of a plate is considered at macroscale, while a square RVE with an elliptical pore is chosen to describe the material properties. Given a random microstructure, the RVE is assumed to have a different orientation in each Gauss' point. The material investigation is illustrated by three groups of tests with different lengths of the semi-major axis of the pore. Each time, ellipticity is changed in an interval $[0, 1]$ where the lower limit corresponds to pores with zero thickness and the upper limit to circular ones. The results show that in the moment when pores appear, even if their thickness can be neglected, the material parameters decrease at once; furthermore, with pore growth, Young's and bulk modulus undergo a monotonous decrease while Poisson's ratio increases. Calculations also show that voids with elongated shape have a more significant influence on material weakening than voids whose shape is close to the circular one.

The second example looks at modeling solution-precipitation creep, which is a diffusional process occurring in polycrystals if pressure and temperature are in the specific range. For this problem, firstly a continuum-mechanical model is proposed where the deformation is decomposed into an elastic and an inelastic part and the total power is written as a superposition of total elastic power and dissipation. The elastic energy is chosen in the standard form, dependent on the Helmholtz free energy, while the dissipated energy is formulated particularly for the process of solution-precipitation creep. It depends on the normal velocity of the crystal boundary due to precipitation or solution of material and on the velocity of material transport within the crystal interfaces. One of the main properties of this model is that the difference between the normal component of the Eshelby stress tensor and its smooth approximation becomes the driving force of the process. Such behavior is already endorsed by the experiments showing that under homogeneous pressure acting on one side of a rectangular crystal, solution-precipitation creep occurs only in edge zones of the sample. Another advantage of the proposed model is that in contrast to other procedures, continuity of stress in triple points is not required. Preliminary results for the behavior of polycrystals are obtained using the Taylor model and show that solution-precipitation creep leads to the elongation of the crystal shape. FEM-based methods are used for more realistic simulations and to estimate the change in effective material parameters over time. Here the most important simulations are those concerning materials with completely random structure and materials with regular structure consisting of hexagonal crystals.

The motivation behind developing the model for the RVE of cancellous bone, which is the last example presented in this work, is to investigate the process of osteoporosis, whose main indicators are the decrease and partial disappearance of the solid phase. The important feature of the model is that the presence of the fluid phase necessitates dynamic interrogation and analysis in the complex domain. According to the geometry of the microstructure it is assumed that the RVE has a cubic form and that it consists of the solid frame and of viscous blood marrow filling the core of the frame. The effective elasticity tensor and the parameters of materials with different microstructure are calculated as the final results at microscale.

Comparison of the real parts of material parameters with the experimental results shows good agreement. The calculations at macrolevel are illustrated by simulating the ultrasonic test where the attenuation coefficient is calculated as a final result, using the ratio of amplitudes of particle oscillations. The obtained numerical values are much smaller than the experimental ones so that an improvement of the model of the RVE is envisaged. Two main ideas for overcoming the problem consist of assuming a new geometry of the solid phase of the RVE, and introducing wave scattering on the interface of the phases.

From the previous overview it can be seen that, although limited by the requirements concerning the size of the RVE, the multiscale FEM can still be applied to modeling composite materials with very diverse microstructures. The examples presented here confirm in particular that the method can be applied efficiently in modeling nonlinear materials with a regular structure and a random structure, which mostly exceeds the abilities of analytical solutions and other numerical methods.

Bibliography

[1] R.B. Ashman, J.D. Corin, W.C. Van Buskirk and J.C. Rice, A continuous wave technique for the measurement of the elastic properties of cortical bone, *J. Biomechanics, 17(5),* (1984), 349-361.

[2] R.B. Ashman, J.D. Corin and C.H. Turner, Elastic properties of cancellous bone: measurement by an ultrasonic technique, *J. Biomechanics, 20(10),* (1987), 979-986.

[3] R.B. Ashman and J.Y. Rho, Elastic modulus of trabecular bone material, *J. Biomechanics, 21(3),* (1988), 177-181.

[4] Y. Bard, Non-linear Parameter estimation, Academic Press, New York, (1974).

[5] J.L. Batoz and M.B. Tahar, Evaluation of new quadrilateral thin plate bending element, *Int. J. Num. Meth. Eng., 18,* (1982), 1655-1677.

[6] T. Belytschko, W.K. Liu, B. Moran, Nonlinear Finite Elements for Continua and Structures, John Wiley & Sons, LTD, (2001).

[7] Y. Benveniste, A New Approach to the Application of Mori-Tanaka's Theory in Composite Materials, *Mech. Mater., 6,* (1987), 147-157.

[8] M. Beran, Use of the variational approach to determine bounds for the effective permittivity of a random media, *Nuovo Cimento, 38,* (1956), 771-782.

[9] M.J. Beran, Statistical Continuum Theories, Wiley (Interscience), New York, (1968).

[10] M.A. Biot, Theory of propagation of elastic waves in fluid-saturated porous solid. I. Low-frequency range, *Jour. Acoust. Soc. Am., 28(2),* (1956), 168-178.

[11] M.A. Biot, Theory of propagation of elastic waves in fluid-saturated porous solid. II. Higher frequency range, *Jour. Acoust. Soc. Am., 28(2),* (1956), 179-191.

[12] J.L. Buchanan, R.P. Gilbert and K. Khashanah, Recovery of the poroelastic parameters of cancellous bone using low frequency acoustic interrogation, In A. Wirgin (ed.), Acoustic, Mechanics, and the related Topics of mathematical Analysis, World Scientific, (2002), 41-47.

[13] J.L. Buchanan, R.P. Gilbert and K. Khashanah, Determination of the parameters of cancellous bone using low frequency acoustic measurements, *J. Comput. Acoust., 12(2),* (2004), 99-126.

[14] J.L. Buchanan and R.P. Gilbert, Determination of the parameters of cancellous bone using high frequency acoustic measurements, *Mathematical and computer modelling, (to appear).*

[15] B. Budianski, On the elastic moduli of some heterogeneous materials, *J. Mech. Phys. Solids, 13,* (1965), 223-227.

[16] P.P. Castañeda, The effective mechanical properties of nonlinear isotropic composites, *J. Mech. Phys. Solids., 39(1),* (1991), 45-71.

[17] P.P. Castañeda, New variational principles in plasticity and their application to composite materials, *J. Mech. Phys. Solids., 40(8)* , (1992), 1757-1788.

[18] P.P. Castañeda and J.R. Willis, On the overall properties of nonlinearly viscous composites , *Proc. R. Soc. Lond., A, 416,* (1988), 217-244.

[19] P.G. Ciarlet, Mathematical elasticity, Volume 1: Three dimensional elasticity, Elsevier Science Publishers B.V., (1988).

[20] R.L. Coble, A model for boundary diffusion controlled creep in polycrystalline materials, *J. of Appl. Physics, 34,* (1963), 1679-1682.

[21] R.F. Cooper, D.L. Kohlstedt and K. Chyung, Solution-precipitation enhanced creep in solid liquid aggregates which display a non-zero dihedral angle, *Acta Metallurgica, 37,* (1989), 1759-1771.

[22] D. Elliott, Deformation paths in structural geology *Geol. Soc. America. Bull., 83,* (1972), 2621-2638.

[23] D. Elliott, Diffusion Flow Laws in Metamorphic Rocks *Geol. Soc. America. Bull., 84,* (1973), 2645-2664.

[24] M. Epstein and G.A. Maugin, On the geometrical material structure of anelasticity, *Acta Mechanica, 115,* (1996), 119-131.

[25] J.D. Eshelby, The elastic field of an ellipsoidal inclusion, and related problems,*Proc. R. Soc. Lond., 241, A,* (1957), 376-396.

[26] M. Fang, R.P. Gilbert, A. Panachenko and A. Vasilic, Homogenizing the Time Harmonic Acoustics of Bone, *Mathematical and Computer Modelling,* (2007).

[27] M. Fang, R.P. Gilbert and X. Xie, Deriving ultrasound equation for soft tissue, *Computers and Mathematics with Applications, (to appear).*

[28] J.M. Ford, J. Wheeler and A.B. Movchan, Computer simulation of grain boundary creep, *Acta Materialia, 50,* (2002), 3941-3955.

[29] J.M. Ford, N.J. Ford and J. Wheeler, Simulation of grain boundary diffusion creep: analysis of some new numerical techniques, *Proc. R. Soc. Lond., A, 460,* (2004), 2395-2413.

[30] S. Ghosh and S.N. Mukhopadhyay, A material based finite element analysis of heterogeneous media involving Dirichlet tessellations, *Comp. Met. Appl. Mech. Eng., 104,* (1993), 211-247.

[31] S. Ghosh and S. Moorthy, Elastic-plastic analysis of arbitrary heterogeneous materials with the Voronoi Cell finite element method, *Comp. Met. Appl. Mech. Eng., 121,* (1995), 373-409.

[32] L.J. Gibson, The mechanical behaviour of cancellous bone, *J. Biomechanics, 18(5),* (1985), 317-328.

[33] K. Hackl, A. Mielke and D. Mittenhuber, Dissipation distances in multiplicative elastoplasticity,

In W. Wendland and M Efendiev, (ed.), Analysis and simulation of multifield Problems, Springer Verlag, (2003), 87-100.

[34] K. Hackl and S. Ilic, Solution-precipitation creep – continuum mechanical formulation and micromechanical modelling, *Arch. Appl. Mech., 74,* (2005), 773-779.

[35] J. Hadamard, Numerical Initial Value Problem in Linear Partial Differential Equations, Yale University Press, New Haven, (1923).

[36] Z. Hashin and S. Shtrikman, On some variational principles in anisotropic and nonhomogeneous elasticity, *J. Mech. Phys. Solids, 10,* (1962), 335-342.

[37] Z. Hashin and S. Shtrikman, A variational approach to the theory of the elastic behaviour of polycrystals, *J. Mech. Phys. Solids, 10,* (1962), 343-352.

[38] Z. Hashin and S. Shtrikman, A variational approach to the theory of the elastic behaviour of multiphase materials, *J. Mech. Phys. Solids, 11,* (1963), 127-140.

[39] C. Herring, Diffusional viscosity of a polycrystalline solid *Jour. Appl. Physics, 21,* (1950), 245-278.

[40] R. Hill, The elastic behaviour of a crystalline aggregate, *Proc. Phys. Soc., London, A, 65,* (1952), 349-354.

[41] R. Hill, Elastic properties of reinforced solids: some theoretical principles, *J. Mech. Phys. Solids, 11,* (1963), 357-372.

[42] R. Hill, A self-consistent mechanics of composite materials, *J. Mech. Phys. Solids, 13,* (1965), 213-222.

[43] R. Hill, On Constitutive Macro-Variables for Heterogeneous Solids at Finite strain, *Proc. R. Soc. Lond., A, 326,* (1972), 131-147.

[44] C.E. Hoffler, K.E. Moore, K. Kozloff, P.K. Zysset, M.B. Brown and S.A. Goldstein, Heterogeneity of Bone Lamellar-Level Elastic Moduli, *Bone, 26,* (2000), 603-609.

[45] A. Hosokawa and T. Otani, Ultrasonic wave propagation in bovine cancellous bone, *Jour. Acoust. Soc. Am., 101,* (1997), 558-562.

[46] C. Huet, Universal conditions for assimilation of a heterogeneous material to an effective medium, *Mech. Res. Commun., 9(3),* (1982), 165-170.

[47] C. Huet, On the definition and experimental determination of effective constitutive equations for assimilating heterogeneous materials, *Mech. Res. Commun., 11(3),* (1984), 195-200.

[48] C. Huet, Application of variational concepts to size effects in elastic heterogeneous bodies, *J. Mech. Phys. Solids, 38(6),* (1990), 813-841.

[49] T.J.R. Hughes, The Finite Element Method, Prentice Hall, Englewood Cliffs, NJ, (1987).

[50] S. Ilic and K. Hackl, Homogenisation of random composites via the multiscale finite-element method, *PAMM, 4,* (2004), 326-327.

[51] S. Ilic and K. Hackl, Solution-precipitation creep – micromechanical modelling and numerical results, *PAMM, 5,* (2005), 277-278.

[52] S. Ilic and K. Hackl, Multiscale FEM in modelling of solution-precipitation creep, *PAMM, 6,* (2006), 483-484.

[53] D. Kuhl, Finite Elemente Methode I, Ruhr Universität Bochum, (1999).

[54] E. Kröner, Elastic moduli of perfectly disordered composite materials, *J. Mech. Phys. Solids, 15,* (1967), 319-329.

[55] P. Laugier, P. Giat, C. Chappard and G. Berger, Clinical assessment of the backscatter coefficient in osteoporosis, *In: IEEE Ultrasonics Symposium, 2,* (1997), 1101-1104.

[56] J. Litniewski, P. Giat, A. Nowicki and A. Sawicki, Detection of bone disease with ultrasound - comparison with bone densitometry, *Ultrasonics, 38,* (2000), 693-697.

[57] T.H.K. Lohkämper, G. Jordan, R. Costamagna, B. Stöckhert and W.W. Schmahl, Phase shift interference microscope study of dissolution-precipitation processes of nonhydrostatically stressed halite crystals in solution, *Contrib. Mineral. Petrol., 146,* (2003), 263-274.

[58] J.E. Marsden and T.J.R Hughes, Mathematical foundations of elasticity, Dover Publications, (1983).

[59] G.A. Maugin, "Material" mechanics of materials, *Theor. Appl. Mech., 27,* (2002), 1-12.

[60] C. Miehe, J. Schotte and J. Schröder, Computational Micro-Macro Transition and Overall Moduli in the Analysis of Polycrystals at Large Strains, *Comp. Mat. Sci., 16,* (1998), 372-382.

[61] C. Miehe, J. Schotte and M. Lambrecht, Homogenisation of inelastic Solid Materials at Finite Strains based on Incremental Minimization Principles, *J. Mech. Phys. Solids, 50,* (2002), 2123-2167.

[62] C. Miehe, J. Schröder and J. Schotte, Computational Homogenisation Analysis in finite plasticity, Simulation of Texture development in Polycrystalline Materials *Comp. Met. Appl. Mech. Eng., 171,* (1999), 387-418.

[63] C. Miehe, J. Schröder and C. Bayreuther, On the homogenisation Analysis of Composite Materials Based on Discretized Fluctuations on the Microstructure, *Acta Mechanica, 155,* (2002), 1-16.

[64] C. Miehe, J. Schröder and M. Becker, Computational Homogenization Analysis in Finite Elasticity: Material and Structural Instabilities on the Micro- and Macro-Scales of Periodic Composites and their interaction, *Comp. Met. Appl. Mech. Eng., 191,* (2002), 4971-5005.

[65] A. Mielke, Energetic formulation of multiplicative elasto-plasticity using dissipation distances, *Cont. Mech, 15,* (2003), 351-382.

[66] A. Mielke, Evolution of rate-independent inelasticity with microstructure using relaxation and Young measures, In C. Miehe (ed.), IUTAM Symposium on computational Mechanics of solid materials at large strains, Kulwer, (2003), 33-44.

[67] A. Mielke, Evolution in rate-independent systems (ch.6), In C. Dafermos and E. Feireisl (ed.),

Handbook of Differential equations, Evolutionary equations, volume 2, Elsevier B.V., (2005), 461-559.

[68] T. Mori and K. Tanaka, Average stress in matrix and average elastic energy of materials with misfitting inclusions, *Acta Metallurgica, 21,* (1973), 571-574.

[69] H. Moulinec and P. Suquet, Intraphase strain heterogeneity in nonlinear composites: a computational approach, *Europ. J. of Mech., A/Solids , 22,* (2003), 751-770.

[70] T. Mura, Micromechanics: overall properties of heterogeneous solids, Kluwer Academic Publishers, (1993).

[71] F.R.N. Nabarro, Deformation of crystals by the motion of single ions *in Report of a conference on the strength of solids: Phys. Soc. Proc.,* (1948), 75-90.

[72] S. Nemat-Nasser and M. Hori, Micromechanics: overall properties of heterogeneous materials, Nord-Holland Series in: Applied Mathematics and Mechanics, 37, (1993).

[73] R.W. Ogden, Non-linear elastic deformations, Dover Publications, (1984).

[74] J.T. Oden and T.I. Zohdi, Analysis and adaptive modeling of highly heterogeneous elastic structures, *Comp. Met. Appl. Mech. Eng., 148,* (1997), 367-391.

[75] M.S. Paterson, A theory for granular flow accommodated by material transfer via an intergranular fluid, *Tectonphysics, 245,* (1995), 131-151.

[76] J. Renner, B. Evans and G. Hirth, On the rheologically critical melt fraction, *Earth Plan. Sci. Lett., 181,* (2000), 585-594.

[77] A. Reuss, Calculation of flow limits of mixed crystals on the basis of the plasticity of mono-crystals, *Z. Angew. Math. Mech., 9,* (1929), 49-58.

[78] J.Y. Rho, R.B. Ashman and C.H. Turner, Young's modulus of trabecular and cortical bone material: Ultrasonic and microtensile measurements, *J. Biomechanics, 26(2),* (1993), 111-119.

[79] J. Schröder, Homogenisierungsmethoden der nichtlinearen Kontinuumsmechanik unter Beachtung von Stabilitäts Problemen, Habilitationsshrift, Universität Stuttgart, (2000).

[80] J.C. Simo and T.J.R Hughes, Computational Inelasticity, Springer Verlag, (1997).

[81] H.C. Sorby, Über Kalkstein-Geschiebe mit Eindücken, *Neues Jahrb. Mineralogie,* (1863), 801-807.

[82] H.C. Sorby, On the application of quantitative methods to the study of rocks, *Geol. Soc. London Quart. Jour., 61* (1908), 171-233.

[83] P. Suquet, Effective Properties of Nonlinear Composites, in P. Suquet (ed.), Continuum Micromechanics, CISM, 377, Springer Wien New York, (1997).

[84] D.R.S. Talbot and J.R. Willis, Variational Principles for Inhomogeneous Non-linear Media, *IMA-Journal of Applied Mathematics, 35,* (1985), 39-54.

[85] R.L. Taylor, Finite element analysis of linear shell problems, in J.R Whiteman (ed.), The Mathematics of finite element and Applications, VI, Academic Press, London, (1998).

[86] S. Torquato, Random heterogeneous materials: microstructure and macroscopic properties, Springer Verlag, New York, (2002).

[87] W. Voigt, Über die Beziehung zwischen den beiden Elasticitätskonstanten isotroper Körper, *Ann. Phys. (Leipzig), [3], 38,* (1889), 573-587.

[88] C. Wanji and Y.K. Cheung, Refined quadrilateral discrete Kirchhoff thin plate bending element, *Int. J. Num. Meth. Eng., 40,* (1997), 3937-3953.

[89] J.F. Wendt, Computational Fluid Dynamics, Springer-Verlag, (1992).

[90] J.L. Williams and W.J.H. Johnson, Elastic constants of composites formed from PMMA bone cement and anisotropic bovine tibial cancellous bone, *J. Biomechanics, 22(6/7),* (1989), 673-682.

[91] J.L. Williams, Prediction of some experimental results by Biot's theory, *Jour. Acoust. Soc. Am., 91,* (1992), 1106-1112.

[92] J.R. Willis, Bounds and self-consistent estimates for the overall properties of anisotropic composites, *J. Mech. Phys. Solids, 25,* (1977), 185-202.

[93] J.R. Willis, Variational and Related Methods for the Overall Properties of Composites, *Advances in Applied Mechanics, 21,* (1981), 1-78.

[94] J.R. Willis, Elasticity theory of composites, *Mechanics of solids,* the Rodney Hill 60th Anniversary Volume, Oxford: Pergamon, (1982), 653-686.

[95] J.R. Willis, The overall elastic response of composite materials, *J. Appl. Mech., 50,* (1983), 1202-1209.

[96] J.R. Willis, The structure of Overall Constitutive Relations for a Class of Nonlinear Composites, *IMA-Journal of Applied Mathematics, 43,* (1989), 231-242.

[97] O.C. Zienkiewicz and R.L. Taylor, The finite element method, Butterworth-Heinemann, (2000).

[98] T.I. Zohdi, J.T. Oden and G.J. Rodin, Hierarchical modeling of heterogeneous bodies, *Comp. Met. Appl. Mech. Eng., 138,* (1996), 273-298.

[99] T.I. Zohdi and P. Wriggers, A domain decomposition method for bodies with heterogeneous microstructure based on the material regularization, *Int. J. Sol. Struct., 36,* (1999), 2507-2525.

[100] T.I. Zohdi, P. Wriggers and C. Huet, A method of substructuring large-scale computational micromechanical problems, *Comp. Met. Appl. Mech. Eng., 190(13),* (2001), 5639-5656.

[101] T.I. Zohdi and P. Wriggers, Introduction to Computational Micromechanics, Springer Series in: Lecture Notes in Applied and Computational Mechanics, 20, (2005).

[102] P.K. Zysset, X.E. Guo, C.E. Hoffler, K.E. Moore and S.A. Goldstein, Elastic modulus and hardness of cortical and trabecular bone lamellae measured by nanoindentation in the human femur, *J. Biomechanics , 32,* (1999), 1005-1012.

[103] P.K. Zysset, A review of morphology-elasticity relationships in human trabecular bone: theories and experiments, *J. Biomechanics*, *36*, (2003), 1469-1485.

Mitteilungen aus dem Institut für Mechanik

Nr. 1 Theodor Lehmann:
Große elasto-plastische Formänderungen (Dezember 1976)

Nr. 2 Bogdan Raniecki/Klaus Thermann:
Infinitesimal Thermoplasticity and Kinematics of Finite Elastic-Plastic Deformations. Basic Concepts (Juni 1978)

Nr. 3 Wolfgang Krings:
Beitrag zur Finiten Element Methode bei linearem, viskoelastischem Stoffverhalten Stoffverhalten (Januar 1976)

Nr. 4 Burkhard Lücke:
Theoretische und experimentelle Untersuchen der zyklischen elastoplastischen Blechbiegung bei endlichen Verzerrungen (Januar 1976)

Nr. 5 Knut Schwarze:
Einfluß von Querschnittsverformungen bei dünnwandigen Stäben mit stetig gekrümmter Profilmittellinie (Februar 1976)

Nr. 6 Hubert Sommer:
Ein Beitrag zur Theorie des ebenen elastischen Verzerrungszustandes bei endlichen Formänderungen (Januar 1977)

Nr. 7 H. Stumpf/F. J. Biehl:
Die Methode der orthogonalen Projektionen und ihre Anwendungen zur Berechnung orthotroper Platten (März 1977)

Nr. 8 Albert Meyers:
Ein Beitrag zum optimalen Entwurf von schnellaufenden Zentrifugenschalen (April 1977)

Nr. 9 Berend Fischer:
Zur zyklischen, elastoplastischen Beanspruchen eines dickwandigen Zylinders bei endlichen Verzerrungen (April 1977)

Nr. 10 Wojciech Pietraszkiewicz:
Introduction to the Non-Linear Theory of Shells (Mai 1977)

Nr. 11 Wilfried Ullenboom:
Optimierung von Stäben unter nichtperiodischer dynamischer Belastung (Juni 1977)

Nr. 12 Jürgen Güldenpfennig:
Anwendung eines Modells der Vielkristallplastizität auf ein Problem gekoppelter elastoplastischer Wellen (Juli 1977)

Nr. 13 Pawel Rafalski:
Minimum Principles in Plasticity (März 1978)

Nr. 14 Peter Hilgers:
Der Einsatz eines Mikrorechners zur hybriden Optimierung und Schwingungsanalyse (Juli 1978)

Nr. 15 Hans-Albert Lauert:
Optimierung von Stäben unter dynamischer periodischer Beanspruchung bei Beachtung von Spannungsrestriktionen (August 1979)

Nr. 16 Martin Fritz:
Berechnund der Auflagerkräfte und der Muskelkräfte des Menschen bei ebenen Bewegungen aufgrund von kinematographischen Aufnahmen (Juli 1979)

Nr. 17 H. Stumpf/F. J. Biehl:
Approximations and Error Estimates in Eigenvalue Problems of Elastic Systems with Application to Eigenvibrations of Orthotropic Plates (Dezember 1979)

Nr. 18 Uwe Kohlberg:
Variational Principles and theirNumerical Application to Geometrically Nonlinear v. Karman Plates (Juli 1979)

Nr. 19 Heinz Antes:
Über Fehler und Möglichkeiten ihrer Abschätzung bei numerischen Berechnungen von Schalentragwerken (Januar 1980)

Nr. 20 Czeslaw Wozniak:
Large Deformations of Elastic and Non-Elastic Plates, Shells and Rods (März 1980)

Nr. 21 Maria K. Duszek:
Problems of Geometrically Non-Linear Theory of Plasticity (Juni 1980)

Nr. 22 Burkhard von Bredow:
Optimierung von Stäben unter stochastischer Erregung (Dezember 1980)

Nr. 23 Jürgen Preuss:
Optimaler Entwurf von Tragwerken mit Hilfe der Mehrzielmethode (Februar 1981)

Nr. 24 Ekkehard Großmann:
Kovarianzanalyse mechanischer Zufallsschwingungen bei Darstellung der mehrfachkorrelierten Erregungen durch stochastische Differentialgleichungen (Februar 1981)

Nr. 25 Dieter Weichert:
Variational Formulation and Solution of Boundary-Value Problems in the Theory of Plasticity and Application to Plate Problems (März 1981)

Nr. 26 Wojciech Pietraszkiewicz:
On Consistent Approximations in the Geometrically Non-Linear Theory of Shells (Juni 1981)

Nr. 27 Georg Zander:
Zur Bestimmung von Verzweigungslasten dünnwandiger Kreiszylinder unter kombinierter Längs- und Torsionslast (September 1981)

Nr. 28 Pawel Rafalski:
An Alternative Approach to the Elastic-Viscoplastic Initial-Boundary Value Problem (September 1981)

Nr. 29 Heinrich Oeynhausen:
Verzweigungslasten elastoplastisch deformierter, dickwandiger Kreiszylinder unter Innendruck und Axialkraft (November 1981)

Nr. 30 F.-J. Biehl:
Zweiseitige Eingrenzung von Feldgrößen beim einseitigen Kontaktproblem (Dezember 1981)

Nr. 31 Maria K. Duszek:
Foundations of the Non-Linear Plastic Shell Theory (Juni 1982)

Nr. 32 Reinhard Piltner:
Spezielle finite Elemente mit Löchern, Ecken und Rissen unter Verwendung von analytischen Teillösungen (Juli 1982)

Nr. 33 Petrisor Mazilu:
Variationsprinzipe der Thermoplastizität I. Wärmeausbreitung und Plastizität (Dezember 1982)

Nr. 34 Helmut Stumpf:
Unified Operator Description, Nonlinear Buckling and Post-Buckling Analysis of Thin Elastic Shells (Dezember 1982)

Nr. 35 Bernd Kaempf:
Ein Exremal-Variationsprinzip für die instationäre Wärmeleitung mit einer Anwendung auf thermoelastische Probleme unter Verwendung der finiten Elemente (März 1983)

Nr. 36 Alfred Kraft:
Zum methodischen Entwurf mechanischer Systeme im Hinblick auf optimales Schwingungsverhalten (Juli 1983)

Nr. 37 Petrisor Mazilu:
Variationsprinzipe der Thermoplastizität II. Gekoppelte thermmomechanische Prozesse (August 1983)

Nr. 38 Klaus-Detlef Mickley:
Punktweise Eingrenzung von Feldgrößen in der Elastomechanik und ihre numerische Realisierung mit Fundamental-Splinefuntionen (November 1983)

Nr. 39 Lutz-Peter Nolte:
Beitrag zur Herleitung und vergleichende Untersuchung geometrisch nichtlinearer Schalentheorien unter Berücksichtigung großer Rotationen (Dezember 1983)

Nr. 40 Ulrich Blix:
Zur Berechnung der Einschnürung von Zugstäben unter Berücksichtigung thermischer Einflüsse mit Hilfe der Finite-Element-Methode (Dezember 1983)

Nr. 41 Peter Becker:
Zur Berechnung von Schallfeldern mit Elemtmethoden (Februar 1984)

Nr. 42 Diemar Bouchard:
Entwicklung und Anwendung eines an die Diskrete-Fourier-Transformation angepaßten direkten Algorithmus zur Bestimmung der modalen Parameter linearer Schwingungssysteme (Februar 1984)

Nr. 43 Uwe Zdebel:
Theoretische und experimentelle Untersuchungen zu einem thero-plastischen Stoffgesetz (Dezember 1984)

Nr. 44 Jan Kubik:
Thermodiffusion Flows in a Solid with a Dominant Constituent (April 1985)

Nr. 45 Horst J. Klepp:
Über die Gleichgewichtslagen und Gleichgewichtsbereiche nichtlinearer autonomer Systeme (Juni 1985)

Nr. 46 J. Makowsky/L.-P. Nolte/H. Stumpf:
Finite In-Plane Deformations of Flexible Rods - Insight into Nonlinar Shell Problems (Juli 1985)

Nr. 47 Franz Karl Labisch:
Grundlagen einer Analyse mehrdeutiger Lösungen nichtlinearer Randwertprobleme der Elastostatik mit Hilfe von Variationsverfahren (August 1985)

Nr. 48 J. Chroscielewski/L.-P. Nolte:
Strategien zur Lösung nichtlinearer Probleme der Strukturmechanik und ihre modulare Aufbereitung im Konzept MESY (Oktober 1985)

Nr. 49 Karl-Heinz Bürger:
Gewichtsoptimierung rotationssymmetrischer Platten unter instationärer Erregung (Dezember 1985)

Nr. 50 Ulrich Schmid:
Zur Berechnung des plastischen Setzens von Schraubenfedern (Februar 1987)

Nr. 51 Jörg Frischbier:
Theorie der Stoßbelastung ortotroper Platten und ihr experimentelle Überprüfung am Beispiel einer unidirektional verstärkten CFK-Verbundplatte (März 1987)

Nr. 52 W. Tampczynski:
Strain history effect in cyclic plasticity (Juli 1987)

Nr. 53 Dieter Weichert:
Zum Problem geometrischer Nichtlinearitäten in der Plastizitätstheorie (Dezember 1987)

Nr. 54 Heinz Antes/Thomas Meise/Thomas Wiebe:
Wellenausbreitung in akustischen Medien Randelement-Prozeduren im 2-D Frequenzraum und im 3-D Zeitbereich (Januar 1988)

Nr. 55 Wojciech Pietraszkiewicz:
Geometrically non-linear theories of thin elastic shells (März 1988)

Nr. 56 Jerzy Makowski/Helmut Stumpf:
Finite strain theory of rods (April 1988)

Nr. 57 Andreas Pape:
Zur Beschreibung des transienten und stationären Verfestigungsverhaltens von Stahl mit Hilfe eines nichtlinearen Grenzflächenmodells (Mai 1988)

Nr. 58 Johannes Groß-Weege:
Zum Einspielverhalten von Flächentragwerken (Juni 1988)

Nr. 59 Peihua LIU:
Optimierung von Kreisplatten unter dynamischer nicht rotationssymmetrischer Last (Juli 1988)

Nr. 60 Reinhard Schmidt:
Die Anwendung von Zustandsbeobachtern zur Schwingungsüberwachung und Schadensfrüherkennung auf mechanische Konstruktionen (August 1988)

Nr. 61 Martin Pitzer:
Vergleich einiger FE-Formulierungen auf der Basis eines inelastischen Stoffgesetzes (Juli 1988)

Nr. 62 Jerzy Makowski/Helmut Stumpf:
Geometric structure of fully nonlinear and linearized Cosserat type shell theory (Dezember 1988)

Nr. 63 O. T. Bruhns:
Große plastische Formänderungen - Bad Honnef 1988 (Januar 1989)

Nr. 64 Khanh Chau Le/Helmut Stumpf/Dieter Weichert:
Variational principles of fracture mechanics (Juli 1989)

Nr. 65 Guido Obermüller:
Ein Beitrag zur Strukturoptimierung unter stochastischen Lasten (Juni 1989)

Nr. 66 Herbert Diehl:
Ein Materialmodell zur Berechnung von Hochgeschwindigkeitsdeformationen metallischer Werkstoffe unter besonderer Berücksichtigung der Schädigung durch Scherbänder (Juni 1989)

Nr. 67 Michael Geis:
Zur Berechnund ebener, elastodynamischer Rißprobleme mit der Randelementmethode (November 1989)

Nr. 68 Günter Renker:
Zur Identifikation nichtlinearer strukturmechanischer Systeme (November 1989)

Nr. 69 Berthold Schieck:
Große elastische Dehnungen in Schalen aus hyperelastischen inkompressiblen Materialien (November 1989)

Nr. 70 Frank Szepan:
Ein elastisch-viskoplastisches Stoffgesetz zur Beschreibung großer Formänderungen unter Berücksichtigung der thermomechanischen Kopplung (Dezember 1989)

Nr. 71 Christian Scholz:
Ein Beitrag zur Gestaltsoptimierung druckbelasteter Rotationsschalen (Dezember 1989)

Nr. 72 J. Badur/H. Stumpf:
On the influence of E. and F. Cosserat on modern continuum mechanics and field theory (Dezember 1989)

Nr. 73 Werner Fornefeld:
Zur Parameteridentifikation und Berechnung von Hochgeschwindigkeitsdeformationen metallischer Werkstoffe anhand eines Kontinuums-Damage-Modells (Januar 1990)

Nr. 74 J. Saczuk/H. Stumpf:
On statical shakedown theorems for non-linear problems (April 1990)

Nr. 75 Andreas Feldmüller:
Ein thermoplastisches Stoffgesetz isotrop geschädigter Kontinua (April 1991)

Nr. 76 Ulfert Rott:
Ein neues Konzept zur Berechnung viskoplastischer Strukturen (April 1991)

Nr. 77 Thomas Heinrich Pingel:
Beitrag zur Herleitung und numerischen Ralisierung eines mathematischen Modells der menschlichen Wirbelsäule (Juli 1991)

Nr. 78 O. T. Bruhns:
Große plastische Formänderungen - Bad Honnef 1991 (Dezember 1991)

Nr. 79 J. Makowski/J. Chroscielewski/H. Stumpf:
Computational Analysis of Shells Undergoing Large Elastic Deformation Part I:Theoretical Foundations

Nr. 80 J. Chroscielewski/J. Makowski/H. Stumpf:
Computational Analysis of Shells Undergoing Large Elastic Deformation Part II: Finite Element Implementation

Nr. 81 R. H. Frania/H. Waller:
Entwicklung und Anwendung spezieller finiter Elemente für Kerbspannungsprobleme im Maschienebau (Mai 1992)

Nr. 82 B. Bischoff-Beiermann:
Zur selbstkonsistenten Berechnung von Eigenspannungen in polykristallinem Eis unter Berücksichtigung der Monokristallanisotropie (Juli 1992)

Nr. 83 J. Pohé:
Ein Beitrag zur Stoffgesetzentwicklung für polykristallines Eis (Februar 1993)

Nr. 84 U. Kikillus:
Ein Beitrag zum zyklischen Kiechverhalten von Ck 15 (Mai 1993)

Nr. 85 T. Guo:
Untersuchung des singulären Rißspitzenfeldes bei stationärem Rißwachstum in verfestigendem Material (Juni 1993)

Nr. 86 Achim Menne:
Identifikation der dynamischen Eigenschaften von hydrodynamischen Wandlern (Januar 1994)

Nr. 87 Uwe Folchert:
Identifikation der dynamischen Eigenschaften Hydrodynamischer Kopplungen (Januar 1994)

Nr. 88 Jörg Körber:
Ein verallgemeinertes Finite-Element-Verfahren mit asymptotischer Stabilisierung angewendet auf viskoplastische Materialmodelle (April 1994)

Nr. 89 Peer Schieße:
ein Beitag zur Berechnung des Deformationsverhaltens anisotrop geschädigter Kontinua unter Berücksichtigung der thermoplastischen Kopplung (April 1994)

Nr. 90 Egbert Schopphoff:
Dreidimensionale mechanische Analyse der menschlichen Wirbelsäule (Juli 1994)

Nr. 91 Christoph Beerens:
Zur Modellierung nichtlinearer Dämpfungsphänomene in der Strukturmechanik (Juli 1994)

Nr. 92 K. C. Le/H. Stumpf:
Finte elastoplasticity with microstructure (November 1994)

Nr. 93 O. T. Bruhns:
Große plastische Formänderungen - Bad Honnef 1994 (Dezember 1994)

Nr. 94 Armin Lenzen:
Untersuchung von dynamischen Systemen mit der Singulärwertzerlegung - Erfassung von Strukturveränderungen (Dezember 1994)

Nr. 95 J. Makowski/H. Stumpf:
Mechanics of Irregular Shell Structures (Dezember 1994)

Nr. 96 J. Chroscielewski/J. Makowski/H. Stumpf:
Finte Elements for Irregular Nonlinear Shells (Dezember 1994)

Nr. 97 W. Krings/A. Lenzen/u. a.:
Festschrift zum 60. Geburtstag von Heinz Waller (Februar 1995)

Nr. 98 Ralf Podleschny:
Untersuchung zum Instabilitätsverhalten scherbeanspruchter Risse (April 1995)

Nr. 99 Bernd Westerhoff:
Eine Untersuchung zum geschwindigkeitsabhängigen Verhalten von Stahl (Juli 1995)

Nr. 100 Marc Mittelbach:
Simulation des Deformations- und Schädigungsverhaltens beim Stoßversuch mit einem Kontinuums-Damage-Modell (Dezember 1995)

Nr. 101 Ulrich Hoppe:
Über grundlegende Konzepte der nichtlinearen Kontinuumsmechanik und Schalentheorie (Mai 1996)

Nr. 102 Marcus Otto:
Erweiterung des Kaustikenverfahrens zur Analyse räumlicher Spannungskonzentrationen (Juni 1996)

Nr. 103 Horst Lanzerath:
Zur Modalanalyse unter Verwendung der Randelementemethode (Juli 1996)

Nr. 104 Andreas Wichtmann Entwicklung eines thermodynamisch konsistenten Stoffgesetzes zur Beschreibung der Reckalterung (August 1996)

Nr. 105 Bjarne Fosså Ein Beitrag zur Fließflächenmessung bei vorgedehnten Stoffen (Oktober 1996)

Nr. 106 Khanh Cha Le:
Kontinuumsmechanisches Modellieren von Medien mit veränderlicher Mikrostruktur (Dezember 1996)

Nr. 107 Holger Behrens:
Nichtlineare Modellierung und Identifikation hydrodynamischer Kupplungen mit allge- meinen diskreten Modellansätzen (Januar 1997)

Nr. 108 Johannes Moosheimer:
Gesteuerte Schwingungsdämpfung mit Elektrorheologischen Fluiden (Juli 1997)

Nr. 109 Dirk Klaus Anding:
Zur simultanen Bestimmung materialabhängiger Koeffizienten inelastischer Stoffgesetze (Oktober 1997)

Nr. 110 Stephan Weng:
Ein Evolutionsmodell zur mechanischen Analyse biologischer Strukturen (Dezember 1997)

Nr. 111 Michael Straßberger:
Aktive Schallreduktion durch digitale Zustandsregelung der Strukturschwingungen mit Hilfe piezo-keramischer Aktoren (Dezember 1997)

Nr. 112 Hans-Jörg Becker:
Simultation des Deformationsverhaltens polykristallinen Eises auf der Basis eines monokristallinen Stoffgesetzes (Dezember 1997)

Nr. 113 Thomas Nerzak:
Modellierung und Simulation der Ausbreitung adiabatischer Scherbänder in metallischen Werkstoffen bei Hochgeschwindigkeitsdeformationen (Dezember 1997)

Nr. 114 O. T. Bruhns:
Große plastische Formänderungen (März 1998)

Nr. 115 Jan Steinhausen:
Die Beschreibung der Dynamik von Antriebssträngen durch Black-Box-Modelle hydrodynamischer Kupplungen (August 1998)

Nr. 116 Thomas Pandorf:
Experimentelle und numerische Untersuchungen zur Kerbspitzenbeanspruchung bei schlagbelasteten Biegeproben (August 1998)

Nr. 117 Claus Oberste-Brandenburg:
Ein Materialmodell zur Beschreibung der Austenit-Martensit Phasentransformation unter Berücksichtigung der transformationsinduzierten Plastizität (Juni 1999)

Nr. 118 Michael Märtens:
Regelung mechanischer Strukturen mit Hilfe piezokeramischer Stapelaktoren (Dezember 1999)

Nr. 119 Dirk Kamarys:
Detektion von Systemveränderungen durch neue Identifikationsverfahren in der experimentellen Modalanalyse (Dezember 1999)

Nr. 120 Wolfgang Hiese:
Gültigkeitskriterien zur Bestimmung von Scherbruchzähigkeiten (Januar 2000)

Nr. 121 Peter Jaschke:
Mathematische Modellierung des Betriebsverhaltens hydrodynamischer Kupplungen mit hybriden Modellansätzen (Februar 2000)

Nr. 122 Stefan Müller:
Zum Einsatz von semi-aktiven Aktoren zur optimalen Schwingungsreduktion in Tragwerken (Februar 2000)

Nr. 123 Dirk Eichel:
Zur Kondensation strukturdynamischer Aufgaben mit Hilfe von Polynommatrizen (Juni 2000)

Nr. 124 Andreas Bürgel:
Bruchmechanische Kennwerte beim Wechsel im Versagensverhalten dynamisch scherbeanspruchter Risse (August 2000)

Nr. 125 Daniela Lürding:
Modellierung großer Deformationen in orthotropen, hyperelastischen Schalenstrukturen (März 2001)

Nr. 126 Thorsten Quent:
Ein mikromechanisch begründetes Modell zur Beschreibung des duktilen Verhaltens metallischer Werkstoffe bei endlichen Deformationen unter Berücksichtigung von Porenschädigung (Mai 2001)

Nr. 127 Ndzi C. Bongmba:
Ein finites anisotropes Materialmodell auf der Basis der Hencky-Dehnung und der logarithmischen Rate zur Beschreibung duktiler Schädigung (Mai 2001)

Nr. 128 Henning Schütte:
Ein finites Modell für spröde Schädigung basierend auf der Ausbreitung von Mikrorissen (August 2001)

Nr. 129 Henner Vogelsang:
Parameteridentifikation für ein selbstkonsistentes Stoffmodell unter Berücksichtigung von Phasentransformationen (Dezember 2001)

Nr. 130 Jörn Mosler:
Finite Elemente mit sprungstetigen Abbildungen des Verschiebungsfeldes für numerische Analysen lokalisierter Versagenszustände (Dezember 2002)

Nr. 131 Karin Preusch:
Hierarchische Schalenmodelle für nichtlineare Kontinua mit der p-Version der Finite-Element Methode (Mai 2003)

Nr. 132 Christoph Müller:
Thermodynamic modeling of polycrystalline shape memory alloys at finite strains (August 2003)

Nr. 133 Martin Heiderich:
Ein Beitrag zur zerstörungsfreien Schädigungsanalyse (Juni 2004)

Nr. 134 Raoul Costamagna:
Globale Materialbeziehungen für das geklüftete Gebirge (Juli 2004)

Nr. 135 Markus Böl:
Numerische Simulation von Polymernetzwerken mit Hilfe der Finite-Elemente-Methode (Januar 2005)

Nr. 136 Gregor Kotucha:
Regularisierung von Problemen der Topologieoptimierung unter Einbeziehung von Dichtegradienten (August 2005)

Nr. 137 Michael Steiner:
Deformations- und Versagensverhalten innendruckbeanspruchter Stahlrohre durch Stoßbelastung (Februar 2006)

Nr. 138 Dirk Bergmannshoff:
Das Instabilitätsverhalten zug-/scherbeanspruchter Risse bei Variation des Belastungspfades (Dezember 2006)

Nr. 139 Olaf Schilling:
Über eine implizite Partikelmethode zur Simulation von Umformprozessen (Januar 2007)

Nr. 140 Jörn Mosler:
On the numerical modeling of localized material failure at finite strains by means of variational mesh adaption and cohesive elements (Mai 2007)

Nr. 141 Rainer Fechte-Heinen:
Mikromechanische Modellierung von Formgedächtnismaterialien (Juni 2007)

Nr. 142 Christian Grabe:
Experimental testing and parameter identification on the multidimensional material behavior of shape memory alloys (Juni 2007)

Nr. 143 Markus Peters:
Modellierung von Rissausbreitung unter Verwendung der p-Version der XFEM mit einer adaptiven Integrationsmethode (Juli 2007)

Nr. 144 Claus Oberste-Brandenburg:
Thermomechanical modeling of shape memory alloys at different length scales (Juli 2007)

Nr. 145 Stefan Reichling:
Das inverse Problem der quantitativen Ultraschallelastografie unter Berücksichtigung großer Deformationen (Juli 2007)

Nr. 146 Kianoush Molla-Abbasi:
A Consistent Anisotropic Brittle Damage Model Based on the Concept of Growing Elliptical Cracks (Januar 2008)

Nr. 147 Sandra Ilic:
Application of the multiscale FEM to the modeling of composite materials (August 2008)

Mitteilungen aus dem Institut für Mechanik
RUHR-UNIVERSITÄT BOCHUM
Nr. 147

978-3-935892-25-4